FORSCHUNGSZENTRUM DRESDEN-ROSSENDORF

Formation of Si Nanocrystals for Single Electron Transistors by Ion Beam Mixing and Self-Organization – Modeling and Simulation

D I S S E R T A T I O N

zur Erlangung des akademischen Grades

Doctor of Philosophy
(Ph. D.)

vorgelegt

dem Bereich Mathematik und Naturwissenschaften der Technischen Universität Dresden

von

Thomas Prüfer

geboren am 14. April 1986 in Olesno, Polen

Eingereicht am 20.10.2019

Die Dissertation wurde in der Zeit von März/2016 bis August/2019 am Helmholtz-Zentrum Dresden-Rossendorf angefertigt

Gutachter:

1. Prof. Dr. rer. nat. habil. Jürgen Faßbender, Helmholtz-Zentrum Dresden-Rossendorf
2. Professor Kai Nordlund, Ph. D., University of Helsinki

Abstract

The replacement of the conventional field effect transistor (FET) by single electron transistors (SET) would lead to high energy savings and to devices with significantly longer battery life. There are many production approaches, but mostly for specimens in the laboratory. Most of them suffer from the fact that they either only work at cryogenic temperatures, have a low production yield or are not reproducible and each unit works in a unique way. A room temperature (RT) operating SET can be configured by inserting a small (few nm diameters) Si-Nanocrystal (NC) into a thin (<10 nm) SiO_2 interlayer in Si. Industrial production has so far been excluded due to a lack of manufacturing processes. Classical technologies such as lithography fail to produce structures in this small scale. Even electron beam lithography or extreme ultraviolet lithography are far from being able to realize these structures in mass production.

However, self-organization processes enable structures to be produced in any order of magnitude down to atomic sizes. Earlier studies realized similar systems using a layer of Si-NCs to fabricate a non-volatile memory by using the charge of the NCs for data storage. Based on this, it is very promising to use it for the realization of the SET. The self-organization depends only on the start configuration of the system and the boundary conditions during the process. These macroscopic conditions control the self-formed structures. In this work, ion beam irradiation is used to form the initial configuration, and thermal annealing is used to drive self-organization. A $Si/SiO_2/Si$ stack is irradiated and transforms the stack into $Si/SiO_x/Si$ by ion beam mixing (IBM) of the two Si/SiO_2 interfaces. The oxide becomes metastable and the subsequent thermal treatment induces self-organization, which might leave a single Si-NC in the SiO_2 layer for a sufficiently small mixing volume. The transformation of the planar SiO_x layer (restriction only in one dimension) into a small SiO_x volume (restriction in all three dimensions) is done by etching nanopillars with a diameter of less than 10nm. This forms a small SiO_x plate embedded between two Si layers. The challenge is to control the self-organization process. In this work, simulation was used to investigate dependencies and parameter optimization.

The ion mixing simulations were performed using binary collision approximation (BCA), followed by kinetic Monte Carlo (KMC) simulations of the decomposition process, which gave good qualitative agreement with the structures observed in related experiments. Quantitatively, however, the BCA simulation seemed to overestimate the mixing effect. This is due to the neglect of the positive entropy of the $Si\text{-}SiO_2$ system mixing, i.e. the immiscibility counteracts the collisional mixing. The influence of this mechanism increases with increasing ion fluence. Compared to the combined BCA and KMC simulations, a larger ion mixing fluence has to be applied experimentally to obtain the predicted nanocluster morphology. To model the ion beam mixing of the Si/SiO_2 interface, phase field methods have been applied to describe the influence of chemical effects during the irradiation of buried SiO_2 layers by 60 keV Si^+ ions at RT and thermal annealing at 1050°C. The ballistic collisional mixing was modeled by an approach using Fick's diffusion equation, and the chemical effects and the annealing were described by the Cahn Hilliard equation. By that, it is now possible to predict composition profiles of Si/SiO_2 interfaces during irradiation. The results are in good agreement with the experiment and are used for the predictions of the NCs formation in the nanopillar.

For the thermal treatment model extensions were also necessary. The KMC simulations of Si-SiO_2 systems in the past were based on normed time and temperature, so that the diffusion velocity of the components was not considered. However, the diffusion of Si in SiO_2 and SiO_2 in Si differs by several orders of magnitude. This cannot be neglected in the thermal treatment of the Si/SiO_2 interface, because the processes that differ in speed in this order of magnitude are only a few nanometers apart. The KMC method was extended to include the different diffusion coefficients of the Si-SiO_2 system. This allows to extensively investigate the influence of the diffusion. The phase diagram over temperature and composition was examined regarding decomposition (nucleation as well as spinodal decomposition) and growing of NCs.

Using the methods and the knowledge gained about the system, basic simulations for the individual NC formation in the nanopillar were carried out. The influence of temperature, diameter, and radiation fluence was discussed in detail on the basis of simulation results.

Content

Abbreviations

a.u.	arbitrary units
APCVD	plasma enhanced chemical vapor deposition
BCA	binary collision approximation
BCC	body-centered cubic
BJT	bipolar junction transistor
CMOS	complementary metal-oxide-semiconductor
CVD	chemical vapor deposition
DFT	density functional theory
EFTEM	electron filtered transmission electron microscopy
FCC	face-centered cubic
FET	field effect transistor
GT	Gibbs-Thomson
IBM	ion beam mixing
KMC	Kinetic Monte-Carlo
LPCVD	low pressure chemical vapor deposition
LSW	Lifschitz-Slyozov-Wagner
MC	Monte Carlo
MCS	Monte-Carlo steps
MD	molecular dynamics
MOS	metal-oxide-semiconductor
MOSFET	metal-oxide-semiconductor field effect transistor
NC	nanocrystal
NN	nearest neighbor
NNN	next-nearest neighbor
NPN	negative-positive-negative
OR	Ostwald Ripening
PECVD	plasma enhanced chemical vapor deposition
PVD	physical vapor deposition
RT	room temperature
SC	simple cubic
SED	single electron device
SET	single electron transistor
SRIM	stopping and range of ions in matter
TRIDYN	TRIM.SP dynamical
TRIM	transport of ions in matter
UHVCVD	ultrahigh vacuum chemical vapor deposition

1 Introduction

In the microelectronics industry, the most important task in improving the performance of electronic devices has been to reduce the size of semiconductor components. Smaller electronics require less power and allow the number of computing units per volume to be increased. This saves energy and manufacturing costs. Since the dimensions of the conventional metal-oxide-semiconductor field-effect transistor (MOSFET) are reduced to the nanometer range, engineers face more fundamental challenges that have not been an issue until now, such as quantum effects or final limits in mass production processes [1]. In order to continue this development through further miniaturization, physical barriers must be overcome by new technologies. Some promising future devices are based on completely new approaches, such as the storage of data in DNA, quantum computers, or spin waves. However, most of them are not compatible with established production lines based on complementary metal oxide semiconductor (CMOS) technology. An outstanding group of these technologies is based on single electrons. The basic idea of so-called single electron devices (SED) is to use the smallest controllable physical particle for the construction of memory and logic. While this approach promises to be the most energy-efficient technology for microelectronics, it is still compatible with today's manufacturing processes. Using a single electron to store a bit of data or perform a logical operation gives engineers the most powerful tool for developing future electronic devices.

1.1 From Field Effect Transistors to Single Electron Transistors

The idea of today's most valuable electrical device—the field-effect transistor (FET)—dates back to 1925, when Julius Edgar Lilienfeld applied for a patent for his "Apparatus for controlling electrical currents" [2]. At that time, there was no semiconductor with the required degree of purity, and this FET patent remained overlooked [3]. Another group of transistors uses a current instead of a field to control it. These transistors were demonstrated in 1947 by William Shockley [4] and are called bipolar junction transistors (BJT). They replaced the usual vacuum tubes [5] and enabled the introduction of integrated circuits [6], [7] in 1959. The transistor made it possible for electronics engineers to design electronic circuits much more effectively than with individual electrical components. The reduction of the component packet density made it possible to achieve high computing power and large data memory. However, BJT suffers from high power dissipation since it requires a running control current when switched on. The voltage-controlled MOSFET solved this problem and paved the way for the development of microelectronics.

The field of microelectronics actually began in 1963 when the first integrated CMOS circuits [8] based on the MOSFET, were introduced. The most important improvement was a much lower input current compared to the BJT that enabled engineers to integrate more and more components and increase the density and complexity of their devices. The metal-oxide-semiconductor (MOS) basic structure consists of a silicon (Si) substrate, a layer of silicon dioxide (SiO_2), and a metal layer on top. This structure corresponds to a planar capacitor with the Si substrate and the metal layer as electrodes. If one considers a certain voltage between two strong n-doped regions on a p-doped substrate, the p-

doped substrate region acts as an insulator. The basic architecture of a so-called NPN (negative-positive-negative) field effect transistor is created by adding a SiO_2 layer and a metal layer to it and create a MOS structure. By applying a certain voltage to both electrodes (metal and Si-p-doped substrate), the capacitor (SiO_2) is charged and causes exhaustion of the positively charged holes in the p-doped Si substrate. This gives a thin area near the Si/SiO_2 interface the conductive character of an n-doped Si. For a sufficiently high voltage (threshold voltage), the layer provides a conductive area and an electron current is generated between drain and source. Because this assembly generally does not depend on any kind of size limitation, the well-known scaling of CMOS technology could begin. Around this time, Gordon Moore introduced his popular Moore's Law [9]: An increase in integration density by a factor of two per year would minimize the cost per transistor.

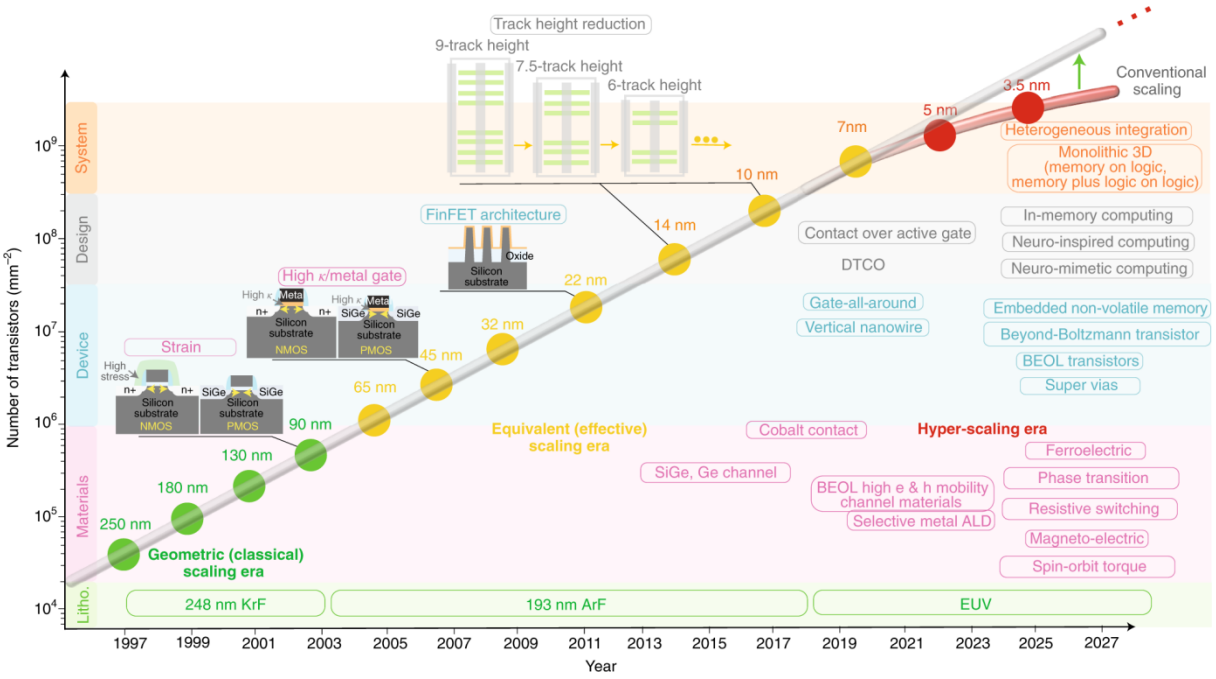

Figure 1-1: Three eras of CMOS technology scaling: (Green) The classical scaling era, which was characterized by only optimizing fabrication processes and reducing the size of the gate length, continued from the 1970s until 2003. (Yellow) The "equivalent" scaling era was based on innovations of the used materials. (Red) The hyper-scaling era is predicted to be based on innovations in device integration technologies (e.g., devices with logic and memory functions). Taken from ref. [10].

Surprisingly, the industry has succeeded in keeping pace with this statement for many decades. The basic approach is to reduce gate length and width to reduce run time, drain current, and threshold voltage. This paves the way for increasing the frequency and density of component packages [11]. Figure 1-1 shows an overview published by Sayeef Salahuddin in *Nature Electronics* in 2018. It shows the transistor density of the "three eras of CMOS technology scaling". The classical scaling began when the first MOSFET was introduced in the 1970s. There are two main approaches—constant field scaling and constant voltage scaling [12]—in which the structure size gets smaller. To keep the field constant, the voltage needs to be decreased; to keep the voltage constant, the current needs to be increased. If the structure size is reduced by the factor k ($k < 1$), the power consumption decreases by k^2 and the switching time by k [12]. This increases the number of circuits per area without increasing the total power dissipation. Because the major drawback in this system is a different voltage for the

newer chips, the industry used constant voltage scaling for years. These approaches made it possible to downgrade the first MOSFET to 100 nm without any major problems.

However, since the structure sizes began entering dimensions where quantum effects start to have an impact, fabrication became limited by fundamental issues [13] and new materials and processes needed to be invented. This is the second era of scaling (see Figure 1-1). For example, new dielectric materials, such as hafnium silicon oxynitride, replaced SiO_2 in order to reduce the leakage current through tunneling effects [14]. The continuous problem of heat dissipation [15]–[17] was overcome again and again by more and more complex innovations so that the industry was able to keep pace with Moore's Law over a rather long time. The non-planar Fin-FET [18] is now the best choice to further advance scaling in the sub-10 nm range. But FinFETs have also defined their final limits due to quantum effects [19].

There are several approaches based on graphene [20], MoS2 devices [21], or heterojunction tunnel field effect transistors [22], [23]. These technologies are supposed to enable the era of hyper-scaling (see Figure 1-1) that might even overtake the conventional scaling trend, according to Moore's Law. Single electron devices are one of the most promising approaches because they are based on the smallest controllable particle, can be made compatible with today's CMOS technology and can be introduced into today's production lines [24]–[26]. However, they are still far beyond application and might even come after the era of hyper-scaling (see Figure 1-1). The biggest problems are still new approaches for manufacturing processes and innovations in circuit diagram creation [26].

1.2 Outline of the Thesis

This work focuses on simulation and modelling within the framework of the IONS4SET project with the aim of developing a manufacturing process for the mass production of SETs, which can realize computing units for microelectronic devices. The main approach is *self-organization* leading to the production and positioning of the necessary structures. Therefore the processes of *ion irradiation* and *thermal treatment* are utilized. In order to enable the application of SETs in devices, it is necessary to ensure the reliability of the production process. The functionalitiy of single elctron devices is strongly sensitive to geometrical variations what leads to a different behavior of the transistor and is unusable for application in an integrated circuit. Chapter 6 discusses the influence of different manufacturing conditions (ion irradiation and thermal treatment) on the reliability of the individual structures. In order to obtain and interpret these results, it is necessary for:

Accurate models that can reproduce existing experimental results by simulations. The used approaches in this thesis are the kinetic Monte Carlo Method (thermal treatment), calculations using the Binary Collision Approximation and Phase Field models (ion irradiation). During the IONS4SET project, a discrepancy was found between the simulation results and experimental results. Therefore, this difference was investigated and modeled in Chapter 5. For that, the experimental results for diffusion and solubility of Si and O in Si and SiO_2 had to be described more accurately than in the past. For this, the kinetic Monte Carlo model was extended (described in Chapter 4.1).

Parameters for the models and manufacturing steps were extracted from the experimental results of the project and data from the literature. This was done for the kinetic Monte Carlo model in

Chapter 4.2 by a comprehensive literature search. For the new approach to model the ion irradiation in Chapter 5, the model parameters were extracted from experiments within the IONS4SET project.

Knowledge of how the system behaves in different isolated situations. The main component of the SET is a single nanocrystal (diameter <4nm). The formation of this nanocrystal (NC) is based on nucleation, interactions between existing NCs, spinodal decomposition, relaxation of interfaces and interactions of interfaces with existing NCs. To correctly interpret the results of individual NCs in the SET-assembly, it is necessary to understand the behavior and dominant interactions for each of the individual processes. This is simulated and discussed in Chapter 4.3.

This work is divided into five main subsections:

1. Introduction of the SET, challenges, opportunities and the new fabrication process is presented in Chapter 2.
2. The study of the first step of SET production (ion irradiation) is discussed in Chapter 3. The irradiation process must be controlled, limits identified, and optimal parameters determined. The individual processes during irradiation (displacement of target atoms and implantation) are also discussed.
3. The second production step (thermal treatment) is modeled, parameterized, and investigated in Chapter 4. Each important individual processes (Si/SiO_2 interface relaxation, growth, etc.) are simulated and discussed. Important conclusions for the interpretation of the results in Chapter 6 are drawn.
4. The discrepancy between experimental and simulation results is discussed in Chapter 5 by presenting and parameterizing a new model.
5. Chapter 6 will examine different influences on the production process of the SET. The results of Chapter 5 for ion irradiation will be used as input configurations to simulate the thermal treatment. The results of Chapters 3 and 4 will be used to interpret and discuss the observations.

2 Manufacturability of a Single Electron Transistor

The idea of the single electron transistor (SET) dates back to 1951 when C. J. Gorter successfully measured the Coulomb blockade [27]. However, there was a long time before it began to play a role in microelectronics. The first SET was realized in the mid-1980s and presented by Averin and Likharve [28]. They showed how it was possible to control the charging and discharging of a conducting particle and realize a flow of single electrons. This conducting particle is also known as the *island.*

Such an island charged with a single electron results in an extremely sensitive system, paving the way for a variety of applications. SETs based on nanowires [29], [30] have already proven themselves at room temperature. They can be used as a charge sensor [31]. Placing a second element (tube, wire, nano particle) near the SET influences the conductivity, resulting in an ultrasensitive signal dependence on the state of charge of this element in real time [31]–[33]. With this charge detection, other devices, such as detectors for infrared radiation [34] or ultra-sensitive microwaves [35], can also be realized. The conductance of SETs is sensitive enough to detect a phonon excited electron [36], [37] or different spins [38]–[41]. Other applications that use the sensitivity of an SET are the ultra-sensitive electrometer [42], [43] and electron spectroscopy [44].

Unfortunately, the realization of computational logic by SETs is not possible for microelectronic devices due to several technological limitations. An XOR (Exclusive OR) gate was realized in 2000 and working at 40K [45]. But realizing integrated circuits by just replacing FETs with SETs is not the optimal approach. The integration into logic cells has been successfully realized [46] with strong advantages over classical FET circuits, since the discrete charging levels allow multiple value operations [47]. So integrated circuits in a different, new way may allow multi-valued logic and memory [48]–[53].

The communication of an SET with the rest of the electronic device is also an important issue that can be solved by a hybrid SET–FET architecture [54]. The logic is realized by a number of SETs and communication with the external electronics by FETs. These FETs then work essentially as signal amplifiers, which allow the CMOS technology to be further reduced in size without sacrificing the FET as the main component. Nevertheless, the main task—logical operation—is performed by the extremely power-saving SETs. One interesting approach is the so-called SETMOS architecture that includes a SET with CMOS in a hybrid technology that realizes logic building blocks [55]. If operation at low temperature is acceptable, like for some microscopic applications that take place at cryogenic temperature, the realization is less crucial. Individual SETs have already been used in sensors for scanning microscopes [56]–[58] and even as assembled arrays [57] with a yield of 60%.

It is not yet possible to realize the SET as a technology for microelectronics, but the revolutionary possibilities in the application cause a high interest in research and development. Computing units, memory, and sensors could be realized by interactions between individual electrons. The current thesis concentrates on the realization of a manufacturing process for SETs.

2.1 The Physics of a Single Electron Transistor

A SET bases on the physical effect of the coulomb blockade. It was first explained in 1951 [27] and observed in 1962 [59]. To understand the physics of a SET, consider an uncharged spherical particle as the island in a vacuum. Figure 2-1 schematically shows how placing one electron onto such an island (a) increases the charge by $-\mathrm{e}$ and creates an electric field $\vec{E}$. This field generates a repulsive force $-\mathrm{e}\vec{E}$ and adding a second electron will then require more energy, which can be calculated as

$$E_{\mathrm{C}} = \int \vec{F} = \frac{\mathrm{e}^2}{2C}, \tag{1}$$

where C is the total capacity of the island and e is the charge of an electron. The capacity scales proportionally with the size of the island. For larger islands, less energy is therefore needed to add the second electron. Above a certain size, the energy is in the range of thermal noise and can no longer be determined. In order to use the effect for technological applications, this energy difference must be as *large* as possible and thus the island as *small* as possible.

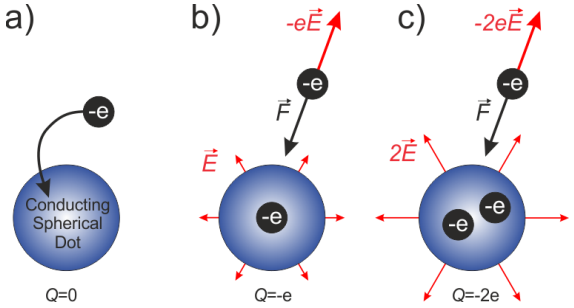

Figure 2-1: The Coulomb blockade is shown schematically. A spherical uncharged conducting particle (a) is charged by one electron, (b) by two electrons, and (c) gets the charge $Q = -\mathrm{e}$ and $Q = -2\mathrm{e}$, respectively.

Technological Usage of the Coulomb Blockade

The repulsive force of the charged island can be reduced by applying an overlapping electric field. This can be achieved by placing an electrode (gate electrode) close to the island and charge it with the gate charge Q_{C}. This electrode must be placed so close that it has a significant influence on the island, but so far, interactions such as tunneling between the gate and island are avoided. After lowering the necessary potential by the electric field, the energy (Equation (1)) is reduced and more excess electrons can be added to the island. These electrons must be provided by another electrode (source electrode), which must also be placed near the island. This time, the distance must be so small that electrons can tunnel onto the island. As soon as the potential of the island is sufficiently reduced by the gate electrode, the electrons begin to flow until the Coulomb blockade is rebuilt. After the repulsion force has compensated the electric field of the gate electrode, the flow stops and the island is charged. A subsequent decrease of the gate charge Q_{C} leads to an increase in the repulsion force of the electric field around the island and makes it necessary to dissipate the excess electrons. This can be achieved by adding a third electrode (drain electrode) with a lower potential than at the island. If this is placed close enough, the excess electrons can flow by tunneling onto the drain electrode until the island is neutral again. Figure 2-2 schematically shows the potential energies along the electrons pathway at a closed circuit (a) & (b) and an open circuit (c) & (d). If the gate contact is neutral, the potential of the island is higher than the potential of the source contact and

the Coulomb blockade prohibits tunneling from the source to the island. The configuration of the electrons is shown in Figure 2-2 (a) and the corresponding energy levels in (b). To enable tunneling, it is necessary for the electrostatic energy of the system to decrease. This energy can be expressed as

$$E_{\mathrm{el}} = \frac{(n_{\mathrm{ND}}\mathrm{e} - Q_{\mathrm{C}})^2}{2C}, \tag{2}$$

where n_{ND} is the number of electrons on the island. Figure 2-2 (c) and (d) show the electron configuration and potential energies when the potential on the gate electrode is increased. The potential of the island is reduced, the Coulomb blockade disappears, and electron tunneling is possible from the source contact to island and from island to the drain contact. The increase of the island potential by switching off the gate voltage stops this flow again. This is the functional principle of a conventional FET. But instead of *conducting*, the electrons *tunnel,* and instead of *hundreds* of electrons at the same time, it is only *one* electron after another.

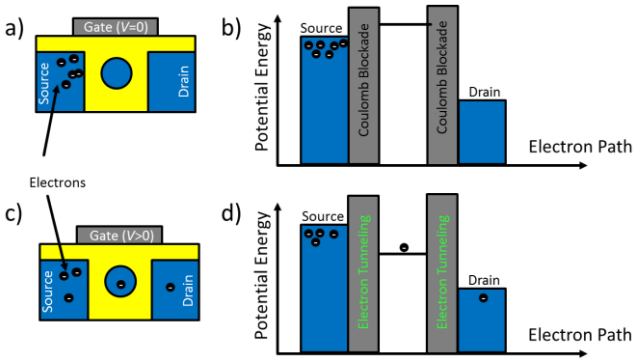

Figure 2-2: Schematic illustration of the potential energy levels of a SET to the corresponding configuration of electrons in the case of a closed circuit (a) & (b) and in the case of an open circuit (c) & (d).

2.2 Room Temperature Operation and Mass Production

Building prototypes in the laboratory is the first step for a successful technology. But a new technology has a hard road to go from individual prototypes to mass production. Finally, it needs to work reliably and be produced at a low cost. Unfortunately, there was no way to realize a SET that can be operated at room temperatures. The thermal noise has destroyed any significant signal for higher temperatures. Nowadays, it is possible to create smaller structures so that the Coulomb blockade appears strong enough to surpass the temperature fluctuations and allow operation even at room temperature. However, even the most promising manufacturing processes are far from being used for industrial production. Further, the most important requirement for the cooperation of the individual transistors is a reliable reproduction, whereby the two most important physical effects - tunneling and Coulomb blockade - are very sensitive to geometric variations such as size, position and shape of the island [60], [61]. The aim of research in this field is to develop a process that can guarantee the constancy of these properties.

Fabrication Approaches

Basically, there are three different types of islands used for a SET: a metal nanowire [62], [63], a single nanoparticle [64], [65], or an individual atom [66]. The first SET was realized in 1987 working at 1.7 K [67]. Innovations in fabrication present many promising ideas for mass manufacturing [65],

[68]–[71] and for basic studies [72], [73]. To accurately produce individual prototypes, techniques using the focused ion beam [72], [73] can be applied. This precisely fabricated individual SET can be used to study the influence of geometrical variations or operating conditions. Nanowires can be used to trap electrons in an electro static box that is created by two gates [74]. Electron beam lithography can be used to assemble two electrodes and one nanoparticle [65], [68]–[71].

Another promising approach are nanogaps that can be filled with nanoparticles by trapping them using electronic fields [64], [75], [76]. Nevertheless, these methods struggle with room temperature operation and the positioning is not accurate enough. For large distances, the island needs to react strongly to the electric fields, which is possible to reach with gold particles as island. To avoid this, it is possible to use DNA origami to position the islands [77], making the process more independent from materials choice and making the positioning much more accurate. However, this is a very complex, self-assembling process that is difficult to utilize in production of integrated circuits. Although it has a good yield, it is far away from being employed in mass production.

Another successful technique is to use the self-limiting effect of oxidation, which occurs at low temperatures and limits the oxidation of Si nano particles [78] and nano wires [79] very precisely. Called pattern-dependent oxidation (PADOX), this process is dependent on the initial structure of its surroundings [30], [80]–[83]. PADOX makes it possible to accurately downsize the structures, especially the nanoparticle for the island. Although used in the 1990s to fabricate room temperature SETs [80], PADOX is struggling with the SET characteristics and contacting. For example, having different threshold voltages does not allow for designing electronic circuits. A bottom-up approach [84] was used to solve the characteristic problem, allow for tuning the properties, and easily contact SETs electrically but only for cryogenic temperatures.

Manufacturing Electronic Devices Based on SETs

The two main challenges for manufacturing electronic devises based on SETs are operation at room temperature and mass fabrication. This work focuses on the realization of a manufacturing process that allows for both.

Room temperature operation was the main roadblock for a long time until today. The charging energy E_C depends strongly on the strength of the Coulomb blockade. In case of high temperature, the thermal fluctuations can be strong enough to charge the particle and enable the tunneling from the source to the drain by only thermal activation. To realize a SET, the range of E_C needs to be much higher than the energy of thermal activations. So either the charging energy is getting increased by lowering the size of the island, or the temperature needs to be decreased. The latter was already realized numerous times over the last decades, before the production of a SET that operates at room temperature was successful. Laboratory realization of individual prototypes has been proven so far but only with great effort.

A mass production process for SETs is still missing. Even if it is possible for such a device to work, it is still necessary to find new technologies realistic for mass production. Classical lithography may fabricate sub-10 nm structures, but single electron devices need structures even smaller than 5 nm. One promising option might be electron beam or UV lithography, which theoretically can form structures in the range below 10 nm. However, these technologies are still very expensive for industrial application.

The industrial production of structures under 5nm is so far only possible with self-assembly methods. These have already shown their potential in the past for devices such as memories [85] or solar cells. However, not only is it difficult to fabricate a small enough island, but the integrated circuit also needs to be in a similar size. This might cause issues with current leakage and breakthrough voltages. In case of very different characteristics, the realization of logical operations becomes impossible. So even if there is an array with thousands of working SETs, unless one has a different current-voltage characteristic curve (I-V-curve), SETs are useless for industrial applications.

2.3 Scheme of a CMOS-Compatible RT-SET Fabrication

The manufacturability of all known realization approaches fails because of at least one of the following 4 problems: low manufacturing yield, not electrically contactable, operating characteristics vary from unit to unit, or no room temperature operation.

The approach in the current work to the formation of a nanoparticle between two electrodes is based on two manufacturing steps: (i) ion irradiation of $Si/SiO_2/Si$ stacks to mix Si into the SiO_2 and (ii) subsequent annealing to induce self-organization of NCs inside the SiO_2 out of the mixed Si. It was done in the framework of a European project “Ions 4 Single Electron Transistor” (IONS4SET) [86].

Figure 2-3 shows a schematic representation of the two systems investigated in the IONS4SET project and this thesis. Figures (a)-(d) show the entire process for forming a NC *layer* in the $Si/SiO_2/Si$ stack. The configuration shown in a) is achieved by oxidation of a Si substrate and covering by Si using chemical vapor deposition (CVD). This $Si/SiO_2/Si$ stack is the initial system to be irradiated in the next step (b). The upper subplot shows a more detailed representation of the propagation of a Si^+ ion through the target material. Atomic collisions cause displacements of Si and O atoms, leaving interstitial and vacancy defects. Thus the configuration of pure Si and pure SiO_2 domains is mixed and the SiO_2 layer is supersaturated by the introduced Si (c). A detailed illustration can be seen in the lower subplot of Figure 2-3. Si atoms are distributed over the SiO_2 and oxygen atoms are implemented in the upper and lower Si. The irradiation takes place in a chamber, which is usually operated at room temperature. This mixture does not change at low temperatures and remains (meta-) stable. At higher temperatures, however, the excess Si fuses inside the SiO_2 and forms NCs. This is done by self-organization and will be explained in more detail in the next chapter.

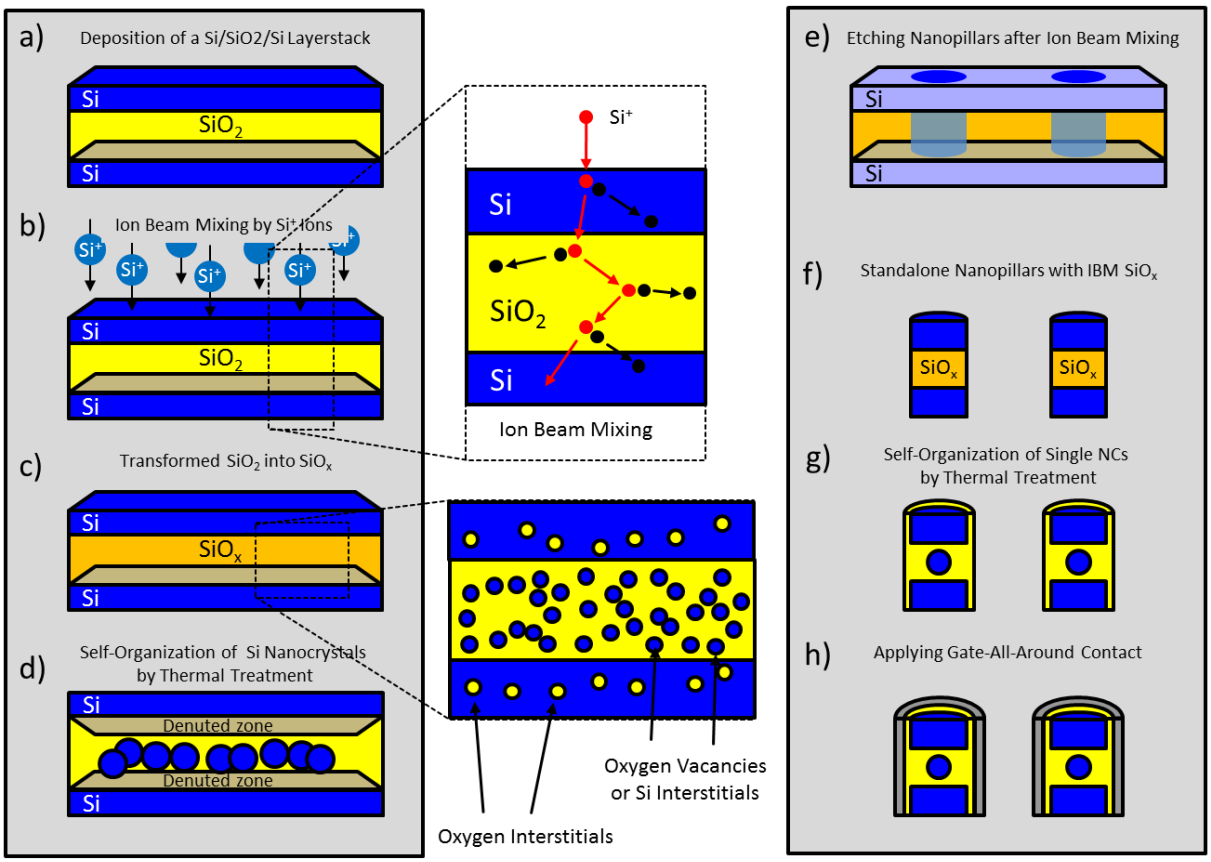

Figure 2-3: Schematic of the formation process of a NC layer in (a)–(d) and the fabrication process to produce the SET in (e)–(h).

This structure was already used in an earlier European project (NEON, see Ref. [87], [85]) for the production of non-volatile memories. The distance of the NCs in the SiO_2 to the two Si interfaces was sufficiently small so that they could be charged by tunneling electrons and thus the data storage was realized. This system was also used for the IONS4SET project and this thesis to perform basic studies.

Figure 2-3 e)-h) shows the individual steps for manufacturing the SET. This starts with the Si/SiO_2/Si stack after irradiation (e) and will etch out the *nanopillars* (f) in the first step. Compared to the system in (c), the nanopillars have an additional boundary condition that contributes to the formation of NCs through the outer surface of the nanopillar to the vacuum. This gives the process a further limitation and only allows the formation of NCs in a spatially limited volume. The thermal treatment of this system in (f) can then lead to the formation of only one Si-NC (g). When a gate is placed on the surface, an assembly is formed that implements the concept of a SET, as described in the last chapter. The upper and lower silicon are then the source and drain contacts and the Si-NC the island, which can be charged by tunneling electrons.

The requirements for such an assembly are high. The scheme shown in Figure 2-3 requires a Si-NC with a diameter of less than 4 nm and distances to the electrodes of less than 2 nm to work at RT [61]. These are insurmountable challenges for classical manufacturing processes (see Chapter 2.2). Only the formation of the small nanopillars (10-20nm) of the production scheme presented in Chapter 2.3 can be realized with classical methods. The production by electron beam lithography (EBL) [88] achieved high reliability with the diameter of the nanopillar and the thickness of the SiO_2 layer. The tunneling and the control of the current through the gate contact are, however, the

decisive steps in practical operation. They react most sensitively to small geometric variations [60], [61]. In addition, it is necessary to ensure the equality of each individual SET on an entire wafer before starting to design applications [61]. But the low yield of equivalent SETs is a major barrier to mass production.

Self-organization methods can form structures in arbitrary scales. In this way, an industrial manufacturing process for the realization the non-volatile memories was possible. Recent studies also showed a finer location-controlled formation of individual Si-NCs in a 7 nm thick SiO_2 interlayer [89] by self-organization. In order to realize the mass production of a single Si-NC in a nanopillar, as described in Chapter 2.3, the approach shown in Figure 2-3 is therefore very promising.

2.4 Using Self-Organization to Form a Single NCs in a Nanopillar

Supersaturated SiO_2 is a metastable mixture of Si and O, but does not change its configuration at low temperatures (< 800°C). Therefore, no change in the $Si/SiO_2/Si$ stack is to be expected immediately after irradiation and the SiO_2 layer remains "frozen". However, this is energetically less favorable than a properly separated configuration with domains of pure Si and pure SiO_2. Heat treatment at temperatures above 1000°C leads to diffusion processes, and Si and O atoms perform a random walk thrgouh the mixture. However, local configurations with low free energy will statistically last longer. For a Si atom surrounded only by other Si (a pure Si region), the free energy is lowest, which leads to a strong stabilization of this configuration. The volume is limited by the two Si/SiO_2 layers and the separation of the domains takes place mainly in the center of the SiO_2. This leads to the formation of NCs in the arrangement of a layer in SiO_2. The influence of the two Si/SiO_2 interfaces will be described in more detail by Chapter 2.4.2.

The Self-Organized System via the Reaction Pathway to Equilibrium

In general, self-organization occurs when a system in a non-equilibrium configuration is brought towards equilibrium and has to go through some specially ordered intermediate configurations on its way. The evolution follows a defined *reaction pathway*, creating intermediate structures called the *self-organized system*.

However, the SET is a much more sensitive structure than the memory in ref [85]. A reliable formation of a *single* NC is a great challenge for a self-organization process. Direct manufacturing gives each manufacturing step a specific uncertainty with which the intended structures are formed, and leads to a corresponding uncertainty with which the transistor works. A self-organization process creates clearly defined structures on its way to equilibrium. However, certain fluctuations occur between the individual reaction pathways, which then lead to uncertainties in the production process.

2.4.1 Leading the Reaction Pathway of the System to Intended Structures

Figure 2-4 shows schematically how the self-organization of an exemplary system works. The example system consists of NCs and the decisive property that must be organized is the number of NCs. Two different developments are highlighted; one has slightly more NCs in the start configurations (red) than the other (blue). Each of these reaction pathways gives the system a specific way to organize the NCs. However, in order to form a certain number reliably, each of these reaction pathways must have the same number of NCs for a certain period of time. This period is indicated by the two uncertainty rings in Figure 2-4. During this time, all reaction pathways offer a specific number of NCs with certain uncertainty.

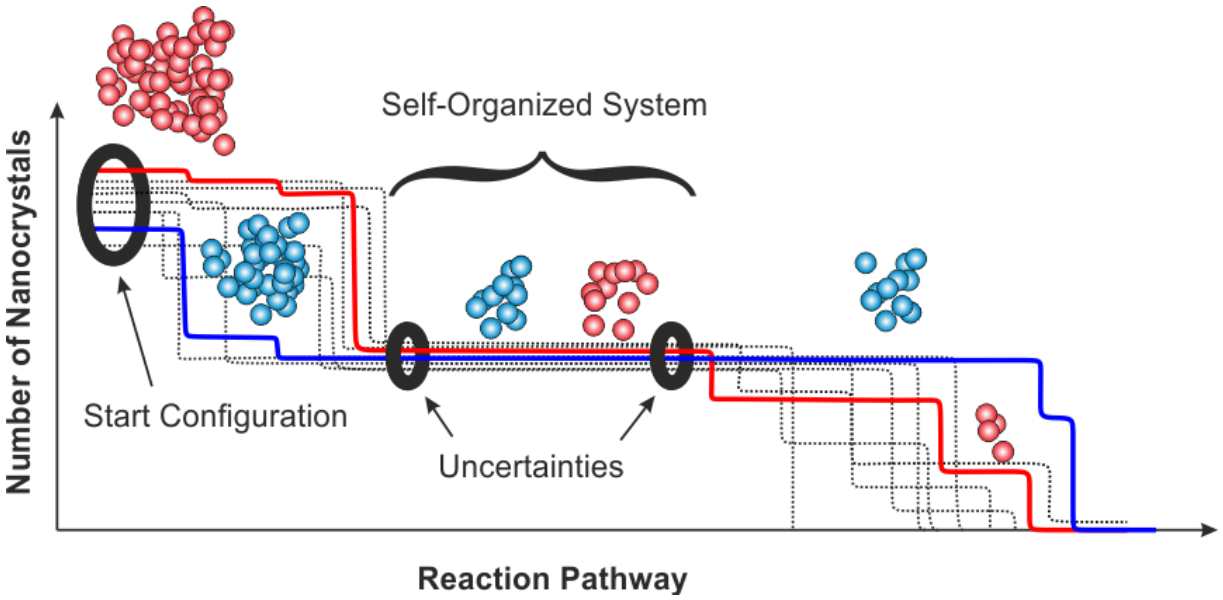

Figure 2-4: Schematic representation of the number of NCs during the reaction pathway of a self-organizing system. The system organizes the NCs to a certain number with a certain uncertainty. All reaction pathways give an individual way of the system, but always go through the same intermediate state.

For a similar system as Figure 2-4, Strobel [90] has already shown how each reaction pathway develops equally. Supersaturation was achieved by point-like implantations. He optimized the parameters and achieved the formation of a series of identical single NCs. Figure 2-5 shows two ensembles with 16 reaction pathways from his work [91] for three points in time. The reaction pathways in (a-c) are very different and lead to high uncertainty in the formation of a single NC. The reaction pathways for optimized parameters are shown in (d-f). Here, all 16 reaction pathways develop differently, but end up in the same intermediate state with only one NC each.

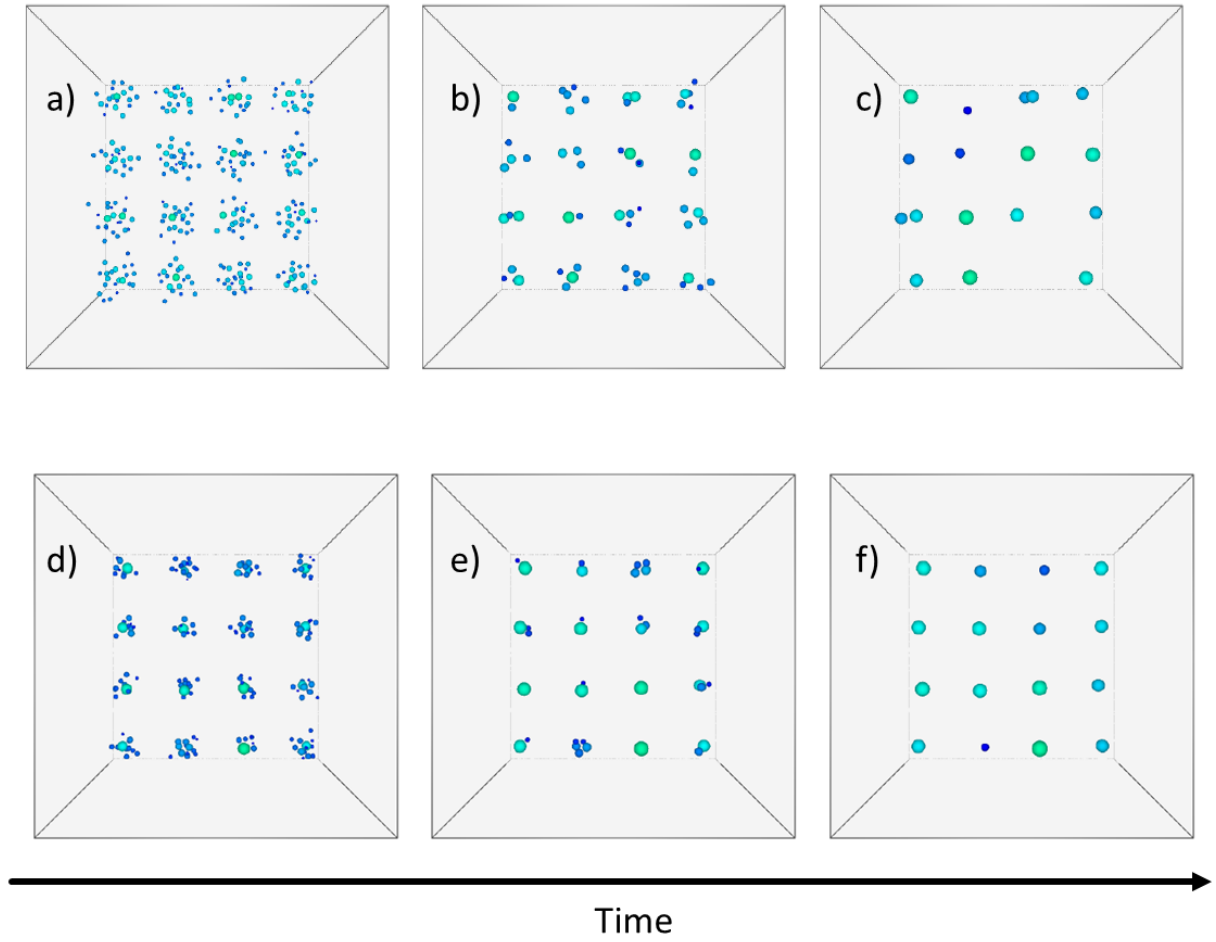

Figure 2-5: Reaction pathways of an ensemble of NCs after point-like implantations of an immiscible substance. An arrangement of 16 reaction pathways for this system is shown in a)-c), which usually leads to individual NCs at each position. For optimized parameters, the reaction pathways in d)-f) show considerably higher reliability of this self-organized system. These results were achieved with the help of reaction-diffusion equations. The figure was taken from ref. [90].

In this work, irradiation fluence, annealing temperature, annealing duration, ion energy and the diameter of the nanopillar are the possible parameters for controlling the reaction pathways. Chapters 3 and 5 will show how the formation of the initial configuration for the annealing process is controlled. The ion beam mixing results in a very specific composition and can be controlled very well. The self-organization then takes place during the annealing process. Chapter 4.3 shows all important processes that take place during annealing and influence the reaction pathway of the system. It is possible to restrict the freedom of reaction pathways in such a way that they inevitably have to pass through certain intermediate states.

2.4.2 Controlling Self-Organization by Initial Configurations and Boundary Conditions

Annealing a SiO_2 that is homogeneously low supersaturated by excess Si (<10%) leads to the formation of an ensemble of NCs. However, inhomogeneous boundaries will influence the formation of NCs and can cause specific structures [92]–[94].

The Si/SiO_2 interface is a very strong boundary condition to supersaturated SiO_2. Such restrictions of diffusion pathways and surface effects have been intensively investigated since the 1990s [95]–[97]. The strong absorption power of the interface leads to the formation of a denuded zone near the interface and to the formation of a layer of NCs. This was described in [98]–[101] and experimentally proven in [102]–[104]. The next chapters will discuss this in more detail.

A surface without absorbing effect still can influence the reaction pathway. The SiO_2 surface of the nanopillar in Figure 1-1 can be exposed to either a vacuum or oxygen rich environment. This also has effects on the self-organization and is discussed in Chapter 6.2.3.

Curvatures in the composition can also lead to an influence on the structured formation of NCs. A cylindrical interface can lead to the formation of rings [98], [105], [106] and a spherical confined mixture can form shells [99] or lines of NCs [89].

An inhomogeneous distribution of heat is also a control element for self-organization. Temperature gradients can trigger the formation of concentration fluctuations and influence the reaction pathway [106]. This can be achieved for example by direct laser heating [107], [108].

2.4.3 Ostwald Ripening induced Self-Organization of NCs

The first stage of thermal annealing of a low supersaturated mixture is dominated by nucleation and growth of NCs. Each individual Si-NC permanently absorbs and emits monomers, which diffuse from one NC to another. This result in a mechanism of interaction between the NCs: the diffusion of the monomers.

An emitted monomer will randomly diffuse around its source NC until it finds a target NC for attachment. However, this target NC is usually in close proximity to the source. Figure 2-6 schematically shows 2 possible diffusion pathways, one is extremely unlikely (a) and the other is one of the most likely (b). In general, the diffusing monomers will mainly be exchanged between the nearest neighbor NCs. This means that each NC is screened by its surrounding neighbors and there is no *direct* influence of a boundary if it is behind its nearest neighbors. This effect is called diffusion screening and quantified by the diffusion screening length [109]. This length depends mainly on the size and density of NCs [99].

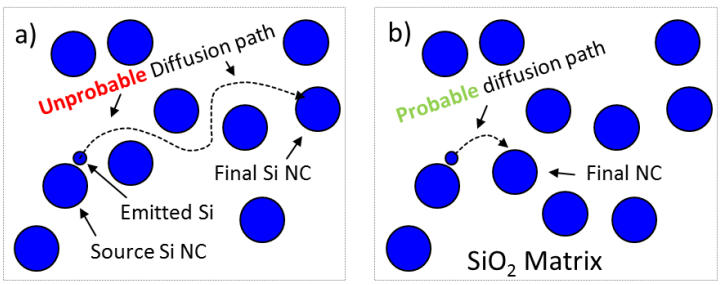

Figure 2-6: Schematically shown two different diffusion pathways of an emitted Si monomer in an ensemble of Si-NCs. One is unlikely to appear (a) and one is likely to appear (b).

In case a NC is screened by its neighbours and is not influenced by a boundary (e.g. an interface or surface), indirect influence can still occur. If the boundary induces certain changes to the neighbors (e.g. let them grow or evaporate), these changes can in turn affect the screened NC.

Figure 2-7 shows the self-organization of a shell-shaped structure of NCs, published by S. Reiss et. al. in 1994 [99]. The reaction diffusion equation for 3400 nucleated NCs was solved. The starting configuration was a homogeneous distribution of these NCs in a sphere. An equatorial slice of this configuration is shown in Figure 2-7 a) and the obtained reaction pathway, can be seen in (c) to (d). The NCs in the center of this sphere are completely screened by other NCs and perform so-called *Ostwald Ripening*. However, the outer NCs in Figure 2-7 a) only have neighbors on the inside and can evaporate to the outside. Figure (b) shows this early stage in which most of the outer NCs have disappeared. This leads to an increase in density in the outer area, which serves as addition monomer supply to the next inner NCs. These NCs grow fastest and get the highest absorption power. This in turn leads to the denudation of the more inner region. Figure (e) schematically shows a cross-section plot through the configuration of the system shown in (a)-(d). The second plot of (e) shows the configuration after the outer NCs evaporated. The third plot shows the formation of the first shell of the NCs (b) and the last plot the denudation of the next inner region. This leads to the formation of the next shell according to the same scheme as the first shell was formed. This effect then spreads to the center of the sphere and leads to shells of NCs.

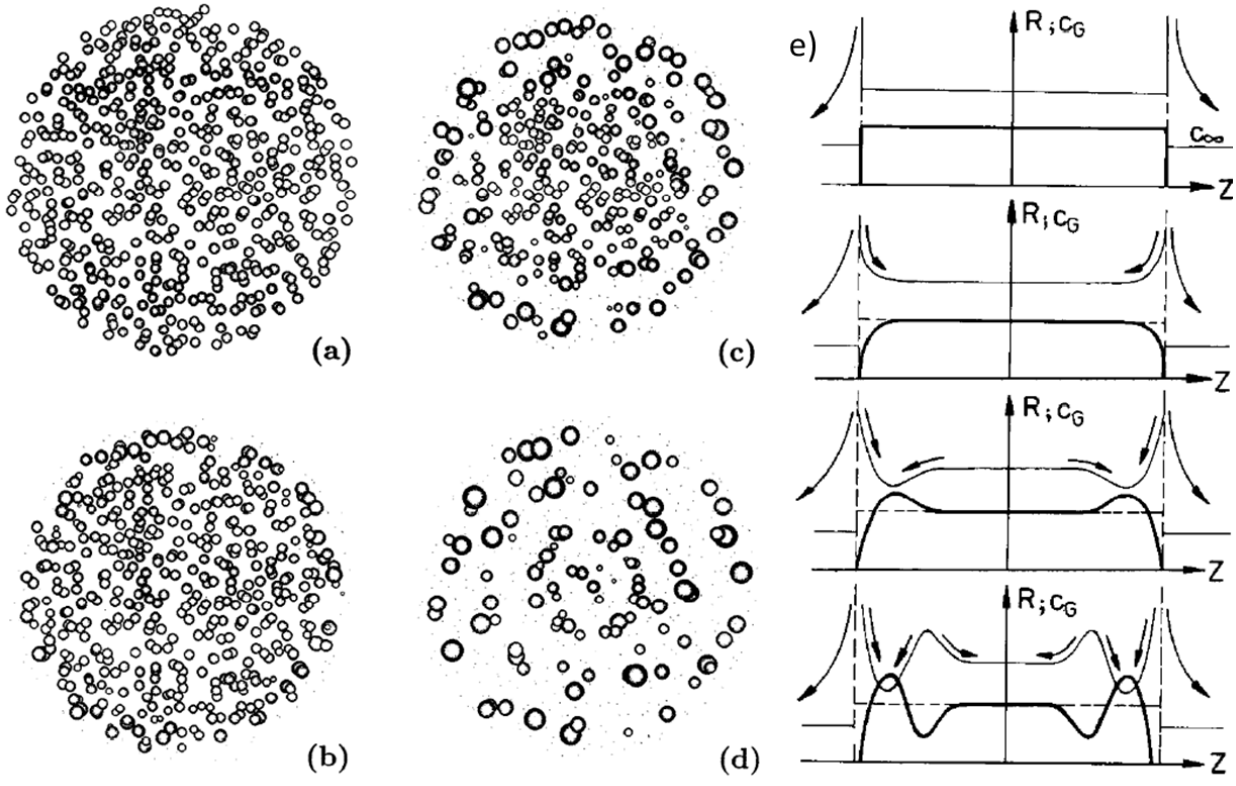

Figure 2-7: Solution of the reaction-diffusion equation of 3400 same-sized NCs uniformly distributed in a sphere (a) over several evolution steps shown in (c)-(d). A schematically plot of the concentrations through the sphere is shown in e). Taken from ref. [99].

The formation of the NC layer in the 7 nm thick SiO_2 layer shown in Figure 2-3 follows exactly the self-organization process described above. The fact that there are two absorbing interfaces and that the film is very thin leads to the formation of a single NC layer.

2.4.4 Nanoconfinment by Interfaces and Surfaces

The restriction of non-equilibrium phases to nanoscale volumes is called nanoconfinment and their self-organization during thermal activation is an increasingly interesting topic [89], [106], [110], [111]. The formation of the Si-NC for the SET takes place in a very small SiO_x volume and is limited by two different boundaries: (i) The Si/SiO_2 interface, which has been investigated in detail in the past and (ii) the mantle surface of the nanopillar to the vacuum.

Figure 2-8 schematically shows how the self-organization of the systems in this thesis is driven. Figure (a) shows the self-organization of NCs in the $Si/SiO_2/Si$ stack. The interfaces absorb fast the Si in the supersaturated SiO_2 in the nearest area and lead to a centering of the remaining Si excess, which forms a layer of NCs. The nanopillar has the surface to the vacuum as an additional boundary, as shown in figure (b). In the case of a pure vacuum environment, this surface neither absorbs Si nor emits oxygen. This means that any Si atom that touches the surface during its diffusion pathway does not react with it and is only reflected. The combination of the reflecting surface and the absorbing interfaces defines the self-organization of the SiO_x in the nanopillar and is shown in Figure 2-7 e).

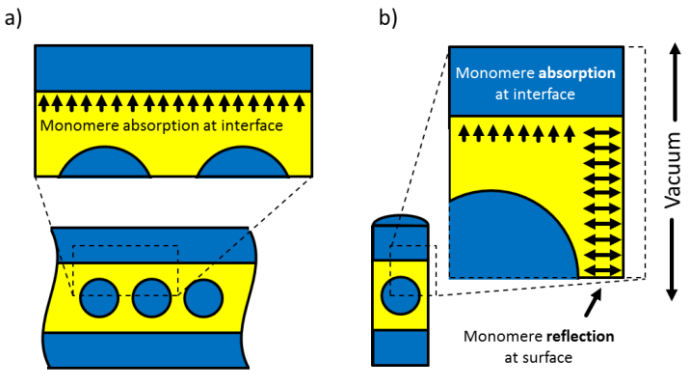

Figure 2-8: Schematically shown driving forces of the two configurations studied in this thesis. The NC layer formation (a) and the nanopillar with an embedded single NC (b).

This results in 6 different possibilities to control the reaction pathway in the nanopillar.

- The Si/SiO_2 interfaces by changing the thickness of the SiO_2 layer
- Reflective SiO_2 surface to vacuum by changing the diameter of the nanopillar
- Composition configuration of the SiO_x by the IBM
- Oxidation of the nanopillar surface by a certain oxygen rich ambient during thermal treatment
- Annealing temperature
- Temperature fluctuations over time and space

This work only includes the change of the SiO_x (variation of the fluence), the annealing temperature and the diameter of the nanopillar. The remaining options go beyond the scope of this thesis.

3 Synthesis of SiO_x by Ion Beam Mixing

The formation of individual nanoclusters (NCs) in the SiO_2 of the nanopillar, as shown in Figure 2-3, is a self-organizing process. Chapter 2.4.1 showed how a system begins in a non-equilibrium state and executes a reaction pathway that can lead to different intended structures. The challenge of the development of such self-organization processes is to find the right starting configuration so that the system has to pass through a certain intermediate state (see Chapter 2.4.2). To enable the system to organize a single NC in the SiO_2 of a $Si/SiO_2/Si$ stacked nanopillar, the first step is to convert the stable SiO_2 to SiO_x by mixing Si and SiO_2. This mixture is energetically less favorable and leads to the above mentioned non-equilibrium configuration. However, self-organization does not follow immediately after mixing because SiO_x is metastable and requires thermal activation to change the configuration (see Chapter 2.4.1). This will be discussed in detail in Chapter 4.1. This chapter deals with the controlled formation of the start configuration. Figure 2-3 shows that both systems (Nanopillar and the NC layer) are based on the irradiation of a $Si/SiO_2/Si$ stack. Therefore only the irradiation of the planar $Si/SiO_2/Si$ stack is considered in this chapter.

Formation of SiO_x

SiO_x can be synthesized by various methods. These differ in technological efficiency but also in physical properties of the SiO_x produced. The most common methods to fabricate SiO_x are as follows.

- **Physical vapor deposition (PVD)** methods include fabrication processes, such as evaporation, sputter deposition or ion deposition. Methods of this group are usually performed in a vacuum to produce thin films and coatings. The material to be deposited is initially in the solid or liquid phase, then turns into vapor or small particles, and condenses or deposits on the target material. In case of producing SiO_x, the two source materials—pure silicon and SiO_2—are mixed in a vacuum and deposited on the target material. The disadvantages are the high effort and the possible absorption of impurities. The advantage is a good control of the SiO_x composition profile. It is possible to dose the amount of Si and SiO_2 time-dependent and thus exactly determine the x of SiO_x over the depth.
- **Chemical vapor deposition (CVD)** methods are mainly used in the form of plasma enhanced chemical vapor deposition (PECVD), but also without plasma enhancement applied at atmospheric pressure (APCVD), low pressure (LPCVD), and ultrahigh vacuum (UHVCVD). Methods in this group realize the formation of films through chemical reactions with the surface of the target material. The basic advantage of CVD is the ability to coat highly structured surfaces homogeneously. Si and O react at the surface and form SiO_x. This method has basically the same advantages and disadvantages as the PVD method regarding the fabrication of the SET.
- **The implantation of oxygen in silicon** is a well-established way to produce SiO_x by ion beam processes. High fluences lead to high supersaturations, and by subsequent annealing it is even possible to form a buried SiO_2 layer. This process is called SIMOX and is used in the industry for the production of SOI (silicon on insulator) wafers. In depths of several 100 nm, the formed SiO_2 layers have a width of approx. 50 nm. But to successfully produce NCs in this

SiO_2, the composition profile of the SiO_x needs to be properly controlled. Also the profile width is not suitable to form NCs with a size of less than 5 nm.

- **The implantation of Si in SiO_2** leads to an excess of Si in the target material and thus to a SiO_x structure. Low energy ion beams can be used to implant Si ions into SiO_2 and form much skewed implantation profiles of excess Si. This has already been used in the past to produce multipoint floating gate memory devices [85]. In order to be able to place the NCs precisely, it is necessary to have a fine control and sharp implantation profiles. In case of [85], this requires low ion energies (< 5 keV) and shallow implantation depths of less than 20 nm. The SiO_2 of the SET is buried in a depth of ~30 nm and has a thickness of only 7 nm. In this case, the implantation of Si excess ions requires high energy (> 30 keV), so that the formation of a skewed implantation profile is not possible. Furthermore, in case the Si ions are implanted into the buried SiO_2, ion beam mixing is taking place only on the upper Si/SiO_2 interface and makes the shape of composition profile very asymmetrical. This will lead to different tunneling distances and will corrupt the functionality of the SET.
- **The ion beam mixing (IBM) of Si/SiO_2 interfaces** is caused by irradiation using energetic ions (in this work, generally Si^+ ions). The entering ion leads to displacements of the Si and O target-atoms by collisions along the penetrating ion pathway. In the region of the Si/SiO_2 interface, this results in a mixed SiO_x configuration around the initial interface. This process allows to produce very thin mixed layers in a controlled way and is therefore ideally suited for the formation of tunnel pathways for electrons as described in Chapter 2.1. IBM is also fast and can easily be integrated into common manufacturing processes in the semiconductor industry.

Ion Beam Mixing

Figure 3-1 shows the basic effects that occur when Si and SiO_2 are irradiated by Si^+ ions. The energetic Si^+ ion penetrates the target and immediately causes displacements. Some of the initial displacements are then sputtered, while others cause further collision cascades throughout the solid. This leads to defects in the target material like vacancies, interstitials, or disordering of the lattice structure. During the first step of irradiation, ballistic binary interactions are the dominant process in the employed energy regime in the range of keV. A subplot in Figure 3-1 enlarges two collisional events and the motion of the ion. Direct collisions of the atoms cause nuclear stopping. On the way between two collisions, the ion experiences an electronic stop caused by interactions with the electronic environment. In contrast to nuclear collisions, these interactions are generally inelastic. They lead for instance to the emission of photons or X-rays (if electrons fall on their original orbit), ionization and atomic excitation by displacing or lifting the electron into a higher orbit or in the lattice structure. For more information on collision trajectories, see [112], [113].

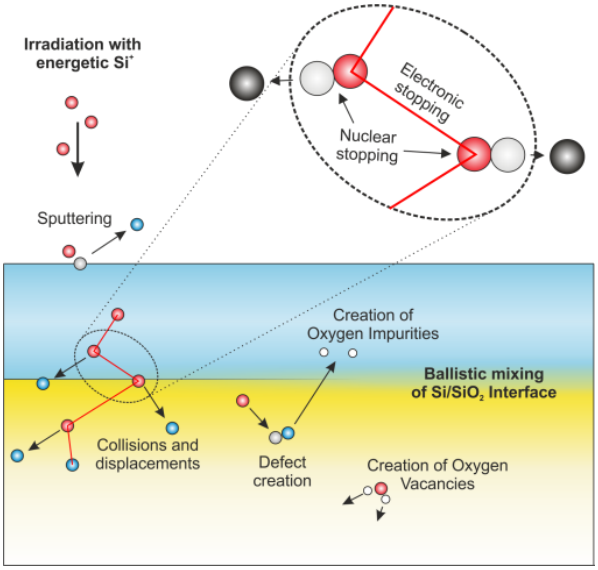

Figure 3-1: Schematic presentation of events occurring during the irradiation of a Si/SiO_2 interface by Si^+ ions. The subplot shows the treatment of electronic and nuclear stopping by BCA. Nuclear stopping is occurring by passing on kinetic energy to the collisional counterpart and electronic stopping along the trajectory between the two collisions.

The irradiation generally results in (i) amorphization of the target structure, (ii) atomic displacements of Si and O, which lead to the mixing at both Si/SiO_2 interfaces, and (iii) implantation of Si^+ ions. For the composition profile of the $Si/SiO_2/Si$ stack, only three parameters are decisive to control these properties:

- **Ion energy**: A slow ion that causes barely any displacements will not lead to efficient mixing of interfaces. Increasing energy above 10 keV shifts the ion range deeper in the target material and gives rise to displacements due to the higher energy transfer by kinetic collisions, also called nuclear stopping. This leads to efficient mixing of present Si/SiO_2 interfaces. Generally, the ion energy allows for steering the depth of the implanted ions and displacements.
- **Ion fluence**: The ion range will be primarily much deeper than the SiO_2, so that higher fluences are less critical regarding the influence of implanted ions as long as the ion range is deep enough. However, a deeper ion range requires higher irradiation energies, at some point this will lower the nuclear stopping and thus the displacements in the depth of the interface. This will be shown in Chapter 3.1.2. Higher ion fluences also lead to a stronger sputtering of the material and stronger incorporation of impurities from the implant chamber.
- **The depth of the SiO_2 layer**: In case of two Si/SiO_2 interfaces, they will experience a different number of displacements and implanted ions. For low energies, the function of ion range and displacements can be very sharp over the depth and cause high differences for both interfaces. For higher energies, the functions are smoothed and can almost be constant over a certain depth range. The SiO_2 layer of the SET needs to be placed at a depth of approximately 30–40 nm. The conditions of implanted ions and mixed ions need to be studied for this case.

However, there are several known processes that can influence the production step of the IBM:

- **Ion beam contamination** [114]: Due to the low temperature, the ion irradiation process itself usually does not lead to thermodynamic incorporation of impurities from the environment (e.g., oxidation). However, impurities can contribute to the ion beam and thus enter the solid as an energetic ion. In case of a Si^+ ion beam, charged N_2 molecules can be accelerated and participate in the ion beam without being suppressed by the mass filter because of the nearly identical mass. The implantation depths are similar to those of silicon.
- **Moisture absorption** [115] on the sample and/or the presence of an, e.g., native oxide layer on the sample is of negligible influence in view of the comparatively deep position of the SiO_2 layer of around 30nm. Long range diffusion processes during ion irradiation are also not to be expected, as the temperature during irradiation is rather low (< 400°C).

Controlling the Formation of SiO_x

To successfully fabricate the SET with a given geometry of the SiO_2 layer (depth and thickness), two parameters need to be specified: the energy of the ion beam and the fluence it needs for irradiation to form a suitable supersaturated SiO_2 for the self-organization process. The basic pathway of how to control this will be investigated in Chapters 3.1 and 3.2. The positioning of the individual single NCs must be as centered as possible between both interfaces in order to ensure equal tunnel distances. The self-organizing process is mainly dependent on the starting configuration of the SiO_x, and therefore, the composition around the SiO_2 layer after irradiation also needs to be as symmetrical as possible. It is important that the mixing be mostly the same for both interfaces. This is investigated in Chapter 3.2.2. To examine this, the profile needs to be characterized, which will be done in Chapter 3.2.1 by interpretation of the IBM as a diffusion process [116]. This will lead to an effective diffusion coefficient, which describes the profile completely. Chapter 3.2.1 will also deal with mixing in an analytical approximation by partial diffusion equations and will verify the approximation by the diffusion equation.

3.1 Si^+ Ion Beam Irradiation of Si and SiO_2

Interactions at the atomic scale can be simulated by many methods, starting with ab initio approaches like the density functional theory [117]–[119] and more phenomenological methods like molecular dynamics. A high degree of detail and based on basic physical quantum mechanics (ab initio) make these practical tools to investigate atomic interactions. However, the big disadvantages of these tools are the small sizes and the short time. Recently an accelerated program code for simulation of ion irradiation based on molecular dynamics has been published that exploits the advantages of MD for low energy ranges [120]. However, this approach is still far from suitable for the challenges of this work, and other, more specialized, approximations are necessary. A so-called Monte Carlo approach based on the binary collision approximation (BCA) was chosen to study the ion irradiation in this chapter. Strong assumptions of BCA give limits and requirements which need to be clarified first.

Studying Ion Irradiation by Binary Collision Approximation (BCA)

Since Rutherford described elastic particle scattering [121], many scientists have been investigating the interactions theoretically [122]–[125] and by computer simulations [126], [127]. In the middle of the twentieth century, effects such as sputtering, implantation, and collision damage were experimentally investigated [128]–[130]. Later, Sigmund [113], [131]–[133] made a significant contribution to the basic understanding by successfully describing the basics of ion propagation through solid target materials. The variation of parameters is crucial for the optimization of the manufacturing processes for the SET and requires a huge number of calculations to perform. A very well established modeling approach is to neglect the multi-atomic correlations and to simplify the interactions to a binary collision between two atoms [134]–[136]. This is called the binary collision approximation (BCA). According to the obtained scattering, the collision cascade can be calculated. The physical basics will be described shortly in Chapter 3.1.1.

A widely used program code that has implemented the BCA is called Transport of Ions in Matter (TRIM) [137] and is based on Monte Carlo approaches. It is possible to calculate irradiation-induced collision cascades, including the trajectories of each atom involved. The averaging of these cascades leads to accurate predictions for ion ranges and displacements over the depth of the target material. First, Chapter 3.1.1 introduces the BCA and describes the different stopping mechanisms. Then Chapter 3.1.2 examines these relationships and identifies problems in the fabrication of a symmetrical composition. This provides a general understanding of the circumstances involved in irradiating Si/SiO_2/Si stacks, which is necessary to understand the following chapters.

3.1.1 Irradiation Energy and Stopping of Si^+ Ions by BCA

The ion trajectories are decisive and can usually be reproduced very well if only the two basic stopping effects—nuclear stopping and electronic stopping—are considered phenomenologically. This approach is generally very efficient regarding calculation time; however, the BCA requires the following basic assumptions:

- Conservation law/elastic energy transfer,
- Electron stopping and nuclear stopping is taken into account seperatly,
- Sputtering interactions are reduced to the approach of surface binding energies, which allows even higher energized ion sputtering,
- Nuclear collisions are reduced from many body interactions to binary interactions between two atoms: the propagating projectile and the target atom.
- Atomic collisions can be inelastic, if, for example, a nucleus is excited, but they are usually neglected in BCA calculations.

The essential approximation is the neglecting of multi-body interactions during a collision event. A collision by BCA only includes the interaction of two atoms. A source ion with the mass m_1 transfers kinetic energy by collision with a target atom of the mass m_2. The source atom becomes slower and changes its direction, while the target atom begins to move. A binary collision governed by a repulsive Coulomb potential is shown in Figure 3-2. The source and target atom experience the Coulomb potential of each other and are scattered by the angle Θ in the center-of-mass system.

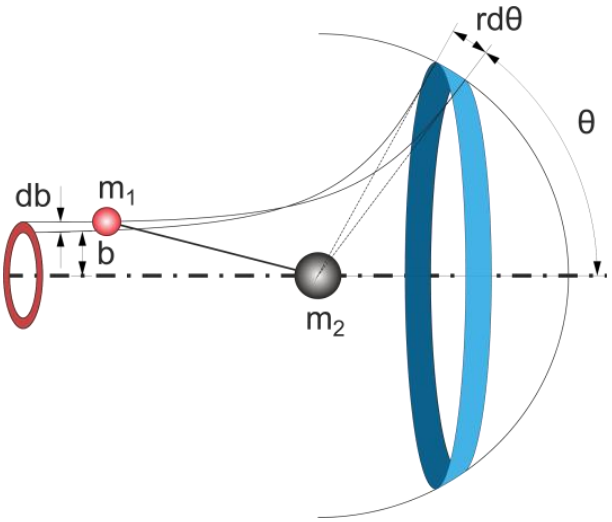

Figure 3-2: Scattering cross section for two particles (mass m_1 and m_2) of a repulsive Coulomb potential with the impact parameter b and the scattering angle θ. The particle m_1 approaching particle m_2 through the red ring will be scattered through the blue ring.

The scattering angle Θ changes depending on the distance b of the target ion to the direction of motion of the source ion. The transmitted elastic kinetic energy can be described as

$$T_{\mathrm{el}} = \gamma E \sin^2 \frac{\Theta}{2}, \tag{3}$$

where E is the kinetic energy of the projectile, Θ is the scattering angle in the center-of-mass system, and γ is the energy transfer factor. The interaction potential between the two atoms is given as

$$V_{\mathrm{c}}(r) = \frac{Z_1 Z_2 \mathrm{e}^2}{4\pi\varepsilon_0 r}, \tag{4}$$

where the charge numbers Z_1 and Z_2 are the source and target particle, respectively. The parameter ε_0 is the electric constant. The electrons shield the nuclear charges, and in order to obtain a suitable potential, the shielded Coulomb potential was introduced by

$$V(r) = V_{\mathrm{c}}(r) f_{\mathrm{S}}(r), \tag{5}$$

where f_{S} is the screening function. A universal screening function developed by Ziegler, Biersack, and Littmark [138] is used in the program code SRIM and in TRIDYN the Kr-C [139]. The transferred energy according to Equation (1) is giving the energy loss by one nuclear collision. The nuclear stopping power can be derived by integrating Equation (3) over all possible distances b and gives

$$S_{\mathrm{nu}}(E) = \frac{\mathrm{d}E}{\mathrm{d}x}\Big|_{nu} = \int_{T_{\mathrm{min}}}^{T_{\mathrm{max}}} T_{\mathrm{el}} 2\pi b \mathrm{d}b(T_{\mathrm{el}}). \tag{6}$$

However, the propagating ion is also interacting with the present electronic structure, and in order to understand the total stopping effect, the electron stopping section must also be investigated and gives two different cases:

For high ion energies with a velocity higher than $\mathrm{v}_0 Z^{2/3}$, with v_0 as the Bohr velocity of the atomic electrons, the ion is much faster than the orbital electrons. This leads to a removing of the ion's electrons and the ion propagates as a "naked" nucleus. The electronic shielding of Equation (5) can then be neglected and the energy loss is calculated by the Bethe formula [122].

At low ion energies with a velocity less than $v_0 Z^{2/3}$, the nucleus begins to capture electrons from the target atoms. Several approaches have been developed to describe this system in detail (see [140], [141]). Basically, this stopping can be approximated accurately from continuous energy loss and thus be calculated by BCA approaches.

The applied energies in this work will be in ranges, where IBM is mostly taking place. Electron stopping, especially at ion energies with a velocity higher than $v_0 Z^{2/3}/3$, is not expected. Effects of high ion energies like ionization or atomic excitation can also be neglected. The electron stopping at low energies can induce atomic vibrations and phonons. This will be an issue in Chapter 5, where the influence of induced vibrations on the IBM process is studied.

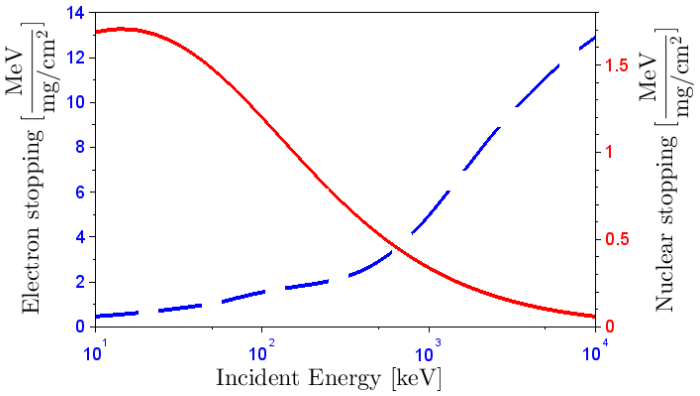

Figure 3-3: Stopping power cross sections for electron (broken blue line) and nuclear (red line) energy loss of Si^+ ions irradiating a Si bulk. Calculations have been done by SRIM-2013 [142].

The total stopping cross section can be described by the sum of nuclear and electronic stopping and gives

$$S(E) = -\frac{1}{n}\left(\frac{\mathrm{d}E}{\mathrm{d}x}\Big|_{\mathrm{nu}} + \frac{\mathrm{d}E}{\mathrm{d}x}\Big|_{\mathrm{el}}\right), \tag{7}$$

where n is the atomic density of the target, nu is indicating the nuclear stopping, and el the electronic stopping. This formula describes the energy loss per unit for both stop mechanisms. The strength of the stopping mechanisms is shown in Figure 3-3 for Si atoms in a silicon target material. The calculation has been done by SRIM 2013 with the default settings. As expected, nuclear stopping dominates at lower energies, while electron stopping becomes decisive at higher energies. Interesting for this work are nuclear stopping processes at the Si/SiO_2 interface, and therefore, according to Figure 3-3, the ion beam energy at the depth of the interface should be less than 100 keV.

In summary, this chapter clarifies which energetic parameters are required for efficient mixing of the interface. Nuclear stopping is the mechanism causing displacements and driving the IBM of interfaces. It draws the following conclusions:

- The most efficient IBM of the Si/SiO_2 interface takes place at energies of less than 100 keV. This shortens the duration of the irradiation process step and leads to a fast manufacturing process.
- Electronic stopping has no effect on the ballistic mixing process. However, it can excite phonons and induce thermal energy in the lattice. Figure 3-3 shows that in the energy range

below 100 keV, the electronic stopping is still 0.2 MeV/(mg/cm^2) and transforms the kinetic ion energy into thermal energy. This affects the IBM at the Si/SiO_2 interface and is discussed in Chapter 5.

3.1.2 Atomic Displacements and Ion Ranges of Si^+ Ions in Si and SiO_2

The correlation between the range of the implanted ions and displacements of recoils leads to asymmetric profiles and swellings. In order to avoid this by optimizing the irradiation parameters and interpreting the results correctly, it is necessary to investigate the correlations between ion implantation and atomic displacements over depth.

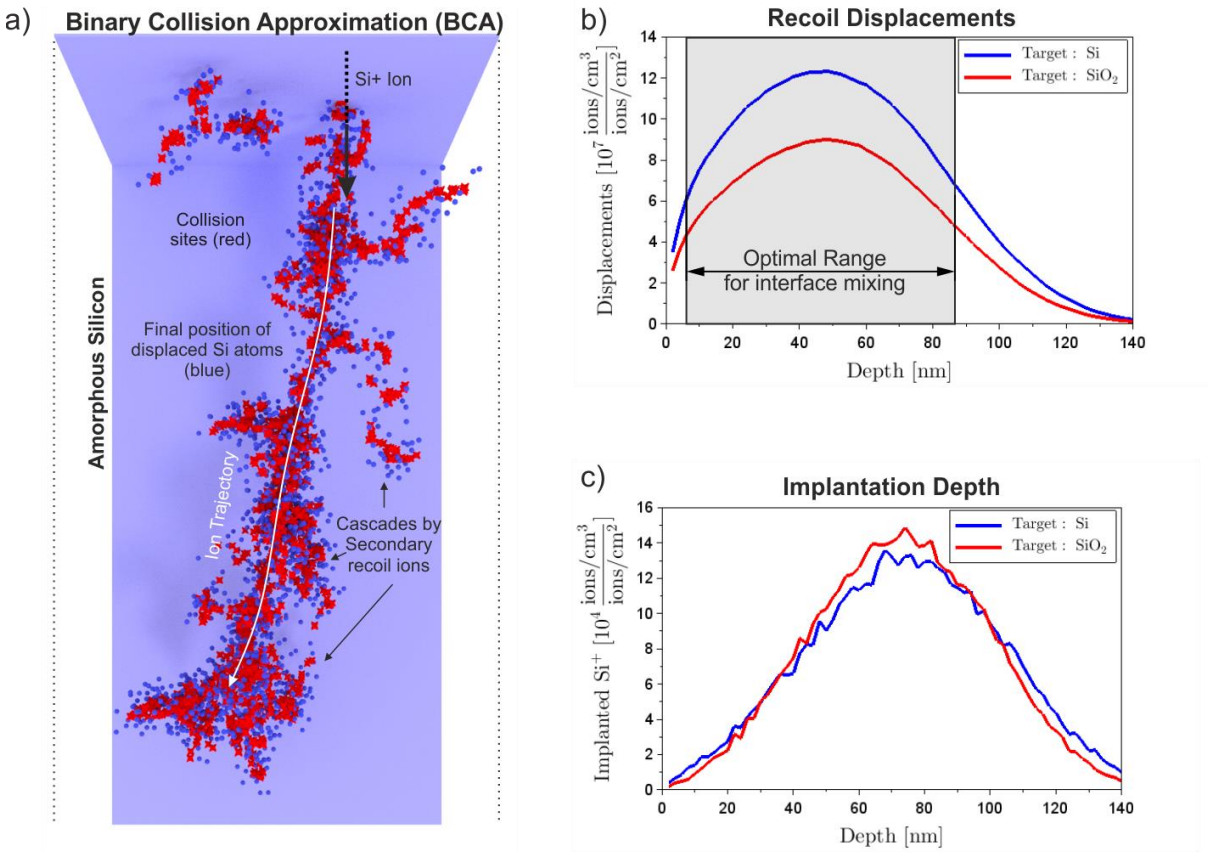

Figure 3-4: Results of a calculation based on the BCA. (a) In a collision cascade of a penetrating ion, the entering ion is causing displacements (red stars) and recoil collision cascades until all displaced atoms find their final place (blue spheres). (b) The number of displacements throughout the depth during irradiation by 50 keV Si^+ ions is shown for irradiation of a Si target (blue) and a SiO_2 target (red). (c) The depth range of the entered ions. Calculations have been done by SRIM-2013 [142].

Figure 3-4 (a) shows an ion penetrating through the target material. The number of total displaced atoms throughout the depth in the case of irradiation by a 50 keV Si^+ ion is shown in Figure 3-4 (b). The blue line shows the value of Si and the red line shows SiO_2 target material. Both have a similar shape, especially the maximum is at the same depth. IBM generally takes place most efficiently at depth ranges with a high number of displacements and thus, according to Figure 3-4 (b), the optimum depth for IBM of a SiO_2 layer by a Si^+ ion with 50 keV is between 10 nm and 90 nm. With a

good position of the SiO_2 layer regarding the displacement curve (depth of ~40 nm), a good mixture can be expected. The corresponding ion ranges, shown in Figure 3-4 (c), are almost identical for both target materials.

In summary, this chapter investigated the depth dependence of displacements and implantation ranges and estimated the parameters for efficient mixing. From this, the following conclusions can be drawn:

- The displacement curve and the ion ranges (Figure 3-4 (b) and (c)) show that the spikes of both functions do not overlap, and there are depth regions mostly modified by displacements and regions mostly modified by implanted ions.
- According to the predictions in this chapter, the formation of a complete symmetrical mixture of the SiO_2 layer is not possible. If the SiO_2 layer is placed on the vertex of the implantation range (Figure 3-4 (c)), the influence of the implantation will be symmetrical, but mixing will only occur at the upper interface. Placing the SiO_2 layer on the vertex of the displacement curve (Figure 3-4 (b)) leads to an asymmetric influence of the implanted atoms. With very thin, deeply positioned SiO_2 layers and with high energies so that both curves are smoothed, however, the difference might be negligible with regard to NC formation.

3.2 Ion Beam Mixing of $Si/SiO_2/Si$ Layered Structures by TRIDYN

The last chapter examined the ranges of displacements and implantation with SRIM and TRIM using predicted profiles over depth. However, these calculations were only performed for irradiation by *one ion* and averaged over thousands calculations, but always at a *virgin* target. None of these codes takes into account the dynamic change of the material due to sputtering or compositional reorder. Thus, the results are basically only valid for one ion and can serve as an approximation for low fluences. For high fluences, the rearrangement of atoms induced by each penetrating ion cannot be neglected. To really clarify the dependence of the composition profile, especially regarding symmetrical aspects, it is necessary to use a dynamic approach that includes the dynamic changes of the material.

A well-established program code using the BCA, which considers the continuous change of the target material by ion irradiation, is called TRIDYN [134], [135]. In addition to atomistic Monte Carlo approaches like this, analytical approaches can also be used to predict the mixing of interfaces by ion beams. The displacements in the target material can be interpreted as a diffusion process similar to classical diffusion by thermal treatment. This will be shown in detail in Chapter 3.2.1. According to Fick's second law of diffusion [116], the classical diffusion can be used to model the composition profile and to convert the strength of mixing into an effective diffusion coefficient. The unknown diffusion coefficient can be determined by adapting the solution of Fick's equation to simulation results using BCA. This gives one diffusion coefficient for each interface and provides a suitable tool to investigate the asymmetry during irradiation. To use this approach, however, it is necessary to first examine the results of the atomistic simulations obtained by TRIDYN calculations and the validity of the diffusion approximation.

The model used in TRIDYN contains atomistic parameters that can be determined by theoretical calculations (e.g., ab initio calculations or molecular dynamic simulation). The experimental comparison also makes it possible to extract model parameters. The BCA model implemented in TRIDYN has several important physical parameters:

- **The surface bond energy** [128] is the main factor for the sputter yield in the BCA method. After an ion has entered the target material and begins to displace the target atoms, the latter may also collide with surface atoms and cause a solid-vacuum transition. The energy required for this displacement is defined by the surface bond energy. The higher the sputtering yield, the more the mean depth of the SiO_2 layer decreases during the irradiation process. This changes the displacements and number of implantation ions at the SiO_2 layer, consequently affecting the composition profiles during irradiation.
- **The energy of the displacement threshold** must be transferred to a target atom to be considered for a stable displacement. Conventially, it is defined for an individual displacement in an otherwise perfect crystalline solid, resulting in values between 10 eV and 80 eV. High-fluence irradiation may result in significantly lower displacement thresholds, as low-energy recoil atoms may by trapped at pre-damaged sites. For the current system, the displacement energy of 8eV is taken in accordance with mixing experiments [143] and theoretical investigations [144].
- **The cut-off energy** is defined as the lowest elementary surface binding energy of all species in the system. All source ions perform their trajectory until their energy falls below this value and they take their final position and the remaining energy is neglected. Strictly, it is transferred into lattice vibrations and thus causes local thermal activation. However, thermally triggered interactions may also influence the mixing efficiency, which will be discussed in Chapter 5. In the present chapter, these effects are neglected.
- **The bulk binding energy** is subtracted from the energy transfer between the particle and target atom before a recoil is generated. To estimate the correct sputter yield, it must be set to 0 [135], [145], [146].

Another effect to be considered is the swelling of the SiO_2 layer caused by built-in Si ions (whether implanted or mixed). The swelling will increase the size of the thickness of the SiO_2 layer and thus also the tunnel distances. In TRIDYN, the system undergoes a relaxation step. After the incident ion and all displaced recoil particles have finished their propagation through the target material, first, the particle mass is added to its final position and then the sizes of the numerical layers are adjusted according to their new composition.

The presented calculations in this chapter have been done by the program code TRIDYN with a simulation depth of 100 nm and a numerical interval distance of 0.5 nm. The proposed assembly of the NC in the project IONS4SET had a top-Si of 30 nm and a SiO_2 thickness of 7 nm, so the calculations in this chapter are done with similar parameters.

3.2.1 Ion Beam Mixing of a Si/SiO_2 Interface as a Diffusion Process

The atomistic calculations by TRIDYN provide the exact results according to the BCA. To analyze the shape of the composition profile, it is necessary to reduce the numerical function over the depth into a simple fitting function. Therefore, it is helpful to investigate the conditions for the approximation of

the TRIDYN results by the diffusion process. This will also be considered in Chapter 5 for modeling the ion beam mixing process by a phase field approach. Another decisive point is the sputtering effect of the ion beam, which is also considered in the calculations with TRIDYN. This effect causes a different depth of the SiO_2 for the later ions and leads to an influence on the evolution of the composition profile.

Figure 3-5 shows the composition profiles of O, the target Si, and the implanted Si after irradiation by a fluence of $4 \cdot 10^{16}$ cm^{-2} Si^+ ions with an energy of 90 keV (a) and 30 keV (b). The high energetic irradiation leads to a composition profile in the shape of an error function, while low-energy irradiation may introduce an asymmetry by the amount of Si^+ ions implanted in the region of the interface. Sputtering for the specified parameters results in a total erosion of approximately 10 nm of the top-Si. However, as will be shown in Chapters 4 and 5, this fluence is rather high for NC formation and values of less than $1.2 \cdot 10^{16}$ cm^{-2} will be sufficient. Calculations have been performed and lead to a maximum sputtering of 3 nm, which can be neglected.

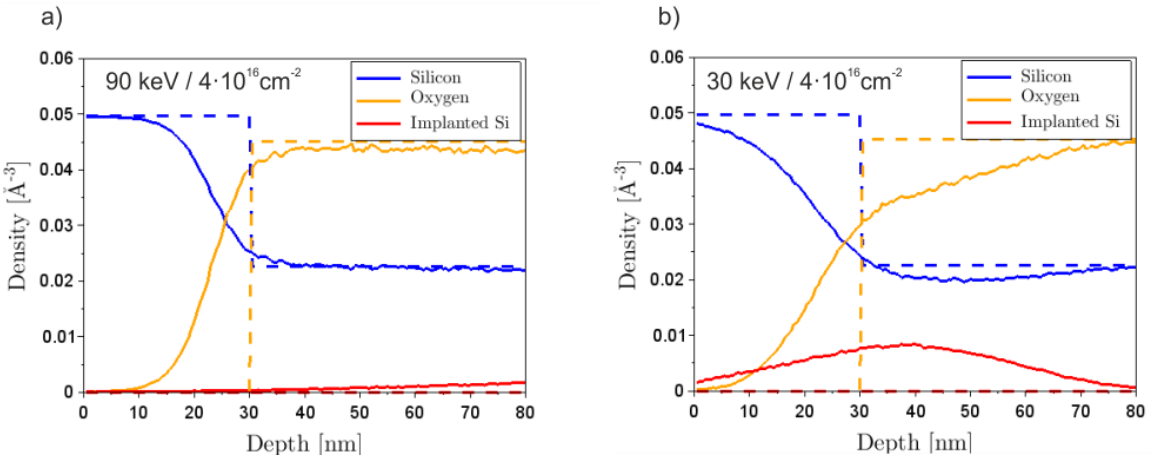

Figure 3-5: Simulation results of Si^+ irradiation of a Si/SiO_2 interface placed in a depth of 30nm. The ion energy was 90 keV (a) and 30 keV (b) with a total fluence of $\mathbf{4 \cdot 10^{16}\ cm^{-2}}$. Calculations were done by TRIDYN.

Characterizing the profile is barely possible by a continuous numerical function of three different species. The mixing process can be transformed into a diffusion process and gives the diffusion coefficient as a quantitative description of the mixing profile. Fick's diffusion equation takes into account a density in the range 0 to 1, which defines the two phases Si and SiO_2. In the following, the non-stoichiometric SiO_x is described as a two-phase system of chemically inert SiO_2 species and excess Si atoms. The fraction of the latter gives a Si excess profile over the depth x

$$c(x) = \frac{n_{\mathrm{tot}}(x)}{2n_{\mathrm{Si}}^0}(3q_{\mathrm{Si}}(x) - 1) \tag{8}$$

with $q_{\mathrm{Si}}(x)$ as the Si atomic fraction, $n_{\mathrm{tot}}(x)$ the total (Si+O) atomic density and n_{Si}^0 the atomic density of crystalline Si. Under the conditions of Figure 3-5 (a), the Si excess profile is mostly governed by ballistic IBM during the irradiation. The Si excess of Equation (8) is governed by the diffusion equation [147]

$$\frac{\partial c}{\partial t}(x,t) = D_{\mathrm{B}} \Delta c \tag{9}$$

with the irradiation time t and D_{B} as the constant "ballistic" diffusion coefficient [148]. For the starting composition profile of the system

$$c(x, t=0) = \begin{cases} 1, & x < 30\ \mathrm{nm} \\ 0, & x > 30\ \mathrm{nm} \end{cases} \tag{10}$$

and the boundary conditions

$$\begin{aligned} c(x,t) &= 0, \quad \text{for } \lim_{x \to \infty} \\ c(x,t) &= 1, \quad \text{for } \lim_{x \to -\infty}, \end{aligned} \tag{11}$$

the solution of Equation (9) is

$$c(x,t) = 1 + \frac{1}{2}\mathrm{erf}\left\{\frac{x - x_1}{2\sqrt{D_{\mathrm{B}} t}}\right\} \tag{12}$$

with x_1 as the position of the interface at time t. To take into account the implanted ions in the composition profile, an artificial Gaussian-shaped term is added to the fit-function of Equation (12), which leads to

$$c(x,t) = 1 + \frac{1}{2}\mathrm{erf}\left\{\frac{x - x_1}{2\sqrt{D_{\mathrm{B}} t}}\right\} + A_{\mathrm{G}} \exp\{-(\mathrm{x} - B_{\mathrm{G}})^2/(C_{\mathrm{G}})^2\}, \tag{13}$$

where the free artificial parameters are $A_{\mathrm{G}}, B_{\mathrm{G}}, \text{and } C_{\mathrm{G}}$. This term describes the Gaussian shaped ion ranges as shown in Figure 3-4. The parameters will change with the fluence. For parameterization of D_{B}, Equation (13) has been fitted to TRIDYN results by least squares optimization. The region of optimization interest was the Si/SiO_2 interface, and $x = 0$ is the position of the initial surface. Fitting results for the system of Figure 3-5 by Equation (13) are shown in Figure 3-6. In Figure 3-6 (b), the overlapping of the Gaussian profile is needed, which describes the implanted ions.

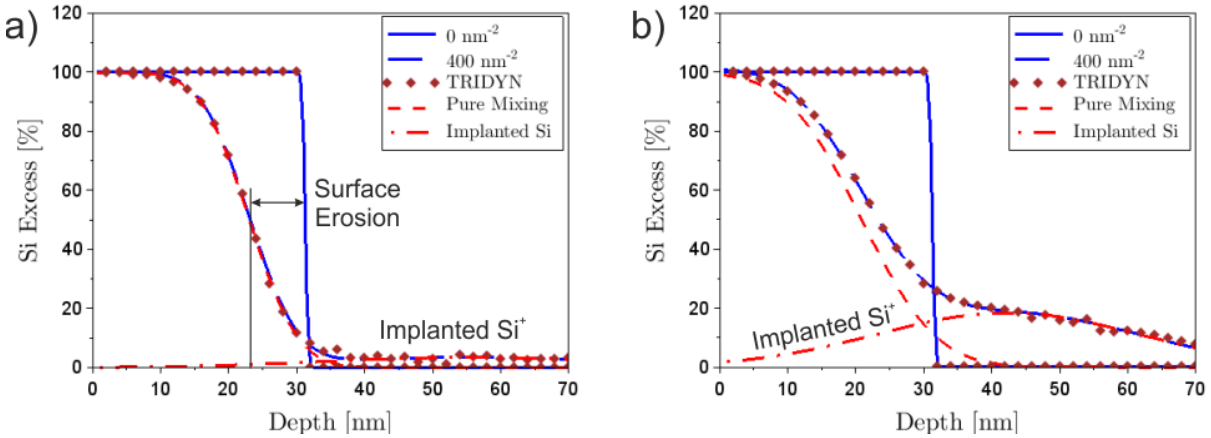

Figure 3-6: Composition profiles (see Equation (8)) calculated by TRIDYN for irradiation of a Si/SiO_2 interface at a depth of 30 nm by Si^+ with 90 keV (a) and 30 keV (b) shown as black dots. The blue lines show the Si excess according to Equation (13) and the dashed lines show the two different terms of Equation (13).

In summary, this chapter has reformulated the composition profile and transformed it into a Si excess parameter according to Equation (8). This shows the equivalence of Si/SiO_2 mixing to a

diffusion process according to Fick's second law by Equation (9). The composition profiles of a Si/SiO_2 interface during irradiation were calculated and the influence of implanted ions was shown. Conclusions are:

- The composition profile during pure IBM can be exactly approximated by Equation (13), which is given by the solution of the diffusion equation in Equation (9). This can be used to reduce the profile characteristics onto one single parameter, the *ballistic diffusion coefficient* D_B. This will be used in Chapter 5 to simulate the irradiation of a buried SiO_2 layer as well as in the next chapter to investigate the symmetry of the composition profile.
- The implanted ions significantly falsify the fit of the TRIDYN results by Equation (12), and the profile requires a Gaussian term to compensate the implanted ions (see Equation (13)). To describe the IBM by Equation (9), the ion ranges need to be much deeper than where the interfaces are placed and/or the fluence is low enough, so that implanted ions at the interface can be neglected.
- Sputtering will not be an issue in the ranges of fluence lower than $2 \cdot 10^{16}\ \mathrm{cm}^{-2}$.

3.2.2 Controlling Composition Profiles of Si/SiO_2/Si by IBM

To provide reliable predictions for the starting configuration, the main task for this subchapter is to precisely control the amount of Si excess without disturbing the symmetry by ion energy and fluence. In Chapter 3.2.1, the possibility of fitting the Si excess profile after pure IBM of the SiO_2 layer by Equation (12) was introduced and derived from the diffusion equation (Equation (9)). It gives one paramete D_B, for each interface, which quantifies the strength of the IBM. In this chapter, this will be used for both interfaces, D_B^{dn} and D_B^{up}, to compare both parameters and identify the differences in symmetry depending on the energy and fluence of the ion beam.

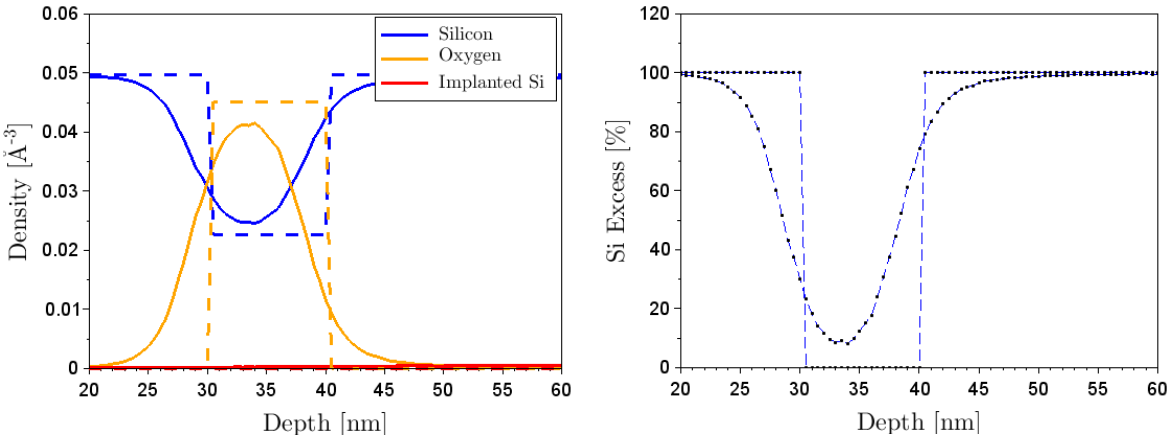

Figure 3-7: Composition profiles calculated by TRIDYN of a buried SiO_2 layer at a depth of 30 nm after irradiation by Si^+ with 60 keV and a total fluence of $0.85 \cdot 10^{16}\ \mathrm{cm}^{-2}$. (a) shows the results for each participating component and (b) shows the calculated Si excess, according to Equation (8) (black points) and the fit by Equation (14) (broken blue line).

The composition profile during irradiation of two interfaces (a buried SiO_2 layer) is simply given by a combination of two solutions to Fick's diffusion

$$c(x,\Phi) = 1 + \frac{1}{2}\left(\operatorname{erf}\left\{ \frac{x - x_1}{2\sqrt{D_\Phi^{\mathrm{dn}}\Phi}} \right\} - \operatorname{erf}\left\{ \frac{x - x_2}{2\sqrt{D_\Phi^{\mathrm{up}}\Phi}} \right\} \right) \tag{14}$$

with the positions of the interfaces x_1 and x_2, the flux $\varphi = \Phi/t$, the total fluence is Φ, the relative diffusion coefficients $D_\Phi^{\mathrm{i}} = D_\mathrm{B}^{\mathrm{i}}/\varphi$ for i = dn (bottom interface), and i = up (upper interface). Figure 3-7 shows the irradiation profile of a buried SiO_2 layer after a fluence of $0.85 \cdot 10^{16}\ \mathrm{cm}^{-2}$ in (a) and the corresponding Si excess including the fit of Equation (14) in (b). The sample was irradiated by a Si^+ ion beam with the energy of 60 keV and shows a slight shift compared to the initial profile. This is attributed to the sputtering of the top-Si and with only 2 nm able to neglect. The crucial part is the difference between D_Φ^{up} and D_Φ^{dn} and how it behaves for different irradiation parameters. Figure 3-8 (a) shows the parameters D_Φ^{up} and D_Φ^{dn} for a buried layer with the thickness of 10 nm at a depth of 30 nm (corresponding to Figure 3-7). The values for D_Φ^{up} are plotted as solid lines and D_Φ^{dn} as dashed lines for different irradiation energies over the fluence.

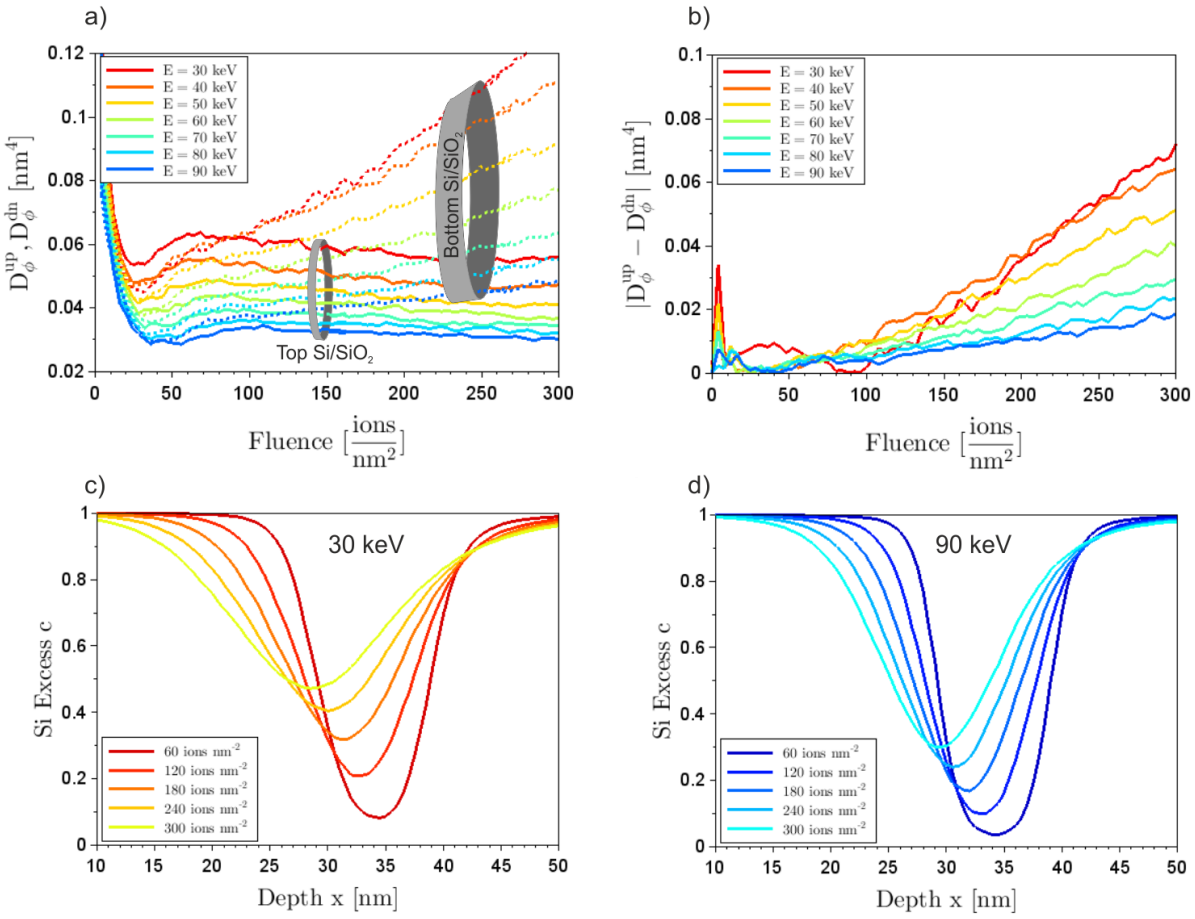

Figure 3-8: Calculations of irradiating a 10 nm thick buried SiO_2 layer at a depth of 30 nm. (a) the parameters D_Φ^{up} and D_Φ^{dn} of Equation (14), which has been fitted to the results obtained by TRIDYN; (b) the difference between D_Φ^{up} and D_Φ^{dn}; (c) the most asymmetric composition profile is caused by an irradiation energy of 30 keV; (d) the most symmetric composition profile occurs with irradiation energy of 90 keV.

As can be expected from the conclusions of Chapter 3.1, the diffusion coefficients show a strong difference for low energies and a much smaller difference for higher energies. This is attributed to a combination of effects done by implanted ions and by displaced ions. At low energies up to 50 keV, the difference is mainly due to the higher amount of implanted ions at the deeper Si/SiO_2 interface. By increasing the energy, this difference decreases. Figure 3-8 (b) shows the total difference between D_Φ^{up} and D_Φ^{dn} over the fluence. At low fluences, there is almost no difference, while at higher fluences, the difference increases linearly. While the mixing power is proportional to the root of fluence, the amount of implanted ions increases linearly with fluence. Initially, only a few ions are necessary to produce a strong mixture, while the implanted ions do not disturb the profile much. After a fluence of $10^{16}\ \mathrm{cm}^{-2}$, the mixture slows down at both interfaces while the increase of implantation stays the same and results in more implanted ions at the deeper Si/SiO_2 interface. This then leads to a linearly growing difference in the mixing. Figures 3-8 (c) and (d) show the Si excess profile during irradiation with Si^+ ions with the energy of 30 keV and 90 keV, respectively. While the actual difference is difficult to see, the mixing efficiency is clearly shown. After a fluence of $1.8 \cdot 10^{16}\ \mathrm{cm}^{-2}$ at an energy of 30 keV, the Si excess in the middle of the SiO_2 layer reaches 0.35 and the 90 keV ion beam needs a fluence of $3 \cdot 10^{16}\ \mathrm{cm}^{-2}$ to reach the same Si excess.

In summary, this chapter shows the composition profile of a buried SiO_2 layer during ion beam irradiation. The different influences of the energy and fluence of the ion beam were studied using the diffusion coefficients of each interface D_Φ^{up} and D_Φ^{dn}. This leads to the following conclusions:

- Although the mixing and implantation do not result in exact symmetrical conditions over the depth of the target material, the SiO_2 layer for the SET can be symmetrical and guarantee equal tunnel distances.
- The combination of two solutions of the diffusion equation results in a suitable function for the composition profile of a buried SiO_2 layer and evaluates the symmetry.
- Higher energies cause less asymmetry but also induce less interface mixing. The correct parameters for energy and fluence need to be carefully adjusted to get the right profile for the annealing process step.

4 Reaction Pathways of SiO_x towards Equilibrium by Thermal Activation

The SET scheme proposed in Chapter 2.3 requires structure sizes (<5nm) beyond all modern direct manufacturing processes in the industry. Self-organization is a very promising approach to overcome this limit. The basic principle is to put a system into non-equilibrium and let it develop towards equilibrium by thermal activation. During this process, the system organizes itself and different patterns emerge (see Chapter 2.4.3). In the case of a pattern according to the production scheme in Figure 2-3, the heat treatment shall be interrupted.

Chapter 3.1 showed how the stable domains of pure Si and pure SiO_2 reached such a non-equilibrium state through the increase of free energy by mechanical work (ion irradiation). Silicon atoms are mixed into SiO_2 (see Chapter 3.2) and lead to supersaturation. However, to get out of this state and reduce the free energy, the system has to overcome energy barriers (see Chapter 4.3.2 and 4.3.5). Defects such as interstitials or open bonds must relax, move or restructure. Heat treatment of the sample can realize the necessary energy fluctuations to overcome these barriers by thermal activation. This reaction pathways to the equilibrium state are controlled by various physical processes can be described approximately theoretically and precisely simulated by suitable models. The task of Chapter 4.1 is to model this heat treatment with the KMC method and to introduce an extension of the existing model.

The simulation can then help to better understand the effects of the processes on the reaction pathways. However, before new predictions can be made, it must be proven that the known is reproducible. To this end, the values for the free parameters of the model in Chapter 4.1 must be selected either by appropriate assumptions or by experimental results. For the Si-SiO_2 system it is possible to measure diffusion (see Chapter 4.2.2) and solubility (see Chapter 4.2.3) experimentally isolated. Basic theories and qualitative observations can also be used to support model development and verification. This is used in Chapter 4.2 to determine parameters of the KMC model.

Furthermore, it is essential for the simulation of the nanopillar in Chapter 6 which processes are dominant in which cases, exert their influence in combination with others or whether they do not occur at all. In order to control the self-organization of the single NC in the nanopillar, it is important to know how these processes depend on temperature, geometry, and the Si excess. Chapter 4.3 examines relevant processes that occur during the reaction pathway of the system. These are then consulted in Chapter 6.2 to understand the simulation results for the nanopillar system.

Influences of Individual Processes on the Reaction Pathway

Each of the processes mentioned above makes a specific contribution to the reaction pathway of the system. Interface reconstruction, nucleation and growth of NCs are dependent on supersaturation and supersaturation is dependent on the presence of interfaces and NCs (see Chapter 2.4.2). Besides, each of these processes takes place at different speeds and depends on temperature. Only if each process can be reproduced correctly the predictions of the simulation are trustful. The following summary gives a brief overview of the individual topics to be covered in this chapter.

Nucleation is the first step that occurs during annealing of an immiscible mixture. In a homogeneous mixture of Si and SiO_2, the nuclei form spontaneously with random time and position. This randomness generally counteracts controllability. However, temperature and Si excess can influence the size and nucleation probability of a nucleus. Chapter 4.3.2 discusses to what extent this is possible.

The growth of nanoclusters can be observed in experiments and analytically described by established theories. Chapter 4.3.2 shows simulation results of the growth of Si-NC and SiO_2-NC. It clarifies which physical processes control the respective growth process. This will be important for understanding the reliability of the individual NC formations in Chapter 6.

The influence of an NC on its environment is decisively changing the development of the system. Due to the different diffusion and reaction rates, Si-NCs and SiO_2-NCs have different influences on the Si excess around them. This, in turn, influences the neighboring NCs and interfaces. In Chapter 4.3.3-4.3.4 the simulation results are compared with the Gibbs-Thomson relationship and the Ostwald Ripening. It shows what Si-NCs and SiO_2-NCs make with their environment and how this depends on size and temperature. This will be important to interpret the observations in the simulation during annealing of a mixed Si/SiO_2 interface (Chapter 4.3.6) and a nanopillar (Chapter 6.2.2).

Ostwald ripening is a process that takes place during the reaction pathways of an ensemble of NCs. There are several established theories on this subject, which, however, can only accurately describe the correlations in individual limit cases. Chapter 4.3.4 compares the simulation results with the known theories and investigates differences between Si-NCs and SiO_2-NCs.

Spinodal decomposition is another mechanism of phase separation and replaces nucleation for highly supersaturated mixtures. Different laws are governing the spinodal decomposition and lead to different dependencies of temperature and Si excess. In Chapter 4.3.5 the theory of Cahn Hilliard is introduced. The double-wall potential is used to study the influence of temperature and Si excess. This is important to interpret the simulation results of the annealing of planar samples (Chapter 4.3.6) and nanopillar (Chapter 6).

Overview

Chapter 4.1 first introduces how to model the SiO_x as a binary alloy on an FCC lattice. Furthermore, Chapter 4.1.3 presents the extensions that were made to model the diffusion and. In Chapter 4.2 the model is parameterized by an extensive search for experimental data in the literature. Chapter 4.3 bases on the phase diagram presented in Chapter 4.3.1. Each sub volume in the nanopillar can be assigned to a specific point in the phase diagram. Chapter 4.3.5 and Chapter 4.3.2 investigate the influence of this point in the phase diagram on spinodal decomposition and nucleation. After the formation of Si domains (sponge-like or NCs) the reaction pathway is investigated. Chapter 4.3.3 shows the effect of individual NCs on their environment and Chapter 4.3.4 the interaction between NCs. Finally, annealing of a mixed Si/SiO_2 interface shows an interaction of all processes.

4.1 Modeling Phase Separation of SiO_x by Kinetic Monte Carlo Method

The functionality of the SET is very sensitive to any variation in geometry because the most sensitive component, the *island* (see Figure 2-2), is made by the most uncertain processes. The island is built in the nanometer range by two statistical processes, IBM by Si^+ ions and self-organization of the nanopillar. Both pass their high randomness to the formed Si-NCs. Chapter 3.1 studied the first process step. The task of this chapter is to simulate the self-organization by heat treatment.

The demands on the model are high. Structures have to be reproduced in high detail in order to investigate the smallest geometric influences on tunneling. Chapter 4.2.2 will study the speed of the different processes in Si and SiO_2, which differ by orders of magnitude. Since the processes in SiO_2 are considerably slower, the computing time will increase if these processes are to be observed. It is necessary to find a method that can model the system on an atomistic scale but at the same time, simulate very long annealing times. The KMC method has already been successfully used in the past to simulate Si and SiO_2 systems [89], [102]–[104]. Mostly, however, it was not performed with experimental parameters and without including the different diffusion constants in Si and SiO_2. In order to accurately simulate the heat treatment of a mixed Si/SiO_2 interface, this cannot be neglected and must be treated carefully.

Overview of Simulation Methods

This thesis uses the BCA, the KMC method and a phase-field approach. Parameters from calculations with other methods are also used. This makes it necessary to first obtain an overview of the available methods around the used ones. Figure 4-1 shows an overview of the groups of methods and their areas of application.

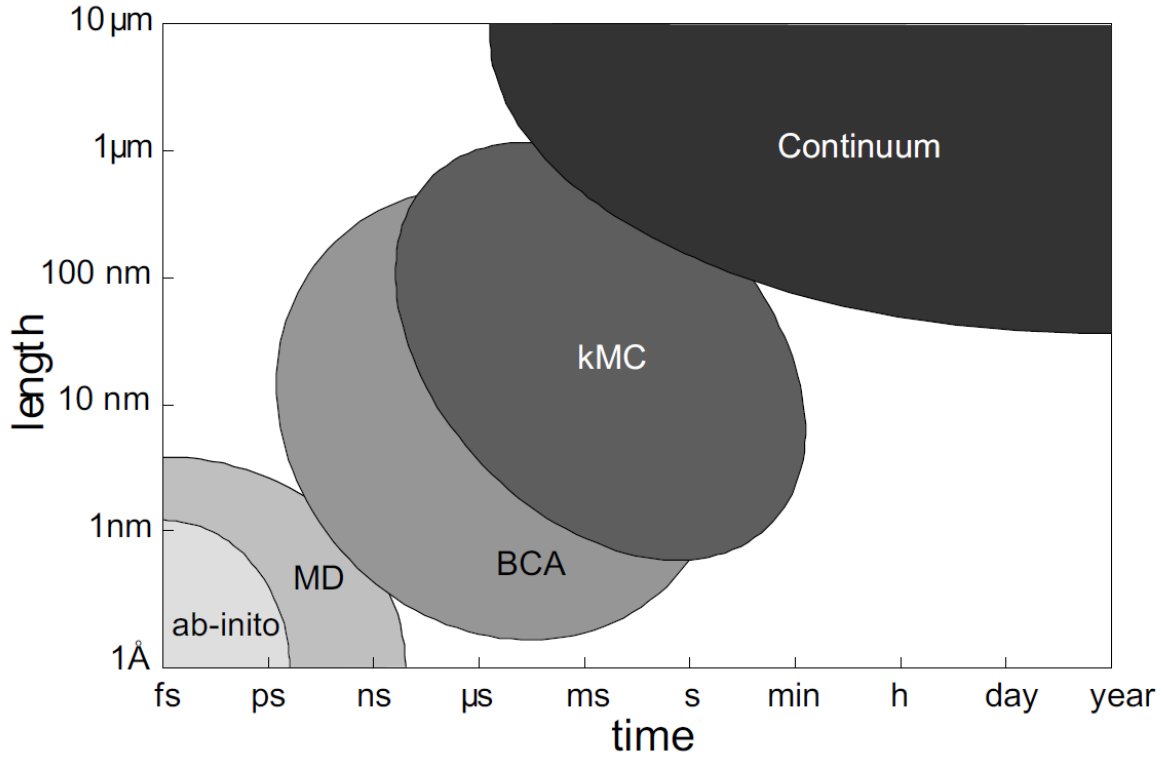

Figure 4-1: Schematic representation of which simulation methods are applied on which length and time scales. Ab-initio and Molecular Dynamics (MD) approaches only support small-scale and short-time simulations, while continuum methods allow to simulate long-term development of large systems. In between, Monte Carlo-based approaches such as BCA and kMC are best suited. Taken from ref. [149].

Ab initio calculations can achieve the highest level of detail with the lowest degree of approximation. Methods from this group simulate the exact development of electronic fields according to the basic quantum mechanical laws, without including experimental knowledge. It is possible to calculate supporting results for approaches such as MD or KMC, but phase separation is strongly out of scope.

Molecular dynamics simulations essentially solve the Newton equations for the atoms involved in a given interatomic multibody potential. It is necessary to select this potential appropriately for the treated system, e.g. surface studies have to use other potentials than the diffusion of interstitials in a lattice. Depending on the system, the potentials can be derived from experimentally motivated or ab initio-based methods. The great advantage is the level of detail that can be achieved by this type of simulation. The biggest problem with MD simulations, however, is the small time scale, which lies in the size of nanoseconds. In the case of phase separation, the MD simulations are limited to the first stages of decomposition.

Methods based on BCA or KMC are derived from more detailed methods by reducing the computing time through strong approximations. This allows the investigation of larger systems for longer periods of time and the main reason for the high popularity of atomistic approaches like the KMC method [150]–[152].

Continuum methods are very efficient methods to simulate large systems for long time periods. These include calculations of magnetic fields, stress fields or fluid mechanics. The simulation of the binary phase system can be realized by solving the reaction diffusion equations. Processes such as Oswald Ripening can be calculated very quickly under complex, non-homogeneous conditions [99], [153], [154]. Phase field approaches can successfully simulate processes such as the evolution of

spinodal structures in a very short computing time [155]–[158]. However, nanoscale processes such as nucleation are not easy to describe. Diffusion as a random pathway on the nanoscale must be modelled by these methods with a diffusion coefficient on the macroscopic scale. The atomic bond at interfaces/surfaces must be modelled by surface tension.

Large spatial and temporal scales are necessary to be able to simulate phase separation, so that ab initio and approaches are definitely out of the question. Due to its limited time, which is only a few nanoseconds even for small systems, molecular dynamics is usually not used. In the present work continuum methods (phase field) and KMC are used, since they serve with the highest possible degree of detail and nevertheless allow the simulation of large systems.

The Kinetic Monte Carlo Method

KMC is a very efficient method for modeling and simulating thermally activated processes [153], [159]–[161]. It has been used in the past for various basic and applied research, such as the growth of nanoclusters [90], and their application in non-volatile memories [85], the temporal evolution of nanoclusters [90], spinodal decomposition [162], [163] and ion beam processing of interfaces and surfaces [149]. The kMC method inherently includes the majority of statistical laws, e.g. the Gibbs-Thomson relation [153], Ostwald Ripening [91] or the Lifshitz Slyozov Wagner (LSW) distribution [93], [94]. But also theories like the reaction diffusion equation [99], [153] can be reproduced. The development of systems described by reaction diffusion equations can in many cases be treated more efficiently by the kMC method due to the simpler implementation of boundary conditions. It has also been used to successfully model experimental observations such as the formation of Au-NCs [164] or the inverse Ostwald Ripening during ion beam irradiation [91], [102]. Further studies also showed relevant results such as pit coarsening during ion erosion [165], [166] or the Raleigh instability of nanowires [167]. Extensions were made to simulate the phase diagram of AlPb including different solubilities of the occurring phases on the basis of many-body interatomic potentials [149]. The KMC method was used as an extension of the program code TRIDYN (based on BCA) to simulate chemical interactions during BCA simulations in a program code called TRIDER [149]. The simulation of the macroscopic order of metals [168]–[171], of ferro- and antiferromagnetism or self-organizing processes during irradiation or annealing [172]–[174] can thus be easily simulated on the basis of basic physics. It is possible to simulate processes of thermodynamics and statistics, nucleation, spinodal decomposition, Ostwald Ripening and the growth of nuclei without modifications [153], [175].

The simulation by KMC is essentially the realization of a Markov process [150] [176]. Based on thermally activated fluctuations, the system gets the possibility to bring itself into equilibrium by changing its state step by step. The modelling of the mixed Si-SiO_2 system as a binary alloy is described in Chapter 4.1.1. Chapter 4.1.2 will introduce how it is possible to simulate the reaction pathway of this system as a Markov chain. Modeling the different diffusion coefficients and solubilities involves several questions. The treatment of the diffusion within a Si excess between pure Si and pure SiO_2 must be clarified and the requirements of the Markov process ensured. This is solved in Chapter 4.1.3 and 4.1.4.

Extending the Kinetic Lattice Monte Carlo Method to Model Diffusion and Solubility

Simulations of systems made of Si and SiO_2 have been extensively carried out in recent decades using the kinetic Monte Carlo (KMC) method. Mostly the systems were interpreted as a binary alloy with two components of the same behavior. One component, as a minority in the other, had the same properties as vice versa. This assumption was appropriate since only the development of the minority phase of one component was simulated in a uniform matrix of the majority phase. It was not yet necessary to treat the annealing of interfaces between Si and SiO_2 in detail. Here it must also be taken into account that diffusion coefficients and the solubility are different, depending on whether it is oxygen in silicon or silicon in SiO_2. Especially the diffusion with a difference of 15 orders of magnitude poses a complicated problem.

A Si excess profile of a mixed Si/SiO_2 interface can be divided into 3 main areas: (i) The area above the Si/SiO_2 interface is an oxygen-supersaturated Si matrix, (ii) the interface itself, which is mainly SiO, and (iii) the SiO_2 matrix, which is Si-supersaturated. The system evolution has a different behavior in each of these regions and the reaction pathway can be divided into 5 different processes.

(i) Separation of SiO_2 Nanoclusters in supersaturated Silicon
(ii) Growing of SiO_2 Nanoclusters
(iii) Reconstruction of the Si/SiO_2 interface by spinodal decomposition of SiO_x in the region of the Interface
(iv) Separation of Si Nanoclusters in supersaturated SiO_2
(v) Growing of Si Nanoclusters

A hardly known and insufficiently explained mixture of Si and SiO_2 represents a difficult challenge for the investigation of self-organization in the nanopillar. It is therefore important to understand the reaction pathways of the system that describe nucleation, NC growing and the reconstruction of the interface. Chapters 4.3.1-4.3.5 examine all relevant processes during annealing. Later, the interaction of all processes during annealing of the mixed Si/SiO_2 interface is shown in Chapter 4.3.6.

In order to simulate the development of nanostructures such as the nanopillar, the model must first be able to reproduce all relevant isolated processes. Chapters 4.1.1 and 4.1.2 present KMC method, which was already used to make relevant research over the past decades [103], [175], [177], [178]. But KMC simulations were largely based on scaled parameters and it was not necessary to identify a quantified agreement with experiments. The inclusion of the differences in diffusion and solubility for each material (Si and SiO_2) made it necessary to parameterize the model using data from the literature (Chapter 4.2).

4.1.1 Modeling SiO_x as a Binary Alloy

The system Si-SiO_2 consists of the two phases Si and SiO_2, which consist of the atoms Si and O. This system can also be reduced to the Si excess (see Chapter 3.2.1) by assuming mass conservation and neglecting pressure. But also in this case the system consists of two components: Si excess and the background matrix SiO_2. All three cases show binary systems, which leads to the approach of a binary alloy.

However, each of them gives different components, individual atoms (Si and O), phases (Si and SiO_2) or species (Si excess and SiO_2 background matrix). The question is what exactly the components of the binary alloy should be and how these components should interact with each other.

The KMC represents the volume of the system in terms of sub volumes on a fixed lattice. This is the big assumption of the method and results in a discretization of the simulation cell. In order to model atomistic interactions, these lattice sites are then scaled to the size of the atoms. The thermodynamic models can be used by linking the lattice to the Ising model.

Mass Transport in SiO_x

What needs to be simulated is the phase separation and how it initiates self-organization. This is mainly due to the formation of Si and SiO_2 domains by the physical property of immiscibility. Si and oxygen atoms diffuse, while pure Si and pure SiO_2 domains are energetically favored and therefore more stable. In order to model the phase separation, it must first define the mass and its diffusion.

However, mass transport in a mixture of Si and SiO_2 has not been clarified yet. The possible processes causing the mass transport are the movement of Si, oxygen interstitials and vacancies of both. According to [179], the migration energies of oxygen vacancies with values between 1.7 and 1.9 eV are small and make them a probable diffusion process. According to [180], it is unlikely that mass transport is caused by the movement of isolated Si interstitials. By generating thousands of different activation events, the authors showed that the most likely mechanism is the dynamic dangling of bonds (either a Si atom or an O atom). Diffusion occurs through the creation, destruction, and movement of single dangling bonds.

It is hardly possible to precisely simulate mass transport on the atomic basis in SiO_x. However, macroscopic effects can easily be reproduced by appropriate approximations. The addition of an excess Si atom to a SiO_2 bulk corresponds to the formation of 2 SiO molecules. The diffusion of a Si interstitial thus corresponds to the diffusion of an oxygen void and leads to the same macroscopic result. The division of the SiO_x into sub volumes of Si and SiO_2 gives the option to model any of the aforementioned mass transport mechanisms.

Mapping the Binary Alloy Hamiltonian on the Ising Hamiltonian

Models based on binary alloys are very successful in modeling thermodynamic driving forces that cause phase separation [153], [160], [161], [181]–[184]. This can usually be traced back to the basis of the ising model. In order to use it also for the model in this thesis, the Hamiltonian of the alloy must first be connected to the ising Hamiltonian.

To determine the Hamiltonian of the alloy, the physical laws between the Si occupied lattice sites and the SiO_2 occupied lattice sites must first be defined. In order to keep things simple, silicon and SiO_2 are assigned to components A and B, respectively. A brief summary of the necessary assumptions is given:

(i) No interstitials allowed.
(ii) Isotropic interactions, same strength in every direction.
(iii) A lattice site is screened by its neighbors and influences of the lattice sites behind the neighbors are neglected.

(iv) Sites are fixed; thermal fluctuations are not resolved as trajectories.

(v) Internal stress is not taken into account.

This leads to 3 different Interactions between the components: AA, BB, AB and the Hamiltonian for this system can be written in

$$H_{\mathrm{ALLOY}} = -\left[J^{\mathrm{AA}}N_{\mathrm{AA}} + J^{\mathrm{BB}}N_{\mathrm{BB}} + J^{\mathrm{AB}}N_{\mathrm{AB}}\right] \tag{15}$$

with the numbers for the different bonds

$$\begin{aligned} N_{\mathrm{AA}} &= \frac{1}{2}\sum_{\langle i,j\rangle} c_i c_j \\ N_{\mathrm{BB}} &= \sum_{\langle i,j\rangle} (1-c_i)(1-c_j) \\ N_{\mathrm{AB}} &= \sum_{\langle i,j\rangle} c_i(1-c_j) \; + \sum_{\langle i,j\rangle} (1-c_i)c_j \end{aligned} \tag{16}$$

with $c_i = 0$ for a site occupied by SiO_2 and $c_i = 1$ for a site occupied by Si. In this case $\langle i,j\rangle$ means that only the closest neighbours are considered. With Equation (15) and (16) the Hamiltonian is described by 2 components, 3 interactions and their number. This must be assigned to the ising-Hamiltonian. The first step is to reduce the number of interactions N_{AA}, N_{AB} and N_{BB}. The total number of nearest neighbors of type A can be described by

$$\eta N_{\mathrm{A}} = \; N_{\mathrm{AB}} + 2N_{\mathrm{AA}} \tag{17}$$

and the total number of next neighbors of species B by

$$\eta N_{\mathrm{B}} = \; N_{\mathrm{AB}} + 2N_{\mathrm{BB}} \tag{18}$$

with η as the number of next neighbors per atom. Each BB-bond in (16) is counted twice, because each AB bond has only one B site as its next neighbor. In a BB bond, however, each of both B sites has a B site as neighbor. The same applies to AA bonds in Equation (17). Considering the total number of atoms

$$N = \; N_{\mathrm{A}} + N_{\mathrm{B}}. \tag{19}$$

Combining with Equation (17) and Equation (18), the numbers of component B can be expressed in terms of numbers of component A

$$N_{\mathrm{B}} = N - N_{\mathrm{A}}, \tag{20}$$

$$N_{\mathrm{BB}} = N_{\mathrm{AA}} + \frac{\eta(N - 2N_{\mathrm{A}})}{2}, \tag{21}$$

$$N_{\mathrm{AB}} = \eta N_{\mathrm{A}} - 2N_{\mathrm{AA}}. \tag{22}$$

This makes it a system of component A in the background of component B. The Hamiltonian of Equation (15) is now given by

$$H_{\mathrm{ALLOY}} = -\left[\left(J^{\mathrm{AA}} - 2J^{\mathrm{AB}} + J^{\mathrm{BB}}\right)N_{\mathrm{AA}} + \left(J^{\mathrm{AB}} - J^{\mathrm{BB}}\right)\eta N_{\mathrm{A}} + J^{\mathrm{BB}}N\frac{\eta}{2}\right]. \tag{23}$$

This can now be converted to the ising model using

$$\mathrm{c}_i = \frac{1}{2}(s_i + 1) \tag{24}$$

with the ising spin states $s_i = \pm 1$. Putting Equation (24) and Equations (17)-(22) together gives

$$\mathrm{N}_{\mathrm{AA}} = \frac{1}{4}\sum_{\langle i,j\rangle} s_i s_j + \frac{\eta}{2}\sum_i s_i + \frac{1}{8}\eta N \tag{25}$$

and

$$\mathrm{N}_{\mathrm{A}} = \frac{N}{2} + \frac{1}{2}\sum_i s_i. \tag{26}$$

By Equations (24)-(26) the Hamiltonian of Equation (15) results in

$$H_{\mathrm{ALLOY}} = -\left[\frac{1}{4}\left(J^{\mathrm{AA}} - 2J^{\mathrm{AB}} + J^{\mathrm{BB}}\right)\sum_{\langle i,j\rangle} s_i s_j + \frac{\eta}{4}\left(J^{\mathrm{AA}} - J^{\mathrm{BB}}\right)\sum_i s_i + \frac{\eta}{8}\left(J^{\mathrm{AA}} + 2J^{\mathrm{AB}} + J^{\mathrm{BB}}\right)\right] \tag{27}$$

what corresponds to the ising Hamiltonian [185]

$$H_{\mathrm{ISING}} = -J\sum_{\langle i,j\rangle} s_j s_i + \mu\sum_i s_i + \mathrm{const.} \tag{28}$$

with

$$J = \frac{1}{4}\left[J^{\mathrm{AA}} + J^{\mathrm{BB}} - 2J^{\mathrm{AB}}\right]. \tag{29}$$

As the coupling factor which defines the bonding energy of s_j and s_i and

$$\mu = \frac{\eta}{4}\left(J^{\mathrm{AA}} - J^{\mathrm{BB}}\right) \tag{30}$$

as the external magnetic field strength μ. This model was developed to simulate phase transitions in magnetic materials [185]. In the case of a positive J, the spin ensemble aligns in parallel and the system becomes ferromagnetic. In the case of a negative J, the system transforms into an antiferromagnetic behavior. For a constant number of atoms (conserved system), the Hamiltonian simplifies into a

$$H_{\mathrm{ISING}} = -J\sum_{\langle i,j\rangle} s_j s_i + \mathrm{const.} \tag{31}$$

In Chapter 4.1.3, however, the coupling factor becomes concentration-dependent and the second term of Equation (28) will no longer, strictly speaking, be constant. This magnetic field μ indicates the chemical potential within the alloy model and does not contribute to the reaction pathway. In view of this, it is assumed that the chemical potential also remains constant. The model presented by Equation (29) and Equation (31) gives a general description of SiO_x by discretization of the volume

and binarization of the concentration. The variables $J^{\mathrm{AA}}, J^{\mathrm{AB}}$ and J^{BB} allow to introduce composition dependent parameters.

The Lattice Structure

Both, the KMC model and the Ising model, are based on a fixed periodic lattice and its Hamiltonians in Equation (27) and Equation (28) can only be calculated by a defined lattice structure. This lattice is the great approximation of the KMC method and requires a certain lattice structure. The most commonly used structures are SC, BCC and FCC. For crystalline materials, the lattice structure observed in the experiment can be used. The Si/SiO_2/Si stack has an amorphous structure after irradiation, which becomes polycrystalline (Top-Si) and monocrystalline (Bottom-Si) during annealing. To the best of the author's knowledge, crystalline facets at the interface between Si and SiO_2 have not been observed. This leads to an amorphous interface. During annealing, the structure of SiO_2 remains viscous and thus also maximally amorphous. The NCs with diameters smaller than 3nm are mostly non-crystalline or the crystal structure is limited to the inner area only. This leads to the assumption of an amorphous structure of the Si- SiO_2 system in this thesis. The crystalline structures of the upper and lower Si are neglected. The FCC lattice has the highest degree of amorphousness of all possible structures and is therefore used for the simulations in this thesis. In order to model processes on an atomic scale, the volume of a lattice site must correspond to the volume of a Si atom. The size of a SiO_2 lattice site has to be estimated. Pure SiO_2 has about twice the volume of pure Si and so the sub volume of a SiO_2 occupied site contains about half the mass of SiO_2, e.g. 0.5*SiO_2.

The last question is how the Hamiltonian for the FCC lattice looks like in the KMC model. Figure 4-2 shows an example of different configurations on the FCC lattice and the corresponding energies in the Ising model and the alloy model. In a) to c) configurations around lattice sites occupied by SiO_2 are shown. A neighboring configuration consisting only of SiO_2 lattice sites (a) yields the alloy energy of $12J^{\mathrm{BB}}$, which corresponds to an ising energy of $-12J$. In the case of a mixed neighborhood (b) the energy is $6J^{\mathrm{BB}} + 6J^{\mathrm{AB}}$ or 0. In a pure Si environment the energy is given by pure A-B interactions with$12J^{\mathrm{AB}}$. This shows how the linear energy increase from $-12J$ to $12J$ is mapped to a combination of interactions between 2 components (Si and SiO_2).

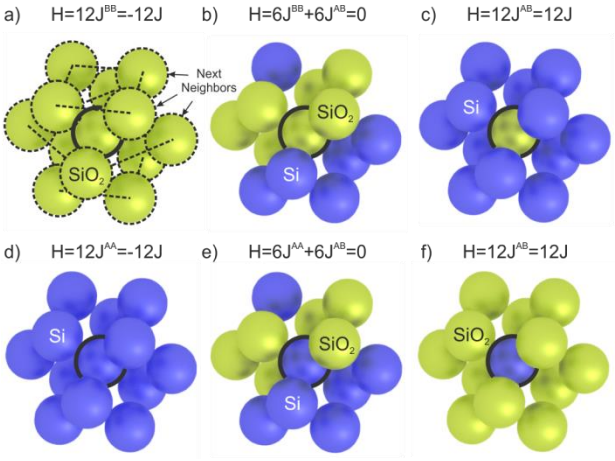

Figure 4-2: Schematically shown are SiO_2 sites in a)-c) and Si sites in d)-f) with 3 different neighboring configurations: In a) and d) the closest neighbors consist completely of the same occupation. In the case of b) and e), the sites are surrounded by a completely mixed environment. In c) and f), both sites are surrounded by foreign occupation. The corresponding bond energies to the nearest neighbors are indicated in terms of the Ising model and in terms of the binary alloy model.

In summary, this chapter showed how the Si-SiO_2 system is discretized on an FCC lattice (see Figure 4-2), modelled as a binary alloy and assigned to the ising model. The binary species are a Si excess

atom implemented in a SiO_2 matrix. The Hamiltonian in Equation (27) describes the energetic configuration of the system on an atomic basis and is mapped to the Hamiltonian of the Ising model in Equation (28). The model gives the possibility to describe a composition-dependent bond between the Si atoms by adjusting the variables $J^{\mathrm{AA}}, J^{\mathrm{AB}}$ and J^{BB} in Equation (27). The Si-SiO_2 system is assumed to be continuously amorphous. Using the FCC lattice, the approach is optimal in terms of a KMC model to describe amorphous materials. This leads to the conclusions:

- Pressure or density change cannot be modelled, which excludes modeling of oxidation. This would require additional extensions.
- Amourphousity is only possible up to the degree of the FCC lattice. For any system that is more amorphous, this could lead to artifacts during simulation.
- Internal stresses are neglected. For low-temperature annealing (<900°C) this can play a role, since stresses at the Si/SiO_2 interface are only released at higher temperatures. This can be seen e.g. in oxidation by so-called self-limiting [79].

4.1.2 The Reaction Pathway by Kawasaki Exchanges

The last chapter defined the thermodynamic state of the system by determining the Hamiltonian in Equation (27) for a given configuration. However, the purpose of the model is to find the reaction pathway of a system from its non-equilibrium state (SiO_x mixture) to its equilibrium state by thermal activation according to Figure 2-4. Therefore, it is now necessary to model the kinetic process of diffusion.

During diffusion, variations of local configurations appear, which can be very different from an energetic point of view. Equation (31) shows that lattice sites with equal occupancy are preferred and thus more stable to thermal fluctuations. This stability leads to phase separation and must be modelled according to the Ising model. However, such movements are only possible at high temperatures (>900°C) (see Chapter 4.2.2). Immediately after mixing, the material is in a "frozen" state. In order to simulate diffusion and phase separation in dependency of temperature over time, a link to experimental data on activation energy and bond energy is required. This will be done in Chapter 4.2. This chapter shows how the diffusion mechanism is modelled by the so-called Kawasaki exchange [186]. Most studies first define the rates of all possible processes, then randomly choose one process according to its rate and finally increment the time. This work uses to simulate this exchange by the Metropolis algorithm [151]. That approach makes it easier to treat the diffusion of Si and O in SiOx.

Kawasaki Exchange

The simulation cell was discretized into a FCC lattice with sites that can be occupied either by Si (with the mass of a Si atom) or SiO_2 (with the mass of half a SiO_2 molecule). The diffusion of a Si atom means that it moves from its site to an adjacent site. The mass conservation and neglect of the pressure leads to a simultaneous movement of the mass from the adjacent site to the site of the Si atom. This exchange is called *Kawasaki exchange* [186] and the selected pair of lattice sites is called *Kawasaki pair*. If a Kawasaki pair consists of two identical atoms, there is no difference by an exchange. Therefore, a Kawasaki pair can only consist of a combination of a Si site and a SiO_2 site. The

change of the configuration by a Kawasaki exchange is however accompanied by a change of energy. The energy of the configuration around a location occupied by component A corresponds to Equation (31)

$$H_{\mathrm{A}} = -E_{\mathrm{NN}} \sum_{i} s_i + \mathrm{const.} \tag{32}$$

with the sum over all 12 next neighbors $i = 1, \ldots, 12$ and the bond energy

$$E_{\mathrm{NN}} = 4J. \tag{33}$$

For the next neighbors (NN). Thus, the energy for the environmental configuration of a Si lattice site can be determined by counting the bonds to other Si lattice sites. This gives the expression

$$H_{\mathrm{A}} = -E_{\mathrm{NN}} n_{\mathrm{A}} + \mathrm{const.} \tag{34}$$

with n_{A} as the number of Si neighbors. This makes it possible to calculate the energy for the occupancy before and after the Kawasaki exchange. The energy difference that must be overcome for the Kawasaki exchange is then given by

$$\Delta H_{\mathrm{A}} = H_{\mathrm{A}}^{\mathrm{f}} - H_{\mathrm{A}}^{\mathrm{i}} = -E_{\mathrm{NN}}(n_{\mathrm{f}} - n_{\mathrm{i}}) \tag{35}$$

with the energy for the Si atom when occupying the initial site $H_{\mathrm{A}}^{\mathrm{i}}$ and the final site $H_{\mathrm{A}}^{\mathrm{f}}$. The number of Si atoms in the configuration for the initial and final site is n_{i} and n_{f}, respectively. Figure 4-3 shows schematic examples of Kawasaki pairs and their surrounding configurations for a FCC lattice. In case a), the Kawasaki pair is surrounded by pure SiO_2 and thus a pure diffusion process of Si in SiO_2 is described. The configuration after the Kawasaki exchange is shown in d). Figure 4-3 c) shows a Kawasaki pair in pure Si. The configuration energy also does not change due to the Kawasaki exchange. However, if the locations of the Kawasaki pair are surrounded by different numbers of Si neighbors, the energy needs to change. Figure 4-3 b) shows how the Si site has 8 Si atoms in its surrounding and the SiO_2 site only 5. This leads to higher energy after the Kawasaki exchange and requires thermal activation. To achieve the configuration shown in e), an energy difference of $3E_{\mathrm{NN}}$ must be overcome.

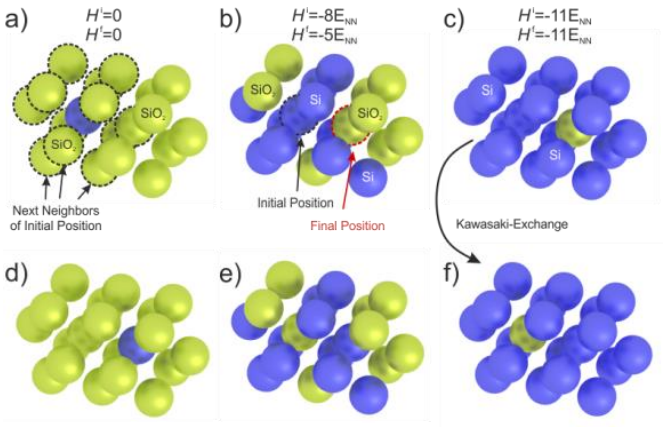

Figure 4-3: Schematically shown Kawasaki pairs with surrounding neighbors in pure SiO_2 (a), mixed SiO_x (b) and pure silicon (c). In d) to f) the configurations after the execution of the Kawasaki exchange are shown.

Modelling Thermal Activation by Metropolis Algorithm

The diffusion is described by a Kawasaki exchange, which can reduce, equalize or increase the free energy of the system depending on the configuration. Reaction pathways based on the simple execution of all possible Kawasaki exchanges which decrease the energy will quickly come to an end. Once a configuration in which no Kawasaki change reduces energy is reached, the system remains stable. However, this state does not necessarily have the lowest possible free energy and can remain in a metastable state.

In order to reduce the energy of the system in the metastable state, it is possible to introduce random fluctuations that model the thermal activation. Here it comes with lower probability also to Kawasaki changes, which increase the free energy, on average however energy-reducing events are preferred. Thus the free energy falls and the chain of configurations results gives the *reaction pathway*.

The Metropolis algorithm offers an established possibility to physically simulate such thermally activated processes [151]. The idea is to give each configuration X a "probability of existence" $P(X)$ by weighting its energy with the Boltzmann probabilities

$$P(X) = A\exp\left\{-\frac{H(X)}{\mathrm{k_B}T}\right\} \tag{36}$$

with the energy $H(X)$ for the temperature T and the Boltzmann's constant $\mathrm{k_B}$. Configurations with high free energy will result in lower probability of existence and vice versa. The difference of 2 states X and Y is then given by

$$\frac{P(X)}{P(Y)} = A\exp\left\{-\frac{H(X) - H(Y)}{\mathrm{k_B}T}\right\} \tag{37}$$

and gives the transition probability from configuration X to configuration Y. The statistical selection of the transitions and the execution according to their probabilities in Equation (37) leads to a sequence of possible events leading to the equilibrium of the system. This is also called the *Markov process* and the pathway is called the *Markov chain*. One step of this Markov chain is the statistical reduction of energy so that the system goes through a large number of different states, but on average towards equilibrium. An exchange process of the components A and B has the exchange probability

$$P_{\mathrm{if}} = \begin{cases} 1, & n_{\mathrm{f}} > n_{\mathrm{i}} \\ \exp\left\{\dfrac{-E_{\mathrm{NN}}(n_{\mathrm{i}} - n_{\mathrm{f}})}{\mathrm{k_B}T}\right\}, & n_{\mathrm{f}} \leq n_{\mathrm{i}} \end{cases} \tag{38}$$

with the Boltzmann constant $\mathrm{k_B}$, the temperature T and the number of Si neighbors n_{i} and n_{f} at their initial and final site, respectively. A Monte Carlo step (MCS) is defined as *N* statistical exchange attempts with *N* as the number of lattice sites of the System. Thus statistically every Si atom had the possibility to diffuse during one MCS. It has been shown by ref. [152] that this algorithm ensures the following

- Ergodism of the system – any atom can reach any lattice site.
- The system converges into the equilibrium state after an infinite number of MCS.
- In thermodynamic equilibrium the detailed balance is fulfilled.

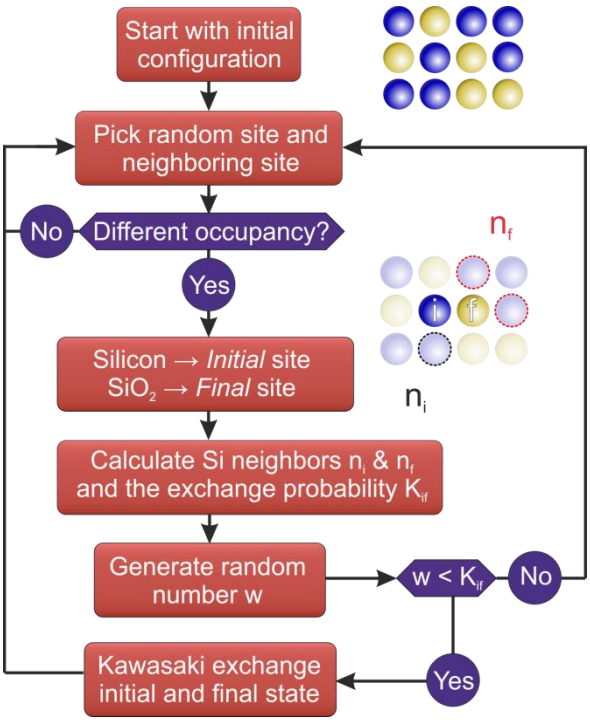

Figure 4-4: Flowchart of the KMC algorithm. A random Kawasaki pair is selected from the start configuration and the Kawasaki exchange is executed in case of a sufficiently high probability.

Figure 4-4 schematically shows the sequence of the attempt to perform a Kawasaki exchange according to the Metropolis algorithm. For the start configuration any Si excess profiles can be used, e.g. results from IBM simulations by TRIDYN or random Si excess distributions. The first step is to statistically determine a Kawasaki pair. The site occupied by Si is defined as the initial site and the site with SiO_2 as the final site. Counting the neighboring Si atoms results in the jump probabilities according to Equation (38), which then determine by means of a random number $w \in [0,1]$ whether the Kawasaki exchange is carried out ($w \leq P_{\mathrm{if}}$) or not ($w > P_{\mathrm{if}}$). Figure 4-5 shows the jump probability over the exponential argument in Equation (37). If the energy is lowered by the exchange, the probability is 1 and the exchange is performed. If the free energy must increase, the random number must be lower than the curve shown.

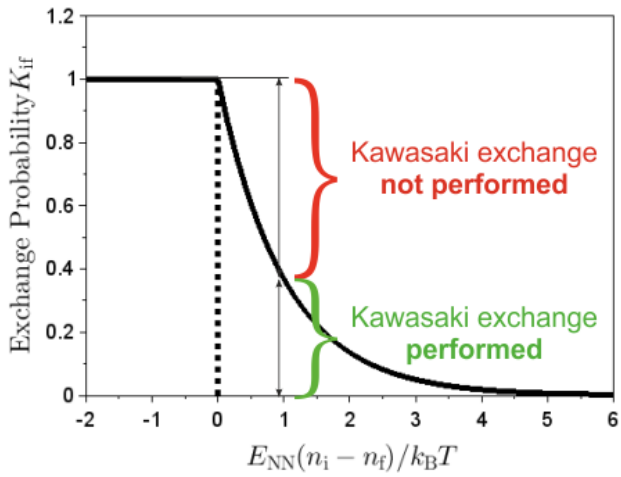

Figure 4-5: Kawasaki exchange probability for a diffusion process in Si according to Equation (39). After counting the nearest neighbors for the initial and final positions ni and nf, the argument for the exponential function can be determined. Using the example of 1 for the argument, the ranges for the random number are indicated. If the random number is smaller than 0.4, the Kawasaki exchange is performed.

From a technical point of view, this algorithm is very inefficient and wastes enormous computing power. In a phase-separated system most bonds consist of 2 identical atoms (Si-Si bond or SiO_2 - SiO_2

bond). Thus, the first step of Figure 4-4 is performed thousand times until a Kawasaki pair is found. In the past, a double-book keeping approach was introduced and the calculation was improved by over an order of magnitude. Parallelization has also been successfully implemented. For further information on the technical improvements of the KMC program codes, the work in ref. [85], [149] is recommended.

Diffusion Slowing down the Markov Process

The algorithm presented in Figure 4-4 can generate a Markov chain that provides a possible reaction pathway for the system from the non-equilibrium state to the equilibrium state. However, the SiO_x remains metastable at temperatures below 800°C. Looking at Equation (38), the algorithm in Figure 4-4 generates a reaction pathway independent of temperature. To be consistent with diffusion experiments, the Kawasaki exchange must be linked to the diffusion coefficient. The exchange probability in Equation (38) depends only on the energy barrier by the bond energy E_{NN}. The energy barrier by diffusion is neglected so far.

At the atomic level, temperature consists of the fluctuations of atoms around their middle position. Their kinetic energy determines the global temperature of the entire system. To diffuse, the kinetic energy of these fluctuations must exceed a certain threshold, *the activation energy*. This energy is added to the already given threshold value and the influence of the diffusion is thus defined by an additional probability term

$$P_{\mathrm{if}} = \frac{1}{\tau_0}\exp\left\{\frac{-E_{\mathrm{A}}}{\mathrm{k_B}T}\right\}\begin{cases} 1, & n_{\mathrm{f}} > n_{\mathrm{i}} \\ \exp\left\{\dfrac{-E_{\mathrm{NN}}(n_{\mathrm{i}} - n_{\mathrm{f}})}{\mathrm{k_B}T}\right\}, & n_{\mathrm{f}} \le n_{\mathrm{i}} \end{cases} \tag{39}$$

with the exchange frequency $1/\tau_0$ and the activation energy E_{A}. According to the Weinberg method [187], the exchange frequency does not change during one diffusion event and can be assumed to be constant over one Kawasaki exchange. However, it should be noted that this endangers the validity of the Markov process as there is no certainty that the probability in Equation (39) is less than 1. This issue will be addressed later.

In summary, this chapter shows how diffusion on the KMC lattice can be modelled by Kawasaki Exchanges (see Figure 4-3). These Kawasaki Exchanges then realize the reaction pathway by a subsequent occurrence as shown in Figure 4-4. This chain of Kawasaki exchanges is also interpreted as a Markov chain with the transition probability to change the configuration in Equation (37) and the process of creation a reaction pathway as a Markov process. The simulation is performed by the Metropolis algorithm and linked to the diffusion process by Equation (39). This leads to the conclusions:

- Each Markov chain generates an individual reaction pathway. In order to control the self-organizing process in Figure 2-3, each reaction pathway must pass through the intended nanostructure. Chapter 6 will examine the reliability of self-organization and must produce a statistically significant number of reaction pathways. These are then generated by the algorithm in Figure 4-4.
- The Markov chain is at risk because the probability P_{if} could be greater than 1 and the expression in Equation (39) must be re-normalized.

4.1.3 Different Diffusions and Solubility in Si and SiO_2

At the end of the last chapter, the Kawasaki exchange was linked with the diffusion coefficient in Equation (39). However, it is a constant in this form, regardless of whether the Kawasaki exchange models the diffusion of Si in SiO_2 or O in Si. But the diffusion of oxygen in Si is almost 15 orders of magnitude faster than the diffusion of Si in SiO_2, what will be discussed in more detail in Chapter 4.2.2. The same case may generally apply to the bond energies and will be studied in Chapter 4.2.3. The activation energy E_A as well as the bond energy E_NN in Equation (39) must therefore depend on whether the Kawasaki pair is in Si or in SiO_2. This is determined by counting the number of next neighbor Si atoms and adjusting both energy values. In the case of a full occupation by Si, the Kawasaki exchange models a diffusion of oxygen in Si and vice versa. In between, both values have to be interpolated.

However, there are only experimental data for the two limit values (diffusion in pure Si and diffusion in pure SiO_2) and interpolation is therefore a pure approximation. In general, E, E_NN and τ_0 must be treated with a dependency on the composition around the Kawasaki exchange pair. The bond energy

$$E_\mathrm{NN} = J^\mathrm{AA} + J^\mathrm{BB} - 2J^\mathrm{AB} \tag{40}$$

for a component A completely surrounded by component B, and vice versa, is as follows

$$E_\mathrm{NN}^\mathrm{tot} = 12J^\mathrm{AB}. \tag{41}$$

Tight binding potentials show a square root dependence on the composition for metals [188] and for several alloys like AlPb, PtCo [149]. For SiO_x, however, there is no information about the dependence of the composition. The simplest approach in this case is a linear interpolation between the two limit cases, Si in pure SiO_2 environment and vice versa. For the KMC lattice model this results in

$$E_\mathrm{NN}(z) = E_\mathrm{NN}(0) + \big(E_\mathrm{NN}(Z_\mathrm{NN}) - E_\mathrm{NN}(0)\big)z \tag{42}$$

with z as the number of the next Si neighbors and Z_NN as the number of considered neighborhood sites of a Kawasaki pair. This gives a $Z_\mathrm{NN} = 18$ for an FCC lattice and the two unknown parameters with $E_\mathrm{NN}(0)$ (pure SiO_2) and $E_{NN}(18)$ (pure Si). For the parameters of diffusion, E and τ_0, unfortunately there is also no deeper information about the dependence on the composition. For this reason, linear interpolation is also used here between the limit cases (diffusion in Si and diffusion in SiO_2)

$$E_\mathrm{A}(z) = E_\mathrm{A}(0) + \big(E_\mathrm{A}(18) - E_\mathrm{A}(0)\big)z, \tag{43}$$
$$\tau_0(z) = \tau_0(0) + \big(\tau_0(18) - \tau_0(0)\big)z. \tag{44}$$

By that, the exchange probability of Equation (39) results in

$$P_\mathrm{if}(\mathrm{z}) = \begin{cases} \dfrac{1}{\tau_0(z)} \exp\left\{\dfrac{-E_\mathrm{A}(z)}{\mathrm{k_B}T}\right\}, & n_\mathrm{f} > n_\mathrm{i} \\ \dfrac{1}{\tau_0(z)} \exp\left\{\dfrac{-E_\mathrm{A}(z)}{\mathrm{k_B}T}\right\} \exp\left\{\dfrac{-E_\mathrm{NN}(z)(n_\mathrm{i} - n_\mathrm{f})}{\mathrm{k_B}T}\right\}, & n_\mathrm{f} \leq n_\mathrm{i} \end{cases} \tag{45}$$

with the number of next neighbors to the Kawasaki pair $z \in [0,..,18]$. Finally, Equations (42) to (45) show an approach, which allows reproducing the experimental results for both limit cases.

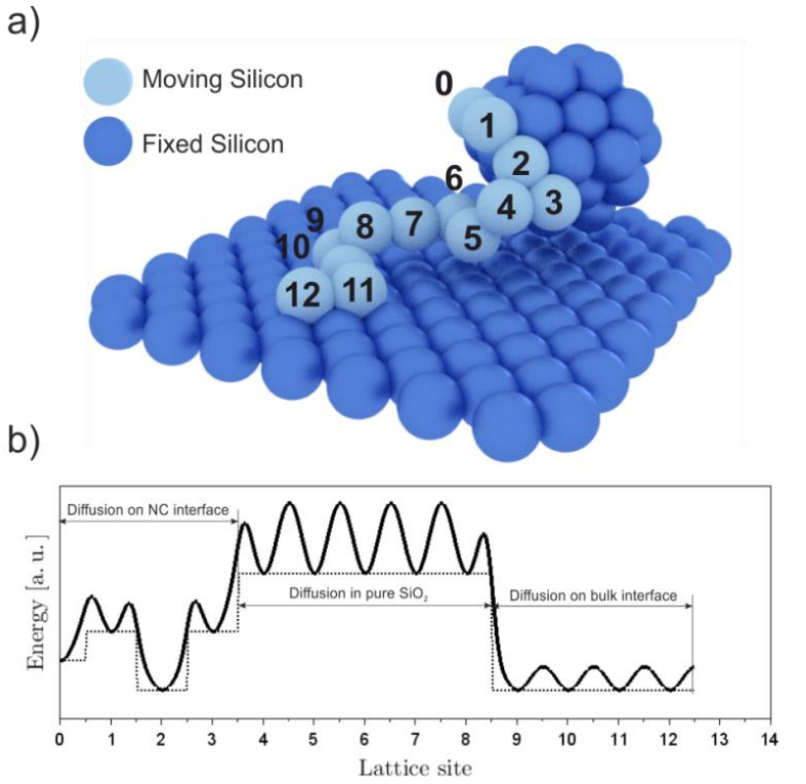

Figure 4-6: Schematically presented the diffusion pathway of a Si component in a) and corresponding energy level along its 13 positions in b). During this exemplary pathway, the rest of the system remained frozen and the SiO_2 was made invisible for imaging purposes. The first 3 Kawasaki exchanges were performed on the surface of a nanocluster. The exchange 4 to 8 was carried out by the pure SiO_2 mass and the last 4 carried out a surface diffusion on a Si interface.

To better understand the energy flow for a diffusion process, Figure 4-6 shows an example of a diffusion pathway of a Si atom through the SiO_2 matrix while leaving the rest of the system untouched. In a) a 3D visualization of the individual sites can be seen and in b) the corresponding energy function along the diffusion pathway. The peaks in b) between the sites give the activation energy E_{A} and the thin lines the bond energy E_{NN}. During the initial stage, the first 4 sites of the Si atom have very fluctuating energy levels due to the curvature of the NC. After the Si atom has overcome the energy barrier of diffusion and bonding, the diffusion pathway from site 4 to 8 is performed in an environment of pure SiO_2. This results in the highest diffusion barriers because diffusion in SiO_2 is the slowest. The diffusion pathway [189] finally reaches the interface of Si/SiO_2 and passes through positions 9 to 12 as surface diffusion. As can be seen, the neighboring sites are occupied partially Si and partially SiO_2, so that also the activation energy in Equations (43) and (44) was adjusted slightly downwards. Thus the diffusion over the surface takes place much faster than the previous diffusion through the SiO_2 mass.

In summary, this chapter shows in Figure 4-6 and Equation (45) how the difference of diffusion and bond strengths for Si and SiO_2 can be modelled by a dependence of the Kawasaki pair on the composition. Since there is no other information, a linear interpolation by Equations (43) and (44) between the two boundary cases (pure Si and pure SiO_2) is assumed. Following conclusions can be made

- The linear interpolation is reliable for the limit cases ($z = 0$ and $z = 18$), but the uncertainty increases with the number of z and has its maximum at z=9. In this case the diffusion is described in a SiO environment, which is mainly the case at a Si/SiO_2 interface. The predictions for this case will show the greatest uncertainty.
- The predictions for the diffusion in a pure Si or pure SiO_2 environment depend only on the uncertainty of the parameters.

4.1.4 Renormalization of Kawasaki Exchanges

The reaction pathway of the system is interpreted as a Markov chain of Kawasaki exchanges (see Figure 4-3) and its evolution is simulated by the Metropolis algorithm (see Figure 4-4). The Kawasaki exchange was linked to the diffusion coefficient by Equation (45) and led to the probability P_{if} for the state transition in Equation (37). However, it is not guaranteed that this value lies between 0 and 1 and must therefore be normalized. In order to interpret the reaction pathway as a Markov chain, P_{if} must be normalized to the highest possible probability. The highest probability is given by the fastest process, which is the diffusion of oxygen in Si. This is modeled by a Kawasaki Exchange using Equation (39) with z=18, which leads to the normed Kawasaki probability

$$K_{\mathrm{if}}(\mathrm{z}) = \frac{\frac{1}{\tau_0(z)}\exp\left\{\frac{-E_{\mathrm{A}}(z)}{\mathrm{k_B}T}\right\}}{\frac{1}{\tau_0(18)}\exp\left\{\frac{-E_{\mathrm{A}}(18)}{\mathrm{k_B}T}\right\}}\begin{cases}1, & n_{\mathrm{f}} > n_{\mathrm{i}}\\ \exp\left\{\frac{-E_{\mathrm{NN}}(z)(n_{\mathrm{i}}-n_{\mathrm{f}})}{\mathrm{k_B}T}\right\}, & n_{\mathrm{f}} \le n_{\mathrm{i}}\end{cases} \tag{46}$$

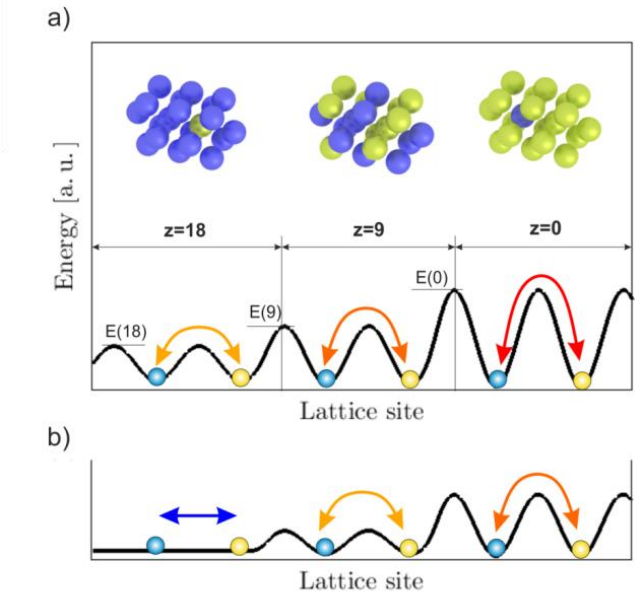

Figure 4-7: The energy barriers for a Kawasaki exchange in different environments. In a) it is represented by P_{if} from Equation (45) and in b) after normalization in Equation (46).

Figure 4-7 shows the diffusion energy barrier for different neighbor configurations in a) and how it looks after the renormalization according to Equation (46) in b).

Figure 4-7 b) shows the diffusion of O in pure Si is "infinitely fast" within the Metropolis algorithm [151]. After this renormalization, the model finally describes all essential points of the system and must now be investigated.

In summary, this chapter ensures the validity of the Markov process and the Equation (37) by normalizing the expression for P_{if} from Equation (39) to the probability K_{if} for the Kawasaki exchange results in Equation (46). The normalization value is the diffusion of oxygen in Si because this is the fastest process (see Chapter 4.2.2 for more details). The diffusion time of oxygen over the length of the distance of a Kawasaki pair corresponds to one MCS.

4.2 Simulation Parameters

The KMC model from the last chapter provides the description of interactions of individual sub volumes on a FCC lattice as shown in Figure 4-3. At a volume size of one Si atom, the interactions are described via activation energy and bond energy E_{NN} in Equation (46) on an atomic basis. In order for the simulation results to agree with the experimental results, it is necessary to determine the free parameters of Equation (46) (E_{A}, τ_0, E_{NN}). If the model can then reproduce the known experiments, it is expected to accurately predict the unknown experiments.

Chapter 4.2.2 will show that diffusion in Si and SiO_2 varies by 15 orders of magnitude and that both diffusion coefficients can only be determined with uncertainties of 1 and 3 orders of magnitude. This uncertainty passes to the results for the time and the temperature parameter of the model. A similarly difficult case is solubility. Chapter 4.2.3 will show that solubility values were found only for oxygen in silicon and also with a deviation of one order of magnitude. Most KMC studies in the past were performed by scaling the diffusion, introducing a relative temperature and a relative time [89], [103], [178]. This made it possible to investigate phase separation at different start configurations and geometric boundaries, but not temporal dependencies. In this work, the O-supersaturated Si and Si-supersaturated SiO_2 are divided only by the Si/SiO_2 interface, as shown in Figure 2-3. This results in a reaction pathway in which the velocity of the events varies by 15 orders of magnitude (see Table 1 and 2), while they are only a few nanometers apart. The model must reproduce this at least approximately. Solubility has a less important aspect, but must still be chosen in the most appropriate way. In general, it is necessary to determine the parameters $E_{\mathrm{NN}}(0)$, $E_{\mathrm{NN}}(18)$, $E_{\mathrm{A}}(0)$, $E_{\mathrm{A}}(18)$, $\tau_0(0)$ and $\tau_0(18)$.

In order to parameterize the KMC model in Equation (46), results from experiments on diffusion and solubility will be used. The activation energy E_{A} can be determined by an experimental diffusion coefficient for different temperatures and the bond energies E_{NN} by the solubility [111]. This is done in Chapter 4.2.2 and 4.2.3. Before this, the size of the lattice constant and the connection between an MCS and a second are determined in Chapter 4.2.1.

4.2.1 The scale of Time and Length

The interactions between the lattice sites are defined by the activation energies and binding energies on an atomic basis in Equation (46). The lattice constant must be determined so that the mass on each lattice site corresponds approximately to that of one atom. The Kawasaki exchange describes diffusion, also on an atomic basis as shown in Figure 4-3. For the fastest process (O diffusion in Si) a Kawasaki exchange takes place on average exactly once per MCS and can therefore be directly assigned to the time of the diffusion process from O in Si in seconds.

However, a SiO_x mixture has neither a lattice with fixed positions nor a defined sub volume of a Si atom (see Chapter 4.1.1). This also induces differences of the diffusion pathway in the KMC lattice to the experiment, in addition to the uncertainty in 3 orders of magnitude. In this chapter, appropriate assumptions are made and the limitations of the model in terms of time and duration of the simulation are discussed.

The Link from Time in Seconds to Time in MCS by the Diffusion Coefficient

The connection of the time between the diffusion pathway in the KMC lattice and the diffusion pathway in the real material is a complex matter. As already mentioned, the coefficients for the diffusion of O in Si vary over 3 orders of magnitude, giving the time in seconds an uncertainty of factor 1000. This certainly does not lead to accurate predictions in time. However, the difference between the velocity of events in pure Si and events in pure SiO_2 varies by 15 orders of magnitude, making the uncertainty of 3 orders of magnitude acceptable. Thus the predicted time is not reliable, but not the influence of the velocity differences on the reaction pathway. In order to connect the seconds with MCS, the time alignment between diffusion pathways in the experiment and the simulation is required. The system is normalized to the diffusion of O in Si (z=18) (see Equation (46)), so that the diffusion coefficient of oxygen in silicon can be determined by [189]

$$D_{\mathrm{theo}}(18) = \frac{1}{\tau_0(18)} \exp\left\{\frac{-E_{\mathrm{A}}(18)}{\mathrm{k_B}T}\right\} \frac{{a_{\mathrm{lat}}}^2}{\xi} \tag{47}$$

with the lattice constant a_{lat} and the coordination number ξ of the used lattice structure ($\xi_{\mathrm{fcc}} = 12$). It gives the lattice diffusion coefficient for SiO_2 sites performing a random walk [189] on a discrete Si lattice by jumping along nearest neighbor sites. The frequency $1/\tau_0(18)$ gives the duration time of the atomic jumps. The coupling to the experimental diffusion coefficient can be made by comparing the diffusion lengths

$$l = \sqrt{2D_{\mathrm{exp}}^{\mathrm{Si}} t} = \sqrt{2D_{\mathrm{theo}}(18)\, \tau k_{\mathrm{MCS}}} \tag{48}$$

with k_{MCS} as the number of Monte Carlo steps, $D_{\mathrm{exp}}^{\mathrm{Si}}$ as the diffusion coefficient of O in Si and

$$\tau = \tau_0(18) \exp\left\{\frac{E_{\mathrm{A}}(18)}{\mathrm{k_B}T}\right\} \tag{49}$$

as the time constant of the diffusion event. To calculate the experimental time for a KMC step, Equations (47) and (48) must be combined

$$D_{\mathrm{theo}}(18)\tau k_{\mathrm{MCS}} = \frac{{a_{\mathrm{lat}}}^2}{\xi} k_{\mathrm{MCS}} = D_{\mathrm{exp}}^{\mathrm{Si}} t \tag{50}$$

and thus the experimental time is given by

$$t = \frac{{a_{\mathrm{lat}}}^2 k_{\mathrm{MCS}}}{\xi D_{\mathrm{exp}}^{\mathrm{Si}}} \tag{51}$$

and for a single MCS

$$\Delta t = \frac{{a_{\mathrm{lat}}}^2}{\xi D_{\mathrm{exp}}^{\mathrm{Si}}}. \tag{52}$$

The Size of the Simulation Cell in Agreement with the Experimental Size

For the present work, the lattice constant is chosen so that the density of pure silicon is reproduced correctly. Under the assumption that the pure silicon lattice has to reproduce the atomic density of $n_{\mathrm{Si}}^0 = 4.9 \cdot 10^{22}\mathrm{cm}^{-3}$, the lattice constant for the KMC Modell follows with a=0.4338nm.

In summary, this chapter combined the time of one MCS with the time in seconds by Equation (52) and gave the lattice a size of $a_{\mathrm{lat}} = 0.4338\mathrm{nm}$. This leads to the following conclusions:

- The indication of the time of one MCS in seconds makes it necessary to have an experimental diffusion coefficient for oxygen in Si (see Equation (47)). Then it would be possible to make predictions about the annealing time of the system.
- The size of the FCC lattice does not depend on the composition.

4.2.2 Diffusion Constants and Activation Energies

Although it makes no sense to make predictions about time, the parametrization of the diffusion is crucial to investigate the influence of different diffusion constants in Si and SiO_2 on the reaction pathway. The Si-SiO_2 system is very important in microelectronics and there is a lot of data in the literature that can be used for parameterization. The diffusion coefficients for Si and SiO_2 have been investigated experimentally [25], [190]–[193] and theoretically (mainly by molecular dynamics) [194], [195] in the past. Unfortunately, however, the results provide values that scatter over 10 orders of magnitude (for the diffusion of oxygen in Si), which is not possible due to experimental uncertainties only. This indicates a dependence on the material conditions (crystalline, amorphous, etc.). SiO_2 can be divided into 2 basic categories: (i) monocrystalline quartz and (ii) vitreous SiO_2. The diffusion of Si in Si enriched crystalline SiO_2 showed the lowest diffusion coefficients [196]–[198] with a rather high activation energy of 6-7.6 eV. A very similar material system was investigated with 30 Si^+ implanted in SiO_2 [191] and showed significantly lower activation energies of 4.74-6 eV. These results were also

confirmed by molecular dynamic simulations [194], [195]. However, it should be noted that the Si of the Si matrix is bound, while the implanted isotopes act as interstitials. In the case of exchange between matrix Si and 30 Si^+ isotopes, the isotope remains bound in the matrix, while the 29Si performs the diffusion, but does not contribute to the measured diffusion. This could lead to a certain underestimation of the diffusion coefficient. But not only local material conditions influence the diffusion coefficient, geometric properties can also influence the mobility of Si in SiO_2. A Si/ SiO_2 interface has a strengthening effect on the self-diffusion of Si in SiO_2 [199].

While the implantation of 30 Si^+ isotopes and the measurement of their distribution after a certain time is a rather direct approach, some researchers tried to reconstruct the diffusion coefficient by observing the growth of nanoclusters [200], [201] or spinodal decomposition [202]. This led to the highest value for the diffusion energies of Si in SiO_2 in the literature of 1-2 eV. However, this approach suffers from additional experimental steps such as the measurement of NC sizes and theoretical approximations of growth models. For the present system of ion beam mixing, however, we can assume that it makes sense to use only the measurement results for vitreous SiO_2 determined by the measurement of implanted Si. This limits the found results to activation energies of 4.74 to 6 eV. In order to fully parameterize the diffusion in the KMC model, it is necessary to determine the diffusion rates for both limit cases (z=0 and z=18 in Equation (46)). A Kawasaki exchange in a complete Si environment corresponds to the diffusion of oxygen in silicon and results in the following relation

$$D_{\mathrm{exp}}^{\mathrm{Si}} = D_0^{\mathrm{Si}} \exp\left\{-\frac{E_{\mathrm{exp}}^{\mathrm{Si}}}{\mathrm{k_B}T}\right\} = \frac{1}{\tau_0(18)} \frac{{a_{\mathrm{lat}}}^2}{\xi} \exp\left\{-\frac{E_{\mathrm{A}}(18)}{\mathrm{k_B}T}\right\}. \tag{53}$$

A Kawasaki exchange in the surrounding of pure SiO_2 gives the relation

$$D_{\mathrm{exp}}^{\mathrm{SiO2}} = D_0^{\mathrm{SiO2}} \exp\left\{-\frac{E_{\mathrm{exp}}^{\mathrm{SiO2}}}{\mathrm{k_B}T}\right\} = \frac{1}{\tau_0(0)} \frac{{a_{\mathrm{lat}}}^2}{\xi} \exp\left\{-\frac{E_{\mathrm{A}}(0)}{\mathrm{k_B}T}\right\}. \tag{54}$$

By that, the necessary parameters for KMC are given by

$$\tau_0(0) = \frac{{a_{\mathrm{lat}}}^2}{\xi D_0^{\mathrm{SiO2}}} \text{ and } \tau_0(18) = \frac{{a_{\mathrm{lat}}}^2}{\xi D_0^{\mathrm{Si}}} \tag{55}$$

and

$$E_{\mathrm{A}}(0) = E_{\mathrm{exp}}^{\mathrm{SiO2}} \text{ and } E_{\mathrm{A}}(18) = E_{\mathrm{exp}}^{\mathrm{Si}}\,. \tag{56}$$

The parameters for z=1,…,17 are then interpolated according to Equations (42) to (44). The found data in literature can be seen in Table 1 and 2

Table 1: Literature data for the diffusion coefficients of Si in SiO_2. The number in the last column indicates the lines in Figure 4-8 a)

$D_0^{SiO2}\left[\frac{\mathrm{cm}^2}{\mathrm{s}}\right]$	$E_{\mathrm{exp}}^{\mathrm{SiO2}}[\mathrm{eV}]$	Ref.	T [°C]	Comment	No. in Figure 4-8 a)
1.378	4.74	[191]	1050-1150	SIMS	1
33.2	5.34	[192]	1000-1200	SIMS	2
0.8	5.2	[193]	1150-1300	SIMS	3
0.26	4.94	[194]		MD	4
328	6	[196]	1110-1410	SIMS	5
0.046	4.69			Fitted	Broken black line

Table 2: Literature data for the diffusion coefficients of O in Si. The number in the last column indicates the line in Figure 4-8 b).

$D_0^{\mathrm{Si}}\left[\frac{\mathrm{cm}^2}{\mathrm{s}}\right]$	$E_{\mathrm{exp}}^{\mathrm{Si}}[eV]$	Ref.	T [°C]	Comment	No. in Figure 4-8 b)
0.21	2.55	[203]		Calculated	1
22.6	3.15	[204]	1000-1280	Nuclear reaction analysis	2
0.23	2.56	[205]		Internal friction measurements	3
3.2	2.9	[206]	1000-1375	CPA analysis	4
0.07	2.44	[207]	700-1240	Wet oxidation	5
0.025	2.43	[208]		Theoretical	6
0.13	2.53	[209]	350-1300		7
0.17	2.54	[210]	330-1240	Internal friction measurements	8
0.14	2.53	[211]	700-1160		9
0.13	2.50	[211]	700-1100		10
0.11	2.51	[212]	650-1050		11
0.224	2.59			Fitted	Broken black line

The values from the literature (Table 1 and Table 2) vary by orders of magnitude, but the KMC model only needs one value for the Equation (46). For this, Equations (53) and (54) were adapted to the results of the literature using the least squares method by variation of E and D_0. Figure 4-8 shows the data for the diffusion coefficient of Si in SiO_2 in a) and for SiO_2 in Si in b). The additional broken black lines show the fit for the diffusion coefficients. These give values for E of 4.69 eV for Si diffusion in SiO_2 and 2.59 eV for oxygen species diffusing in silicon.

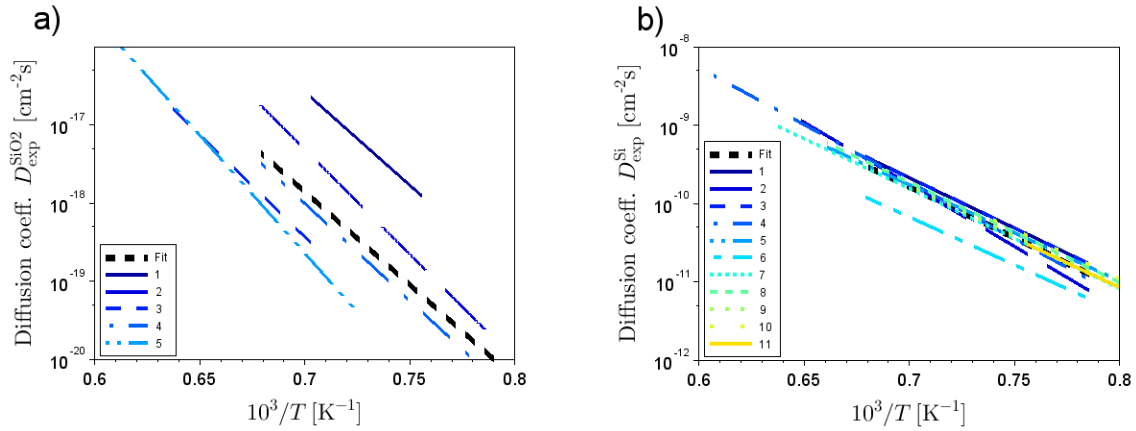

Figure 4-8: The diffusion coefficients, as obtained from the literature for Si in SiO_2 (a) and SiO_2 in Si (b), shown over inverse temperature. The thick dashed black line shows the fit to determine the numbers of Equation (46) for the KMC model. The exact values for the D0 and the activation energy E are given in Table 1 and 2 according to the number in the legend.

The values for diffusion for compositions between pure Si and SiO_2 remain an approximation by linear interpolation (see Equations (43) and (44)). This is shown in Figure 4-9 a) and the resulting diffusion coefficients over the inverse temperature in b). The model of Equation (46) is now able to reproduce the diffusion of Si in SiO_2 and O in silicon according to the experimental observations.

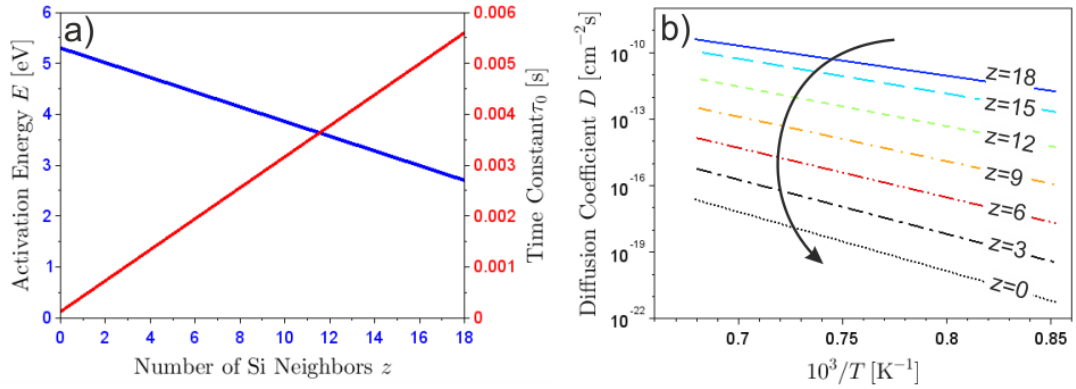

Figure 4-9: The parameters in Equation (46) for the diffusion. In a) the interpolation of $E(z)$ and $\tau_0(z)$ over the composition ($z=0,\ldots,18$) is plotted. In b) these numbers are used to calculate the diffusion coefficient over the inverse temperature.

In summary, various methods for measuring the diffusion coefficients of Si in SiO_2 and O in Si were presented. In the case of diffusion of Si in SiO_2, the results differed by 10 orders of magnitude. This cannot be based only on experimental uncertainties; so that the selection of the literature data was limited to values for vitreous SiO_2 (see Table 1). The diffusion of Oxygen in Si is about 15 orders of magnitude faster and the coefficients found in literature are shown in Table 2. The necessary parameters in Equation (46) for the model regarding diffusion were derived and interpolated according to Equations (43) and (44). However, the uncertainty in the diffusion of Si in SiO_2 remains at a factor of 1000, which leads to the following conclusions

- The uncertainty is too great to predict reasonable time spans by simulations.
- With a difference of 15 orders of magnitude for the diffusion in Si and in SiO_2, the uncertainty of 1000 is not so decisive. The influence of the difference on the reaction pathway is not limited by the uncertainty, even though it is a factore of 1000.
- The values for the parameters in Equation (46) for diffusion at the interface will be completely in the interpolated range. Therefore, the simulation results concerning the interface will be highly questionable.

4.2.3 Solubility and Bond Energies

The solubility of one substance in the other indicates how much can be dissolved in a state of equilibrium without achieving supersaturation. This can be measured by the substance coming into contact with the material to be dissolved, e.g. an interface Si/SiO_2 in case of solubilities of Si and O. This leads to attachments and detachments of dissolved monomers at the interface. In a state of equilibrium, the attachments and detachments will balance each other out, resulting in a so-called *detailed balance*. The bond energy E_{NN} defines the strength with which a Si atom is bound to the interface of SiO_2. If the bond is low, the tendency for Si to be bonded is reduced, thus increasing the solubility of Si in SiO_2. Past studies [153] showed how a given Si saturation in the equilibrium leads directly to a certain solubility. This solubility can be measured experimentally and thus the bond energy E_{NN} can be determined.

For the measuring of solubility of oxygen in Si, pioneering work was done in 1959 by studying absorption bands in the infrared spectra of oxygen in silicon and linking them to the concentration [213]. This technique was widely used to obtain additional results [212], [214]. Later, the more sensitive charged particle activation analysis (CPAA) was used to determine the oxygen concentration in the semiconductor [204], [206], [215]. These results are presented in Table 1 and form the basis for the parameter $E_{\mathrm{NN}}(18)$. Unfortunately, the other side of the phase diagram is hardly investigated and the solubility of Si in SiO_2 is only very vaguely known. A theoretical result with values of $c_0 = 1.09 \cdot 10^{22}\ \mathrm{cm}^{-3}$ and $E = 0.36\ \mathrm{eV}$ was found in the literature and a quantitative statement that the solubility in SiO_2 [216], [217] is "extremely low". However, this data is not sufficient and the parameter of $E_{\mathrm{NN}}(0)$ is treated as unknown for the present work. Therefore its influence must be examined in every relevant case.

The Bond Energy $E_{\mathrm{NN}}(18)$ Gauged by Literature Data

With the same bonding energies for Si in SiO_2 and O in Si, the solubility in the framework of the KMC Model can be described by [153]

$$c_{\infty} = 4.02\ {a_{\mathrm{lat}}}^{-3}\ \exp\left\{-\frac{5.99\ E_{\mathrm{NN}}}{\mathrm{k_B}T}\right\} \tag{57}$$

with the method described in [153] using the experimental values it is possible to determine the E_{NN} for equation (46). The solubility from the experiment is given by

$$c_{\mathrm{exp}}^{\mathrm{Si}} = c_{\infty}^{0}\exp\left\{-\frac{E_{\mathrm{S}}^{\mathrm{Si}}}{\mathrm{k_B}T}\right\} \tag{58}$$

with c_{∞}^{0} and E_{S} as the solubility parameters. To determine the parameter for $E_{\mathrm{NN}}(18)$, Equations (58) and (57) must now be compared. This results in the following relationship

$$E_{\mathrm{NN}}(18) = \frac{1}{6}\left(\mathrm{k_B}T\ \ln\left(\frac{4}{c_{\infty}^{0}\ {a_{\mathrm{lat}}}^{3}}\right) + E_{\mathrm{S}}^{\mathrm{Si}}\right). \tag{59}$$

The literature data found for the solubility of oxygen in silicon are listed in Table 3 and shown in Figure 4-10 a) as a curve over the inverse temperature. The dashed black line shows the fitting curve to all experimental data for the temperature range between 800°C and 1400^C. This was done analogously to the determination of the diffusion coefficients in Chapter 4.2.2. The values obtained are $c_{\infty}^{0} = 2.4 \cdot 10^{22}\ \mathrm{cm}^{-3}$ and $E_{\mathrm{S}} = 1.35\ \mathrm{eV}$. Inserting the fitted data in eq (59) gives the bond energy for *z*=18

$$E_{\mathrm{NN}}(18) = \frac{1}{6}\left(\mathrm{k_B}T\ \ln\left(\frac{4}{2.4 \cdot 10^{22}\ (0.4338 \cdot 10^{-7})^{3}}\right) + 1.34\ \mathrm{eV}\right) \tag{60}$$

≈0.24 eV.

For the solubility of Si in SiO_2, the bond energy $E_{\mathrm{NN}}(0)$ remains unknown and is varied as shown in Figure 4-10 b). The investigated value is much higher than $E_{\mathrm{NN}}(18)$, equal and much lower. For other compositions (*z*=1,…,17) the bond energy is interpolated as described in Chapter 4.1.3.

Table 3: Solubility data from literature for O in Si. The number in the last column indicates the lines in Figure 4-10 a).

$c_{\infty}^{0}[\mathrm{cm}^{-3}]$	$E_S[\mathrm{eV}]$	Ref.	T [°C]	Comment	No. in Figure 4-10 a)
9.3x10^21	1.2	[206]	1000-1375	Charged particle analysis (CPA)	1
4.81015	0.18	[218]	800-1000		2
9E22	1.52	[219]	850-1400	CPA+SIMS	3
$2.6*10^{22}$	1.4	[212]	650-1050		4
2.458D+21	1.07	[204]	1000-1280	Nuclear reaction method	5
0.013* 10^23	0.95	[213]	1000-1400		6
1.6* 10^23	1.65	[214]	600-1350	Infra-red measurements	7
2.40340D+22	1.3488		1000-1200	Fit	Broken black line

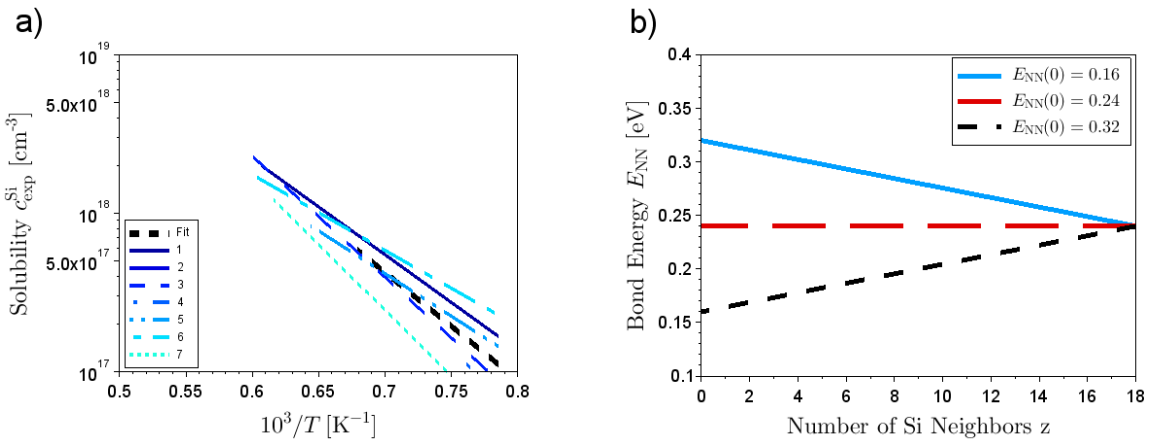

Figure 4-10: Solubiliy of the system Si and SiO_2 with the least squares optimized average (black broken line). The numbers in the legend indicate the entries of Table 3.

The literature data on solubility is given by the fitted function (dotted black line in Figure 4-10 a)) and the theoretical data on solubility by Equation (57) with the $E_{\mathrm{NN}}(z)$ determined in Equation (60). Furthermore, the solubility can also be simulated with the data obtained for $E_{\mathrm{NN}}(z)$. Figure 4-11 shows the simulation of the solubility as a graphical representation (a) and all three values as a function of the inverse temperature (b). The calculations were started with a SiO_2 volume of 27nm x 27nm x 27nm, limited by interfaces to pure Si. The Si excess in equilibrium in the simulation corresponds to the values determined from Equation (57) and the literature data (fitted curve in Figure 4-10 a)).

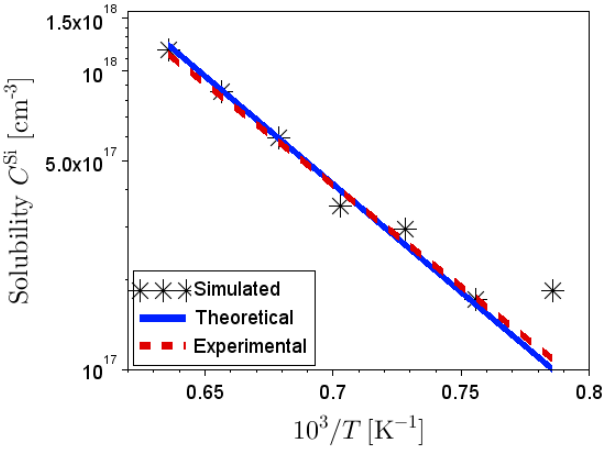

Figure 4-11: Results for the solubility of O in Si. The stars show the KMC calculation, the blue line shows Equation (57) with the value for $E_{\mathrm{NN}}(z)$ from Equation (60) (0.24 eV) and the red line shows Equation (58) with the averaged values from the literature in Table 3. The volume of the simulation cell had the size of 27nm x 27nm x 27nm and was started with the expected equilibrium concentration observed up to 1,000,000,000 MCS without significant change.

In summary, this chapter linked the bond energy E_{NN} of Equation (46) with the solubility and obtained comprehensive data of literature (table 3) to parametrize the bond energies of the KMC model. Unfortunately, there are no data found in literature for the solubility of Si in SiO_2 and needed to be varied as shown in figure 4-10 b). This leads to the following conclusions

- The solubility can be simulated accurately by the proposed model in Chapter 4.1
- The asymmetric diffusion does not influence the reproduction of experimental results for solubility as shown in Figure 4-11.

- The bond energy $E_{\mathrm{NN}}(z=0)$ of Si in SiO_2 remains an unknown parameter and needs to be examined in the crucial cases.

4.3 Simulating Phase Separation of SiO_x by KMC

In order to control the geometric variations with the necessary attention to detail, the individual processes must also be understood with the same attention to detail. Chapter 6 shows how the self-organization of the individual NC in the nanopillar depends on temperature, supersaturation and diameter. All processes that influence the reaction pathway are also dependent on these variables. In order to interpret the different behaviour of the reaction pathway, it is therefore necessary to understand the influence of each individual process, e.g. nucleation, spinodal decomposition, Ostwald Ripening, etc. Each of these must be examined in isolation for its dependence on temperature and supersaturation. These dependencies will then continue on the reaction pathway of the nanopillar. For this purpose, the phase diagram will be used as a basis and phase separation and reaction pathway for the different combinations of temperature and supersaturation will be investigated.

Phase Diagram

Each physical alloy can be present in different phases depending on the thermodynamic conditions of the system such as pressure, concentration, magnetization or temperature. The present system is treated as a binary mixture that neglects pressure, so the interesting phase diagram is the so-called isobaric phase diagram. This shows the local phases of the alloy over temperature and composition. For further information, the literature of [220], [221] is recommended.

The self-organizing process is initiated by phase separation, so that phase separation is the first step of the reaction pathway. The phase diagram for a binary alloy is shown in Figure 4-12. At a sufficiently high temperature, there is only one stable phase, regardless of the concentration (point "0"). This is either a homogeneous mixture or vapour where the system is fully miscible and no stable phase separation occurs. The coexistence curve defines the so-called *miscibility gap*. In the area below this curve, the system is no longer miscible and phases of the pure components are energetically more favorable. According to the mean field theories [220] the miscibility gap can be divided into 2 regions: the metastable and the unstable region. The main difference is the separation mechanism. In the metastable region the phases are separated by nucleation and in the unstable region by spinodal decomposition. For KMC models of Si-SiO_2 with the same diffusion coefficient, the coexistence curve has already been successfully determined for scaled parameters [91].

For the present work, however, it is necessary to investigate the influence of the difference in the diffusion and solubility of the system. The difference in solubility should strongly influence the phase diagram and is investigated in Chapter 4.3.1. Here the influence of the unknown bond energy $E_{\mathrm{NN}}(0)$ (see Chapter 4.2.3) will be very relevant. The results will then be the basis for the following chapters, which examine phase separation and reaction pathway as a function of location in the phase diagram.

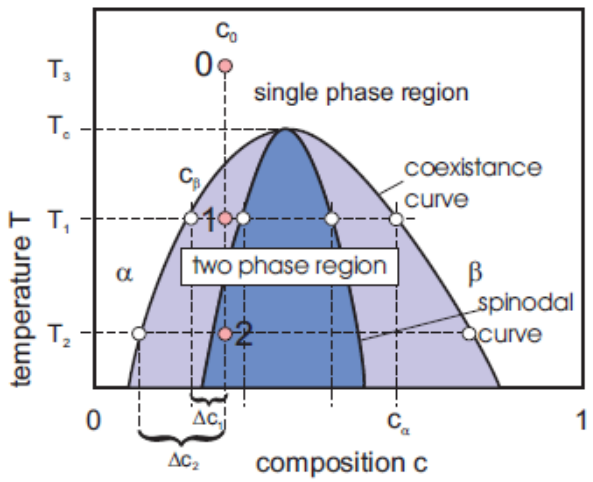

Figure 4-12: Schematically shown a phase diagram of a immiscible binary alloy with c as the concentration. Taken from ref. [85].

Nucleation and Growth

The first step in the growth of NCs takes place at the atomic level. This point in time determines in a decisive way the development of the later reaction pathway. For low supersaturations (metastable range in the phase diagram, Figure 4-12), the phases are predominantly separated by nucleation. In the case of the Si/SiO_2 system, the nucleation and growth of an NC takes place differently depending on the initial configuration and boundary conditions, e.g. the time for the formation and growth of a Si-NC is much longer than for a SiO_2-NC. The position of a nucleated NC as well as the moment of nucleation is random and passes this randomness on to the reaction pathway, which makes its control considerably more difficult. However, this process is strongly dependent on the position in the phase diagram. Temperature and supersaturation have a significant influence on the radius and time of nucleation. Very detailed descriptions can be achieved by molecular dynamics. However, the low time scales and small dimensions of the MD models make it impossible to treat the growth of NC [222], [223]. The KMC model from Chapter 4.1 simulates nucleation internally and results are discussed in Chapter 4.3.2. Simulations of the sequential growth of the NCs are then shown in Chapter 4.3.3.

Ostwald Ripening and Size Distributions

The mutual screening of NCs (see Chapter 2.4.3) and the competition for excess atoms for growth are important processes that will also exert their influence on the reaction pathway of the nanopillar (see Chapter 6). Chapter 2.4.3 has already shown how this is described as Ostwald ripening and how it is a decisive factor for self-organization. Once NCs form, they must share the same environment and compete to grow for the available supersaturation. This complex system of multiple interactions between NCs has been extensively studied over the last century. A successful theoretical derivation of the radii of this ensemble of NCs was performed by Lifshitz [94] and is now called *LSW theory* with the *LSW distribution* of NCs sizes. The decisive assumption was a negligible volume fraction of the minority phase. The interaction between the NCs is only via an average monomer concentration, which is determined by the collective. Direct diffusion interactions between NCs are completely neglected. Unfortunately, this result is not experimentally observed and more realistic modifications for non-zero solubility and non-ideal solutions were made by [224], [225]. Several researchers have

made a lot of effort to extend this theory to more realistic circumstances, especially at higher volume fractions [226]–[229]. However, the exact dependence on the volume fraction is still unclear [230], [231]. Mean field approaches have successfully solved the Ostwald Ripening effect by assuming NC as point sources with a strength corresponding to the radius of NC [92], [154]. In addition to the LSW distribution, there were also approaches to investigate the Ostwald Ripening of inhomogeneously distributed configurations [99], [232]. It was possible to describe the self-organisation of NCs in bands by Ostwald Ripening and to show that spatial self-organisation is an inherent property of the inhomogeneous characteristics of NCs [98]. These approaches are mostly developed for demanding cases.

However, all of the above approaches are based on the LSW distribution, which exists for two unreachable ideal cases. If the reactions at the interface are much faster than the diffusion, the growth of an NC depends only on how fast the supply of further monomers is. This growth is then referred to as diffusion-controlled. The opposite is called reaction-controlled. These two cases were described by LSW and two different size distributions were determined, one for each case. For the binary alloy, these were extensively investigated with the KMC method in the past by Strobel [91], [153], [166]. He successfully simulated both limit cases, the reaction-controlled Ripening of Wagner [94] and the diffusion-controlled Ripening of L.S.W. [93]. The present system is a combination of both. Si-NCs tend to diffusion controlled growth and SiO_2-NCs tend to reaction controlled growth. This is investigated in Chapter 4.3.4.

Spinodal Decomposition

The phase separation mechanism of spinodal decomposition occurs when the system starts much deeper inside the miscbibility gap (see Figure 4-12) in the unstable region. This is the case, for example, with mixed Si/SiO_2 interfaces. The area of the interface is converted into a Si excess of about 50% and thus controlled by spinodal decomposition. A system in this region of the phase diagram is no longer metastable. According to spinodal theories [155]–[157], even arbitrarily small fluctuations are sufficient to separate the phases. The reaction pathway is still strongly influenced by the temperature and supersaturation of the mixture. There is no strict limit between nucleation and spinodal decomposition in the phase diagram. The separation mechanism of spinodal decomposition simply increases continuously with supersaturation and replaces the nucleation. In the past, this was already done with the KMC model from Chapter 4.1.1 and showed how sponge-like structures are formed and grown after spinodal decomposition and compared with experiments [162]. However, an exponential rapid growth of small amplitude fluctuations, as predicted by this theory, was not observed in the experiment [161], [233]. In Chapter 4.3.5, the dependence of spinodal decomposition and the further reaction pathway on the initial state in the phase diagram is investigated.

Phase Separation of Mixed Si/SiO_2 Interfaces

The main component of the $Si/SiO_2/Si$ stacked nanopillars and the most important component to simulate is the Si/SiO_2 interface. The mixed Si/SiO_2 interface includes the entire composition range of the phase diagram. All possible processes from nucleation and growth of Si-NCs, through the spinodal decomposition of the interface, to nucleation and growth of SiO_2-NCs take place simultaneously, while they are only a few nanometers apart. After all processes have been

investigated separately (nucleation, Ostwald ripening, spinodal decomposition) in Chapter 4.3.2 to 4.3.5, the annealing of Si/SiO_2 interfaces is investigated in Chapter 4.3.6. In the former NEON project [87]similar systems were experimentally investigated and the successful formation of NC by implantation of Si in SiO_2 was reported. The control of size, positions and number was possible, and annealing and irradiation conditions could be used to control the final system morphology. The KMC model was successfully used to realize this parameter adjustment. Detailed information can be found at [234]–[238]. Experimental studies showed a successful synthesis of Si-NCs layers parallel to a SiO_2/Si interface [237] using cross-sectional electron microscopy (XTEM). TEM images have confirmed the lattice structure of the NCs [238]. This work includes the same model with the extension by parameterization of diffusion and solubility (see Chapter 4.2).

4.3.1 Phase Diagram of SiO_x as Predicted by KMC

The KMC model neglects the pressure and the density is fixed (see Chapter 4.1.1). Thus the state in which the mixture is at the beginning of the annealing step is given by a position in the isobaric phase diagram (see Figure 4-12). This position can have different properties, especially with regard to the separation mechanism. In the metastable region of Figure 4-12 the phases are separated by nucleation while in the unstable region spinodal decomposition takes place. Furthermore, there is no fixed boundary between unstable and metastable region. The boundary between the metastable region and the unstable region has a continuous transition and is very difficult to determine. In order to control the reaction pathway, the influence of the position in the phase diagram needs to be understood. However, the coexistence curve (see Figure 4-12) is defined by a first-order phase transition. This can be determined using simulations. The average number of free bonds per lattice site of a given configuration is

$$N_{\mathrm{Si}} = \frac{N_{\mathrm{AB}}}{N_{\mathrm{A}}} \tag{61}$$

with N_{AB} as the total number of free bonds between Si and SiO_2 sites and N_{A} as total number of Si atoms in the system. For a given temperature T, a KMC simulation was performed with a homogeneous distribution as starting configuration. The size of the simulation cell was $(25\mathrm{nm})^3$ and the results were averaged over 10 different calculations. The simulation was performed until N_{Si} did not change anymore (equilibrium). This value was taken as $N_{\mathrm{Si}}(T, c)$ for the used temperature T and the used Si excess for the start configuration.

Figure 4-13 a) shows $N_{\mathrm{Si}}(T, c)$ over the temperature for different Si excess as start configuration. At high temperatures above 7000K, the system is always in a single-phase state and fully miscible. Small nuclei form randomly, but do not reach a stable size and dissolve. A decreasing temperature leads to statistically more nuclei (although not stable), which continuously decrease the free energy. With a Si excess of 50%, the system reaches supersaturation for the first time by reducing the temperature to 6.000K. The first stable domains are formed, which abruptly and permanently reduce the number of free bonds N_{AB}. This is the typical behavior of a first-order phase transition and defines the coexistence curve of the phase diagram. Further temperature decay leads to a stronger separation of both phases and the number of free bonds decreases continuously with further annealing. Figure

4-13 a) was performed with $E_{\mathrm{NN}}(0) = 0.24$ eV and b) shows the extracted coexistence curve for a variation of $E_{\mathrm{NN}}(0)$ from 0.08 to 0.4 eV. Values outside this range are unlikely.

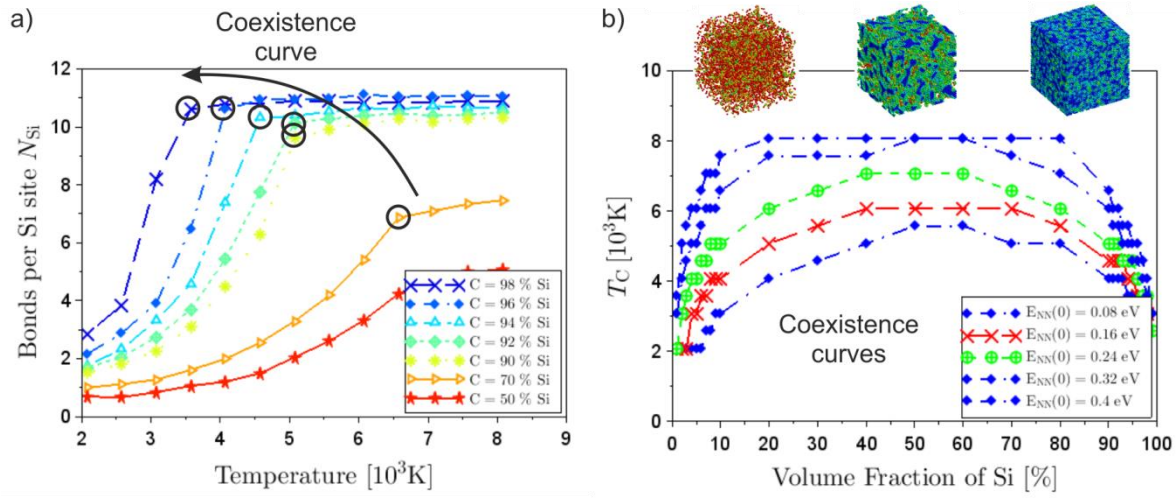

Figure 4-13: Determination of the phase diagram for the Si- SiO_2 system by KMC calculations. In a) the average number of Si neighbors (Equation (61)) for different Si excess over temperature is shown. The black rings show the point at which a first order phase transition occurs, which determines the coexistence curve. In b) this is shown for different values of $E_{\mathrm{NN}}(0)$. The calculations were performed in a volume box of the size $(25\mathrm{nm})^3$ until the system reached its equilibrium state.

In summary, this chapter has determined the phase diagram of the Si-SiO_2 system using the model from Chapter 4.1 and is shown in Figure 4-13. In case of $E_{\mathrm{NN}}(0)$= $E_{\mathrm{NN}}(18)$ the mixture is completely miscible over a temperature of 7000K. The variation of $E_{\mathrm{NN}}(0)$ changes this temperature from 6000K to 8000K for values from 0.08 eV to 0.4 eV. The solidus of Si remains similar in the phase diagram for different values of $E_{\mathrm{NN}}(0)$. However, the solidus of SiO_2 is very different. The results lead to the following conclusions

- $E_{\mathrm{NN}}(0)$ has a strong influence on the phase diagram as shown in Figure 4-13. Any process that depends on the phase diagram is generally also dependent on $E_{\mathrm{NN}}(0)$.
- Molecular dynamic calculations resulted in a temperature of approx. 6100K for a volume fraction of 70% [239]. This would correspond to a value of 0.16 eV for $E_{\mathrm{NN}}(0)$.
- With a symmetric solubility $E_{\mathrm{NN}}(0) = E_{\mathrm{NN}}(18)$), the phase diagram appears also symmetric, which proves that asymmetric diffusion of Equation (43) and (44) has no influence on the phase diagram. It only affects the time scale (see Equation (52)).
- The number of bonds per Si site in Figure 4-13 a) shows a first order transition which defines the coexistence curve. However, the estimated spinodal curve in Figure 4-12 does not show any influence.

4.3.2 Controlling the Nucleation of NCs

The nucleation and growth of an NC depends on how strongly the atoms are connected and how fast the supply of additional monomers takes place. Chapter 4.2.2 showed the big difference between

diffusion in Si and SiO_2. In particular, the growth of an NC can be controlled by diffusion or reaction and is therefore strongly influenced by the diffusion rate of the monomers.

When annealing a Si/SiO_2 interface, Si-NCs appear on the side of SiO_2 and vice versa. The difference in the speed of diffusion is also reflected in the speed of the reaction pathway on both sides. This can not only lead to different time scales, but also to different ways in which the reaction pathway of the NCs appears.

The classical nucleation theory [240]–[242] describes phase separation as a random occurrence of spherical domains of the minority component. This theory provides a prediction for the size of the newly formed nucleus and a probability for this event. The growth process then begins at these locations and makes use of the surrounded supersaturation. Although the randomness here is very high, there are differences for the individual regions in the phase diagram of Figure 4-13. In this chapter, the nucleation and growth of Si and SiO_2-NC will be investigated regarding different temperatures and supersaturations.

Nucleation in a Supersaturated Solution

For a temperature above the coexistence curve, nanoparticles form and evaporate randomly – but no stable domains can be observed. Entropy dominates the system and all separating tendencies are overruled by temperature fluctuations. The requirement for nucleation is supersaturation. To make supersaturation it is necessary to cool down the system until the (c, T) state crosses the coexistence curve. Once supersaturation is reached, a separated domain of the minority component is energetically more favorable and nuclei appear. For the homogeneous nucleation two types of energy changes must be considered, the volumetric energy and the surface energy. The volumetric Gibbs energy released by the transformation from liquid to solid is given by

$$\Delta G_{\mathrm{vol}} = -\frac{4}{3}\pi r^3 P_{\mathrm{R}} \tag{62}$$

with r as particle radius and P_{R} as hydrostatic pressure. This energy makes a negative contribution to the total free energy and promotes the formation of a separated phase. The second contribution is the surface free energy required to create a new interface around the separated domain and is given by

$$\Delta G_{\mathrm{inter}} = 4\pi r^2 \gamma_{\mathrm{R}} \tag{63}$$

with γ_{R} as the interface tension. This energy makes a positive contribution to the free energy and must be compensated by ΔG_{vol} to realize the formation of a separated phase. For a stable NC to nucleate, the sum of Equations (62) and (63) gives the free Gibbs energy

$$\Delta G_{\mathrm{R}} = 4\pi r^2 \gamma_{\mathrm{R}} - \frac{4}{3}\pi r^3 P_{\mathrm{R}} \tag{64}$$

and must be negative. This equation gives the energy required to form a spherical particle of radius r [236]. If such a particle is created by thermal fluctuations, it will develop in such a way that the free energy decreases. Figure 4-14 schematically shows the interfacial and volume energy over the radius and the sum of both. With small radii, the interfacial energy dominates and the free energy will only

be reduced if the particle decreases again. With larger radii, the volume energy dominates and the free energy will only be reduced if the particle continues to grow. The highest value for DG results at the critical radius, which is given by

$$r_{\mathrm{crit}} = \frac{3\gamma_{\mathrm{R}}}{P_{\mathrm{R}}}. \tag{65}$$

In order for an NC to form and grow, a certain energy barrier $\Delta G_{\mathrm{R}}(r_{\mathrm{crit}})$ must be overcome by reaching this critical radius.

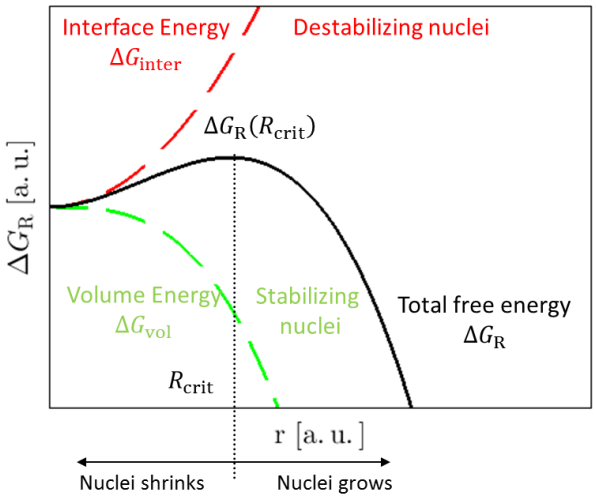

Figure 4-14: The free energy of a spherical NC over the radius. This consists of the sum of the surface energy (red line) and volume energy (green line).

The energy barrier $\Delta G_{\mathrm{R}}(r_{\mathrm{crit}})$ and the critical radius determines when and where nucleation takes place and which radius the new NC will have. This depends on the hydrostatic pressure and the interfacial energy, which in turn depend on temperature and supersaturation. In order to influence the reaction pathway via nucleation, a different point in the phase diagram can be aimed at. In order to benefit from this, the behaviour of ΔG_{R} and r_{crit} must first be investigated in different points of the phase diagram. To obtain the temperature dependence, it is possible to use the Gibbs-Thomson equation, which gives the critical radius according to classical nucleation theory by [243], [244]

$$r_{\mathrm{crit}}^{\mathrm{classical}} = \frac{2\gamma_{\mathrm{R}} T_{\mathrm{coex}}}{\rho_0 L (T_{\mathrm{coex}} - T)} \tag{66}$$

with T_{coex} as the temperature of the coexistence curve for the given composition, ρ_0 as density and L as "heat of fusion". The heat of fusion is the necessary energy to separate a given NC by thermal energy. It also corresponds to the energy taken from the free energy when the NC is rebuilt. After cooling down from an area in the phase diagram above the coexistence curve, the critical radius is initially quite large and decreases rapidly. This gives the temperature dependence of the critical radius for a given supersaturation. Next, the dependency on supersaturation for a given temperature must be clarified. Starting with a homogeneously distributed Si excess at a low temperature without supersaturating the SiO_2, in the phase diagram this would be a position to the left of the miscibility gap. The solution is in the single phase and no NC can form. Artificial freezing of the system and the

addition of more and more Si excess atoms then corresponds to an increase in pressure. This approach offers the thermodynamic option to express the ΔG_{vol} according to [245]

$$\Delta G_{\mathrm{vol}} = \mathrm{R}T\ln\left(\frac{p_1}{p_0}\right) \tag{67}$$

with p_0 as saturation pressure, p_1 as the supersaturated pressue and R as gas constant. This can also be expressed as the supersaturation ratio

$$\Delta_S = \frac{p_1}{p_0}. \tag{68}$$

Thus, the critical radius is given by

$$r_{\mathrm{crit}}^{\mathrm{classical}} = \frac{2\gamma_{\mathrm{R}}}{\rho_0 \mathrm{R}T\ln(\Delta_S)}. \tag{69}$$

This means that the greater the supersaturation in the initial configuration, the smaller the critical radius. With Equations (64) and (66) the activation energy for the nucleation process results as isobaric approximation depending on the temperature in

$$\Delta G_{\mathrm{crit}}^{\mathrm{classical}} = \frac{16\pi\gamma_R^3 T_{\mathrm{coex}}^3}{3\rho_0^2 L^2 (T_{\mathrm{coex}} - T)^2} \tag{70}$$

and in the case of an isothermal approximation, the dependence on supersaturation results in

$$\Delta G_{\mathrm{crit}}^{\mathrm{classical}} = \frac{16\pi\gamma_R^3}{3\left(\rho_0 \mathrm{R}T\ln(\Delta_S)\right)^2}. \tag{71}$$

In summary, this chapter examines the dependence of nucleation for different points in the phase diagram (see Figure 4-12). Nucleation is defined by the critical radius r_{crit} and the nucleation energy barrier ΔG_{R}. The radius as well as the energy barrier ΔG_{R} decreases with decreasing temperature and increasing supersaturation. This leads to the following conclusions

- Nucleation is a decisive tool for controlling the reaction pathway of the system. For the nanopillar or the Si/SiO_2 interface, the temperature can be used to determine the minimum size of the nucleated NCs. The use of a high temperature prevents the system from forming small NCs and only large ones can appear.
- The nucleation barrier indicates the probability of nucleus formation. If ΔG_{R} is too small, too many NCs appear and no single NC can form in the nanopillar. If ΔG_{R} is too high, the SiO_x only reconstructs back to a layered nanopillar without NCs.

4.3.3 Growing of Si and SiO_2-NCs in Supersaturated Solution

As shown above, nucleation is strongly dependent on the position of the system in the phase diagram (see Figure 4-12). After nucleation, the surrounding monomers are absorbed on the surface of the new NC. While the absorption outweighs the adsorption, the NC grows and reduces the supersaturation in its surrounding. However, this supersaturation also decreases with increasing

temperature and must re-diffuse after absorption. This happens with different speeds for Si-NC and SiO_2-NC (see Chapter 4.2.2). Therefore, the temperature dependence of the NC growth and the differences between Si-NC and SiO_2 must be investigated.

The growth consists of 2 mechanisms [246]:

- The monomers diffuse to the interface of the NC. If this happens much faster than the absorption by the NC, the supersaturation can be assumed to be constant and the growth is only limited by the absorption. In this case one speaks of "reaction controlled" growth. This is the case with SiO_2-NC because the diffusion of oxygen in Si is incredibly high (see Table 2).
- The monomers react at the interface. If the absorption by the surface happens much faster than the diffusion, the limiting factor for the growth is the missing monomer supply. In this case the growth is called "diffusion controlled". This is the case with Si-NC, since the diffusion of Si in SiO_2 is very low (see table 1).

According to the Gibbs-Thomson equation, the equilibrium concentration at the curved interface depends on the size of the NC [247]. This also affects the surrounding supersaturation. In the case of diffusion-controlled growth, the Gibbs-Thomson relationship [248] gives the concentration over the radius r

$$c^{\mathrm{GT}}(r) = c_{\infty} \exp\left\{\frac{R_{\mathrm{cap}}}{r}\right\} \tag{72}$$

with the capillarity length R_{cap} and c_{∞} as the equilibrium concentration at a flat interface (the solidus of the phase diagram in Figure 4-13). This is a good approximation for highly diluted systems and gives information about the supersaturation on the surface of the NC. This supersaturation decreases with the size of the NC $\sim \exp\left\{\frac{1}{r}\right\}$ and the temperature dependence can be derived by c_{∞} from the phase diagram (see Figure 4-12). Strobel [91] showed that the KMC accurately reproduces this relationship. Figure 4-15 shows what can be expected for the Si excess profile around a single NC according to Equation (72). If the Si excess is higher than the Si excess at the NC surface (a), the Si excess gradient leads to a flow from Si excess to NC according to the Ficks diffusion equation. This can be achieved by reducing supersaturation c_{∞}, by lowering the temperature (see phase diagram Figure 4-12) or by increasing the radius (see Equation (72)). If c_{b} is kept constant, the NC continues to grow. If c_{b} is below c^{GT}, the gradient changes in the opposite direction and the Si excess flows away from the NC. This causes the NC to act as a source of monomers and dissolve. It can be achieved by either increasing c_{b} (temperature increase according to Figure 4-15) or decreasing the NC size (according to Equation (72)).

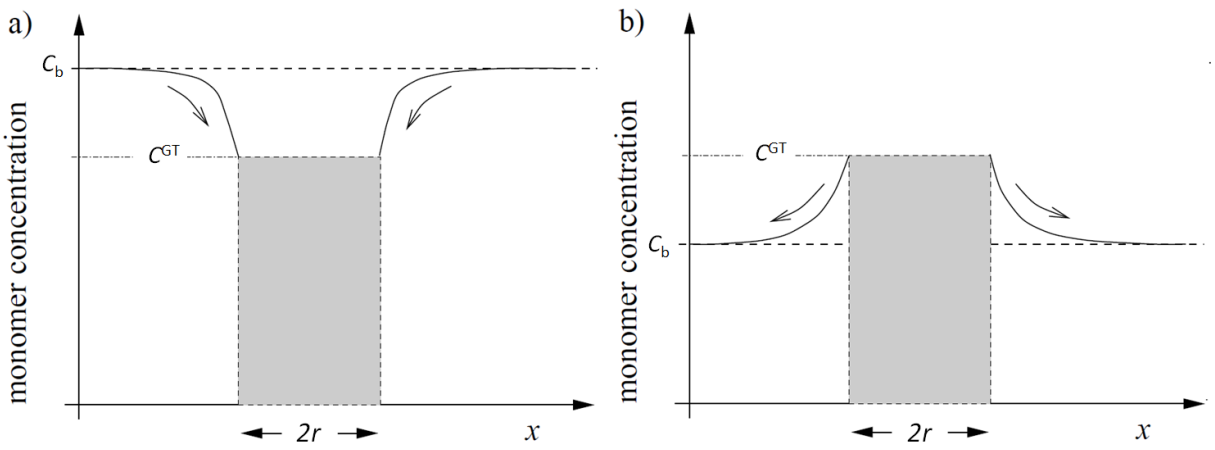

Figure 4-15: The Si excess around an NC (grey area), schematically shown. In a) one sees the case of a supersaturated environment and in b) an unsaturated environment. The Si excess of the environment is cb and the Si excess at the surface is cGT according to Equation (72). The arrows indicate the flow of the monomers according to the Ficks diffusion equation. Taken from ref. [91].

However, the ideal case according to Figure 4-15 is neither expected for Si-NC nor for SiO_2-NC. Since the physics are very different (diffusion/reaction control, see Chapter 4.3.3), the influence of the NCs on their surrounding supersaturation looks very different. Figure 4-16 shows an NC embedded in a small calculation box with a size of 27nm and a fixed surrounding concentration of 0.012% at a distance of 13nm. The results show the temperature dependence of the processes around the NC. The calculation was started with an NC with a radius of 1.25 nm for cases where the Si excess results in supersaturation and with an NC of 1.75 nm if it does not result in supersaturation. In the first case it leads to growth and in the second to evaporation. At a time with a radius of 1.5 nm, the calculation was stopped and the Si excess averaged over the radial distance. In a) the Si excess can be seen and in b) the excess of SiO_2 sites (1-*c*). The profile clearly shows the difference between diffusion controlled growth (a) and reaction controlled growth (b). In the case of Si-NC, monomers are immediately absorbed by the surface, denuding this region. To grow further, it needs some time until the next monomers diffuse to the surface. Thus, the growth rate is mainly determined by the diffusion constant. The profile is also strongly influenced by the temperature, as at higher temperatures the adsorption exceeds the absorption and immediately increases the concentration in the surface area. But in this case the slow diffusion limits the escape of the unbound monomers and the Si excess at the surface increases rapidly. The reverse case can be seen with a SiO_2-NC in Si, as shown in Figure 4-17 b). The diffusion is fast and ensures an almost constant supply of monomers over the entire volume outside the NCs. Only the difference between absorption and adsorption determines the growth rate. In comparison to Figure 4-16 a), the Si-NC corresponds very well to the predictions by Equation (72). A SiO_2-NC however, hardly influences the surrounding Si excess, which remains almost the same over time. Only the reaction on the surface determines the growth.

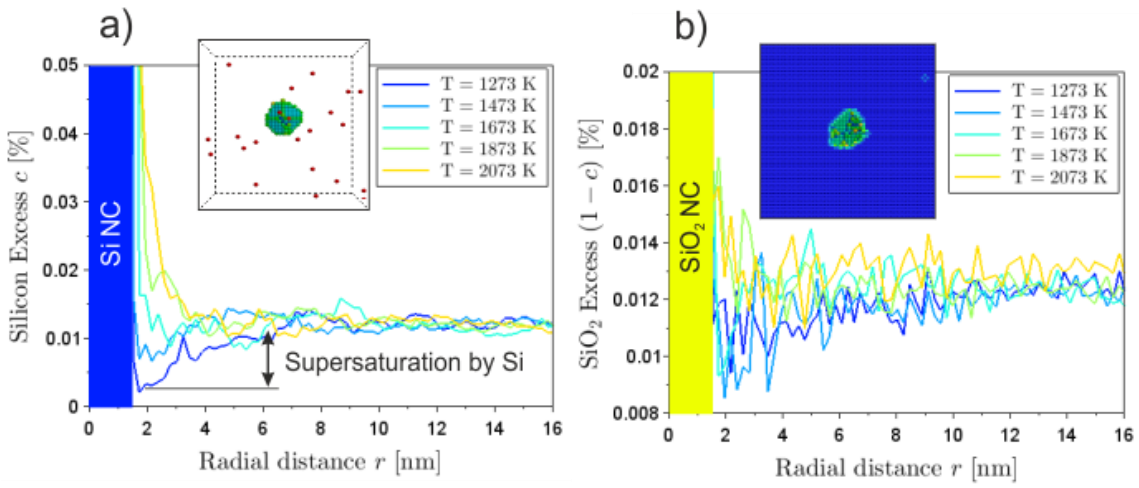

Figure 4-16: The radial Si excess profile around a Si-NC (a) and SiO_2-NC (b) with a radius of 1.5nm for different temperatures. An NC was embedded in a simulation cell and the outer Si excess at a radial distance of 13 nm was kept constant at 0.012%. The NC had started with a radius of 1.25nm and 1.75nm in case of growth or evaporation, respectively. The calculation was stopped when the radius was 1.5nm and the Si excess was radially averaged.

The influence of the NC on the surrounding supersaturation also depends on its size (see Equation (72)). Figure 4-17 a) shows the Si excess profile for NCs of different sizes, determined in the same way as Figure 4-16. Larger NCs show a lower Si excess on the surface, which is also expected by Equation (72). However, the diffusion controlled manner remains the same. Figure 4-17 b) shows the calculation for SiO_2-NC in silicon, which again shows a very reaction-controlled way, especially for small sizes. With larger NC, the curvature of the surface decreases and leads to a lower c^{GT} according to Equation (72). This results in a stronger absorption of monomers by the NC and to a slight increase in the diffusion control of the process. It shows how strongly the absorption of larger NC differs from that of smaller NC, especially SiO_2-NC.

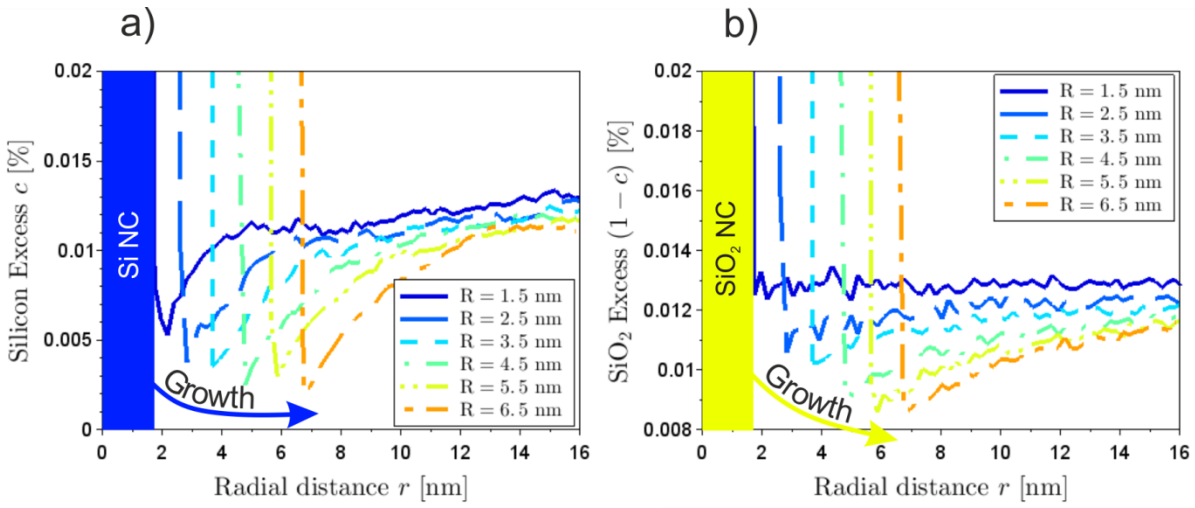

Figure 4-17: The radial Si excess profile around one Si-NC (a) and SiO_2-NC (b) for different sizes. An NC was embedded in a simulation cell and the outer Si excess at a radial distance of 26 nm was kept constant at 0.012%. The NC had started with a radius smaller by 0.25 and the calculation was stopped when the radius reached the entered size. The Si excess was then averaged radially. The temperature was 1373K.

In summary, this chapter examines the influence of a NC on the surrounding Si excess in Figure 4-16. Depending on size, temperature and supersaturation, an NC can serve as a sink or source for Si excess (see Figure 4-15). The increase in supersaturation or in NC size will increase the influence as a sink. The decrease in supersaturation or in NC size will increase the influence as a source. Figure 4-17 showed, that the influence on the environment can be diffusion controlled or reaction controlled. Si-NC influence their environment diffusion controlled and SiO_2-NC reaction controlled. This leads to the following conclusions

- The diffusion controlled influence of the Si-NC shows a fast formation of a denuded zone above the interface in Figure 4-16 and Figure 4-17. This will support the formation of the tunnel gap in the nanopillar.
- The difference between reaction controlled and diffusion controlled will also influence the interaction of the NCs with each other. The Ostwald Ripening of an ensemble of NCs is expected differently for Si-NC and SiO_2-NC. This is examined in detail in Chapter 4.3.4.
- Figure 4-16 shows that Si-NCs with a diameter of approx. 2nm are no longer stable at a temperature above 1600K and evaporate. This will be interesting for the temperature study of the nanopillar in Chapter 6.
- Figure 4-16 and Figure 4-17 show that SiO_2-NCs do not denude their environment very quickly. The probability for a denuded zone at the Si/SiO_2 interface to the SiO_2-NC is therefore low.

4.3.4 Oswald Ripening of Si and SiO_2-NCs

The annealing of the mixed interfaces might lead to the formation of NC at distances of less than 10 nm. The different nature of Si-NC and SiO_2-NC to influence their environment will also affect the interaction among each other (see Chapter 2.4.3).

The development of an ensemble of NCs is called Ostwald Ripening and must be studied separately for Si-NC and SiO_2-NC. It is the crucial process of self-organization (see Chapter 2.4), but difficult to describe theoretically. As mentioned before, there are only the limit cases of the purely reaction-controlled and purely diffusion-controlled Ostwald Ripening, which is used for the analysis of the Si-SiO_2 system in this paper. The characteristic feature is the radius distribution $\eta_R(r)$ with $\eta_R(r)\mathrm{d}r$ as the number of NC with the radius $\mathrm{d}r$. To make this function independent of size and time of the system, the distribution can be normalized to the mean radius ($\rho = r/< r >$) and the number of NCs ($\int \eta_R(\rho)\,\mathrm{d}\rho = 1$). The behaviour of an ensemble of Si-NC must be compared with the behaviour of an ensemble of SiO_2-NC. Chapter 4.3 introduced different approaches to derive the size distribution depending on the physical basis of the interaction between the NCs. To determine the size distribution in the case of NCs growing diffusion controlled, I.M. Lifshitz and V.V. Slyozov and C. Wagner have pioneered and derived the LSW distribution [93], [94]

$$\eta_{\mathrm{diff}}(\rho) = \frac{4}{9}\rho^2 \left(\frac{3}{3+\rho}\right)^{\frac{7}{3}} \left(\frac{1.5}{1.5-\rho}\right)^{\frac{11}{3}} \exp\left\{\frac{-\rho}{1.5-\rho}\right\}. \tag{73}$$

This expression is based on the assumption of a highly diluted concentration at which each NC is considered in isolation. This surrounding concentration is an average value generated by all NCs. This

is a time-independent size distribution that can only deviate in the initial stage if the start configuration does not already correspond to the LSW distribution. For long development times, however, Equation (73) will appear as the size distribution of the System [93], [94]. This theory is based on several assumptions:

- The NC of the minority phase is assumed as spherical particle in a majority phase.
- The total mass is conserved
- The continuum description of a discrete number of NC is only valid in case of a sufficiently large system with enough NCs
- No direct interactions between particles are allowed, only grow or shrink depending on the mean field concentration
- The coarsening rate of the nuclei is independent of their environment, which means that it is a mean field approach to the growth rate of the particles.
- The fraction of the dissolved phase in the considered volume is nearly zero.
- The supersaturation around the existing nuclei is nearly zero, which prevents the formation of further nuclei.

However, these assumptions can hardly be realized in experiments. Figure 4-18 shows the LSW distribution faded in over different size distributions and shows a very asymmetrical shape. However, investigations of NC formation in alloys showed a more symmetrical size distribution [249], [250] and a dependence of the time constant on the volume fraction [251]. This theory was the first of its kind and many groups followed [154], [227], [229], [252] with further improvements for cases with limited volume and higher volume fractions. Another important work was done by Wagner [94], who derives a distribution for the reaction-controlled case of Ostwald ripening. This is given by

$$\eta_{\mathrm{react}}(\rho) = \frac{4}{9}\rho\left(\frac{2}{2-\rho}\right)^{5}\exp\left\{\frac{-3\rho}{2-\rho}\right\}. \tag{74}$$

The main difference is that this distribution is somewhat wider and more symmetrical than the distribution for the diffusion-controlled case. Later, a combination of reaction and diffusion control of the Ripening process was also described [253]. The basic KMC model was already used by Strobel [153] to simulate the Ostwald Ripening for fully symmetric systems and showed that it is possible to simulate diffusion- and reaction-controlled growth of NC ensembles.

The key question, however, is how pronounced the difference is in the growth of Si and SiO_2-NCs in terms of diffusion and reaction control. Figure 4-18 shows the simulation of a homogeneously distributed mixture with a minor phase fraction of 2%. The calculation with an O minority is shown in a) to d) and with a Si minority in e) to h). During the heat treatment small NCs appear, continue to grow and compete with the others for the available Si excess. As already shown in Chapter 4.3.3, the larger NCs act as a drain and grow at the expense of the smaller NCs. This is best illustrated by the example of the Si-NC e) to h) shown in Figure 4-18. The diffusion-controlled Ripening shows an incredibly slow process compared to the SiO_2-NC Ripening in silicon. To achieve the same average radius, it is necessary to anneal the Si-NC for 47 hours, while the SiO_2-NCs need only 0.35s. This is due to the difference in diffusion coefficient.

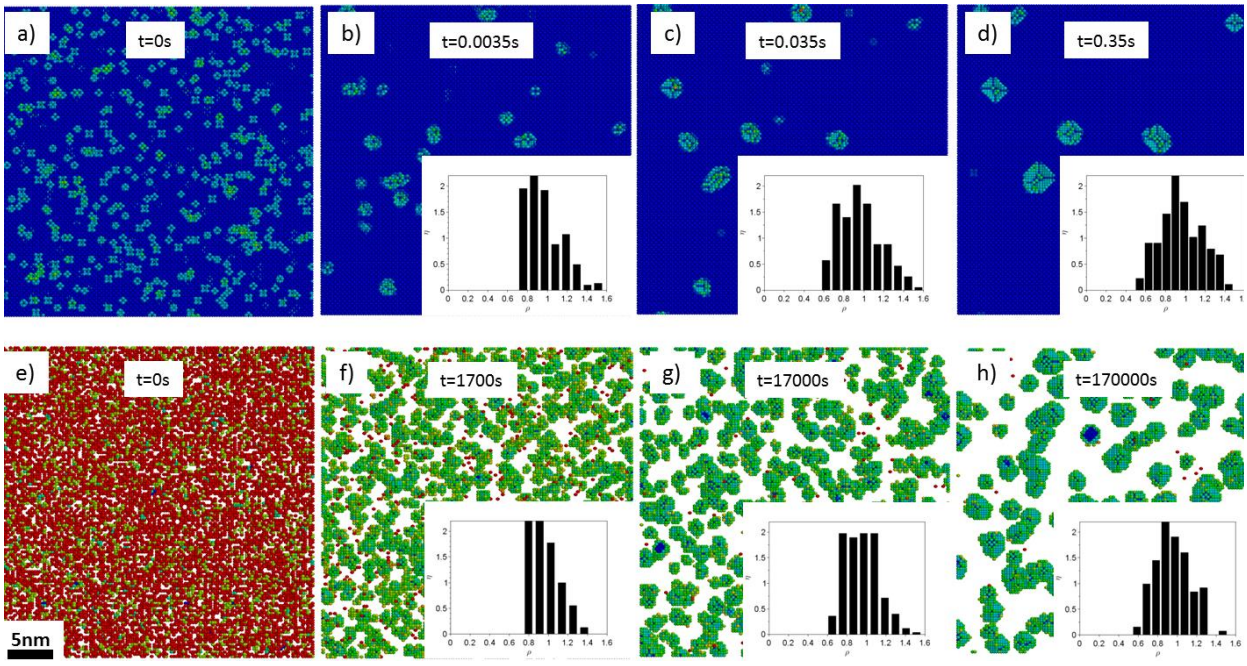

Figure 4-18: Annealing simulation of a homogeneously distributed Si- SiO_2 mixture with a minority phase content of 2%. In a)-d) the reaction pathway is shown in the case of a SiO_2 minority phase and in e)-h) in the case of a Si minority phase. The atoms shown are the sites occupied by Si. The sites occupied by SiO_2 have been made invisible for representation purposes. For the annealing simulation b) to d) and f) to h) the radius distribution is shown embedded. The simulation was performed with a temperature of 1373K in a calculation box of $(27\mathrm{nm})^3$.

Chapter 4.2.3 showed a comprehensive literature search for solubility data and derived the bond energy $E_{\mathrm{NN}}(z=18)$ for Si. Values for SiO_2 were not found and the parameter $E_{\mathrm{NN}}(z=0)$ remained unknown. However, the bond energy is the parameter that defines the attachment and detachment rates at the interfaces and thus the reaction control of the system. In order to identify this influence on Ostwald-Riepening, the calculations shown in Figure 4-19 were performed for different values of $E_{\mathrm{NN}}(z=0)$ and also with much more statistics. The results are averaged over 50 different reaction pathways with the same size of the simulation cell. The varied values for $E_{\mathrm{NN}}(z=0)$ are 0.16 eV, 0.24 eV and 0.32 eV for SiO_2-NCs ((a) to (c)) and Si-NCs ((e) to (f)).

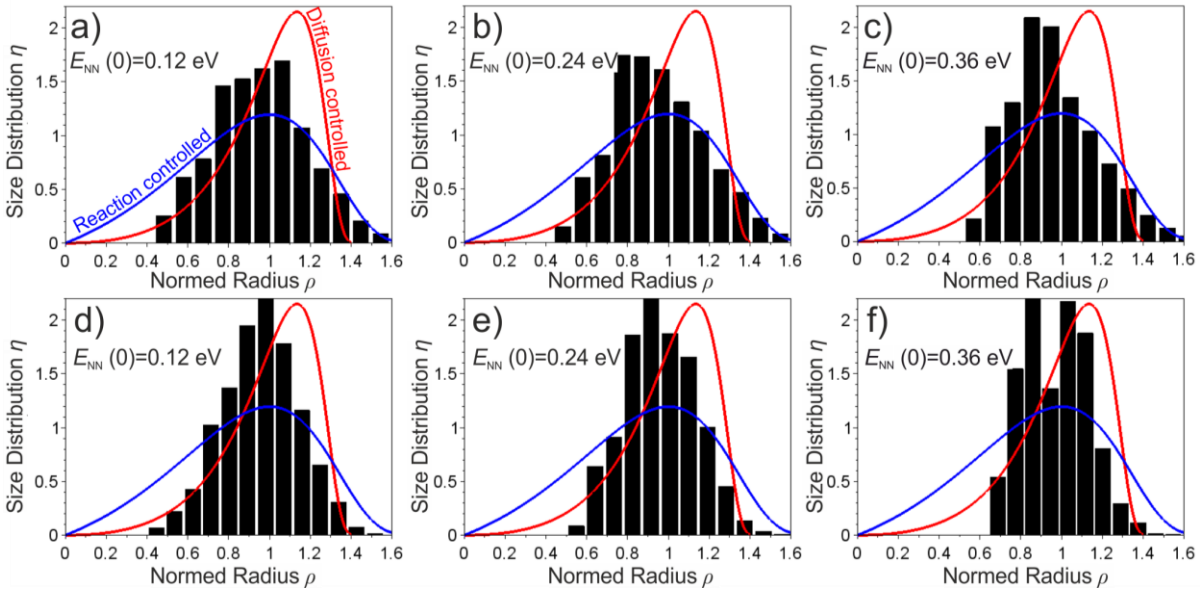

Figure 4-19: Scaled radius size distribution for SiO_2-NC in a)-c) and Si-NC in d)-f). The red and blue lines show the diffusion and reaction controlled LSW distributions according to Equations (73) and (74), respectively. The simulations were made (analogous to Figure Figure 4-18) until an average NC radius of 1.2nm was reached with the indicated values for $E_{\mathrm{NN}}(0)$.

Chapter 4.3.3 showed a strong difference between Si-NCs and SiO_2-NCs in the influence on their environment. In contrast to SiO_2-NCs, Si-NCs showed a very pronounced diffusion control. This can also be observed in the size distribution in Figure 4-19. Although the shape of the distribution in Si-NCs (d-f) is not as asymmetrical as predicted by LSW, it has already been mentioned that this cannot be observed in the experiment either. Since the influence of the reaction in this case is small, the different values for $E_{\mathrm{NN}}(z=0)$ do not change the distribution significantly.

The size distribution of SiO_2-NCs shows a significantly lower, more symmetrical and wider form of distribution than Si-NCs. It corresponds much better to the size distribution according to Equation (74) (blue curve) than to the size distribution according to Equation (73) (red curve). A slight dependence on $E_{\mathrm{NN}}(z=0)$ can be observed here. For high values, the Si excess atoms are coupled more strongly to the surface, which increases the depletion of Si excess above the interface. To compensate this, the supply of further Si excess atoms has to be faster, which leads to a stronger influence of diffusion. Lower values for $E_{\mathrm{NN}}(z=0)$ lead to slower growth, i.e. the concentration around the growing NC can be more easily adjusted by diffusing Si excess atoms.

In summary, this chapter showed the simulation of the Ostwald ripening process by the model presented in Chapter 4.1. The size distributions shown in Figure 4-19 were compared with the theoretical distributions of LSW [93] for diffusion-controlled ripening (Equation (73)) and Wagner [94] for reaction-controlled ripening (Equation (74)). It can be observed in Figure 4-19 how the ripening of Si-NC is diffusion controlled, while the ripening of SiO_2-NC is reaction controlled. Solubility does not seem to have a strong influence. Nevertheless, Figure 4-19 d)-f) shows a tendency towards diffusion-controlled growth for large values of $E_{\mathrm{NN}}(0)$. This leads to the following conclusions

- The Ostwald ripening confirms the results for growth of NCs in Chapter 4.3.3. Si-NC growth is diffusion controlled and SiO_2-NC growth is reaction controlled (see Figure 4-16). As shown in

Chapter 2.4, it was mainly diffusion-controlled models that showed good self-organization, based on the screening of the NCs by the closest neighbors. The diffusion pathway, as shown in Figure 2-6 b), cannot go far if as soon as the Si excess atom touches an interface, it reacts and gets absorbed. At a low reaction rate, however, the probability of a diffusion pathway as shown in a) increases. However, this was the basis for the self-organization of NC layers, as shown in Figure 2-7. Accordingly, self-organized NC layers of SiO_2 are not expected.

- The unknown value for $E_{\mathrm{NN}}(0)$ of Equation (46) does not seem to be a decisive uncertainty for the simulation of the nanopillar. Figure 4-19 a)-c) shows that the size distribution of Si-NC does not change with the value for $E_{\mathrm{NN}}(0)$.

4.3.5 Spinodal Decomposition and the Phase Diagram

The reaction pathway of a system with a high degree of supersaturation behaves completely differently from a system with a low degree of supersaturation like in Figure 4-18. A Si excess profile of a Si/SiO_2 interface shows a continuous curve from 0 to 1 (see Chapter 3.2). This leads to separations during annealing with all possible Si excess values of the phase diagram. Figure 4-20 shows the simulation of a phase separation with a Si excess from 10% to 90%. At 10%, there is hardly any separation during the simulation time, since the processes are strongly restricted by the slow diffusion in the supersaturated SiO_2. This range corresponds to the SiO_2 layer in the Si/SiO_2 system. The increase of the Si excess allows the system to be separated by spinodal decomposition and forms sponge-like structures. This area corresponds to the region around the interface. A further increase of the Si excess to 70% and 90% leads to much faster development and formation of SiO_2 nanoclusters in silicon. This corresponds to the development in supersaturated Si.

Spinodal decomposition, however, takes place between the nucleation and growth processes and has a direct influence on Si-NCs and SiO_2-NCs. But also the supersaturation in the SiO_2 of the nanopillar can quickly reach the area of the phase diagram in Figure 4-13 where separation by spinodal decomposition occurs. In order to understand the reaction pathways of the nanopillar in Chapter 6, it is necessary to understand the temperature and Si excess dependence of the spinodal decomposition mechanism. Spinodal decomposition does not follow the classical theory of nucleation as shown in 4.3.2. The nucleation region in the phase diagram in Figure 4-12 is directly below the coexistence curve and *metastable*. Deeper in the miscibility gap, the mixture is *unstable*. If the free energy of separated phases is lower, the separation takes place, regardless of temperature. The determination of the temperature and Si excess dependency is therefore better suited by investigating the free energy than the analysis by KMC simulation.

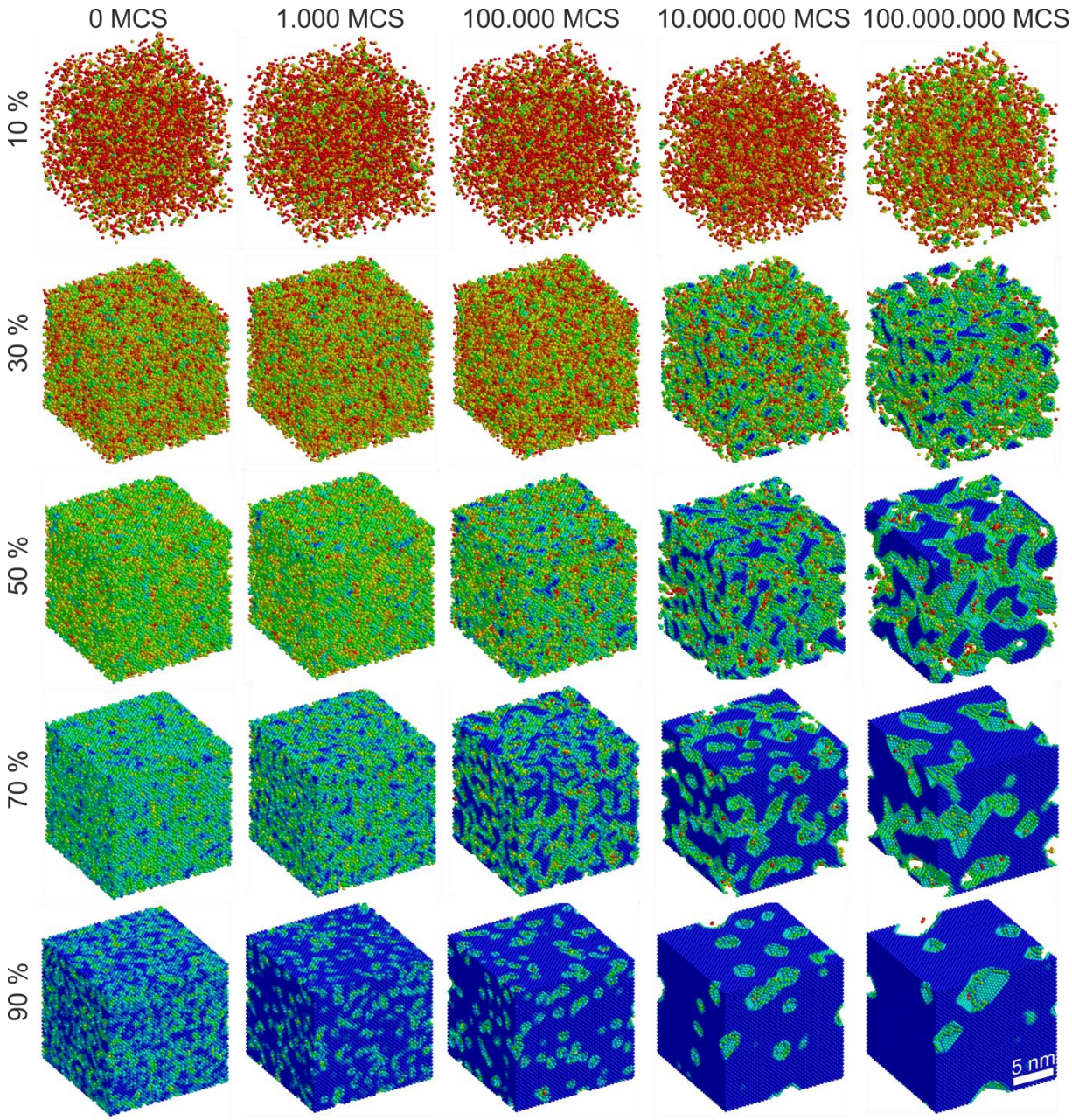

Figure 4-20: Simulation of the phase separation of a homogeneous Si-SiO_2 mixture for different volume fractions of Si and simulation time. The calculation box had the size 27nm^3, the temperature used was 1373K and the atoms shown correspond to the positions occupied by silicon. The bond energy was $E_{\mathrm{NN}}(0)$=0.24eV.

Modeling Spinodal Decomposition by Cahn Hilliard Equation and the Free Energy Potential

On the way into the miscibility gap, the nucleation is continuously replaced by spinodal decomposition. KMC successfully simulates both mechanisms. But in order to study spinodal decomposition in isolation, it is advisable to use Cahn Hilliard's theory [155] for this purpose.

This approach is based on continuous models with partial differential equations. The particle motion in the single stable phase (above the coexistence curve in Figure 4-12) can be described by Fick laws of diffusion (see Chapter 3.2.1)

$$\frac{\partial c}{\partial t}(\vec{r},t) = -\nabla J_{\mathrm{A}} \tag{75}$$

with the position $\vec{r}$, the atomic flux

$$J_{\mathrm{A}} = -D\nabla c \tag{76}$$

and the diffusion coefficient D. This equation does not consider particle interactions. For the high temperatures it is a good approximation, as the thermal energy outweighs any atomic interaction. However, if the system is brought below the coexistence curve by cooling in the phase diagram (see Figure 4-12), interactions become increasingly important and lead to phase separation. To describe this, Cahn and Hilliard [155]–[158] have reformulated the molecular flux by expressing it with the chemical potential

$$J_{\mathrm{A}} = -M\nabla\mu \tag{77}$$

and instead of diffusion, one speaks of mobility M. The chemical potential can be expressed by the variation of the free energy of the system

$$\mu_{\mathrm{F}} = \frac{\delta\mathcal{F}[c]}{\delta c} \tag{78}$$

and results in the so called Cahn Hilliard equation

$$\frac{\partial c}{\partial t}(\vec{r},t) = \nabla\left(M\nabla\left(\frac{\delta\mathcal{F}[c]}{\delta c}\right)\right). \tag{79}$$

The free energy can be expressed by the total free energy functional

$$\mathcal{F}[c] = \int\left(\frac{\varepsilon^2}{2}|\nabla c|^2 + f(c)\right) \tag{80}$$

with ε as a material constant which declares the length of transition regions (see Chapter 5.2.3 for more details) and a double wall potential

$$f(c) = \frac{a}{2}c^2 + \frac{b}{2}c^2 \tag{81}$$

with the 2 free parameters a and b. Figure 4-21 a) shows this function for different values of a and how it is correlated with the phase diagram. The minima of the potential are the stable phases and indicate the coexistence curve. The parameter a is assigned to the temperature. With a<0 the function has 2 minima and with a>0 only a minimum. In the first case, this leads to separation because the free energy at the two minima is lower. For more detailed information about the Cahn Hillard equation [254] is recommended.

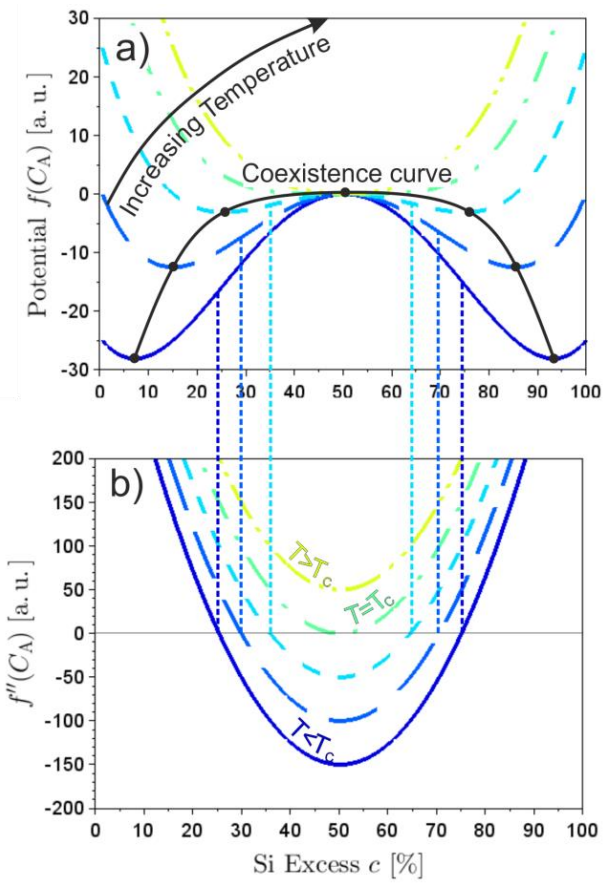

Figure 4-21: Phase diagram, free energy potential in a) and its second deviation in b). The free energy potential f was plotted for different temperatures over the composition fraction. The two energy minima determine the coexistence curve that was superimposed. The compositional range with a negative second derivative of the free energy in b) shows the region of the unstable phase with spinodal decomposition as the main separation mechanism.

Structure Amplification depending on Temperature and Silicon Excess

In the metastable region of the phase diagram, instability requires thermal fluctuations to overcome the energy barrier of Equation (64) (see Figure 4-14). The region of spinodal decomposition, on the other hand, is purely unstable and only requires fluctuations with arbitrarily small amplitudes to initiate the separation of the phases. Such a fluctuation is amplified and leads to a separation in the form of this fluctuation. The simplest approach is to investigate the stability of the Si excess with respect to a fluctuation with a certain wavenumber k. For a homogeneous mixture with a Si excess of C_0 in one dimension this can be realized by

$$c(x,t) = C_0 + c_\mathrm{P}\exp\{st + \mathrm{i}k\,x\} \tag{82}$$

with a small amplitude c_P. If due to such a fluctuation the Si excess is amplified by Equation (82), it comes to phase separation and the system can be described as unstable with respect to this fluctuation. However, if it calms down, the system is in a stable state with respect to this fluctuation. Inserting Equation (82) in Equation (79) and omitting anything higher than $\mathcal{O}(c_\mathrm{P}^2)$ leads to the amplification factor for the fluctuation

$$s(k) = -M(f''(C_0)k^2 + \varepsilon^2 k^4) \tag{83}$$

with the wavenumber k. A positive value of $s(k)$ would let the fluctuation grow, a negative would let the system calm down again.

Figure 4-22 a) shows the amplification factor $s(k)$ for a sinusoidal fluctuation of a mixture below the coexistence curve. For wave numbers with positive $s(k)$, the system is amplified without thermal activation. Figure 4-22 b)-f) shows the development of the Si excess with a small fluctuation at different wavelengths induced in a). The red curve shows the start function according to Equation (82) and the blue curve the evolution after a time t_1, which is equal in all cases b)-f). In b) the amplification $s(k)$ has a small value, which leads to an amplification of the fluctuation, but develops only slowly. The higher wave numbers in c) and d) show a more pronounced amplification, because the amplification factor is significantly higher in these cases. If the wavenumber becomes too high, the Si excess does not become unstable due to the fluctuations and the system calms down again, as can be seen in e) and f). The fastest growing wavenumber in a) is $k_{\max}$ and grows with the amplification factor $s_{\max} = s(k_{\max})$.

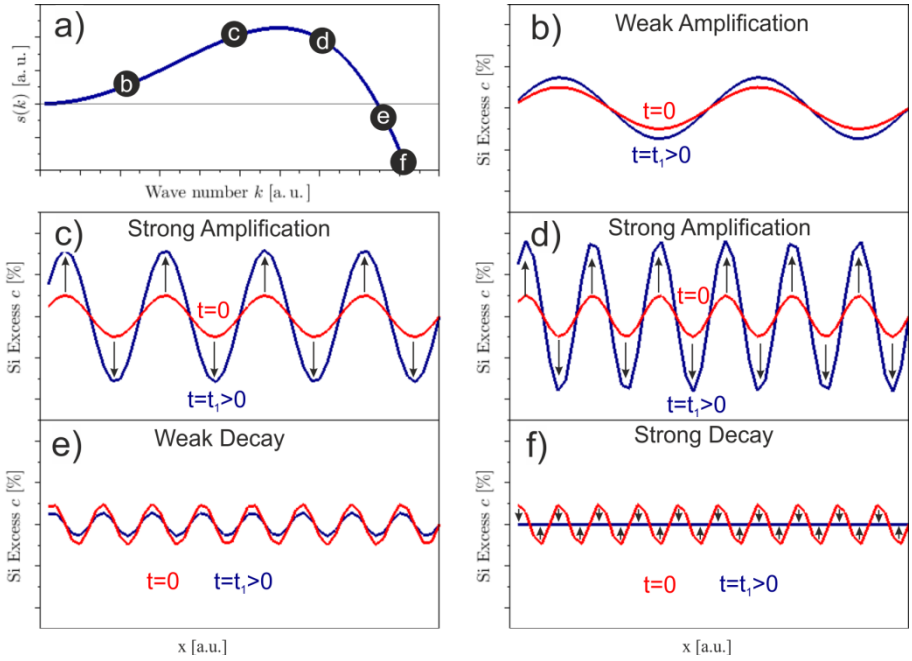

Figure 4-22: The amplification factor $s(k)$ of Equation (83) in a) and examples of composition fluctuations according to (82) and their evolution, calculated by Equation (79) for a time t_1 in b) to e). The wave numbers used are indicated in a).

The curve in Figure 4-22 a) shows the dependence of the amplification on the structural size of the system. This is specific to a certain point in the phase diagram (see Figure 4-12). To investigate the dependence for different points, Figure 4-23 shows these curves for different temperatures (a) and Si excess (b). These curves are directly connected to the free energy shown in Figure 4-21 a) with the respective second derivative in b). Here it is shown how lower temperatures cause a much stronger curvature of the potential. This leads to higher amplification factors as shown in Figure 4-23 a). But also the size of the most amplified structure increases.

The free energy also depends on the Si excess. Figure 4-21 b) shows how the potential f has the strongest curvature in the range of 50% Si excess and thus leads to higher values for the amplification factor in Equation (83). Figure 4-23 b) shows the amplification $s(k)$ for different values of Si excess. For a Si excess of 30% the amplification is very low, which can also be observed in KMC simulations (see Figure 4-20). Here the process is already dominated by spinodal decomposition, but nucleation

still takes place. With increasing Si excess a similar tendency as with increasing temperature can be observed.

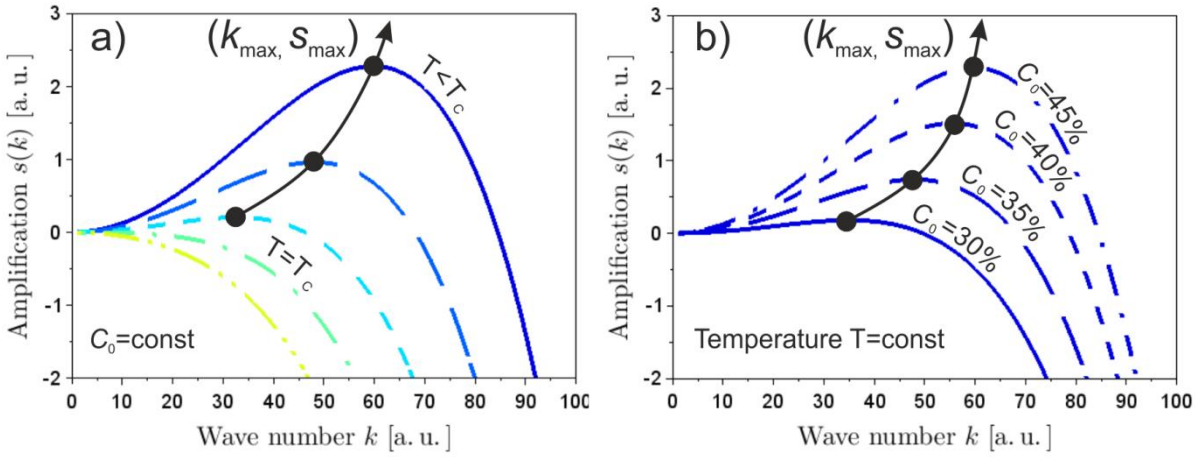

Figure 4-23: The amplification factor $s(k)$ from Equation (83) for different temperatures (a) and compositions (b). The black arrows show the dependence of the maximum amplified wavenumber kmax and its amplification factor smax on temperature (a) and composition (b). The curves are determined by Equations (83) and (81) with different numbers for a (a) and C_0 (b).

In summary, this chapter showed KMC simulation results in Figure 4-20 of how the SiO_x separates in the unstable region of the phase diagram (see Figure 4-12). The free energy from the Equation (80) was investigated with respect to the dependence of temperature and Si excess. Small fluctuations of the Si excess according to Equation (82) can lead to a direct separation. The fluctuation is amplified by the amplification factor $s(k)$ in Equation (83) as a function of their wavenumber k. This amplification function was determined for different temperatures and values for Si excess (see Figure 4-23). This leads to the conclusions:

- It is expected that the process taking place at the interface during annealing corresponds to spinodal decomposition at a volume fraction of 50%. Figure 4-20 showed how fast this process is compared to the nucleation of Si-NC. The nucleation of Si-NC will therefore take place while the interface is already reconstructed. This allows one to expect a very pronounced denuded zone between Si-NCs and the Si/SiO_2 interface.
- The nucleation of SiO_2-NC will take place while the interface is not yet reconstructed so that no denuded zone is expected.
- The SiO_2 layer in the nanopillar gives a structure with a distance of 7nm (see Chapter 2.3). This would also correspond to a wavelength of 7nm with its specific amplification $s(k)$. Depending on temperature and Si excess, the amplification of the wavenumber on the scale of the nanopillar can have a decisive influence.
- The influence of the amplification factor can be controlled by different temperatures and Si excess. This can be used to control the reaction pathway of the nanopillar.

4.3.6 Heat Treatment of Ion Beam Mixed Si/SiO_2 Interface

Chapters 4.2.1 to 4.2.3 showed the KMC model parameterized with diffusion constants for Si and SiO_2, which differ by 15 orders of magnitude. Nucleation and grow of Si and SiO_2-NC as shown in Chapter 4.3.2 takes place at different speed, while in between the spinodal decomposition reconstructs the interface. Chapter 4.3.1 showed that spinodal decomposition and nucleation are not separated by a strict line in the phase diagram. Spinodal decomposition replaces nucleation as the dominant separation process for decreasing temperatures and increasing Si excess as was shown in Chapter 4.3.5. The Si-NC formed are controlled by diffusion-controlled growth (see Chapter 4.3.2) and diffusion-controlled Oswald Ripening (see Chapter 4.3.4), while these processes are reaction-controlled in case of SiO_2-NCs. With a mixed interface, as shown in Chapter 3.2, it is difficult to refer to a specific region in the phase diagram of Figure 4-13. Separation of Si excess from the entire composition range takes place, whereby the high difference in diffusion provides for a high temporal offset. This interaction will be very important especially in Chapter 5 and 6 and is therefore discussed in this chapter.

Simulation of Annealing of a Mixed Si/SiO_2 Interface

Figure 4-24 shows the simulation of the heat treatment of a mixed Si/SiO_2 interface after irradiation with different fluences. The SiO_2-NCs are immediately nucleated and start the Ostwald ripening process, which is already completed in approx. 0.2 seconds. Shortly thereafter, the almost complete reconstruction of the interface can be observed at all fluences. According to the Gibbs Thomson relation of Equation (72), the lowest Si excess concentration is obtained at the interface, making it the strongest sink for Si excess atoms. The configuration in SiO_2 remains unchanged over a longer period of time. Stable Si-NC can only be observed after a time of about 2 seconds. While the first Si-NCs appear, a pronounced denuded zone between the interface and the formed Si-NCs can be observed. This has already been discussed in Chapter 2.4.3 and shows the self-organizing effect triggered by the interface.

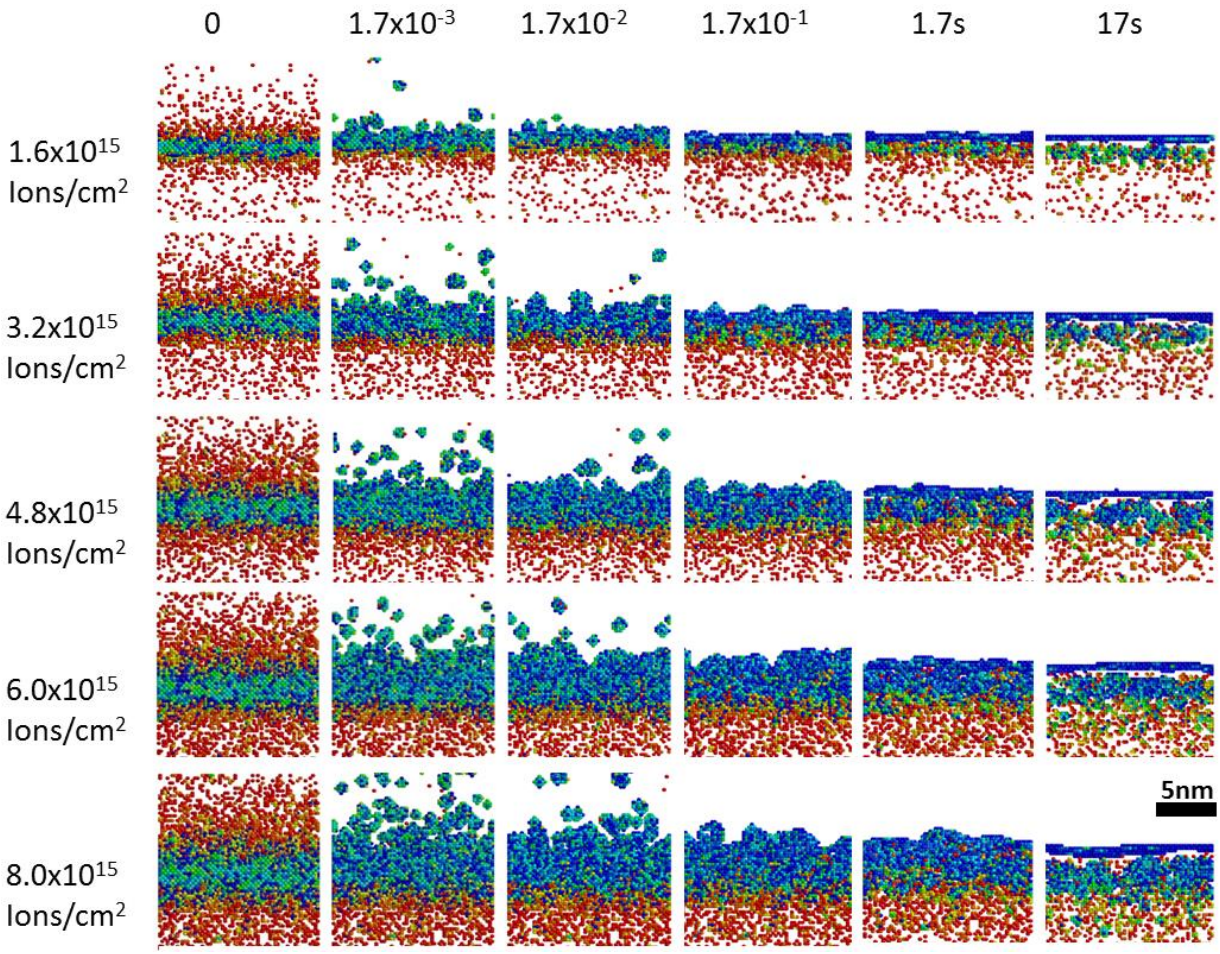

Figure 4-24: Simulation results of annealing a Si(30nm)/ SiO_2 interface after previous irradiation with 60 keV Si^+ ions for the indicated fluences. The irradiation was simulated with TRIDYN analogous to the results in Figure 3-7. Annealing was simulated by KMC at a temperature of 1373K for the indicated annealing times. The atoms shown are the interface atoms of the Si/ SiO_2 interface. The calculation box had the size of 27x27x13 nm3 and shown is a lamella with a thickness of 13nm.

In summary, this chapter shows the simulation of the annealing of a mixed Si/SiO_2 interface after irradiation by different fluences in Figure 4-24. In the case of Si-NCs, there is a distinct denuded zone to the Si/SiO_2 interface, whereas in the case of SiO_2-NC no denuded zone is observed. This is due to the large discrepancy in the diffusion coefficients (see Chapter 4.2.2). This leads to the following conclusions

- Figure 4-24 confirmed the conclusions from Chapter 4.3.3: There is no denuded zone between the SiO_2-NC and the interface.
- The interface acts as a strong sink for Si excess and immediately eliminates the formed SiO_2-NCs. This was expected in Chapter 4.3.3 due to the strong denuding at the surface of the NCs as shown in Figure 4-16.
- SiO_2-NCs are not expected to form during annealing of the Si/SiO_2/Si stack or the stacked nanopillar, because of the much longer annealing times than 2s shown in Figure 4-24.
- The time difference of the processes in Si and SiO_2 gives the possibility for further approximations to save computing time. This will be used for the calculations in the next chapters. The processes in Si are in full equilibrium for a long time, while the processes in

SiO_2 are only in the initial stage. This makes it possible to neglect the fast speed of the processes in Si.

- The fast interface reconstruction will ensure a good tunnel distance.

5 Confined Si-NC Formation in a $Si/SiO_2/Si$ Stack

The use of ion irradiation processes in combination with interfaces of Si and SiO_2 has gained increasing importance in recent years [102], [103], [175], [178], [255]. Top-down processes for the production of non-volatile memories [103] and light-emitting diodes [256] have been developed based on the irradiation of Si and SiO_2. Similar to Chapter 4.3.6, NCs were fabricated at close distances to Si/SiO_2 interfaces to take advantage of the quantum mechanical tunneling of electrons. The memory from [103] is above all a good example of how the manufacturing processes presented here can be used for the industrial products. This showed that NCs in direct proximity to Si/SiO_2 interfaces are an excellent option to use tunneling for technical applications. The experimental studies [102], [103], [202] on this topic were supported by theoretical work [102], [149], [178], [257], [258] that provided reliable predictions. In the case of the SET from this work, the detail fidelity of the models becomes much more decisive. It is necessary to control the placement of single NCs (<4nm) in 7nm thick SiO_2 layers (<4nm). Experimentally, the realization of site controlled formation of individual NCs in the SiO_2 (7nm) of a planar $Si/SiO_2/Si$ stack could already be shown [89]. These were also produced by a combination of IBM with Ne+ ions and subsequent annealing.

The formation of a single NC for the SET, as illustrated in Chapter 2.3, is an even more delicate matter. Here the lateral direction is additionally limited by the nanopillar with a diameter of 10nm. The simulation of self-organizing processes in these scales needs a reliable understanding of the physical mechanisms during manufacturing. A $Si/SiO_2/Si$ stack system is the best example for preliminary investigations of the process steps. With the models and methods of Chapters 3 and 4 alone, it was possible to perform simulations and obtain predictions for NC formation in the buried SiO_2. However, the experiments led to different results. The NC morphology observed in the experiment did not correspond to that predicted by the simulation. It was necessary to use higher fluences in the experiment to obtain the morphology of the NCs from the simulation. Chapter 3 discussed the approximations and assumptions for the IBM model and Chapter 4.1 for the KMC model. In principle, the cause of the discrepancy could lie in both process steps. In order to make reliable predictions for the fabrication of the SET, it is therefore necessary to first find and model the exact reason.

This chapter discusses all possible reasons for the discrepancy and states that simulations based on the BCA overestimate the IBM at the Si/SiO_2 interfaces. In Chapter 5.1.1 the discrepancy is first discussed in detail and Chapter 5.1.2 then shows a quantitative comparison between experiment and simulation results. Chapter 5.2.1 will then first show how chemical effects can be included in the simulations by phase field approaches (Chapter 5.2.1), then the modelling of annealing (Chapter 5.2.2), the combination of both (Chapter 5.2.3) and present the predictions for IBM of the $Si/SiO_2/Si$ stack.

5.1 Simulation by TRIDYN and Kinetic Monte Carlo Method

In principle, any of the approximations made in Chapters 3 and 4 may be the reason for the discrepancy between experiment and simulation. In addition, the annealing model actually has an unknown parameter $E_{\mathrm{NN}}(z=0)$ (see Chapter 4.2.3), which could also have an influence.

In this chapter, the the discrepancy and its reasons are analyzed in Chapter 5.1.1. The discrepancy is then quantified and a dependence on the radiation fluence is discussed in Chapter 5.1.2. The $Si/SiO_2/Si$ stacks used in experiments were large planar systems and in order to reproduce them correctly, it is necessary to calculate similar large systems. In addition, the interesting values need to be averaged over several reaction pathways, which require a high number of calculations. To realize this, it is necessary to reduce the long calculation times (see Chapter 4.2.2) by further assumptions. This is shown in Appendix B.

5.1.1 The discrepancy between Experiment and Simulation due to incomplete description of IBM

The discrepancy has been disclosed by the comparison of the Si-NCs observed in the EFTEM analysis and that found by KMC simulations for the same parameters. The samples were irradiated with 60 keV Si^+ ions for a fluence of $0.85 \cdot 10^{16}$, $1.7 \cdot 10^{16}$ and $2.6 \cdot 10^{16}$ ions/cm^2. Experimental samples always showed NCs in buried SiO_2. However, the results of the simulation did not for any fluence above $1.2 \cdot 10^{16}$ ions/cm^2. There is unfortunately no practical experimental method at the scale of a few nanometers to measure the SiO_x depth profile after IBM, thus a direct comparison with BCA simulations is not possible. This leads to the fact that both, the model for IBM (BCA, in Chapter 3) and the model for annealing (KMC, in Chapter 4.1) could be responsible for the discrepancy. This chapter will explain the reason for this and provide a deeper understanding of the problem.

Experimental Analysis of $Si/SiO_2/Si$ stack after Irradiation and Subsequent Annealing

A thin SiO_2 layer ((7±0.5) nm) was produced by thermal oxidation of [100] Si with subsequent sputter deposition of 25 nm Si. For IBM, irradiation with Si^+ ions at room temperature was performed with an irradiation energy of 60 keV and an angle of incidence of 7° relative to the normal surface. The total fluences of of $0.85 \cdot 10^{16}$, $1.7 \cdot 10^{16}$, and $2.6 \cdot 10^{16}$ ions/cm^2 were achieved by ion fluxes of $0.0007 \cdot 10^{16}$ ions/scm^2. Subsequently, RTA was applied at a temperature of 1323 K for 30 seconds. A Zeiss NVision 40 device for classic lamella preparation by sawing, grinding, polishing, dents and final Ar^+ ion milling was used for the preparation of cross-sectional TEM samples to produce thin lamellae down to a thickness of several nanometers. An EFTEM analysis was performed at positions with a lamella thickness of 20-30 nm using a FEI Titan 80-300 microscope. Figure Figure 5-1 shows the EFTEM images of samples with the treated fluences at an electron energy loss of 17 eV corresponding to the plasmon loss peak of Si. The potential influence of the e-beam on the Si NP morphology was verified by multiple images of the same sample position. Significant changes were detected only after 5-fold imaging (a single electron beam exposure for imaging does not change the sample structure). Based on the knowledge of the mean free pathway of electrons, the Si mass contrast was determined [89], [111] and the size and area density distributions of the NPs were calculated.

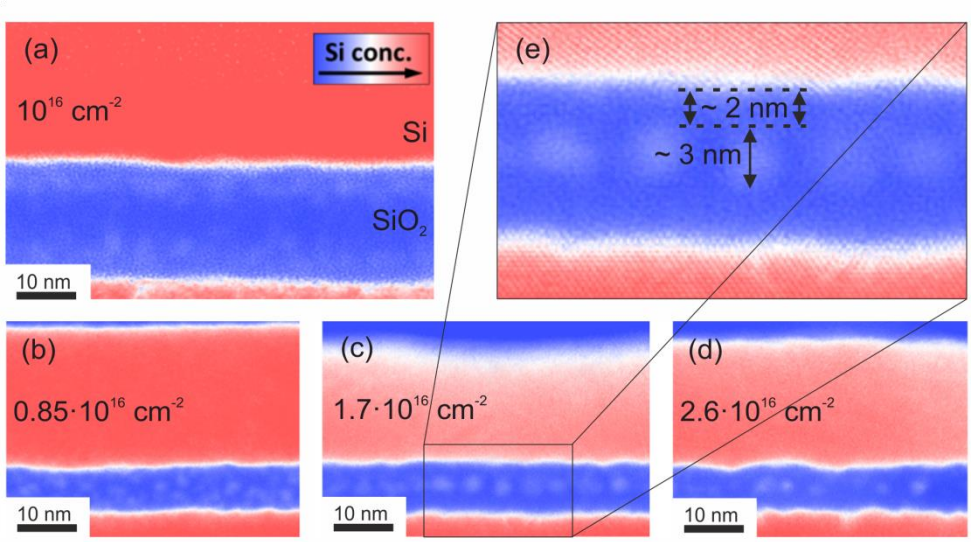

Figure 5-1: EFTEM images of cross-sectional lamellas with a thickness of 20-30nm of planar Si/SiO_2/Si stacks Si/ SiO_2 /Si. The lamellas were prepared according to the procedure explained in the text. The used SiO_2 thickness was 15nm (a) and 7nm (b-e). The Si^+ ion beam used had an energy of 50 keV (a) and 60 keV (b-e). The top Si thickness was 50 nm (a) and 30 nm (b-e), the temperature used in the rapid thermal annealing was 1050°C and the annealing time was 30s (a,c,d,e) and 60 s(b) in a N2 atmosphere. Taken from ref. [111].

Figure Figure 5-1 shows EFTEM images of experimentally produced Si/SiO_2/Si stacks with different parameters. In a), a stack with a large SiO_2 thickness of 15 nm was irradiated by 50 keV Si^+ ions for a fluence of 10^{16} ions/cm^2 and subsequently annealed for 30 s at a temperature of 1050 °C. Both interfaces were mixed separately and the self-organization of the two NC layers runs essentially independently of each other. A similar system has already been investigated in the past and used for non-volatile memories [85], [102], [103], [175]. The samples shown under b) to d) with significantly smaller SiO_2 thickness were irradiated by 60 keV Si^+ ions with increasing fluence ($0.85 \cdot 10^{16}$, $1.7 \cdot 10^{16}$ and $2.6 \cdot 10^{16}$ ions/cm^2). In any case NCs can be observed. The lower fluence leads to a low supersaturation and thus to a higher number of nucleations (see Chapter 4.3.2). Many small NCs then form in the later stage as seen in Figure Figure 5-1 b). The increase in fluence leads to a higher supersaturation of the SiO_2 and thus to larger NCs in the annealing process (c). These are very well centered and have a distance of ~2nm to the Si interfaces. This and the diameter of 3nm makes it very well suited for RT operation of the SET. A further increase in fluence lets expect a further increase in supersaturation and larger NCs (even spinodal decomposition) during annealing, according to predictions made in Chapter 3.2.2 and 4.3.5. However, the numbers for size and density of the sample after irradiation with a fluence of $2.6 \cdot 10^{16}$ ions/cm^2 have remained almost the same compared to the sample after irradiation with a fluence of $1.7 \cdot 10^{16}$ ions/cm^2 (see Table 4). The values were determined and averaged using EFTEM images. The only difference using a higher fluence is a decrease in the density of the NCs from 0.016 to 0.014 nm^{-2}. One possibility to explain this is that the interface is strongly structured (see Figure Figure 5-1 d)), what increases the size of the interface and thus more nucleated NCs touch the interface and disappear due to wetting.

Table 4: Experimental results for the samples shown in Figure 5-1.

Ion fluence [10^{16} cm^{-2}]	0.85	1.7	2.6
Areal density [nm^{-2}]	0.018	0.016	0.014
Mean diameter [nm]	1.96	2.23	2.23

Comparison to Simulation Results by TRIDYN and KMC

The simulations results using BCA and KMC with the parameters corresponding to the experimental results of Figure Figure 5-1 are shown in Figure 5-2. The irradiation was simulated by TRIDYN and used to randomly fill the KMC lattice according to the 1D Si excess profile obtained by equation (8). These Si excess profiles are plot in Figure 5-3 a) and show high values of Si excess above 50% inside the SiO_x layer. Looking at the phase diagram in Chapter 4.3.1, Figure 4-20 shows spinodal decomposition occurs already at Si excess of 30%. The reaction pathway of the Si/SiO_2/Si stack in Figure 5-2 (a-c) starts with a Si excess of 40% in the center (see Figure 5-3) and shows mainly separated Si domains attached at the upper and lower silicon, which disappear quickly by wetting. This deduces to separation by spinodal decomposition (see Chapter 4.3.5), what is expected regarding the Si excess profiles. However, the experimental results in Figure Figure 5-1 show isolated NCs, which mainly suggests nucleation.

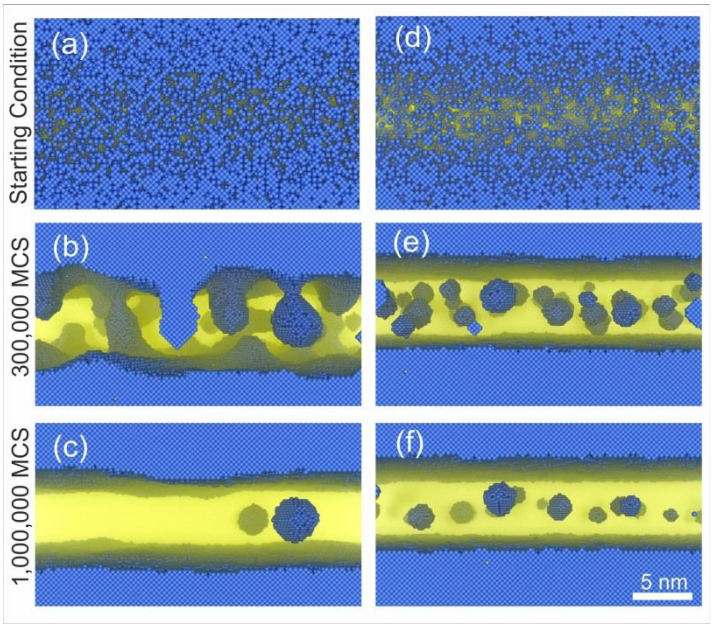

Figure 5-2: Two reaction pathways (a-c) and (d-f) of a planar Si(30nm)/SiO_2(7nm)/Si stack with randomly distributed Si excess atoms according to a profile obtained by BCA calculations (TRIDYN, see Chapter 3.2.2) as a starting configuration. The blue spheres show the Si excess atoms and the yellow-transparent "fog" the SiO_2 matrix of a 25 nm thick lamella, visualized by Blender [259]. The IBM simulations were performed by TRIDYN using 60 keV Si^+ ions with a fluence of $1.7 \cdot 10^{16}$ ions/cm^2 (a) and $0.85 \cdot 10^{16}$ ions/cm^2 (b) and converted into a Si excess profile according to Equation (8). The subsequent KMC simulation was performed using the adjustments proposed in this chapter with an E_{NN} (z=0) of 0.21 eV.

The combination of BCA and KMC for irradiation and annealing was already used in previous studies [86], [103], [175], [178] [260]. However, most of them were based on the annealing of implanted profiles [175], [178], [261] or the discrepancy appeared too weak because it was only a single interface. However, due to the sensitive nature of the SET (Chapter 2.1), the discrepancy shown in Figure 5-1 and Figure 5-2 is unacceptable and needs to be corrected.

The Reason for Discrepancy of NC Formation

Ion beam mixing of Si/SiO_2 interfaces, implantation of Si and phase separation of SiO_x are the processes that can contribute to the discrepancy. In order to develop advanced models, it is necessary to identify exactly the reason. There are three possible explanations:

- **Implanted Si ions** in the region of SiO_2 lead to additional supersaturation. In case the simulation underestimates the range of Si^+ ions, the proportion of implanted ions in SiO_2 would be higher than in the experiment. This would lead to an overestimation of the supersaturation and an explanation of the observed discrepancy. However, the ion trajectories predicted by the BCA are very well established [262] and the results can be considered reliable for use in the Si and SiO_2 systems. Further, Chapter 3.2.1 showed that the implanted ions stop in a much deeper range and already contribute less than 1% supersaturation in the simulation at a fluence of $0{,}85 \cdot 10^{16}\ \mathrm{ions/cm^2}$ (see Figure 3-7). In order to let the separation be dominated by the nucleation mechanism, a Si excess of less than 20% is necessary, but is predicted to be over 50% (see Figure 5-3). Even the complete neglect of the implanted ions would not make a significant difference.
- **The contribution of KMC simulation** to the discrepancy is more complicated. In the past, KMC simulations of phase separation have reproduced the experimental findings several times, e.g. EFTEM analysis of NC formation and spinodal decomposition [103], atomic probe tomography of phase separation of Ni-Al-Mo alloys [263] or spinodal decomposition of an Fe-Cr mixture [264]. But especially the studies by Müller [85] give some examples for the good agreement of KMC simulations of the SiO_x system with experimental results. However, these results are mainly based on homogeneous or implanted supersaturation. The mixing of a Si/SiO_2 interface has not yet played a significant role. Figure 5-3 shows the mixing profile of the SiO_2 layer for different irradiation fluences up to $2 \cdot 10^{16}\ \mathrm{ions/cm^2}$. This already leads to a supersaturation of 50% in the center of the SiO_2. In general, spinodal decomposition occurs directly (see Chapter 4.3.5) and no atom has the possibility to diffuse to the interface before phase separation. The Si excess profiles shown in Figure 5-3 must therefore undoubtedly lead to purely spinodal phase separation and this is predicted by the KMC simulation. Chapter 4.3.5 shows in Figure 4-20 the development of a configuration with this supersaturation. At 50%, the SiO_x separates by pure spinodal decomposition and no isolated NCs appear. One possible explanation could be the unknown value for the bond energy E_{NN} (z=0). This will be discussed in Chapter 5.1.2.
- **The last possibility** to explain the discrepancy is an overestimation of the IBM by the BCA: When applying low fluence (Figure 5-2), the simulation results show isolated NCs as observed in the experiment for higher fluences. Thus, a lower mixing efficiency would lead to a better agreement. The ion channeling and its influence on the ion range was neglected in the calculation. However, SiO2 is immediately amorphous and the material can be assumed to be amorphous during irradiation. The calculations by TRIDYN give two possibilities to overestimate the mixing: (i) a too low chosen binding energy or (ii) the neglect of chemical effects.

Overestimation of IBM by BCA

The mixing of the Si/SiO_2 interface is mainly based on the knocking out of Si and O atoms (see Chapter 3.2). The transfer of kinetic energy necessary to knock an atom out of its embedded position is given by the displacement threshold energy U_d. For crystalline materials there are tabular values [265]–[267]. In the case of Si the default value of TRIDYN with 8 eV is based on the proposal of Sigmund et al from their theoretical study with 7.8 eV [144]. The 7.8 eV is a mean value over all directions in the diamond lattice, where the displacement energy for different directions differs by one order of magnitude. This 7.8 eV seemed to be a good choice and is successfully used in several ion mixing studies [262]. But if displacements occur strongly, the target material will be destroyed and becomes amorphous. In addition, the present system is a mixture of Si and oxygen, which makes the determination of the displacement threshold energy more complex. Results from MD-calculations showed values with with $U_\mathrm{d}(\mathrm{Si}) = 70.5$ eV and $U_\mathrm{d}(O) = 28.9$ eV for quartz [268], and $U_\mathrm{d}(\mathrm{Si}) = 33.5$ eV and $U_\mathrm{d}(\mathrm{O}) = 16.3$ eV for amorphous SiO_2 [269]. This could lead to a weakening of the IBM and at least partially explain the discrepancy. For the SiO_x mixture, the displacement thresholds are interpolated by

$$U_\mathrm{d}(\mathrm{Si}) = 15\ \mathrm{eV} + \frac{1}{2}\frac{q_\mathrm{O}}{q_\mathrm{Si}}(33.5\ \mathrm{eV} - 15\ \mathrm{eV}) \tag{84}$$

with q_O and q_Si as the local oxygen and silicon atomic fractions, respectively, and

$$U_\mathrm{d}(\mathrm{O}) = 16.3\ \mathrm{eV}. \tag{85}$$

Figure 5-3 b) shows the composition profiles after irradiation with a fluence of $2 \cdot 10^{16}$ ions/cm^2 and compares the results at different displacement threshold energies. The use of a fixed value of 8 eV and a variable composition-dependent energy according to Equation (84) show a marginal difference. Although the lower displacement threshold energy shows as expected a stronger mixing, it does not explain the strong discrepancy between Figure Figure 5-1 and Figure 5-2. This leads to the conclusion that the overestimation of the IBM by the TRIDYN simulations might be due to a neglect of the chemical effects by the BCA.

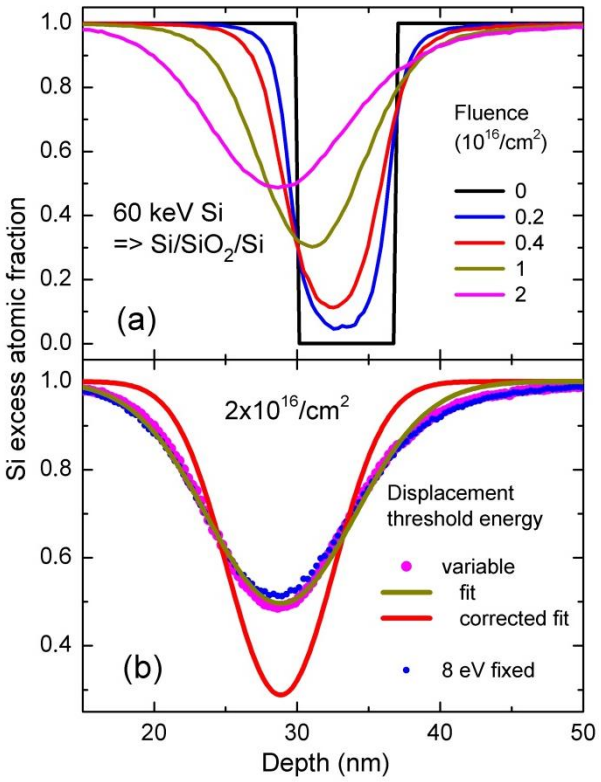

Figure 5-3: Si excess profiles of a Si(30nm)/SiO_2 (7nm)/Si stack during irradiation by 60 keV Si^+ ions with increasing fluence (a) and several Si excess profiles for the used fluence of $2 \cdot 10^{16}$ ions/cm^2 (b). One with a displacement threshold energy of 8 eV (blue), variable according to Equation(84) (magenta points), one is a fit to the magenta colored according to the diffusion Equation (14) (green) and the Si excess profile correction by means of alpha (red). The calculation has been performed by TRIDYN [134].

Adding Chemical Effects to BCA Simulations of IBM of Si/SiO_2

The first stage of irradiating a solid with energetic ions is a collision cascade dominated by ballistic binary interactions [270], [271], which transfers the ions kinetic energy to the target atoms. After the primary ion and the recoils reach their final position, the remaining kinetic energy causes local heating by so-called elastic thermal spikes [128], which can thermally activate chemical reaction-diffusion processes [272]–[276].This strongly depends on the target material, e. g. the cohensive energy of a mixture. Cohensive energy is the energy required to separate components, e.g. a Si monomer from a Si-NC. Previous studies have investigated bimetallic systems and developed semi-empirical models to describe the IBM including the influence of cohensive energy [277]–[279]. The studies of B. Liedke [149] introduced a combination of KMC and TRIDYN, which describes this influence by atomistic interactions. In miscible systems the chemical effects enhance the IBM and in immiscible systems the chemical effects reduce the IBM. The mixture of Si and oxygen has a high cohensive energy and is a strongly immiscible mixture. In this case, the neighborhood of two identical components reduces the energy, which can lead to local phase separation in the sub volume of the thermal spikes. This leads to a stabilization of the interface and lowers the supersaturation in the SiO_2.

In summary, this chapter compared the simulation results of irradiation (TRIDYN) and subsequent annealing (KMC) of the Si/SiO_2/Si with corresponding experimental studies. The observation leads to the following conclusions

- The BCA simulation is overestimating the IBM and the most probable reason are chemical effects which are not treated by BCA simulations

5.1.2 Correction Factor for the Binary Collision Approximation

The influence of thermal spikes during irradiation, as outlined in detail in Chapter 5.1.1, is neglected by the BCA and leads to a strong disagreement between simulation (Figure Figure 5-1) and experiment (Figure 5-2). However, Figure 5-2 e)-f) shows how the simulation results show a very similar morphology to that seen in the EFTEM results obtained in Figure Figure 5-1. The only difference is the applied fluence. This means that a high fluence in the experiment leads to similar results as a low fluence in the simulation. To understand and quantify the influence of the thermal spikes, an artificial correction factor alpha is introduced. By quantifying the discrepancy in that way, this leads to a deeper understanding and shows that the discrepancy increases linearly proportional to the fluence.

Reproducing the Experimental Results by KMC Simulations with Input of Scaled BCA Profiles

The NC morphology obtained by the experiment can only be reproduced in simulations by applying lower fluence. For this purpose, the difference shall be investigated using a correction factor α, by setting the Equation (14) to

$$c(x,\Phi) = 1 + \frac{1}{2}\left(\mathrm{erf}\left\{\frac{x - x_1}{2\alpha\sqrt{D_\varphi \Phi}}\right\} - \mathrm{erf}\left\{\frac{x - x_2}{2\alpha\sqrt{D_\varphi \Phi}}\right\}\right). \tag{86}$$

This factor can now be determined for each available experimental result (e.g. Figure Figure 5-1). For a α of less than 1, it artificially reduces the mixing efficiency and thus the supersaturation in SiO_2. Figure 5-4 shows how the correction factor α is determined for the sample c) in Figure Figure 5-1 (fluence of $1.7 \cdot 10^{16}$ ions/cm^2). The density (a) and the average size of the NCs (b) are displayed as a color map depending on the correction factor and annealing time. In case of $\alpha = 1$, it's the Si excess profiles obtained by pure BCA as shown in Chapter 3.2.2 with a subsequent annealing simulation by KMC. This case is shown in Figure 5-2 (a-c). Only a very low amount of large NCs survive the annealing process. In case α decreases, the mixing efficiency decreases and leads to less supersaturation. This case can be observed in Figure 5-2 (d-f) with a higher amount of small NCs. In the colormaps of Figure 5-4, this can be observed at lower values for α. The initial annealing stage consists of nucleation of Si-NCs leading to a high number of small NCs. An increasing annealing time leads to the disappearance of the smallest NCs due to Ostwald ripening (see Chapter 4.3.4) and causes growth of the larger ones. Figure 5-4 a) shows how the density first increases rapidly and then decreases slowly until the density at the black line corresponds to the experimental value. In case of the average diameter in b), however, the size of the NCs is mostly dependent on the alpha factor. The black lines show iso-lines with the experimental value from Table 4 for the areal density in a) and the average diameter in b). Both lines cross at the black point that is displayed in both color maps. This unique pair of size and density of the NCs obtained in experiment appears in the simulation only with a unique combination of correction factor α and annealing time in MCS.

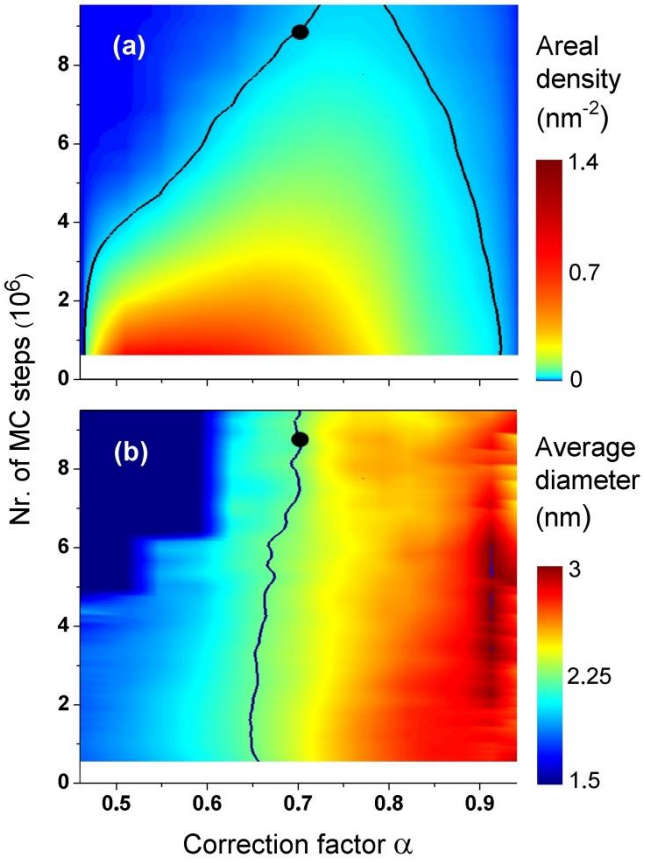

Figure 5-4: Colorplot of the areal density (a) and the mean diameter (b) of Si-NCs over the correction factor alpha and the number of MCS for a Si(30nm)/ SiO_2 (7nm)/Si stack after irradiation by 60 keV Si^+ ions for a fluence of $1.7 \cdot 10^{16}$ ions/cm^2 and subsequent annealing at 1050°C. The experimental results for density and diameter of these irradiation and annealing settings are shown as black isolines. The black dot marks a unique combination of the number of MCS and correction factor where the simulation results match the experiment.

Figure 5-5 shows the determined correction factors for the considered samples using different values for E_{NN} (z=0). As expected, the discrepancy decreases with a lower E_{NN} (0). A low E_{NN} (0) means a higher solubility and thus a higher Si excess in the equilibrium state (see Chapter 4.3.1). This Si excess therefore does not participate in the phase separation process. Only the supersaturation in addition to what is in equilibrium can be separated in Si-NC. However, this change in α remains a tendency and cannot explain the discrepancy. The reason for the discrepancy can only be the influence of thermal spikes during irradiation. However, the fluence dependence of the correction factor was not to be expected. This non-linear behavior of the correction factor also indicates a local non-linearity and will affect the shape of the mixing profile.

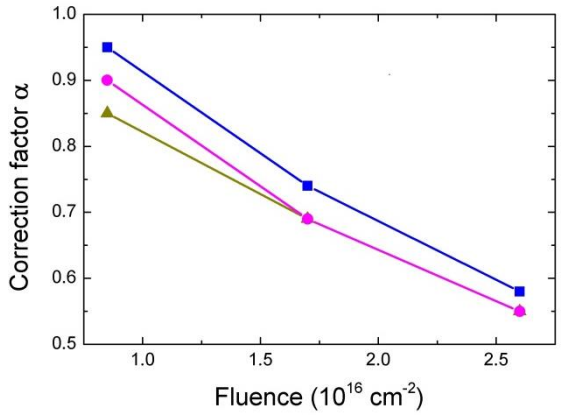

Figure 5-5: Correction factor Alpha over the fluence used in experiments, obtained using the method shown in Figure 5-4. The determination was performed with different values for the bond energy E_{NN} in SiO_2 surrounding (z=0) of Equation (46). The KMC calculations have been performed using E_{NN} (0)=0.15 eV (blue squares), 0.21 eV (magenta circles) and 0.27 eV (green triangles). The lines are only an orientation aid for the eyes.

In summary, the discrepancy of experiment and simulation of Chapter 5.1.1 was formally removed by a correction factor α which artificially replaced the mixing profile by one of lower ion irradiation fluence. The results lead to the following conclusions

- The experiments can be successfully reproduced by the simulations using the correction factor α
- The unknown $E_{\mathrm{NN}}(0)$ parameter is influencing the correction factor weakly and reduces the discrepancy with low values slightly. But this is a marginal influence and can be neglected.
- The correction factor is decreasing with fluence, which leads to a non-linear behavior of the influence of the thermal spikes. For higher supersaturations, the influence is stronger.

5.2 Treating IBM as Diffusion-Reaction Process Simulated by a Phase Field Method

The introduction of the correction factor α showed a nonlinear behavior regarding to supersaturation of this counteraction. It can be assumed with certainty that this non-linearity also influences the shape of the mixed Si excess profile. It is well-known that IBM can be treated approximately as a diffusion process (see Chapter 3.2.1). Here the "diffusion coefficient" can be extracted from TRIM or TRIDYN simulations. On the other hand, chemical effects like the phase separation in mixtures can be treated by the Cahn-Hilliard Equation (79). In this thesis, a phenomenological approach is applied to model the influence of thermal spikes by combining the diffusion equation with the Cahn Hilliard equation. However, Equation (79) is mainly used to describe spinodal decomposition. For use in phase separation of low supersaturated SiO_2, however, nucleation is the main process, which is not easy to model by phase field methods. This is a major challenge, especially with an inhomogeneous profile, e.g. Chapter 3.

Ion Beam Mixing including Chemical Effects and Subsequent Thermal Treament

Although the influence of chemical effects on IBM is well known as described in Chapter 5.1.1, these dynamic processes are complex and hardly understood even for widely used materials such as silicon. Various methods can simulate the IBM process under chemical interactions [149], [177], [280]–[283]. The basic approach is to assume that the chemical effects continuously cause segregation, while the irradiation causes mixing. Previous studies [273], [282] used the description of IBM as a diffusion process and introduced an effective diffusion coefficient that depends on the heat of mixing. Depending on the material, the heat of mixing is negative or positive and leads to enhencement or weakening of the IBM. However, if the effective diffusion coefficient is fluence independent then the mixing is not described in a correct manner (see Figure 5-5). An advanced approach was developed by Liedke [149], [177] who implemented BCA simulations in a KMC framework called TRIDER. Chemical interactions between the components could then be realized in detail on an atomistic basis. Conversely, chemical effects were also implemented in a modified version of TRIM [281].

However, these approaches suffer from an excessive number of parameters that are not available for the Si-SiO_2 system. Therefore, a simplified phase field approach is applied in this work. The diffusion equation (Equation (9)) is extended by a term which causes phase separation (Equation (79)). The

diffusion process is known by BCA-based simulations and the phase separation can be parameterized by the experimental results.

5.2.1 Decelerated IBM due to Chemical Effects described by the Cahn Hilliard Equation

The influence of chemical effects is based on (i) the complex individual movements of the components within a thermal spike and on (ii) the transformation of kinetic energy of the ion into lattice vibrations by interaction with the electron system. For miscible materials, such as in Si-metal systems, the mixing efficiency is amplified [284], [285], whereas for non-miscible materials (e.g. the present system) the mixing efficiency is suppressed [111], [286].

Limited experimental information, expensive computational resources, and insufficient physical understanding make it necessary to use simplified approaches for practical applications. In this work, a mean field approach is used to describe this complex process. Instead of local thermal spikes induce local demixing, an assumed high sample temperature induces global demixing. Similar approaches have already been applied successfully [284], [287]. Therefore, the Cahn Hilliard Equation can be utilized (see Chapter 4.3.5)

$$\frac{\partial c}{\partial \Phi}(x,t) = D_\Phi \Delta(c^3 - c) - D_\Phi \epsilon^2 \Delta^2 c \tag{87}$$

with D_Φ as the thermal spike-related diffusion coefficient, defined by the global heating during irradiation, and ϵ as the interaction length. During irradiation, the system is additionally controlled by the ballistic diffusion equation (Equation (9)). In Chapter 3.2.2 this equation resulted in a diffusion coefficient D_Φ^{up} and D_Φ^{dn} for the upper and lower interface. However, it was also shown that the profile for the parameters used is almost symmetrical and in Figure 3-8 it can be seen that the values of D_Φ^{up} and D_Φ^{dn} are almost equal. Thus it can be assumed that the diffusion coefficient for the ballistic mixing is $D_\mathrm{B} = D_\Phi^{\mathrm{up}} = D_\Phi^{\mathrm{dn}}$ for each interface. The temporal change can then be interpreted as a superposition of Equations (9) and (87) and leads to the model for irradiation

$$\frac{\partial c}{\partial \Phi}(x,t) = D_\Phi \Delta(c^3 - c) - D_\Phi \epsilon^2 \Delta^2 c + D_\mathrm{B} \Delta c \tag{88}$$

with D_Φ and ϵ as the only unknown parameters. The equation was solved in three dimensions by using the semi-implicit Fourier-spectral method introduced by Chen and Shen [288] with periodic boundary conditions. By discretizing and applying a linearly stabilized scheme [289] and transforming it into the discrete Fourier space [290], [291], the spatial evolution was determined by integrating Equation (88). The calculations were done using the open source software Scilab [292]. Numerical verification has been conducted to ensure that sufficient resolution is achieved.

A linear addition of both terms (Equations (9) and (87)) neglects all non-linear interactions. Overlapping collision cascades can lead to a dependence on flow. Whereby this is unlikely given the low flux density (see Chapter 5.1.1). The time scales of the ballistic collision cascade and the subsequent thermal spike have been investigated experimentally [293] and theoretically [294]–[299]

to a large extent and are generally in the order of 0.1 ps and 10 ps, respectively. Thus it can be assumed that both processes run sequentially and do not influence each other. Another point is the interaction of the propagating ion with the bulk matrix by phonons, which are assumed to induce a small temperature rise along the ion pathway [300]. According to molecular dynamic simulations, however, the influence of this effect is insignificantly small [300], [301].

Before simulating the irradiation, it is necessary to determine the equilibrium Si excess profile of the $Si/SiO_2/Si$ stack. For this purpose, a sharp-edged profile (according to Equation (10)) was used as starting function and relaxed to equilibrium by solving Equation (88) with D_B=0. This equilibrium distribution can then be used as a starting configuration for the irradiation simulation by Equation (88) with a D_B corresponding to the IBM obtained by pure BCA calculations. Figure 5-6 shows the equilibrium Si excess profiles for different values of ϵ and D_Φ as black lines. The equilibrium Si excess profile is only dependent on ϵ and it seems to make the interfaces smoother for higher ϵ. This will be parameterized in Chapter 5.2.3 using lattice distances and sizes of NCs.

During irradiation, nucleation may be induced by the thermal spikes [102], [282], [283], [296]. Previous studies have shown the formation of NCs during implantation in bulk systems [164] or IBM of interfaces [283], [302], [303] with immiscible materials. After reaching a certain supersaturation, nucleation occurs and further implanted or mixed atoms find their way to bind to existing NCs. The collision displacements, however, cause a detachment and a shrinkage of the existing NCs [102]. The competition between both processes leads to an equilibrium of small NCs during irradiation [102], [283], [304]. For the present system, no NCs were found in irradiated samples, regardless of fluence or energy. Thus one can assume that the destructive effect of the IBM is stronger and prevents NC from forming during irradiation or - the other possibility - the stationary size of the NCs during irradiation is too small to be resolved by EFTEM analysis.

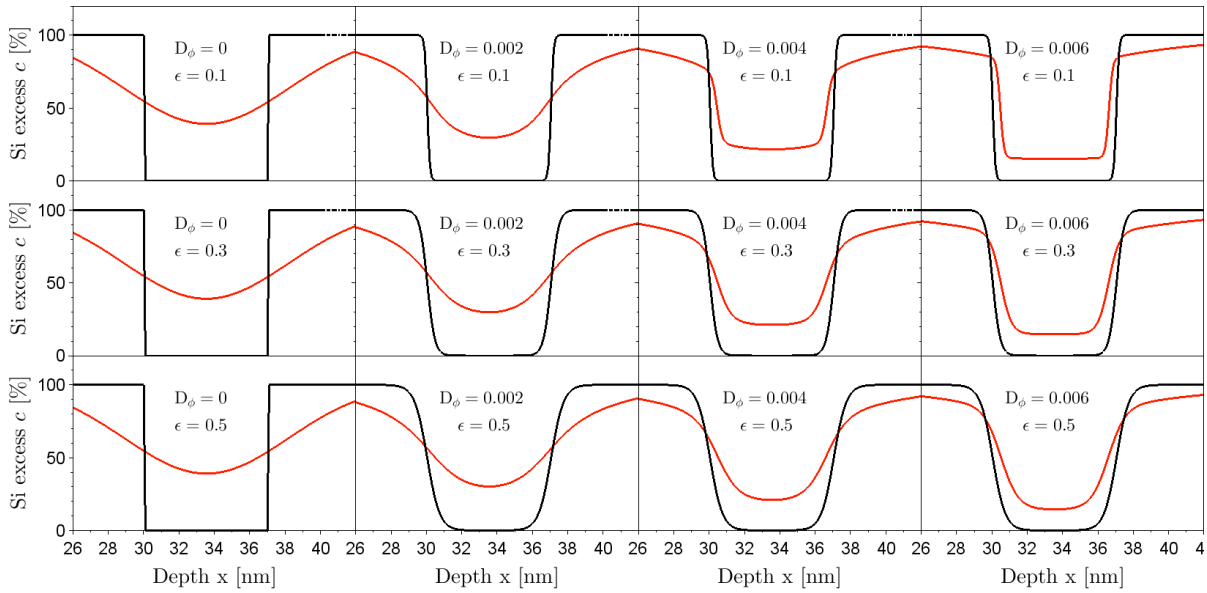

Figure 5-6: The Si excess profiles calculated by Equation (88) for a $Si(30nm)/SiO_2(7nm)/Si$ stack with different values for D_φ and ϵ, as given in units of nm^2s^{-1} and nm, respectively. The black lines show the equilibrium profiles with D_B=0 nm^2s^{-1}. These give the profile before irradiation. The red lines show the simulated Si excess profiles for a fluence of $2.6 \cdot 10^{-16}$ ions/cm^2. The value of D_B was obtained using BCA simulations by TRIDYN and is D_B=0.0036 nm^2s^{-1}.

Figure 5-6 shows the Si excess profiles of a $Si/SiO_2/Si$ stack after irradiation by 60 keV Si^+ ions for a fluence of $2.6 \cdot 10^{16}\ \mathrm{ions/cm^2}$. The simulations were done with different values for ϵ and D_Φ. Without the influence of chemical effects (D_Φ=0), the profile corresponds to pure BCA results by Equation (12). If the value for D_Φ increases, the counteracting effects can be observed. The interfaces are sharpened and the excess silicon in the SiO_2 layer is reduced. This is due to the phase stabilizing force induced by the first two terms in Equation (88). The Si excess in the center of the SiO_2 layer is essentially independent of ϵ. Instead, it significantly changes the shape of the mixing profile.

In summary, the ion beam mixing was modeled by a combination of Fick's diffusion (Equation (9)), which models the binary collisions and Cahn Hilliards Equation (87) to model the chemical interactions. Simplified assumptions were made and only 2 parameters necessary to simulate composition profiles during IBM of Si/SiO_2 interfaces.

5.2.2 Phase separation of SiO_x described by the Cahn Hilliard Equation

The IBM simulation, including the thermal spikes leads to mixed Si excess profiles as shown in Figure 5-6. However, direct comparison with the experiment is not possible (see Chapter 5.1.2) as long as the mixing Si excess profiles cannot be measured experimentally. To determine the free parameter D_Φ of Equation (88), the same approach as in Chapter 5.1.2 is used and the Si-NCs are compared with the experiment (see Figure 5-4). Therefore it is also necessary to simulate the phase separation by the phase field approach.

In contrast to KMC simulation, nucleation is not an intrinsic property of the model. It needs to be proven, that after nucleation, the NCs follow the Ostwald Ripening and that the LSW distribution is an attractor [305] of the governing differential equation. In the KMC lattice, the size and number of NCs could be determined relatively easily (see Chapter 4.3.4). Determining the size of the NCs in a 3D field function is less simple.

This chapter describes the nucleation, NC measurement in the 3D phase field simulation cell and examines the Ostwald Ripening to ensure that the model is justified. The governing law for the thermal annealing simulation is again the Cahn Hilliard equation (see Chapter 4.3.5)

$$\frac{\partial c}{\partial t}(x,t) = D\Delta(c^3 - c) - D\epsilon^2\Delta^2 c. \tag{89}$$

But instead of the influence of thermal spikes, the thermally activated process is simulated. This step is quantified by the thermal diffusion coefficient D.

Modelling the Nucleation Process by Phase Field

Nucleation means that a new phase appears within another (metastable) mixture phase because the additional free energy due to the formation of the interface is lower than the free energy of the pure phase (see Chapter 4.3.2 or [306], [307]). It is a purely stochastic process and generally a demanding task to be modeled by phase field methods. To nucleate, the metastable phase needs to overcome the nucleation energy barrier, generally by thermal activation (Chapter 4.3.1).

Basically, two common approaches are used to model nucleation by phase field methods: 1. self-formation by introducing random composition fluctuations [308], [309] and 2. the manual incorporation of single nuclei according to specific nucleation rules [309]–[311]. The first class of approaches is mainly realized by an additional noise term, which serves local energy fluctuations for phase formation. However, noise terms give rise to further crucial parameters and demand on high discretization, as it is necessary to numerically resolve the fluctuations. Depending on the noise nature and the parameter choice, an artificial underlying pattern may emerge [312] and falsify results. The second class of approaches assumes that nucleation occurs much faster in comparison to changes in its surroundings and tries to approximate nucleation as an adiabatic process [313]. Briefly described, one assumes the temporal evolution of the environment stops while the adiabatic process occurs. For technical realization, stable and randomly located nuclei are incorporated in between two time steps [309]–[311], [314]. These algorithms need modifications of the surrounding composition and have further free parameters. For the calculation of NC distributions, it is not relevant which nucleation algorithm is applied as long as the Lifshitz-Slyozov-Wagner (LSW) distribution [93] is an attractor of the model [305], because this is the main driving force for self-organization (see Chapter 2.4.3).

For the nonhomogenous shape of the composition profiles, the realization of nucleation is the most challenging. A simple approach is to use the Johnson-Mehl-Avrami-Kolmogorow equation [315] and assume a high nucleation rate, while the growth rate remains small. This leads to sudden nucleation and forms a unimodal distribution of NCs with the critical nucleation size. By that, the starting configuration can be modeled as an assembly of NCs with the critical radius and neglect any complicated nucleation algorithms. Self-organizing processes based on Ostwald ripening were successfully simulated with a similar approach [99].

Evaluation of the Ostwald Ripening of an Ensemble of NCs by Phase Field

During the simulation, the cluster size distribution must transfer to the LSW distribution (Equation (89)) regardless of the starting configuration. To ensure this, the evolution of different nuclei size distributions (bimodal and unimodal) in a 51 nm large cube with an average Si density of 10% was calculated by solving Equation (89). Periodic boundaries, a spatial discretization of 0.1nm, time discretization of 0.01s, and a diffusion coefficient of $1nm^2s^{-1}$ were used. The calculations were done by the mathematical libraries of Numerical Recipes [316] and implemented in an own c++ code. The NC distribution was evaluated and compared to the LSW distribution. The results were averaged over 10 calculations and are shown in Figure 5-7 (e) and (f). A homogenous distribution of NCs with a radius of 5nm (unimodal) is shown in (c), and the corresponding distribution function is shown in (e). The red bar shows the starting configuration and the blue bars the distribution after a short time. Another distribution with two different radii (0.5nm and 1nm, bimodal) is shown in (d), and the corresponding distribution function is presented in (f). As one can see, variations of the start configuration have no influence on the final form of the NC distribution. It immediately follows the LSW shape.

Chapter 4.3.4 showed that the LSW distribution can change greatly depending on whether the system is diffusion controlled or reaction controlled. In the case of Si-NC in a SiO_2 environment, the distribution tends to be diffusion controlled (Figure 4-19). This is due to the very slow diffusion of Si in SiO_2 (Chapter 4.2.2). The size distribution in Figure 5-7 e) and f) corresponds to the distribution calculated by the KMC simulation (see Figure 4-19 d-f). It follows that in the case of the phase field simulation the Ostwald Ripening can be successfully reproduced and is also diffusion controlled.

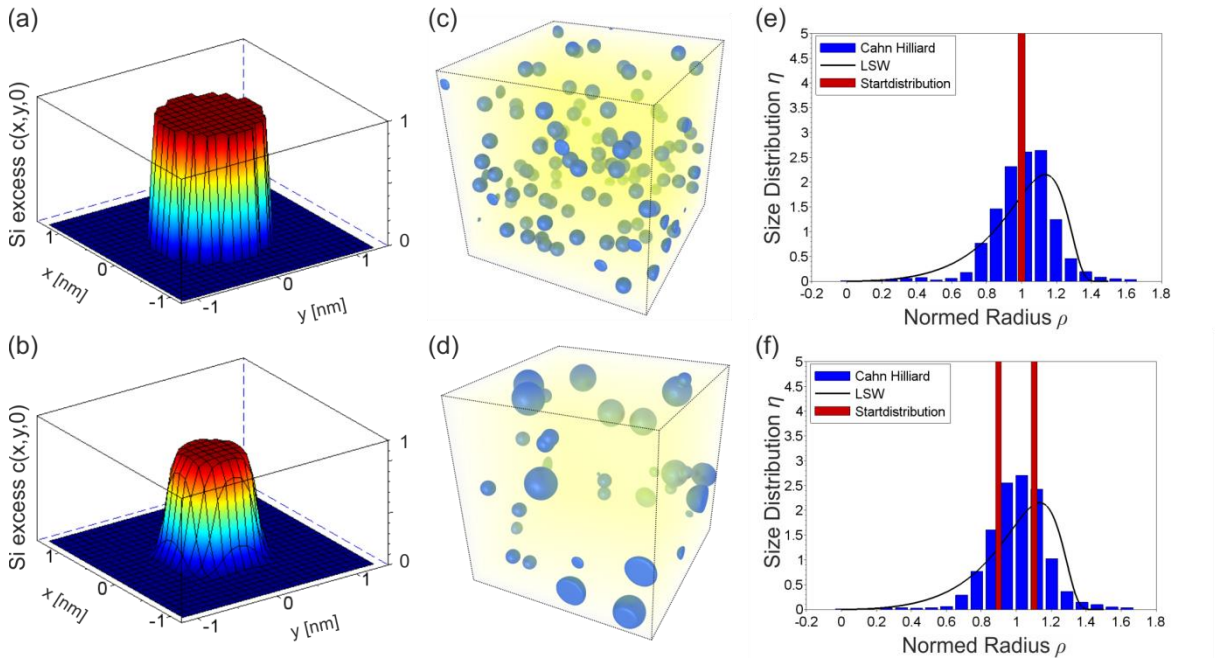

Figure 5-7: The implementation of nucleation in the phase field model of Equation (89). Si excess profiles of an equatorial section through an NCs (r=0.8nm) in a cube-shaped simulation cell with the side length 2nm as a voxel-sharp start configuration (a) and in a stationary state (b). Such NCs were distributed unimodal (c) with a radius of 0.5nm and bimodal (d) with radii of 0.5nm and 1nm in cube-shaped simulation lines with the side length of 50nm randomly and the evolution was calculated according to Equation (89). The radius distribution of the results for the start configuration (red bars) and after a short calculation time (blue bars) is shown in e) (unimodal) and f) (bimodal). The black line shows the diffusion controlled LSW distribution (Equation(73)).

5.2.3 Irradiation and Subsequent Annealing of Si/SiO_x/Si by Phase Field Methods

The results for mixed profiles by Equation (88) show the expected behavior in Figure 5-6. The phase field model of nucleation and annealing also fullfills the required properties (Reproduction of Ostwald Ripening and spinodal decomposition, see Chapter 4.3.5 and 5.2.2).

However, the treatment of the Si/SiO_2/Si stack by irradiation and annealing leads to a continuous mixing profile, which contains each area in the phase diagram (Figure 4-13). The next task is now to clarify how this mixing profile is brought into the simulation cell in the form of nuclei.

Simulating the Annealing of the irradiated Si/SiO_2/Si Stack

In Chapter 5.2.2, the nucleation process was presented, according to which the entire space is promptly nucleated in the first moment. First the size of the nucleus has to be determined and the execution of the simulation according to Equation (89) has to be discussed. For the present system, the unimodal NC distribution is chosen to create the initial configuration. Experimental analysis unveiled Si-NCs with a radius of 0.45nm and defined the upper limit for the critical radius. A lower limit can be calculated by the model itself. Spherical Si domains can be used as starting configuration and the equilibrium calculated by Equation (89). However, to do so, it is necessary to find a lower limit for the parmeter ϵ. The equilibrium solution of Equation (87) for an interface with respect to the x-axis is [156]

$$c(x) = 0.5 + 0.5\tanh(\frac{x}{\sqrt{2}\epsilon}). \quad (90)$$

The interface width is defined by the length where the Si excess concentration is between 0.05 and 0.95. This region contains 98.5% of the surface tension stress [317] and led to

$$l_{\text{int}} = 2\sqrt{2}\epsilon\tanh^{-1}(0.9). \quad (91)$$

The length of atomic bonds in the Si/SiO_2 interface structure was theoretically calculated between 0.16 nm and 0.29 nm [318], [319], which is in good agreement with experimental studies [320]. To approximate the minimum value for ϵ, a distance for the nearest neighbors at the Si/SiO_2 interface of l_{int}= 0.23nm is taken and obtained it by using Equation (91)

$$\epsilon = \frac{l_{\text{int}}}{2\sqrt{2}\tanh^{-1}(0.9)} = 0.06\text{nm}. \quad (92)$$

Using this lower limit for ϵ, it is now possible to calculate the size of the nucleus, which is at the limit to dissolve [90], [153]. It was determined by putting sharp-interface seeds with a certain radius in cube volumes and evaluating the equilibrium shape while reducing the chosen radius until the particle dissolves. The cube had a width of 3nm, a spatial discretization of 0.1nm, a time discretization of 0.001s, and an artificial diffusion coefficient of $1\text{nm}^2\text{s}^{-1}$. Equilibrium is defined as the point at which the change of the composition value is lower than 0.001 at every numerical voxel. To avoid interference of the NCs with itself and guarantee mass conservation, Neumann boundary conditions were used by applying discrete cosine transformation instead of fast Fourier transformation to solve Equation (87). The exemplary results for $\epsilon = 0.06\text{nm}$ are shown in Figure 5-7 for the sharp-edge seed and the equilibrium solution in (a) and (b), respectively. During the simulation, the interface of the spherical particle started to smooth, as already shown for a planar interface in Figure 5-6, until it reached its equilibrium shape. Further, the surrounding was enriched by excess Si until it reached its equilibrium concentration [90], [153]. By that, the determined lower limit for the critical radius in the case of $\epsilon = 0.06\text{nm}$ is 0.35nm. This is close to the upper limit of 0.45nm.

In order to design the initial configuration for the annealing simulation, individual nuclei with the size of the critical radius are randomly distributed until the depth-dependent mixing profile (Equation (88)) is reached. Figure 5-8 a) shows an example for a $Si/SiO_2/Si$ stack after irradiation with a fluence of $0.85 \cdot 10^{16}\ \text{ions/cm}^2$. The unimodal nuclei distribution corresponds to the Si excess curve in b).

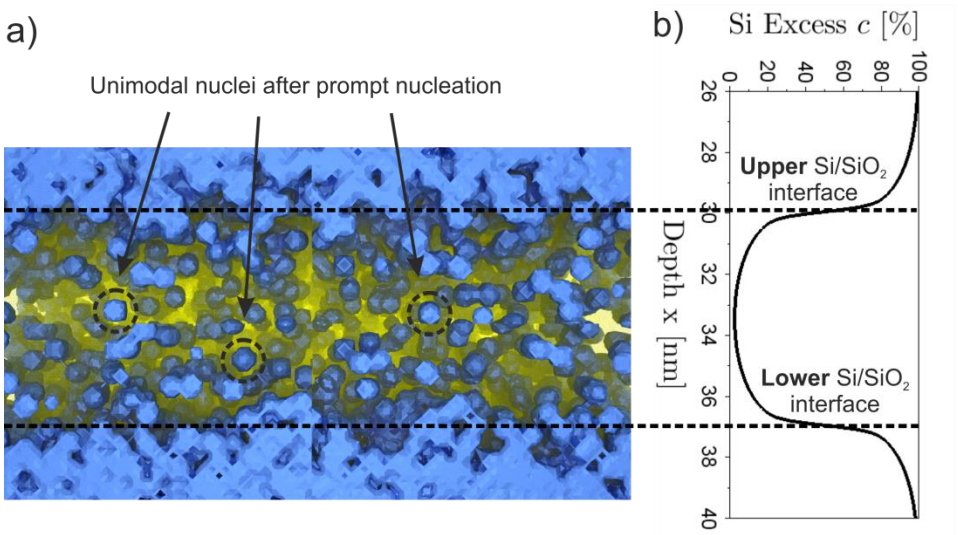

Figure 5-8: Unimodal start configuration for the annealing simulation of a Si(30nm)/ SiO_2 (7nm)/Si stack by the phase field model from Equation (89) (a) and the corresponding Si excess profile in (b). The Si excess profile was obtained by BCA simulations with TRIDYN. Irradiation of the Si/SiO_2/Si stack with 60 keV Si^+ ions for a fluence of $0.85 \cdot 10^{16}$ $\mathrm{ions/cm^2}$was simulated.

To mention is the asymmetric diffusion and asymmetric solubility of the Si/SiO_2 system (see Chapter 4.2). These can generally influence phase separation. However, Chapter 4.3.6 shows in Figure 4-24 how the configuration in the Si mass is already in equilibrium after approx. 0.2s (all NCs evaporated). Since this time, the speed of diffusion of oxygen in silicon has no influence on the reaction pathway in SiO_2. This leads to a neglect of the asymmetry in this chapter.

In summary, the nucleation process for a phase field approach was modeled for the purpose to simulate the self-organization of Si-NC in the SiO_2 layer according to Chapter 5.1.1. The conclusions are

- The critical radius shall be between 0.35 nm and 0.45 nm. A critical NC must be larger than possible in the model and smaller than the NC observed in the experiment.
- The nucleation method can reproduce the process of Oswald Ripening in a very pronounced diffusion controlled manner, what is corresponding to the results obtained in Chapter 4.3.4 for Si-NC in SiO_2. Independent on the nucleation of tiny initial NC, the late stage NC configuration is almost the same, i.e. the Cahn Hilliard equation has an attractor in the NC size distribution: the LSW distribution.

5.2.4 Simulation of Mixing Profiles for Nanopillars by Phase Field Approach

The phase field model for IBM by Equation (88) in Chapter 5.2.1 can describe the influence of thermal spikes in a reasonable way. Figure 5-6 showed that the supersaturation is lower and the interfaces become more stable due to the chemical effects. The subsequent annealing works as expected and can simulate Ostwald Ripening (see Figure 5-7). The last chapter showed how both processes (irradiation and annealing) can be modelled using phase field methods.

To simulate the mixing profiles, however, the values D_B and D_φ and ϵ of Equation (88) must be determined. The only method to do this is to compare the Si-NC from the simulation with the experimental results from Figure Figure 5-1, analogous to how the correction factor was determined. This chapter first shows how to determine the sizes of the NCs from the continuous function c. Then the missing parameters are determined and finally mixed profiles are predicted. These can then be used for the nanopillar simulation in Chapter 6.

Determination of NC Sizes of Annealed SiO_x

In order to compare the results of the simulation with the experiment and to determine the parameters from Equation (88), it must first be defined how the size of the NC is calculated from the 3D field. In the case of configurations from KMC simulations, the morphology was quantified by counting the volumes of the lattice sites of a domain and calculating the radius of a corresponding sphere with the same volume. The phase field approach is treated similarly. The numerical voxels have a volume of $(0.1\ \text{nm})^3$ and are converted in the same way into the volume of a sphere. Voxels with a value above 0 are counted as Si volume and lower than 0 as SiO_2 volume. However, the method in Chapter 4.3.4 did not consider NCs that came into contact with the interface. Technically, these will be part of the upper or lower Si block and will not be considered as NCs. Compared to EFTEM images, this would result in an error. In the case of KMC simulations, the interface reconstructed so quickly that this could be neglected (see Figure 4-24). In the case of the phase field, the reconstruction is not so fast, which is mostly due to the neglect of the asymmetric diffusion of Si and SiO_2. However, this must be taken into account when counting NCs and measuring their sizes. Therefore, the upper and lower Si layers from the simulation cell are converted to SiO_2 before the NCs are counted. This means that the Si bulk is removed voxel by voxel from above until the denuded zone begins. Figure 5-9 shows an example of this. The denuted zones of the profile are at 31 nm depth and 36 nm depth. NCs, even if they come into contact with the interface, are counted as NCs as long as they are between the two denuted zones.

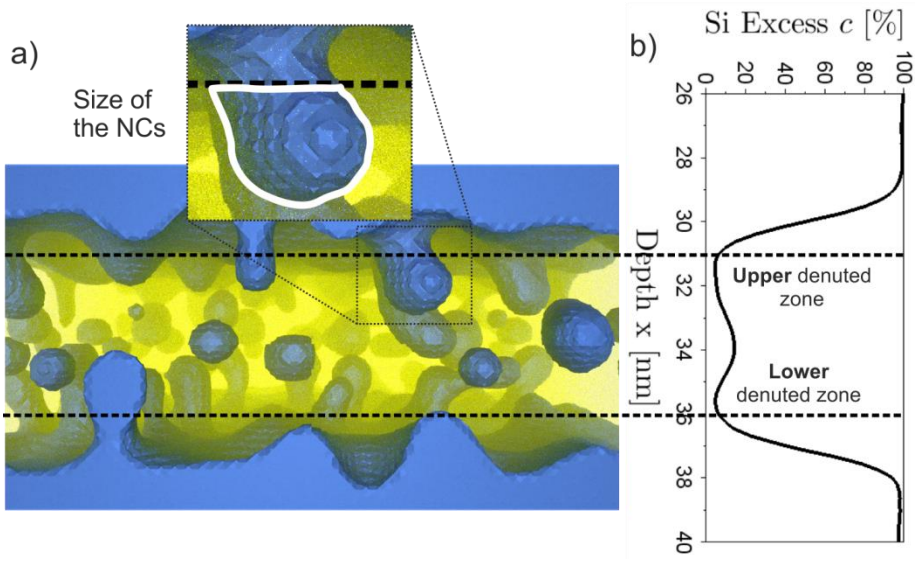

Figure 5-9: Determination of the NC sizes from the results of the phase field model. Before the size of an NC is calculated, it must be cut off from the Si mass as shown in a). The black lines show the position of the denuded zones at both interfaces

according to the Si excess profile after irradiation in b). The Si excess profile was calculated by BCA simulations with TRIDYN using 60 keV Si^+ ions for a fluence of $0.85 \cdot 10^{16}$ ions/cm^2. For the calculation with Equation (89) a start configuration as shown in Figure 5-8 was used.

Determination of Parameters for the Phase Field Model

The ballistic diffucion coefficient D_B was determined using the Monte Carlo simulation results based on BCA. The Si excess profiles for the experimental parameters, shown in Figure 5-10 as dots, were calculated by TRIDYN [134], [135]. Using this data, Equation (9) was fitted by least squares optimization of the parameter D_B. The region of optimization interest was the position of the SiO_2 layer for the complete irradiation time until a fluence of $2.6 \cdot 10^{16}$ cm^{-2} was reached. The results for the treated system are shown in Figure 5-10 as bold lines. The interesting region inside the SiO_2 layer is well reproduced by the fit of Equation (9).

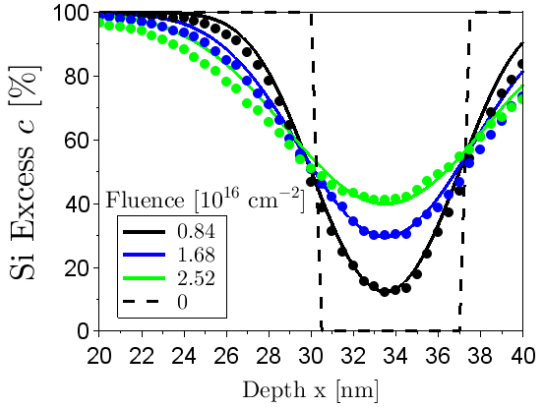

Figure 5-10: Si excess profiles of the $Si/SiO_2/Si$ stack during irradiation by 60 keV Si^+ ions with increasing fluence. The pure BCA results of the TRIDYN calculation (BCA) are shown as points and corresponding fits of Equation (14) as bold lines. The ballistic diffusion coefficient was D_B =0.0036 nm^{2}s^{-1}.

To determine the value for ϵ, it is necessary to consider Equation (92). The interface width l_{int} and the critical radius r_{crit} of the nuclei, which are linearly dependent on ϵ, what results in

$$\epsilon = \frac{l_{int}}{2\sqrt{2}\tanh^{-1}(0.9)} = \frac{r_{crit}}{6}. \tag{93}$$

By narrowing the critical radius to be between 0.35 nm and 0.45 nm, the upper and lower limits for ϵ result in 0.06 nm and 0.07 nm, respectively.

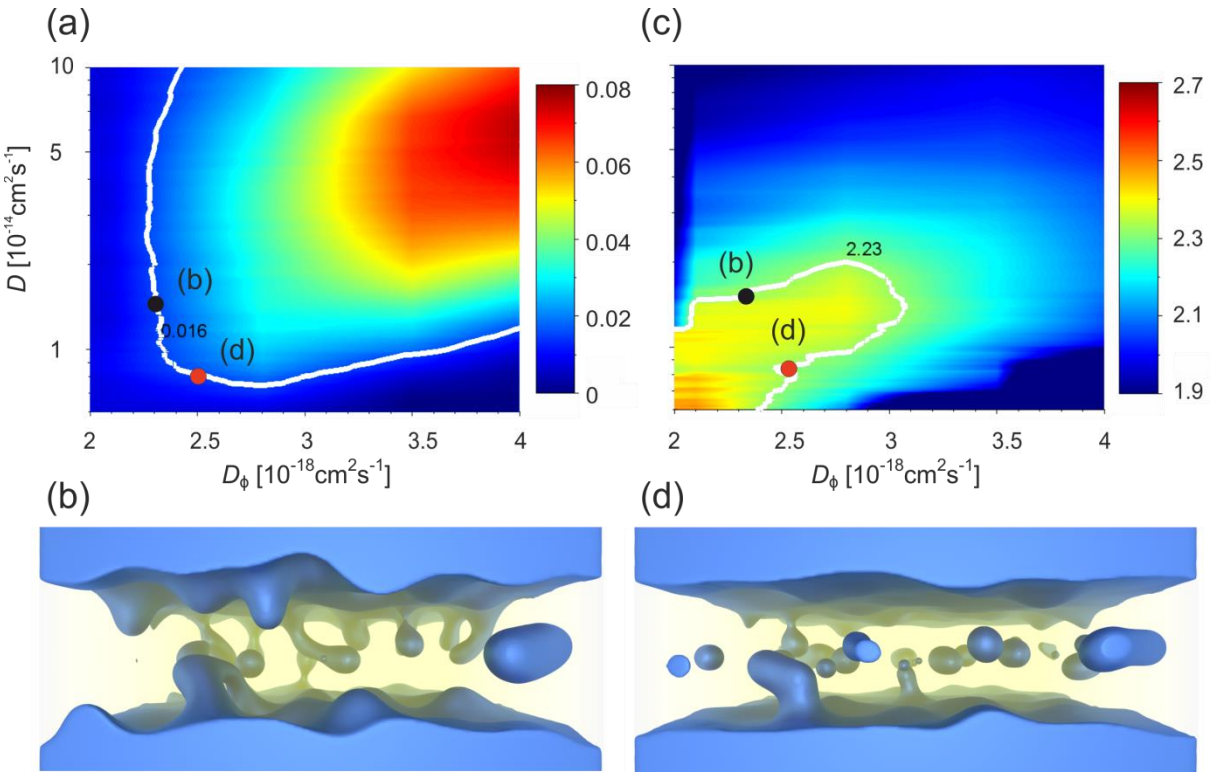

Figure 5-11: Areal density (a) and the mean diameter (b) of the Si-NCs in the Si(30nm)/SiO_2(7nm)/Si stack after irradiation with 60 keV Si^+ ions for a fluence of $1.7 \cdot 10^{16}$ ions/cm^2 and subsequent annealing. The values are shown as a colormap over the diffusion coefficient of the thermal spike model (D_φ) and of the Si atoms in the SiO_2 (D). The results were obtained with unimodal start configurations (r=0.6nm) and calculations by Equation (89). The distributions were performed according to Si excess profiles calculated by equation (88) with an eps of 0.6 and the nucleation algorithm described in Chapter 5.2.2. The white isolines show the corresponding experimental results for the areal density (a) and the mean diameter (b) of the Si-NCs. The red and black dots show 2 combinations of D_φ and D, where the simulation results for areal density and mean diameter correspond to the experimental results. The 3D visualization of a 25 nm thick lamella of simulation results based on the parameter setting of the black and red dot is shown in (b) and (d), respectively.

The simulated and experimental values for NC size and density are compared in Figure 5-11. The NC size (a) and density (b) results are visualized as a color map and the experimental results are implemented as white isolines. There are two combinations that lead to the same values as in the experiment. The main difference between the two solutions is the occurrence of a denuded zone. The solution indicated by the red dot (Figure 5-11 (d)) has a well defined denuded zone as it occurs in experiments, while the solution indicated by the black dot (Figure 5-11 (c)) does not. Thus the combination of the red dot can be used as model parameters for D & D_φ. These are summarized in Table 5.

Results and Discussion

The phase field model can simulate the irradiation including the influence of thermal spikes (Chapter 5.2.1) and the subsequent thermal annealing (Chapter 5.2.2). The basic processes (Ostwald Ripening in Chapter 5.2.2 and spinodal decomposition in Chapter 4.3.5) are intrinistic properties of the model, the parameters were derived from expermental findings and the formation of NCs in the SiO_2 layer can be reproduced well (Figure 5-13). The results of the correction factor in Figure 5-5 showed a strong linear increase of α with fluence. This was attributed to a nonlinear interaction between the

ballistic mixing and the chemical reconstruction. The model of the influence of thermal spikes by Equation (88) and Equation (89) leads to the parameters in Table 5.

Table 5: The parameters of the model in this chapter for Equation (88) and Equation (89).

Irradiation parameters				Annealing parameters		
Fluence [10^{15}cm^{-2}]	D_B [10^{-17}cm^{2}s^{-1}]	D_ϕ [10^{-18} cm^{2}s^{-1}]	ϵ [nm]	D [10^{-15}cm^{2}s^{-1}]	Time [s]	T [°C]
0.85	3.6	2.7	0.06	30	60	1050
1.7		2.5		8	30	
2.6		2.8		9	30	

These results show some uncertainty, but have no significant dependence on fluence. This confirms the approach by a linear combination of the diffusion Equation (9) and the Cahn Hilliard Equation (87) to a uniform governing formula in Equation (88). This leads to a trustful results for the Si excess profiles during irradiation, what finally can be used to simulate the NC formation in nanopillars.

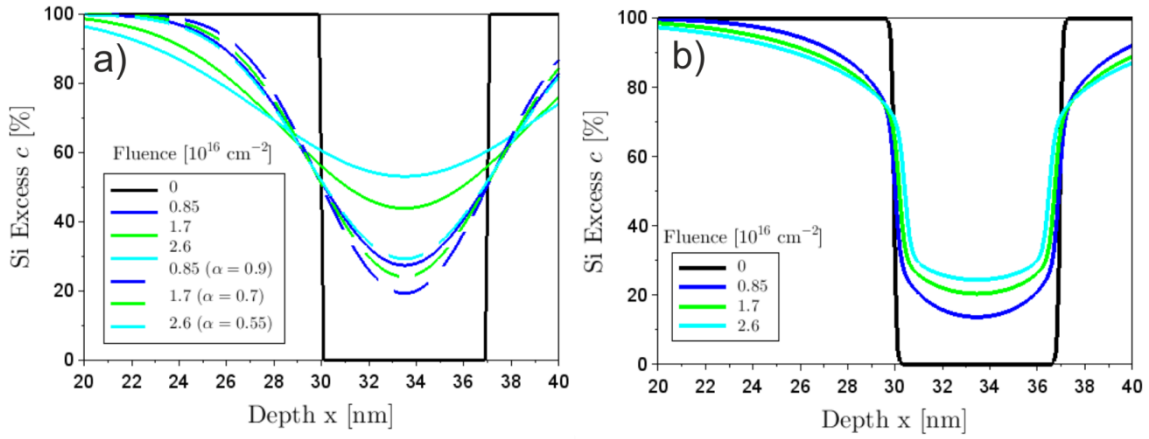

Figure 5-12: Simulated Si excess profiles during irradiation of a Si/SiO_2/Si stack with 60 keV Si^+ ions for the indicated fluences obtained by BCA calculations (bold lines in a), including the correction factor alpha (dashed lines in a) and by the phase field model (b). The BCA calculations show Equation (14) fit to TRIDYN results. The results in b) were calculated using the Equation (88) with an eps of 0.6 nm, a D_φ of $2.7 \cdot 10^{-18}$ cm^{2}s^{-1} (see Table 5) and a D_φ of $3.6 \cdot 10^{-17}$ cm^{2}s^{-1} (obtained from BCA calculations, see Figure 5-10).

Figure 5-12 a) shows the mixed profiles simulated using the BCA (Chapter 3.2.2) and its corrected version by the alpha (Chapter 5.1.2) in (a). The profile simulated with the phase field model (Equation (88)) is shown in (b). The pure BCA results are too far above supersaturation for nucleation to be possible. But also the other supersaturations show surprisingly high values (20-30 %) for the fluence of $2.6 \cdot 10^{16}$ ions/cm^2. However, this fluence leads to formed isolated NCs and confirms the dominance of nucleation as the phase separation mechanism (Figure 5-13). This is attributed to the interface, which rapidly absorbs a large part of the Si excess in the early stages through spinodal decomposition. The remaining excess in the middle region is then low enough to nucleate Si domains.

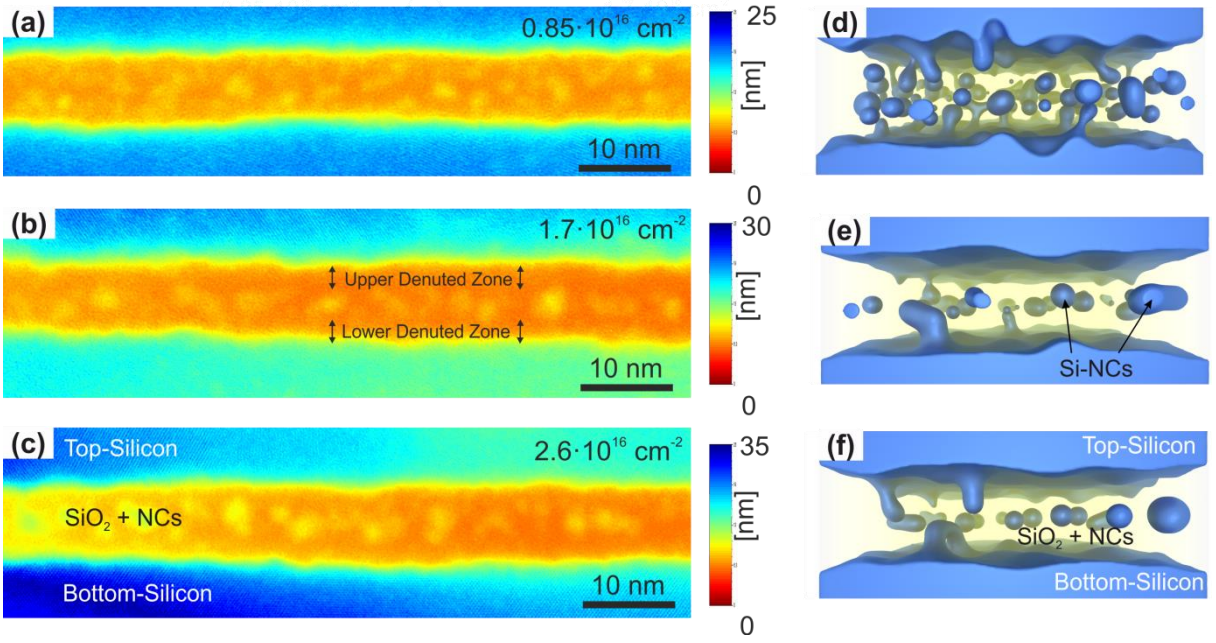

Figure 5-13: Comparison of the experimental (a-c) and simulated (d-f) cross-sectional recording of a Si/SiO_2/Si stack after irradiation with 60 keV Si^+ ions for the indicated fluences and subsequent annealing at 1050°C for 30s (a-b) and 60s (c). The experimental images were obtained by EFTEM analysis (see chapter 5.1.1) with a lamella thickness of 20-30nm and the simulated images by Equation (89) with a lamella thickness of 25nm.

The final question relates to how the diffusion coefficients need to be interpreted. The ballistic diffusion coefficient represents the mobility induced by ballistic collisions. This has been discussed in Chapter 3.2.1. The chemical diffusion coefficient is basically a physical parameter, since it describes the mobility caused by thermal spikes. However, it is assumed that the thermal spikes correspond to a global heat bath and the term of Equation (87) therefore does not represent local mobility within the thermal spike. The thermal diffusion coefficient D (Equation (89)) is also an interesting physical quantity and represents a kind of estimate of an average diffusion coefficient. The obtained values of Table 1 and Table 2 are in the range of $10^{-18}\,\mathrm{cm}^2/\mathrm{s}$ for SiO_2 and $10^{-10}\,\mathrm{cm}^2/\mathrm{s}$ for Si at a temperature f 1200K, while the values in Table 5 give a range of $10^{-14}\,\mathrm{cm}^2/\mathrm{s}$.

In summary, the model purposed in Chapter 5.2.1 and 5.2.2 parametrized using the obtained data from EFTEM experiments shown in Chapter 5.1.1. The simulations lead to the following conclusions

- The model can be parametrized successfully for each experimental fluence.
- The profiles in Figure 5-12 b) confirm the corrected BCA/KMC results in Figure 5-12 a). The supersaturation for a fluence of $2.6 \cdot 10^{16}\,\mathrm{ions/cm}^2$ in the center of SiO_2 is 33 % in a) and 28 % in b). Although the shape of the Si excess profile is different, the overall strength of mixing is similar to the corrected Si excess profiles.
- The obtained global bath diffusion coefficient for the thermal spikes is mostly the same for every sample.

6 Using Self-Organization to Form a Single NCs in a Nanopillar

Chapter 2.2 showed how modern manufacturing processes are not able to form the tiny NCs required for the scheme in Figure 2-3. Chapter 2.3 showed the reasons and challenges for the approach presented in this thesis. Self-organization was presented in Chapter 2.4 as a very promising option for the realization of the nanopillar system and its potential is now examined in this chapter. Figure 2-7 showed how boundary conditions can influence the reaction pathway of a metastable mixture and how nanoconfinment can be realized (see Chapter 2.4.4). In addition to the two Si/SiO_2 interfaces, the nanopillar has a mantle surface to the vacuum, which also influences the reaction pathway.

Chapter 4.3.1 showed the phase diagram and, building on it, investigated nucleation (see Chapter 4.3.2), NC growth (see Chapter 4.3.3 and 4.3.4) and spinodal decomposition (see Chapter 4.3.5) as a function of time and supersaturation for the Si-SiO_2 system. The influences of the individual processes on the reaction pathway were discussed and the interplay in a mixed Si/SiO_2 interface was investigated (see Chapter 4.3.6). This resulted in a complex reaction pathway influenced by all treated processes in Chapter 4.3. These influences are now being investigated with regard to the nanopillar. In order to give a first overview for future work on the dependencies of NC formation in the nanopillar, this chapter examines the reaction pathways for different starting configurations and boundary conditions, e.g. the Si excess profiles, the annealing temperature and the diameter of the nanopillar. The aim is to identify what is controllable.

Overview

The success of an initial configuration (geometry and Si excess profile) must be evaluated with regard to the reliability reproducing a suitable single NC configuration for the SET. To illustrate the influences, this chapter examines the dependence of the NC formation on the starting configuration in Chapter 6.2.1, on annealing temperature in Chapter 6.2.2 and on the nanopillars diameter in Chapter 6.2.3. The nanopillar must also be implemented in the KMC model presented in Chapter 4. The process of etching the nanopillar has to be discussed and a corresponding approximation to the initial configuration on the KMC lattice has to be made. This is done in Chapter 6.1.

Calculations of this Chapter

The calculations in this chapter are performed using the Si excess profiles shown in Figure 5-12. The fluence is varied up to $2.6 \cdot 10^{16}\ \mathrm{ions/cm^2}$ under irradiation with 60 keV Si^+ ions. The Si/SiO_2/Si layer stack consists of Top-Si of 30nm and a SiO_2 layer with a thickness of 7nm. The KMC model of Chapter 4.1 was modified to save computing time. The exact modification can be found in Appendix A.

6.1 Modeling the Fabrication Process of a Single Si-NC in a Nanopillar

The modelling of the SiO_x system by a lattice KMC method was done by discretization of the total volume in subvolumes on the FCC lattice (see Chapter 4.1.1). To model a nanopillar, the basic components are still Si and SiO_2, but during annealing, the diffusion pathway of the Si monomers in SiO_2 can come into contact with the vacuum. This must be considered and implemented in the KMC model. Another problem are observed artifacts caused by the lattice structure which need to be discussed (for more details see [321]) and the modeling adapted by appropriate assumptions.

From Planar $Si/SiO_2/Si$ Stacks to Standalone Stacked Nanopillars

After RCA cleaning, the SiO_2 layer is produced by dry thermal oxidation of the Si substrate. The top Si layer is formed by LPCVD deposition of amourphous Si and this $Si/SiO_2/Si$ stack is then irradiated with Si^+ ions. Direct electron beam writing (EBDW) was performed at 50 kV, followed by dry plasma etching to produce the nanopillars. The subsequent etching of nanopillars then exposes the SiO_x layer to the etching process and subsequently to vacuum. Both steps manipulate the surface of the nanopillar and could even have an influence on the composition of the SiO_x. This and the exposure of the surface to vacuum require appropriate assumptions.

Figure 6-1 schematically shows how the nanopillar is manufactured. The $Si/SiO_2/Si$ stack was irradiated as described in Chapters 3 and 5, the nanopillar was etched out and is present as a single standing object. The surface of the nanopillar is first defined by the etching process. It is known that when silicon is exposed to air, the first layers (~2nm) immediately oxidize and form pure SiO_2, regardless of temperature. To the best of the author's knowledge, this can also be assumed for a SiO_x mixture, so that the area near the surface is never supersaturated prior to heat treatment and any surface structure immediately changes to SiO_2. It is assumed that the configuration of the SiO_x inside the nanopillar is not influenced by any of these processes. The Si excess profile over the depth of an irradiated $Si/SiO_2/Si$ stack is a very well controllable property (see Chapter 3 and Chapter 5) and the mixed profiles obtained in Chapter 5 in Figure 5-12 are used for the calculations in this chapter.

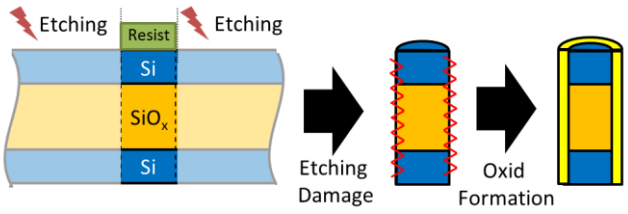

Figure 6-1: Schematically shown fabrication steps of the nanopillar in the framework of the IONS4SET project […].The nanopillars are etched out of the irradiated $Si/SiO_2/Si$ stack and experience short oxidation at RT, which forms a thin layer of SiO_2 on the surface.

However, a shrinkage of the SiO_2 thickness was observed in the framework of the IONS4SET project and attributed to reactive ion etching. It can be assumed that this also has a significant influence on the Si excess profile in the nanopillar. But it was not sufficiently investigated during the IONS4SET project to be considered in this work and the study of this influence is definitely out of scope of this work. The aim of this work is to control of the self-organization of the NCs in the nanopillar. If one day the influences of the etching process can be identified, such as a possible change of the initial configuration (e.g. amount of Si excess) or the system parameters (e.g. diffusion coefficients), an

intermediate modeling step can be initiated at this point. But to study mainly the self-organization, these influences can be neglected.

Modeling the Vacuum Surface as a Reflecting Interface

The reaction pathway of the SiO_x mixture is limited to the nanovolume in the nanopillar by the two Si/SiO_2 interfaces and the nanopillar surface. To model the reaction pathway of this system, it is necessary to describe the reflective effect of the surface to vaccum. One possible solution would be to assign a subvolume "vacuum" in the KMC lattice and to define interactions between Si, SiO_2 and vacuum (like J^{AA}, J^{BB} and J^{AB} for the A- and B-components, see chapter 4.1.1).

However, a simpler approach is employed to avoid complicated extension of the KMC model. Looking at a cylindrical layer of pure SiO_2 (the mantle surface of the nanopillar) the reflection can be modeled by simple permission of Kawasaki exchanges, i.e. no diffusion processes can take place. As long as the environment is free of impurities (including oxygen), such an artificial reflective boundary leads to the same reaction pathways of SiO_x as the presence of vacuum. Figure 6-2 shows how the thermal treatment of the nanopillar is finally modeled by KMC. The basic method is applied as described in chapter 4.1. It is assumed that the reflection takes place at the formed pure SiO_2 surface (~2nm) by prohibiting Kawasaki exchange at the nominal radius of the nanopillar. The implementation scheme is shown in Figure 6-2 a). If one site of the Kawasaki pair is outside the nominal radius, the KMC step is aborted and the next Kawasaki pair is selected. This allows neglecting subvolumes of vacuum.

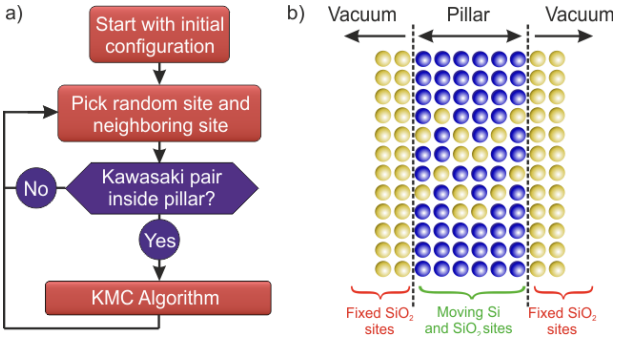

Figure 6-2: Scheme of the KMC program code used for calculating the nanopillar configuration in this chapter. The modification of the KMC mehtod of chapter 4.1 (a) and the placement of the nanopillar in the simulation cell (b)

The Placement of the Nanopillar in the KMC Simulation Cell

The planar $Si/SiO_2/Si$ stack in Chapter 5 was placed with the SiO_2 layer parallel to the (1 0 0) surface in the KMC lattice, since alignment did not play a significant role in such a large system (see [321] for further details). In the case of self-organized chains of NCs, however, previous studies showed significant differences depending on the orientation of the system in the KMC lattice [321]. Especially at lower temperatures, the anisotropy of the surface tension influences the reaction pathway of the system. This is attributed to different surface energies. The (1 1 1) surface in the FCC lattice has the lowest surface energy and is therefore preferred during the reaction pathway. In the case of a nanopillar, artifacts are observed aswell for the alignment of the SiO_2 layer parallel to the energy-unfavorable (1 0 0) surface.

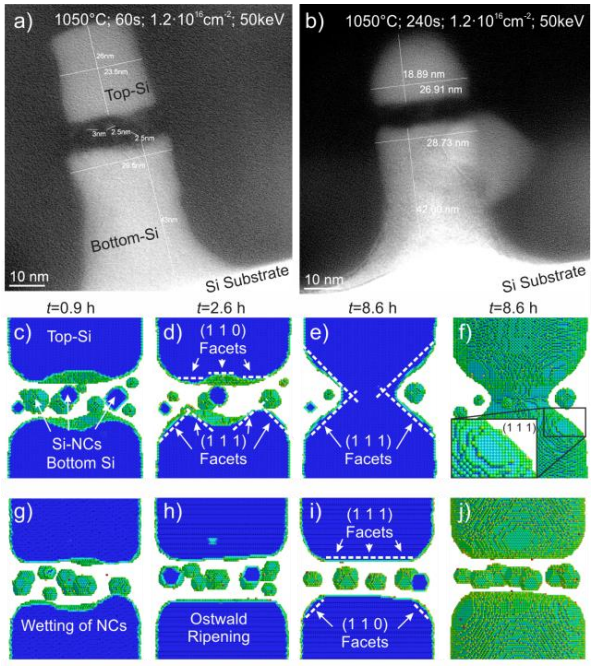

Figure 6-3: EFTEM images of nanopillars after irradiation by 50 keV Si^+ ions for a fluence of $1.2 \cdot 10^{16}$ ions/cm^2 and subsequent annealing at 1050°C for 60 s (a) and 240s (b). Source: […]. Corresponding simulations by KMC with placement of the SiO_2 layer in parallel to the (1 0 0)-surface (c-f) and the (1 1 1) surface (g-j) in the FCC lattice of the KMC simulation cell.

Figure 6-3 shows the comparison between experiment and simulation of a nanopillar for different orientations in the simulation cell. The experimental results are shown in (a) and (b) as EFTEM analysis images of two different experimental examples. The nanopillars were etched from an irradiated Si/SiO_2/Si stack according to Figure 6-1 and tempered at 1050°C for 60s (a) and 240s (b). The ion beam had an energy of 50 keV and was used for a fluence of $1.2 \cdot 10^{16}$ cm^{-2}. The samples were experimentally prepared and analyzed according to the procedure in Chapter 5. If the nanopillar is placed in the simulation cell with the (1 0 0) surface parallel to the SiO_2 layer, the simulation is shown under (c)-(f). The energetically most favourable surface is the (1 1 1) surface and as can be seen in (d), the system prefers this orientation and forms (1 1 1) facets. The continuous growth of these facets finally gives the nanopillar a bridge in the center, which is mainly attributed to an energetic prioritization of the (1 1 1) surfaces.

To the best of the author's knowledge, however, Si facets were never observed at a Si/SiO_2 interface, so that this faceting and bridging is a pure artifact of lattice approximation. It is attributed to an overestimation of the Si/SiO_2 interface energy. To correct this, a different orientation of the nanopillar is chosen. Results for the case that the (1 1 1) surface is placed parallel to the SiO_2 layer are shown under (g)-(j). In this case, the low energy of the (1 1 1) surface will contribute to the stabilization of the Si/SiO_2 interface. This placement leads to the most corresponding simulation results and is selected for each nanopillar in this chapter.

6.2 Reliability of the Self-Organization Process

The manufacture of transistors for use in a computing unit must meet high reliability requirements. Each transistor must behave in the same way to build the intended logic, but SETs are very sensitive to changes in geometry [60], [61]. Figure 6-4 shows a possible configuration that can occur and need to be reliably controlled by the available manufacturing parameters. The existence of multiple NCs

(a) can lead to interactions during self-organization and during operation (co-tunnelling) (see [85] for further details). Asymmetric tunnel distances to the electrodes (b) lead to high performance losses. The interaction between the NC and the gate is influenced by the distance [61]. A decentralized position (c) can disturb this. In principle, none of these circumstances will be an obstacle for the SET as long as it is possible to reproduce it reliably. This means that each nanopillar must contain the same configuration of NCs, the distances to both electrodes must be the same, and the size of each NC must be the same. These uncertainties in the self-organization must be as low as possible, what requires, that every reaction pathway of the system needs to run as close as possible to the optimal intermediate state. Earlier studies showed the formation of individual NCs in an array after point-like implantations (see Chapter 6.3 in ref. [90]). Depending on temperature and supersaturation, the non-equilibrium mixture formed reliably and uniformly one single NC, always with the same size and the same position in each reaction pathway.

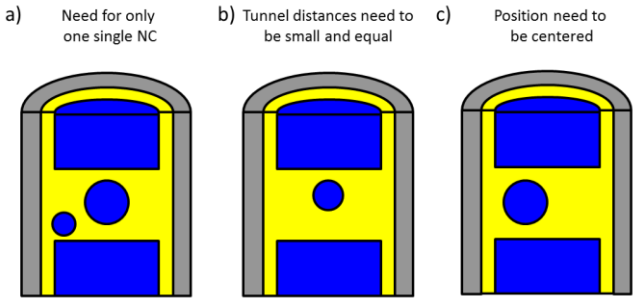

Figure 6-4: Schematically shown examples of NC formation in the nanopillar, which disturb the functionality of the SET.

Before optimizing the tunnel distances or the NC size, however, it is necessary to determine which of the possible intermediate states of the reaction pathway can be reliably reproduced. This chapter will mainly focus on the presence of one single NC and will introduce Single NC Probability. This makes it possible to identify the intermediate states with the highest probability of only one single NC.

Single NC Probability ϕ_S and its Maximization

Even if a simulation leads to a successful formation of a single Si-NC in the nanopillar, which is well positioned in the center with equal tunnel distances, it is only one specific reaction pathway. In an array of thousands of nanopillars, each one follows a different reaction pathway. But each of them should form the same configuration after the same time, i.e. a single NC. This reliability can be defined by the single NC percentage probability

$$\phi_{\mathrm{S}}(t) = \frac{100}{N_{\mathrm{C}}} \sum_{i=1}^{N_{\mathrm{C}}} \begin{cases} 1, & n_{\mathrm{NC}}^{i}(t) = 1 \\ 0, & n_{\mathrm{NC}}^{i}(t) \neq 1 \end{cases} \tag{94}$$

with N_{C} as the number of reaction pathways performed with the same start configuration and $n_{\mathrm{NC}}^{i}(t)$ as the number of NCs in the nanopillar of the reaction pathway i at time t. In a start configuration in which each reaction pathway passes through a state with only one NC at a specific time t, the single NC probability ϕ_{S} is 100%. This is the most important reqiurement for manufacturing in industry, e.g. application as CPUs.

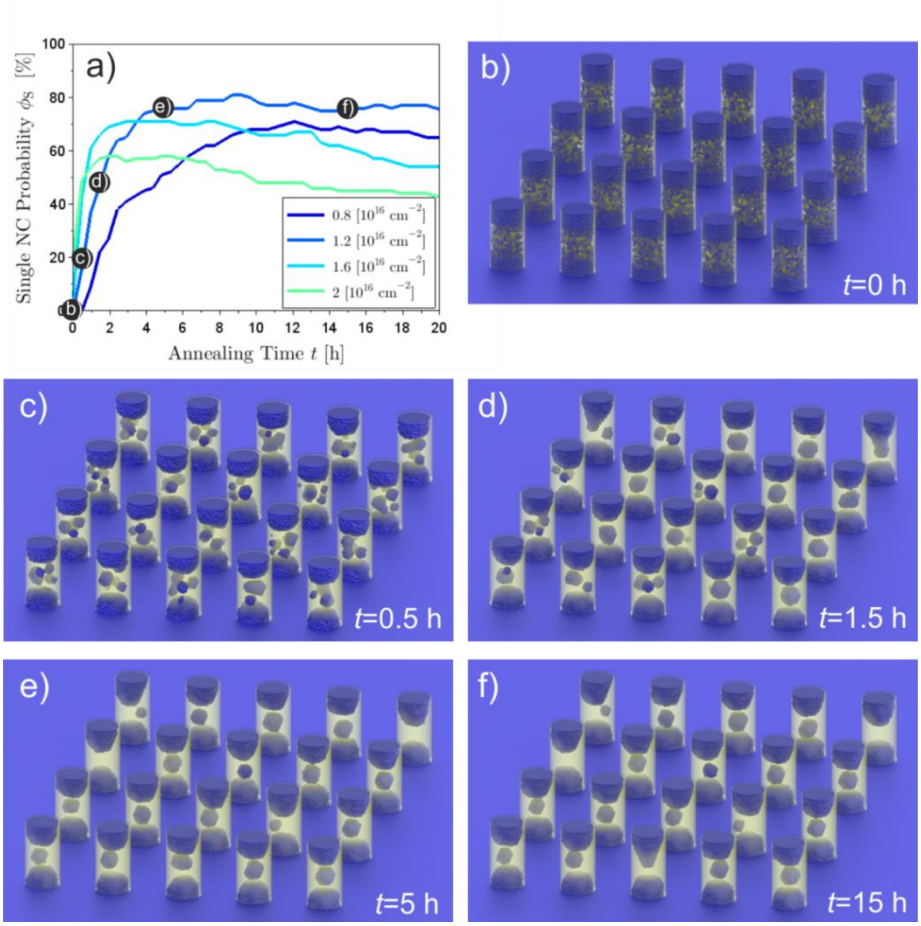

Figure 6-5: Simulation results of annealing a nanopillar after irradiation by 50 keV Si^+ ions for different fluences. In a) the single NC probability is shown (Equation (94)) for different fluences and b)-f) shows an array of 20 different reaction pathways of this system. The ground is only schematically introduced, every reaction pathway was performed in an isolated simulation cell.

The first aim is to maximize the single NC probability ϕ_S. Figure 6-5 a) shows the single NC probability $\phi_S(t)$ for the optimized system parameters. A total of 100 calculations were performed at an annealing temperature of 1373 K and a nanopillar diameter of 6nm. This was done for starting configurations made by irradiation with different fluences from $0.8 \cdot 10^{16}$ to $2 \cdot 10^{16}\ \mathrm{cm}^{-2}$. The maximum ϕ_S is reached in a nanopillar after irradiation with a fluence of $1.2 \cdot 10^{16}\ \mathrm{cm}^{-2}$ and annealing time of 10 hours. In this case, Figure 6-5 shows a set of 20 nanopillars for 4 different annealing times. Figure b) shows the initial configuration. The occupation of the Si sites is randomly distributed according to the Si excess profiles in Figure 5-12. The aforementioned influence of the reactive ion etching might introduce some changes at this step, but they are neglected. Figure 6-5 c) to f) shows the annealing times according to the points in a). After 0.5 h, the early annealing stage leads to the formation of multiple NCs in the SiO_2 layer. These then tend to touch each other and unite as shown under d). In some cases there is still an arrangement of multiple NCs. After further annealing, most nanopillars have one very similarly shaped, positioned and dimensioned NC in the middle of the SiO_2 layer. These are optimal configurations for use in a SET. Figure e) and f) show the long-term development and how stable the individual NCs are. The stability is mainly attributed to the low diffusion coefficient of Si in SiO_2.

Effects which are Disturbing the Single NC Probability $\phi_S(t)$

The greatest success would be a single NC probability $\phi_S(t)$ of 100%, which would make it possible to further optimize the distances for tunneling and gate contact. However, this remains unattainable as it still happens that NCs are either too small and evaporate too early or touch the surface and disappear through wetting. The question is how the reaction pathway can be influenced by the system parameters and why these specific parameters exert their influence. In order to limit the possibilities of the reaction pathway, the individual mechanisms and processes must be understood.

- **Nucleation** occurs in different regions of the phase diagram depending on the temperature and the degree of supersaturation (see Figure 4-13). Chapters 4.3.1 and 4.3.2 examined these areas of phase separation and the conditions for nucleation. This process brings much randomness to the reaction pathway. It is not only the moment of nucleation random, but also the location. This makes it very difficult to control the system to reproduce a particular configuration. One control option is temperature, as nucleation is highly dependent on the critical radius that increases with temperature (see Chapter 4.3.2). This makes it possible to define the minimum size of a newly formed core and thus influence the reaction pathway.
- **The spinodal decomposition** takes place in areas of the phase diagram with a very high supersaturation (see Chapter 4.3.5). There is no strict limit between nucleation and spinodal decomposition and especially in an inhomogeneous configuration the influence of properties such as the amplification factor (Figure Figure 4-23 in Chapter 4.3.5) is unknown. The separation in the region of the interface will mainly occur by spinodal decomposition. However, this separation mechanism is less random, since the spinodal decomposition follows the deterministic law of the Cahn-Hillards equation (see Chapter 4.3.5). In addition, it is influenced on larger scales (see amplification factor, Equation (83)).
- **Ostwald Ripening** governs the stage after nucleation when all supersaturation is exhausted and lets the NC compete (see Chapter 4.3.4). It is possible to describe Ostwald Ripening with deterministic differential equations, which makes it very controllable. But anyway, for this it is necessary to control the nucleation first, which is the most random process.

Depending on the selected parameters, each individual process behaves differently or does not occur at all. It must be identified for which parameter range, which process dominates the reaction pathway and how the formation of a single NC can be controlled. Chapter 6.2.1 examines the reaction pathways of nanopillars with different starting configurations. The variation of the fluence leads to different supersaturations and thus to different points of the system in the phase diagram. This leads to a different ratio of nucleation and spinodal decomposition during annealing. Another possibility to change the position of the system in the phase diagram is the variation of the temperature. This influences the reaction pathway by the same mechanism (ratio of nucleation and spinodal decomposition) and is discussed in Chapter 6.2.2. Finally, the variation of the SiO_x volume is investigated in Chapter 6.2.3, where the reaction pathways in nanopillars with different diameters are simulated.

6.2.1 Dependence on Fluence

The increase in fluence mainly leads to a higher supersaturation of the SiO_2 layer. This changes the state of the mixture in the phase diagram (see Chapter 4.3.1) and influences the separation process.

At a given temperature, the SiO_x mixture separates at low supersaturation by nucleation and tends to spinodal decomposition at higher supersaturation. However, the separation mechanism can rather be seen as a tendency to nucleation or spinodal decomposition. Using low fluences for irradiation, a configuration of multiple NCs is to be expected during annealing, which then performs Ostwald Ripening. High fluences in turn lead to higher supersaturations and a stronger spinodal decomposition mechanism during the annealing, especially in the region near the interfaces. To determine this influence, this chapter examines the reliability of the single NC formation for different starting configurations, e.q. supersaturation by variation of irradiation fluence.

Annealing an Array of Nanopillars with Different IBM

Figure 6-6 shows the simulation of the nanopillars annealing after irradiation with different fluences from $0.6 \cdot 10^{16}\ \mathrm{cm}^{-2}$ (Figure a)-c)) to $2.2 \cdot 10^{16}\ \mathrm{cm}^{-2}$ (Figure m) to o))). The annealing temperature was 1373K and the diameter of the nanopillar was 6 nm. After irradiation with a fluence of $0.6 \cdot 10^{16}\ \mathrm{cm}^{-2}$, the Si excess in the center reaches 10% and the subsequent annealing led to the formation of a large number of small NCs. These are not large enough to fuse, as shown in Figure 6-6. Rather, a multiple NC configuration remains and get absorbed by the two Si/SiO_2 interfaces during Ostwald ripening. Using higher fluences from $10^{16}\ \mathrm{cm}^{-2}$ to $1.4 \cdot 10^{16}\ \mathrm{cm}^{-2}$, the Si excess in the center of the SiO_2 reaches 15% and 18%, respectively. These supersaturations also lead to the formation of multiple NCs during annealing, but in most cases they merge into a one large NC during later annealing stages. By further increasing the fluence to $1.8 \cdot 10^{16}\ \mathrm{cm}^{-2}$ and $2.2 \cdot 10^{16}\ \mathrm{cm}^{-2}$, the supersaturation reaches an excess of 20 and 22%. As shown in Chapter 4.3.5, separation of a mixture in this supersaturation regime is mostly dominated by spinodal decomposition. Although in some cases small NCs can be seen, most of the pillars go through a rather wetting process. The NCs tend to touch the interfaces and disappear through wetting. In some cases, the NCs touch both interfaces and "bridges" are formed as shown in Figure n) and o).

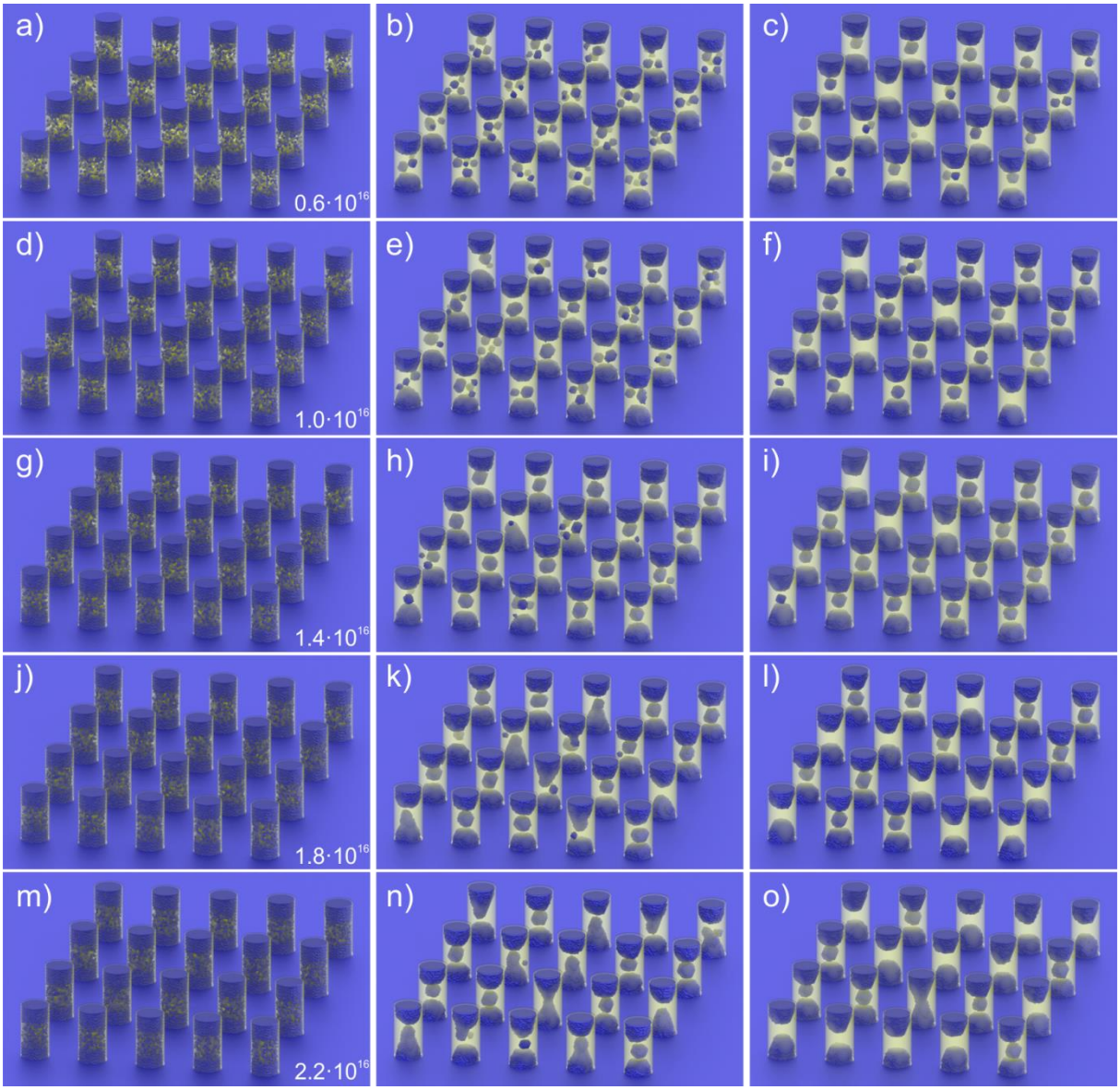

Figure 6-6: Simulation results of annealing a nanopillar after irradiation by 50 keV Si^+ ions with different fluences. Arrays of 20 different reaction pathways are shown for 5 nanopillars after irradiation with 5 different fluences, $0.6 \cdot 10^{16}$ ions/cm^2 In (a-c), 10^{16} ions/cm^2 in (d-f), $1.4 \cdot 10^{16}$ ions/cm^2 in (g-i), $1.8 \cdot 10^{16}$ ions/cm^2 in (j-l) and $2.6 \cdot 10^{16}$ ions/cm^2 in (m-o). The ground is only schematically introduced, every reaction pathway was performed in an isolated simulation cell.

The Competition between Nucleation and Spinodal Decomposition

During annealing of a mixture with a Si excess of more than 20%, essentially spinodal decomposition takes place; below 10%, separation is dominated by nucleation (see Chapter 4.3.5). It follows that near the interface (50% Si excess) pure spinodal decomposition takes place and that in between there is a combination of nucleation and spinodal decomposition. Figure 6-7 shows schematically the structure in nanopillars during annealing for different supersaturations of the starting configurations. In a) it is shown what happens when the nanopillar is annealed after irradiation with a low fluence.

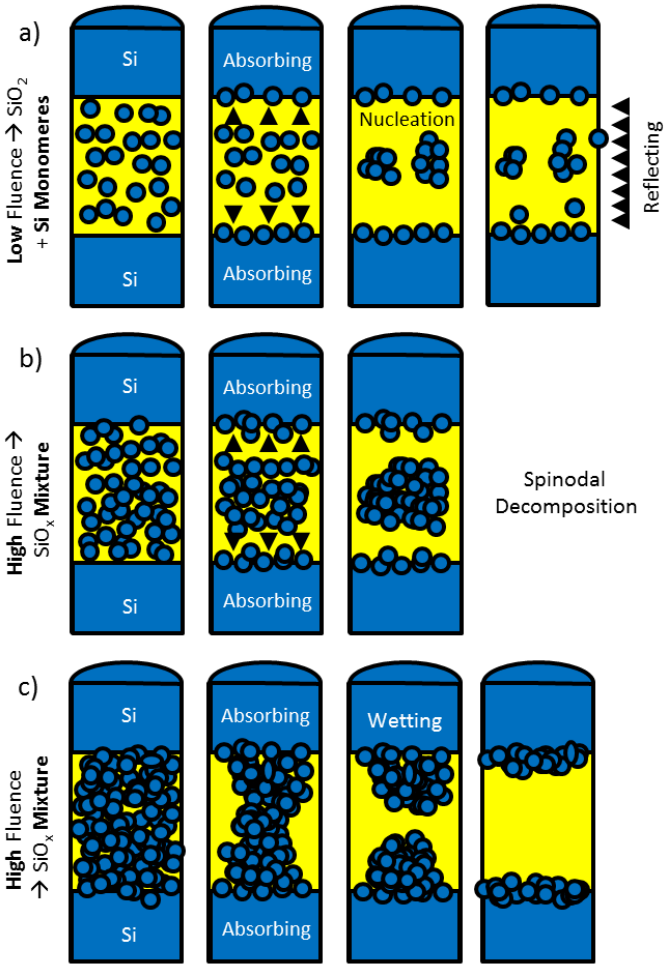

Figure 6-7: Schematically shown how the reaction pathways tend to perform for different ranges of supersaturaton. For low supersaturation in a) to high supersaturation in c).

The low supersaturation inside the SiO_2 leads to nucleation of NCs with a random size and position. The Ostwald Ripening interaction with the Si/SiO_2 interface causes the NCs to evaporate in the later annealing stage. The time frame with only one NC is smaller because (i) the *small* size of the NCs lead to rapid evaporation and (ii) the *similar* sizes of the NCs leads to simultaneous disappearance. Figure 6-5 a) shows how $\phi_S(t)$ is initially very low for a nanopillar irradiated with the lowest fluence ($0.8 \cdot 10^{16}$ cm^{-2}) and rises late compared to the others. In the initial stage most of these nanopillars have more than one NC and the moment when all but one evaporate takes longer. Furthermore, the position of the last NC is not well centered and very random. This makes the controlling of the reaction pathway for nanopillars irradiated with a low fluence very difficult.

An increasing fluence leads to a higher supersaturation (Figure 6-7 b) and thus to more influence of spinodal decomposition. Especially the interfaces with clearly higher supersaturation are affected and the configuration quickly forms the denuded zone. The remaining internal Si excess then merges into larger NCs (see Figure 6-6 e)-f)). The high Si excess leads to either (i) the formation of a single NC or (ii) to multiple NCs which then fuse together. Both of these causes the single NC probability $\phi_S(t)$ value to increase much faster than in case of lower supersaturations (Figure 6-5 a).

If the supersaturation is too high, as shown in Figure 6-7 c), the amplification factor $s(k)$ (see Chapter 4.3.5) might increase for the wavelenght of the SiO_2 layer. This leads to amplification of the present Si excess profile and simple reconstruction of the interfaces.

In order to achieve a high single NC probability $\phi_S(t)$ and control properties such as position and size, the mechanism of spinodal decomposition is most promising. It is much more determinable than nucleation. In the case of a reaction pathway that passes through a certain intermediate state, other reaction pathways will vary less because the randomness of nucleation contributes less. Figure 6-5 a) shows that the $\phi_S(t)$ for nanopillars irradiated with a fluence of $1.2 \cdot 10^{16}\ \mathrm{cm}^{-2}$ has a very high single NC probability $\phi_S(t)$, which is achieved after a much shorter annealing time than for the lower fluence.

In summary, this chapter showed that after irradiation with low fluences the subsequent annealing leads to the formation of a high number of small NCs. This formation is induced by nucleation and the nucleation has 2 random parameters: the position and time of nucleation of a new NC. The reaction pathway with more nucleation events is therefore more random. Higher irradiation fluences lead to less nucleation during the subsequent annealing and a more determined reaction pathway by spinodal decomposition. As shown in Chapter 4.3.5, waves in the composition profile are amplified by spinodal decomposition and there is a maximum amplification factor $s(k)$ for a certain wavelength (see Equation (83)). This wavelength depends on the temperature and the supersaturation, which leads to dewetting in nanopillars irradiated with very high fluences. The following conclusions can be drawn:

- The annealing of nanopillars after irradiation with high fluences makes the process more controllable and thus easier to optimize the probabilities for a single NC.
- A higher supersaturation also leads to a well centered position of the NCs and results in equal tunnel distances. This makes the process very suitable for SET production.

6.2.2 Dependance on Temperature

Every process is generally temperature dependent, but not every process changes in the same way with temperature. This can lead to some temperature ranges being dominated by other processes than others. The reaction pathway is determined by the formation and growth of Si domains (Si-NC or spinodal structures, see Chapter 4.3.2). The growth of Si-NCs requires a supply of supersaturation and a binding of the attached Si monomeres to the Si-NC. Both processes are temperature-dependent, but the diffusion decreases more with decreasing temperature than the bond strength. Figure 6-8 shows the Kawasaki exchange probability K_{if} (see Equation (46)) for diffusion on a surface and emission from the surface. The calculation was performed for configurations as shown in the subplots. These two Kawasaki exchanges have almost the same probability for high temperatures, while at lower temperatures the difference increases to a factor of 1000. This contributes to the difference in behaviour of the reaction pathway for high temperatures. In this chapter, the differences between the single NC probability $\phi_S(t)$ are investigated for different temperatures.

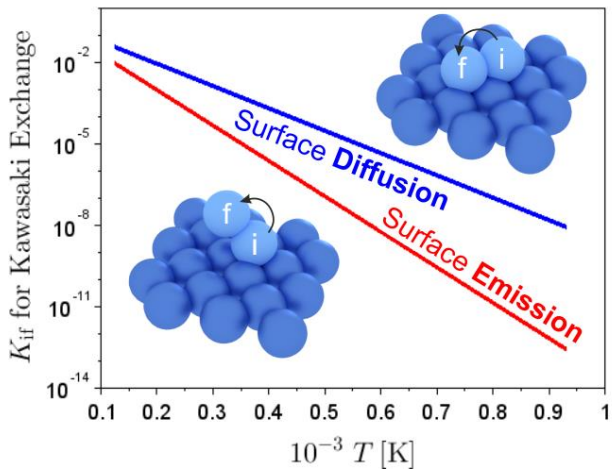

Figure 6-8: The exchange probability of Equation (46) for a surface diffusion and surface emission Kawasaki exchange over the inverse temperature.

Annealing an Array of Nanopillars with Different Temperatures

Figure 6-9 a) shows the single NC probability $\phi_S(t)$ of nanopillars for different temperatures from 1273K to 1873K. The irradiation fluence was $1.2 \cdot 10^{16}\ \mathrm{cm}^{-2}$ with an energy of 60 keV. The nanopillar diameter was 6nm, which at a temperature of 1373K gives the highest single NC probability $\phi_S(t)$ achieved in the simulation. Higher temperatures lead to a general acceleration of all processes and thus to faster evaporation of the NCs. At a temperature of 1873K, the NCs disappear after 2 minutes and the reaction pathway reaches a maximum single NC probability $\phi_S(t)$ of only 50%. Figure 6-9 l)-n) visualizes 20 reaction pathways for 3 points in time. The Si excess concentrates more in the middle and tends to form “bridges” which then disappear due to wetting. This was also observed at higher supersaturations in the last chapter. The highest single NC probability $\phi_S(t)$ requires 10 hours of annealing at a temperature of 1473K. Reaction pathways with this temperature are shown in Figure f) to h) for three points in time. A high density of NCs occurs in the first stages of annealing (f), and then most of them fuse and form a large single NC that is centered in the nanopillar. Reaction pathways at a temperature of 1273K are shown in c) to e). The number of nucleated NC is much higher and the size smaller. The single NC probability $\phi_S(t)$ does not decrease much, but the positioning and sizes of the last NCs are very different.

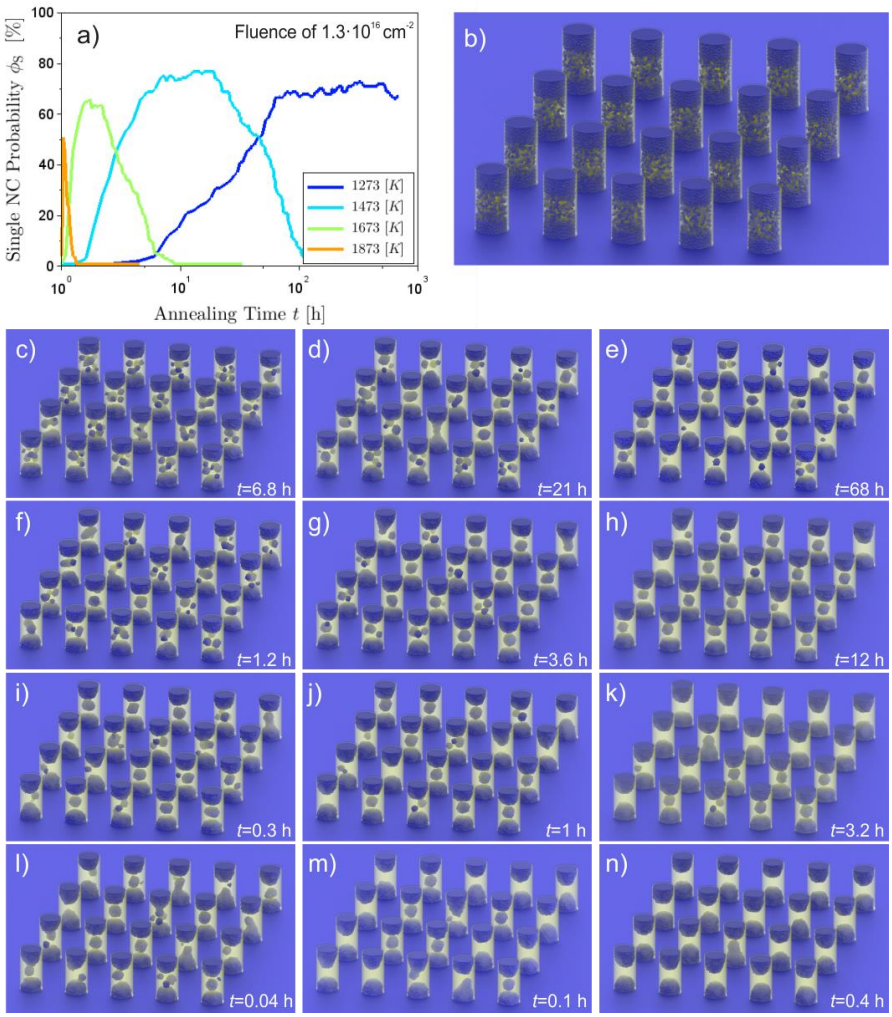

Figure 6-9: Simulation results of annealing a nanopillar after irradiation by 50 keV Si^+ ions for a fluence of 130 cm^-2. In a) the single NC probability $\phi_S(t)$ is shown (Equation (94)) for different temperatures and the corresponding arrays of 20 different reaction pathways for each temperature is shown in (c-e) for 1273K, in (f-h) for 1473K, in (i-k) for 1673K and in (l-n) for 1873K. The ground is only schematically introduced, every reaction pathway was performed in an isolated simulation cell.

Nucleation at Different Temperatures

A variation of temperature influences every process of the system. With increasing temperature, a diffusion event takes place faster and the bond strength of NC surface decreases. Chapter 4.3.2 showed the critical radius for nucleation, which decreases with decreasing temperature. A small critical radius leads to a high number of small NCs during the first stage of annealing. Figure 4-16 shows how an NC with a radius of 1.2 nm grows at temperatures below 1673 due to its stability. For higher temperatures, however, the NC emits more monomers than it absorbs and will evaporate over time. For these temperatures, stability can only be obtained by a larger NC. But the formation of a larger NC due to thermal fluctuations is more unlinkly and thus the probability of nucleation is reduced. This leads to a lower number of NCs while the size of the nucleated NC increases. Due to their large sizes, the NCs tend to merge and form a single NC. Earlier studies by Strobel [90]

investigated nucleation at individual sites supersaturated by implantation. At low annealing temperatures multiple NCs appear, while at higher temperatures only one NC is formed.

In summary, this chapter showed that the formation of a single NC depends on the critical radius of nucleation. Lower annealing temperatures result in a low critical radius (Chapter 4.3.2) and lead to a high number of small NCs in the nanopillar, while higher temperatures increase the size and decrease the number of the NCs. Spinodal decomposition, on the other hand, occurs immediately and has hardly any temperature dependence, as described in Chapter 4.3.5. While the system waits for nucleation rather long for high temperatures, the spinodal decomposition already takes place. This leads to the conclusions:

- Low annealing temperatures result in a high number of small NCs. The position and size of the last NC varies greatly between the calculated nanopillars. Although Ostwald ripening is very deterministic (see Chapter 4.3.4), nucleation contributes massively to the randomness of the reaction pathway through its random position and random nucleation time in the first stage of annealing. This makes the process not controllable and thus not suitable for the fabrication of SETs.
- High temperatures make nucleation only possible for large NCs and prefer a position in the center of the nanopillar. This leads to a large NC in the middle and allows good assembly for SET manufacturing.

6.2.3 Controlling the Reaction Pathway in Larger Nanopillars

The best single NC probability $\phi_S(t)$ of a reaction pathway was achieved in simulation with a nanopillar with a diameter of 6nm. The SET scheme as described in Chapter 2.3 intends to place the gate contact around the nanopillar. In order to realize a sufficient influence of the gate contact on the NC, the distance plays a decisive role [61]. A larger distance leads to a higher necessary voltage of the gate and increases the risk of short passes between the gate and the electrodes. Application in a logic circuit will also loose performance, because the charge will need to be higher and thus need s longer time. Simulation results predict a diameter of the nanopillar of about 12nm [61], where it is still possible to observe the SET characteristics. Figure 6-10 shows the I-V curve of the SET with different nanopillar diameters. For larger diameters no effect of the coulomb blockade can be observerd, what is a result of an insufficient influence of the gate on the NC.

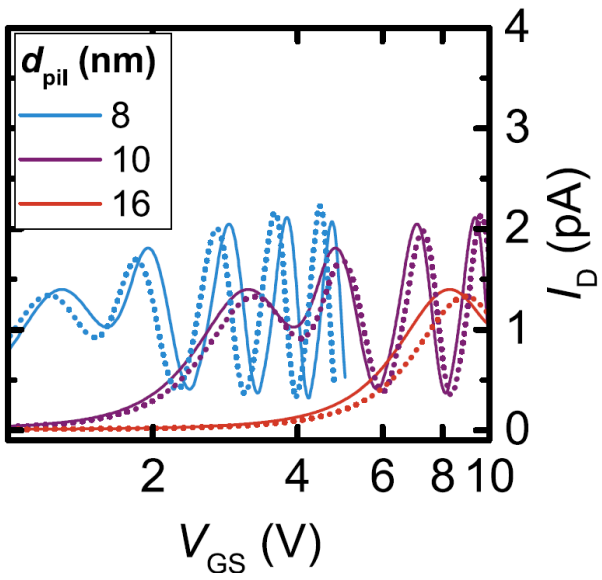

Figure 6-10: A I-V curve for a SET assembly with different diameters oft he used nanopillar. Taken from ref. [61].

Nanopillars with a diameter of 10nm can be realized in experiments [86], but according to the predictions of the KMC simulation, the single NC probability $\phi_S(t)$ will be drastically reduced for this high diameters. A configuration of multiple NCs forms and makes the control of this process difficult, but not impossible. The higher number of nucleations will increase fluctuation in the reaction pathways. However, the outer surface still retains a driving force for the self-organization of NCs. This chapter shows how the reaction pathway in nanopillars with larger diameters can be controlled.

Increasing the Diameter of the Nanopillar

Chapter 6.2 showed that the optimal reaction pathway goes through intermediate states, which are characterised by a small number of large NCs. These tend to merge in the center of the nanopillar and form a single Si-NC. Large, stable and well centered. This was guided by the reflection effect at the mantle surface of the nanopillar and rapid absorption at the Si/SiO_2 interfaces. However, by increasing the diameter, the outer surface loses its influence on phase separation. Figure 6-11 shows the simulation of annealing nanopillars with different diameters from 6nm to 12nm. In all cases, the reflective surface causes a denuded zone on the outer rim of the SiO_2 and drives the structuring as described in Figure 6-11. With small diameters (e.g. 6nm and 8nm) these NCs get to feel the effect of the surface from all sides and form a single NC in the later stages. With larger diameters, the driving force of the surface induces several NCs in the outer areas and a multiple NC configuration becomes unavoidable. However, it has already been shown in Chapter 6.2 how the influence of boundary conditions propagates in waves. This allows controlling the reaction pathway of the nanopillar to a certain degree.

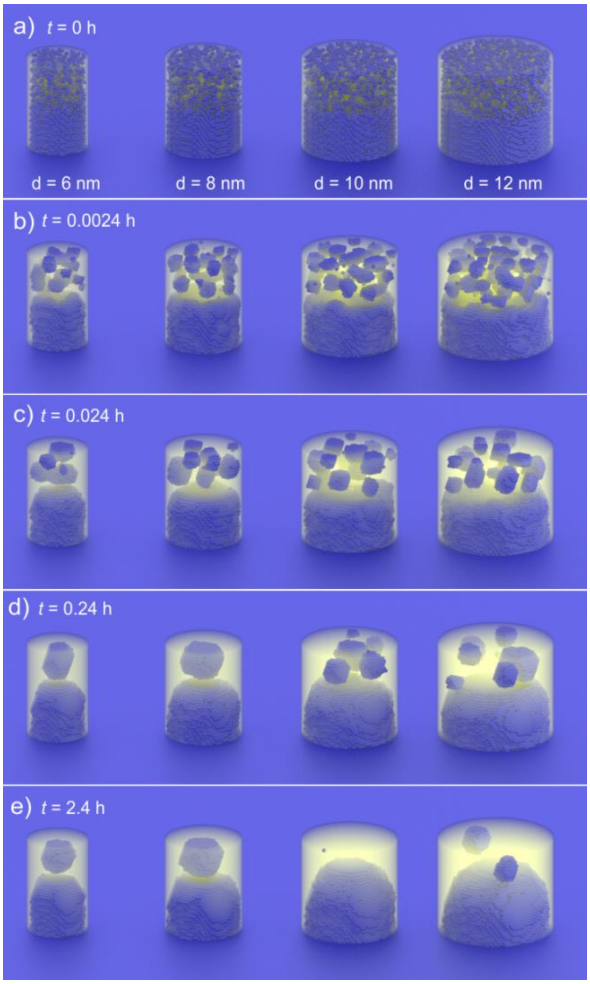

Figure 6-11: Simulation results of annealing a nanopillar after irradiation by 50 keV Si^+ ions for a fluence of 130 cm^{-2}. The annealing temperature was 1373K. The reaction pathways for different diameters are shown from a) to e). The top-Si is removed for better insight. The ground is only schematically introduced; every reaction pathway was performed in an isolated simulation cell.

Influence of the Diffusional Screening on the Reaction Pathway in the Nanopillar

Diffusion screening avoids the direct interactions between a NC and the next but one neighbour. The NC interacts only with its nearest neighbours and influences them, while the nearest neighbours interact with the next but one neighbours. This leads to a wave of interactions. Chapter 2.4.3 has already shown how these types of interactions form shells of NCs in Figure 2-7. This tendency of Si-NC pattern formation during Ostwald ripening can also be observed in the SiO_2 layer, but is damped by the strong absorption of the upper and lowers Si/SiO_2 interfaces.

In contrast to the sphere filled with NCs in Figure 2-7, the nanopillar gives a configuration of a plate filled with NCs. The reaction pathway of this configuration is shown in Figure 6-12. The reflective surface of the nanopillar induces the interaction wave, which forms rings of NCs. The nanopillar is cut through the top of the SiO_2 film for illustration and the initial configuration is shown in a). The fluence used was $1.2 \cdot 10^{16}\ \mathrm{cm}^{-2}$ with an irradiation energy of 60 keV. After short annealing, NCs form and begin to interact through Ostwald ripening, as shown in b) and c). The circular lines mark a preferred radius for the presence of NCs. In d), the rotatorically averaged Si volumes in the SiO_2 plate are displayed and the colored lines correspond to the circles in c). These discrete circles indicate the tendency to form rings of NCs in certain diameters. This happens in analogy to the shells of Figure 2-7 and is the influence of the diffusion screening. This mechanism should be much more pronounced for an absorbing perispheric surface, i.e. by annealing in an oxidizing atmosphere. In addition, this could

increase the distance of the rings to the outer surface and thus the NC probability $\phi_S(t)$ for larger radii.

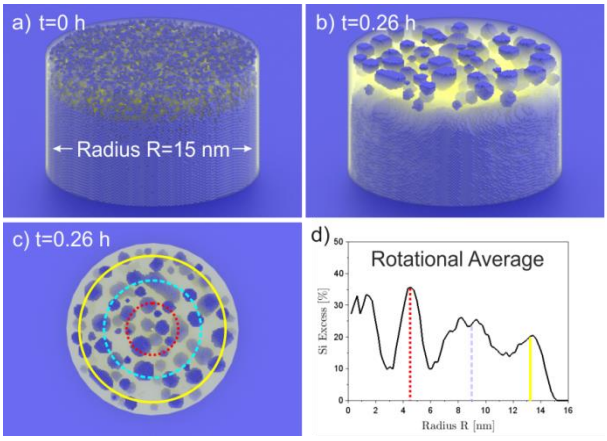

Figure 6-12: Annealing simulation results of a nanopillar after irradiation with 50 keV Si^+ ions for a fluence of 130 cm^-2, illustrated by a cut along the top Si/ SiO_2 interface. In a), the starting configuration is shown and in b) and c) the results after annealing for 0.26h. In d) a rotational average of the Si domains in the SiO_2 layer is plottet over the radius. The ground is only schematically introduced.

The first peak in Figure 6-12 d) ends with a radius of 3nm, which is also the optimal nanopillar radius for the best single NC probability $\phi_S(t)$ of the reaction pathways (see Chapter 6.2). The distance of 3 nm is also approximately the distance of the center of the Si-NC from the Si/SiO_2 interface. This can be attributed to three effects:

- The 3 nm could characterize the Brailsford diffusion length, which is responsible for self-organization processes (see Chapter 2.4.3). However, this is time-dependent since it changes with the size and density of the NCs during the evolution of the system [300].
- The supersaturation in the SiO_2 layer (~20%) is influenced by the spinodal decomposition (see Figure 4-20 and Chapter 4.3.5) and the 3nm could be due to a high amplification (see Equation (83)) of this wavelength $s(k)$. This would indicate the influence of spinodal decomposition.
- The rings form in a later stage of the annealing and spinodal decomposition is only a separation mechanism and therefore takes place at the beginning. However, the amplification of the NC between the Si/SiO_2 interfaces could indicate spinodal decomposition.

Analytically it was shown that the wavelength of the structure is proportional to the critical radius of the NC [322]. This leads to the conclusion that the optimum of 6nm is temperature dependent. It was also shown that the greater the density of the NCs, the smaller the wavelength of the structures [99]. It follows that with higher supersaturation the circles in Figure 6-12 will become smaller.

In summary, this chapter shows how the diffusional screening of NCs by its next neighbours causes a wave of interactions in the SiO_2 of the nanopillar and the tendency to form rings of NCs. From this follows:

- For nanopillars with a larger diameter, it is possible to form rings of NCs by self-organization.
- The optimum diameter of the SiO_x depends on the screening length of the system.This length might depend on different parameters like supersaturation or temperature.

In general, however, it does not mean that the nanopillar must have a diameter of 6 nm to achieve a high single NC probability $\phi_S(t)$ of the reaction pathway. In order to achieve similar results for large nanopillars, it is also possible to oxidize the outer part of the nanopillar. As already mentioned, however, oxidation is outside the scope of this work.

7 Summary and Major Statements

Self-organization is the only industrial tool to form structures down to sub-nm scales. Chapter 2.2 gave an overview of how classical manufacturing methods fail in tasks like manufacturing a SET and Chapter 2.4 showed the incredible possibilities of self-organization. The decisive factor, however, is the control of this self organization. Earlier studies had allowed a two-dimensional layer and one-dimensional chain of NCs to be self-organized. So far, however, neither the exactness of the position, a defined size nor the exact time was relevant. Average sizes such as the average radius or the number of NCs were well controllable, but each layer and each chain of NCs was unique. For the nanopillar from the SET scheme in Chapter 2.3, each reaction pathway must form an NC at the same time, at the same position and with the same size.

Self Organization of Single NCs in the Si/SiO_2/Si Stacked Nanopillar

In 2016, expectations were high for the methods of KMC and BCA, because in the past (e.g. in the NEON project) a good control could be realized. They served with reliable predictions for implantation, interface mixing and phase separation in the Si-SiO_2 system. To guarantee the requirements of reliable control of single NCs in the nanopillar was defined by the NC probability $\phi_S(t)$ (see Equation (94)). The main goal at that time was to find parameter ranges for which the individual NC probability $\phi_S(t)$ (see Chapter 6.2) was 100% and to use these predictions for experimental investigations. Unfortunately, these optimistic expectations could not be fulfilled. The search for a 100% NC probability was unsuccessful and remained at a maximum of 80% (see Figure Figure 6-5). Methods for forming SiO_x with sharper Si/SiO_2 interfaces or higher supersaturation in the center of SiO_2 would increase the $\phi_S(t)$. One can assume that the dependencies shown in Chapter 6.2 remain unchanged and it will be interesting to use the obtained knowledge to optimize the manufacturing.

The investigated dependencies of the individual NC formation in the nanopillar are temperature, fluence and diameter. Different fluences showed a strong influence of the nucleation dependency on the Si excess. Chapter 4.3.2 dealt with nucleation and its behavior for different positions in the phase diagram. Low fluences cause a low supersaturation leading to the formation of more nuclei due to a lower critical radius of nucleation (see Chapter 4.3.2 and Equation (69)). This leads to higher randomness due to their random position, random size and random appearance time. Nucleation is usually a very strong barrier to control the process. Higher fluences showed a separation by more spinodal decomposition, which is more determinable and controllable. The dependence on temperature showed a similar influence of nucleation. Low temperatures also reduce the critical radius for nucleation, resulting in more nuclei, more randomness and less controllability.

The diameter of the nanopillar was optimally determined at 6nm (see Figure 6-5). For larger diameters the formation of rings in Figure 6-12 was observed. This corresponds to earlier studies on the development of shells and rings of NCs presented in Chapter 2.4.3 and attributed to Ostwald Ripening and the diffusion screening. The use of the outer surface of the nanopillar as an oxygen source by annealing in an oxygen environment provides another control instrument that could make

it possible to increase the diameter. The formation of NCs in the outer area is suppressed and only one centered NC can be expected.

Influence of Thermal Spikes during Ion Beam Mixing

In addition to the trust of 2016 to the controllability of the process, there was also high confidence in the models of the KMC and BCA. Previous studies did indeed give correct predictions, but mainly for implanted profiles. The discrepancy presented in Chapter 5.1.1 was not expected and led to the model approach in Chapter 5.2.1. The classical description of the BCA by the diffusion equation was combined with the Cahn Hillard equation as an additional term to describe the influence of thermal spikes and a new model was introduced, parametrized and served for simulation results. This gave a first insight into how mixing takes place on the interface. As it turned out and is shown in Figure 5-12, the influence of fluence is less significant than expected. The counterforce from thermal spikes increases with fluence and seems to define a kind of maximum supersaturation. To increase this, variations of ion energy or even sequential irradiation with different energies for different fluences can be attempted.

Modeling of the Different Diffusion in Si and in SiO_2

The fact that the interfaces were not dealt with so intensively until 2016 was also followed by the fact that the influence of the different diffusions in Si and SiO_2 (see Chapter 4.2.2) did not have to be taken into account. Neither time nor temperature dependence were aspects that were examined. In return, normalized temperatures and times were used to study thermodynamics. The difference in diffusion and especially at different temperatures leads to very different behaviour when annealing the mixed interface. To investigate the difference in diffusion in Si and SiO_2, Chapter 4.1.3 introduced an extension of the KMC method, which models coefficients depending on the surrounding Si excess. In order to investigate the time and temperature dependence, a comprehensive literature search of the diffusion coefficients was carried out (see Chapter 4.2.2) and the KMC model parametrized. Here it came out in Chapter 4.3.6 that there is no exposed zone between SiO_2-NCs and the interface. Diffusion processes take much faster in Si than the reconstruction of the interface. The interface to the Si-NCs, on the other hand, shows a very high sharpness, because relative to the formation of Si NCs, the reconstruction is considerably faster. Also the different behaviour of the growth of Si and SiO_2-NCs was not yet known. Chapter 4.3.3 showed that Si-NCs showed a strongly diffusion-controlled growth while the SiO_2-NCs are rather controlled by the reaction.

Modeling the Solubility of Si in SiO_2 and O in Si

In addition to diffusion, the solubility of oxygen in Si and Si in SiO_2 can also be generally different. Chapter 4.1.3 also introduced a dependency on the surrounding Si excess, which was parameterized in Chapter 4.2.3. Unfortunately, in the literature there are only values for the solubility of oxygen in Si and thus only the bond energies for an environment of Si could be determined. The bond energies for the Si excess in a SiO_2 environment remain unknown and have been varied in several chapters. Chapter 4.3.4 showed in Figure 4-19 how the growth is dependent on the bond energy E_{NN} and a small influence that at high bond energies the reaction-controlled behaviour of Ostwald ripening is more pronounced. Chapter 5.1.2 showed that the discrepancy between experiment and simulation is

reduced by the influence of low bond energies. This was attributed to a lower supersaturation, but to the same extent for each sample. Chapter 4.3.1 showed how the phase diagram is influenced by different bond energies. Experimental measurement of the coexistence curve and comparison with the results in Figure 4-13 would allow estimation of the bond energy $E_{\mathrm{NN}}(z=0)$ of Si in a SiO_2 environment.

The Symmetry of Ion Beam Irradiation of a Si/SiO_2/Si Stack

The irradiation of a Si/SiO_2/Si stack with such a thin SiO_2 layer was also not investigated before in that detail. Irradiation by Si^+ ions always results in a combination of implantation and ion beam mixing. Chapter 2.1 showed the requirements for the SET. Both tunnel distances need to be similar and the NC needs to be centered in the middle. This leads to the requirement of symmetry in the Si excess profile, which was investigated in Chapter 3.2.2. Implantation is mainly far beneath the SiO_2 layer, but still can influence especially the lower influence and induce an asymmetrical influence. The same is done for the ion beam mixing, which is mainly defined by the displacements of atoms. The IBM is more mixing the upper interface than the lower. Figure 3-4 showed how both processes are influencing the Si excess profile asymmetrically. However, the total result is important and Figure 3-7 showed how it is possible to still get a rather symmetrical Si excess profile, which is mostly based beceause of the IBM. This also allows the treatment of BCA by the diffusion equation, because the diffusion equation neglects the implanted ions.

Appendices

A. Model Parameter for the Simulation of Nanopillars

The KMC simulation of the nanopillar as shown in Figure 6-2 uses the same parameters as the calculations in Chapter 4, resulting in similar calculation times. Although small simulation cells (16 nm)^3 were used, the calculation took hours until the first Si-NCs were formed. The statistical study of cluster formation requires several hundred reaction pathways for the same parameter set. The parameters available for optimization are the nanopillars diameter, starting configuration and annealing temperature. Although the systems may be small, long annealing times and thousands of reaction pathways make it necessary to introduce a further approximation in order to reduce the computational effort.

Chapter 4.3.6 showed in Figure 4-24 how phase separation takes place around a mixed Si/SiO_2 interface. The results showed that the reaction pathway in silicon is completed after ~0.2s (NC evaporates, equilibrium reached), while the formation of the denuded zone between the Si/SiO_2 interface and the Si-NCs requires about ~20s. The evolution of the Si-NCs therefore depends only slightly on how fast the processes in the silicon run, because they are finished when the crucial stage of the Si-NC formation begins. The computing time of one MCS remains the same for all parameter sets and is determined by the renormalization in Chapter 4.1.4 by the Equation (46). The probability K_{if} was normalized to the fastest event: diffusion in Si environment (z=18). By slowing down the diffusion in Si surrounding before normalization, the time of one MCS will increase. This will result in less MCS necessary for the same time in seconds and thus in a reduction of calculation effort. The mistake of this approach is an artificially slow-down of the processes in a Si surrounding.

Figure A-1 shows how the diffusion constant is approximated to reduce the computational effort for the nanopillar calculations in Chapter 6.2. The diffusion coefficient is reduced for each Kawasaki pair with a surrounding number of Si sites greater than 9. Figure A-1 b) shows the diffusion coefficient for different numbers of Si neighbors over temperature.

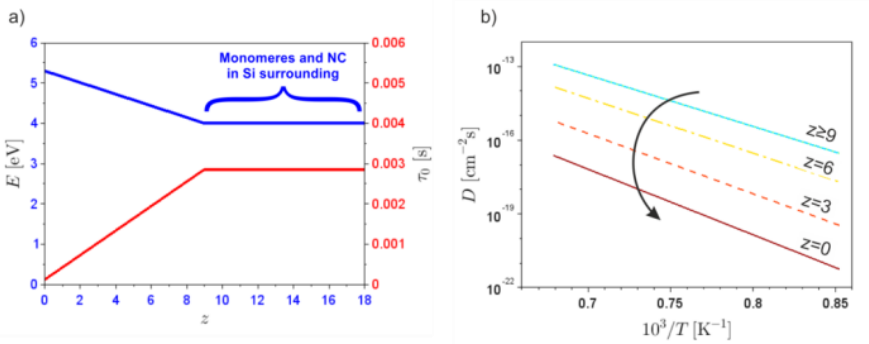

A-1: Approximation oft the diffusion constant for calculations of the nanopillar. The parameters for the activation energy *E* and the pre-exponential factor (see Equation (46)) over the composition (z=0,…,18) in a) and the diffusion coefficient over the inverse temperature in b).

B. Saving Computational Effort with Diffusion in Adiabatic Approximation

Chapter 4.2.2 showed that the diffusivity differs by more than 15 orders of magnitude between the processes in Si and SiO_2. Appendix A already introduced an approximation for Chapter 6.2. A similar approach is used for calculations in Chapter 5.1. The very fast diffusion of oxygen in Si is treated in an adiabatic approximation. As soon as a Kawasaki pair (Equation (46)) performs in pure silicon (z=18), the SiO_2 site carries out a random walk until it reaches another SiO_2 site. Meanwhile every other kinetic is stopped. This approach is justified to a similar extent as the linear interpolation between diffusion in Si and diffusion in SiO_2. In Chapter 4.3, however, it was necessary to estimate temporal processes correctly and Chapter 6 investigates the temperature dependency of Si-NC formation in nanopillars. Since this has less relevance here, such an approach is appropriate.

Bibliography

[1] Y. Taur *et al.*, “CMOS Scaling into the Nanometer Regime,” *Proc. IEEE*, vol. 85, no. 4, pp. 486–504, 1997.

[2] J. E. Lilienfeld, “Method and apparatus for controlling electric currents,” US1745175A, 1926.

[3] J. A. Garraty, M. C. Carnes, and A. C. of L. Societies., *American national biography*. New York: Oxford University Press, 1999.

[4] W. Shockley, J. Bardeen, and W. Brattain, “The first transistor,” *Bell Lab. (Dec. 16, 1947)*, p. 27, 1947.

[5] J. A. Fleming, “Instrument for converting alternating electric currents into continuous currents.,” US803684A, 1905.

[6] J. S. Kilby, “Miniaturized electronic circuits,” US3138743A, 1959.

[7] K. Dawon, “Electric field controlled semiconductor device,” US3102230A, 1960.

[8] F. M. . Wanlass, “Low stand-by power complementary field effect circuitry,” US3356858A, 1963.

[9] G. E. Moore, “Cramming more components onto integrated circuits, Reprinted from Electronics, volume 38, number 8, April 19, 1965, pp.114 ff.,” *IEEE Solid-State Circuits Soc. Newsl.*, vol. 11, no. 3, pp. 33–35, 2006.

[10] S. Salahuddin, K. Ni, and S. Datta, “The era of hyper-scaling in electronics,” *Nat. Electron.*, vol. 1, no. 8, pp. 442–450, 2018.

[11] R. A. Chapman, C. C. Wei, D. A. Bell, S. Aur, G. A. Brown, and R. A. Haken, “0.5 micron CMOS for high performance at 3.3 V,” in *Technical Digest., International Electron Devices Meeting*, 1988, pp. 52–55.

[12] R. H. Dennard, F. H. Gaensslen, V. L. Rideout, E. Bassous, and A. R. LeBlanc, “Design of ion-implanted MOSFET’s with very small physical dimensions,” *IEEE J. Solid-State Circuits*, vol. 9, no. 5, pp. 256–268, 1974.

[13] J. D. Meindl, “Low power microelectronics: retrospect and prospect,” *Proc. IEEE*, vol. 83, no. 4, pp. 619–635, Apr. 1995.

[14] C. Auth *et al.*, “45nm High-k + metal gate strain-enhanced transistors,” in *2008 Symposium on VLSI Technology*, 2008, pp. 128–129.

[15] D. J. Frank, R. H. Dennard, E. Nowak, P. M. Solomon, and Y. Taur, “Device scaling limits of Si MOSFETs and their application dependencies,” *Proc. IEEE*, vol. 89, no. 3, pp. 259–288, 2001.

[16] D. J. Frank and H.-S. P. Wong, “Analysis of the design space available for high-kgate dielectrics in nanoscale MOSFETs,” *Superlattices Microstruct.*, vol. 28, no. 5–6, pp. 485–491, Nov. 2000.

[17] D. A. Buchanan, “Scaling the gate dielectric: Materials, integration, and reliability,” *IBM J. Res. Dev.*, vol. 43, no. 3, pp. 245–264, 1999.

[18] D. Hisamoto, T. Kaga, and E. Takeda, “Impact of the vertical SOI ‘DELTA’ structure on planar device technology,” *IEEE Trans. Electron Devices*, vol. 38, no. 6, pp. 1419–1424, 1991.

[19] J. B. Chang *et al.*, “Scaling of SOI FinFETs down to fin width of 4 nm for the 10nm technology node,” *Dig. Tech. Pap. - Symp. VLSI Technol.*, vol. 12, 2011.

[20] K. Kim, J.-Y. Choi, T. Kim, S.-H. Cho, and H.-J. Chung, “A role for graphene in silicon-based semiconductor devices,” *Nature*, vol. 479, p. 338, Nov. 2011.

[21] Q. H. Wang, K. Kalantar-Zadeh, A. Kis, J. N. Coleman, and M. S. Strano, “Electronics and optoelectronics of two-dimensional transition metal dichalcogenides,” *Nat. Nanotechnol.*, vol. 7, p. 699, Nov. 2012.

[22] A. M. Ionescu and H. Riel, “Tunnel field-effect transistors as energy-efficient electronic switches,” *Nature*, vol. 479, p. 329, Nov. 2011.

[23] M. T. Björk, J. Knoch, H. Schmid, H. Riel, and W. Riess, “Silicon nanowire tunneling field-effect transistors,” *Appl. Phys. Lett.*, vol. 92, no. 19, p. 193504, 2008.

[24] J. J. L. Morton, D. R. McCamey, M. A. Eriksson, and S. A. Lyon, “Embracing the quantum limit in silicon computing,” *Nature*, vol. 479, p. 345, Nov. 2011.

[25] Y. Takahashi, Y. Ono, A. Fujiwara, and H. Inokawa, “Silicon single-electron devices,” *J. Phys. Condens. Matter*, vol. 14, no. 39, pp. R995--R1033, Sep. 2002.

[26] Z. A. K. Durrani, *Single-Electron Devices and Circuits in Silicon*. PUBLISHED BY IMPERIAL COLLEGE PRESS AND DISTRIBUTED BY WORLD SCIENTIFIC PUBLISHING CO., 2009.

[27] C. . Gorter, “A possible explanation of the increase of the electrical resistance of thin metal films at low temperatures and small field strengths,” *Physica*, vol. 17, no. 8, pp. 777–780, Aug. 1951.

[28] D. V. Averin and K. K. Likharev, “Coulomb blockade of single-electron tunneling, and coherent oscillations in small tunnel junctions,” *J. Low Temp. Phys.*, vol. 62, no. 3–4, pp. 345–373, 1986.

[29] M. Saitoh and T. Hiramoto, “Extension of Coulomb blockade region by quantum confinement in the ultrasmall silicon dot in a single-hole transistor at room temperature,” *Appl. Phys. Lett.*, vol. 84, no. 16, pp. 3172–3174, 2004.

[30] Y. Takahashi *et al.*, “Conductance oscillations of a Si single electron transistor at room temperature,” in *Proceedings of 1994 IEEE International Electron Devices Meeting*, 1994, pp. 938–940.

[31] W. Lu, Z. Ji, L. Pfeiffer, K. W. West, and A. J. Rimberg, “Real-time detection of electron tunnelling in a quantum dot,” *Nature*, vol. 423, no. 6938, pp. 422–425, 2003.

[32] R. Schleser, E. Ruh, T. Ihn, K. Ensslin, D. C. Driscoll, and A. C. Gossard, “Time-resolved detection of individual electrons in a quantum dot,” *Appl. Phys. Lett.*, vol. 85, no. 11, pp. 2005–2007, 2004.

[33] L. M. K. Vandersypen, J. M. Elzerman, R. N. Schouten, L. H. van Beveren, R. Hanson, and L. P. Kouwenhoven, “Real-time detection of single-electron tunneling using a quantum point contact,” *Appl. Phys. Lett.*, vol. 85, no. 19, pp. 4394–4396, 2004.

[34] O. Astafiev, V. Antonov, T. Kutsuwa, and S. Komiyama, “Single electron transistors as far-infrared photon detectors,” in *Device Research Conference. Conference Digest (Cat. No.01TH8561)*, 2001, pp. 145–147.

[35] J. M. Hergenrother, J. G. Lu, and M. Tinkham, “The single-electron transistor as an ultrasensitive microwave detector,” *IEEE Trans. Appl. Supercond.*, vol. 5, no. 2, pp. 2604–2607, 1995.

[36] A. Pioda *et al.*, “Single-Shot Detection of Electrons Generated by Individual Photons in a Tunable Lateral Quantum Dot,” *Phys. Rev. Lett.*, vol. 106, no. 14, p. 146804, Apr. 2011.

[37] T. Fujita *et al.*, “Nondestructive Real-Time Measurement of Charge and Spin Dynamics of Photoelectrons in a Double Quantum Dot,” *Phys. Rev. Lett.*, vol. 110, no. 26, p. 266803, Jun. 2013.

[38] J. M. Elzerman, R. Hanson, L. H. Willems van Beveren, B. Witkamp, L. M. K. Vandersypen, and L. P. Kouwenhoven, “Single-shot read-out of an individual electron spin in a quantum dot,” *Nature*, vol. 430, no. 6998, pp. 431–435, 2004.

[39] R. Hanson *et al.*, “Single-Shot Readout of Electron Spin States in a Quantum Dot Using Spin-Dependent Tunnel Rates,” *Phys. Rev. Lett.*, vol. 94, no. 19, p. 196802, 2005.

[40] C. Barthel, D. J. Reilly, C. M. Marcus, M. P. Hanson, and A. C. Gossard, “Rapid Single-Shot Measurement of a Singlet-Triplet Qubit,” *Phys. Rev. Lett.*, vol. 103, no. 16, p. 160503, 2009.

[41] H. Kiyama, T. Nakajima, S. Teraoka, A. Oiwa, and S. Tarucha, “Single-Shot Ternary Readout of Two-Electron Spin States in a Quantum Dot Using Spin Filtering by Quantum Hall Edge States,” *Phys. Rev. Lett.*, vol. 117, no. 23, p. 236802, Nov. 2016.

[42] A. N. Korotkov, D. V. Averin, K. K. Likharev, S. A. Vasenko, and M. Devoret, “Single-Electron Transistors as Ultrasensitive Electrometers,” *Springer Ser. Electron. Photonics*, vol. 31, 1992.

[43] R. J. Schoelkopf, P. Wahlgren, A. A. Kozhevnikov, P. Delsing, and D. E. Prober, “The Radio-Frequency Single-Electron Transistor (RF-SET): A Fast and Ultrasensitive Electrometer,” *Science (80-.).*, vol. 280, no. 5367, pp. 1238–1242, 1998.

[44] P. L. McEuen *et al.*, “Transport spectroscopy of a Coulomb island in the quantum Hall regime,” *Phys. Rev. Lett.*, vol. 66, no. 14, pp. 1926–1929, Apr. 1991.

[45] Y. Takahashi, A. Fujiwara, K. Yamazaki, H. Namatsu, K. Kurihara, and K. Murase, “Multigate single-electron transistors and their application to an exclusive-OR gate,” *Appl. Phys. Lett.*, vol. 76, no. 5, pp. 637–639, 2000.

[46] S. J. Kim *et al.*, “One electron-based smallest flexible logic cell,” *Appl. Phys. Lett.*, vol. 101, no. 18, p. 183101, 2012.

[47] M. AKAZAWA, K. KANAAMI, T. YAMADA, and Y. AMEMIYA, “Multiple-Valued Inverter Using a Single-Electron-Tunneling Circuit,” 1999.

[48] H. Inokawa, A. Fujiwara, and Y. Takahashi, “A multiple-valued logic and memory with combined single-electron and metal-oxide-semiconductor transistors,” *IEEE Trans. Electron Devices*, vol. 50, no. 2, pp. 462–470, 2003.

[49] T. Hanyu, M. Kameyama, and T. Higuchi, “Beyond-binary circuits for signal processing,” in *1993 IEEE International Solid-State Circuits Conference Digest of Technical Papers*, 1993, pp. 134–135.

[50] L. J. Micheel, “Heterojunction bipolar technology for emitter-coupled multiple-valued logic in gigahertz adders and multipliers,” in *[1992] Proceedings The Twenty-Second International Symposium on Multiple-Valued Logic*, 1992, pp. 18–26.

[51] D. Etiemble, “On the performance of multivalued integrated circuits: past, present and future,” in *[1992] Proceedings The Twenty-Second International Symposium on Multiple-Valued Logic*, 1992, pp. 156–164.

[52] S. Kawahito, K. Mizuno, and T. Nakamura, “Multiple-valued current-mode arithmetic circuits based on redundant positive-digit number representations,” in *[1991] Proceedings of the Twenty-First International Symposium on Multiple-Valued Logic*, 1991, pp. 330–339.

[53] F. J. Klüpfel, A. Burenkov, and J. Lorenz, “Simulation of silicon-dot-based single-electron memory devices,” in *2016 International Conference on Simulation of Semiconductor Processes and Devices (SISPAD)*, 2016, pp. 237–240.

[54] E. Amat, J. Bausells, and F. Perez-Murano, “Ion-irradiation-induced Si Nanodot Self-Assembly for Hybrid SET-CMOS Technology - Report on process definition,” 2016.

[55] S. Mahapatra and A. M. Ionescu, “Realization of multiple valued logic and memory by hybrid

SETMOS architecture," *IEEE Trans. Nanotechnol.*, vol. 4, no. 6, pp. 705–714, Nov. 2005.

[56] M. J. Yoo *et al.*, "Scanning Single-Electron Transistor Microscopy: Imaging Individual Charges," *Science (80-.).*, vol. 276, no. 5312, pp. 579–582, 1997.

[57] J. Weber, J. Weis, M. Hauser, and K. v Klitzing, "Fabrication of an array of single-electron transistors for a scanning probe microscope sensor," *Nanotechnology*, vol. 19, no. 37, p. 375301, Aug. 2008.

[58] P. Steinmann, K. A. Lister, and J. M. R. Weaver, "Fabrication of metallic tunnel junctions for the scanning single electron transistor atomic force microscope," *J. Vac. Sci. Technol. B Microelectron. Nanom. Struct. Process. Meas. Phenom.*, vol. 21, no. 5, pp. 2138–2141, 2003.

[59] C. A. Neugebauer and M. B. Webb, "Electrical Conduction Mechanism in Ultrathin, Evaporated Metal Films," *J. Appl. Phys.*, vol. 33, no. 1, pp. 74–82, 1962.

[60] C. Wasshuber, *Computational single-electronics*. Springer Science & Business Media, 2012.

[61] F. J. Klupfel, "A Compact Model Based on Bardeen's Transfer Hamiltonian Formalism for Silicon Single Electron Transistors," *IEEE Access*, vol. 7, pp. 84053–84065, 2019.

[62] M. Yoshihira *et al.*, "Single electron transistors with ultra-thin Au nanowires as a single Coulomb island," *Appl. Phys. Lett.*, vol. 102, no. 20, p. 203117, 2013.

[63] H. Guerin, M. Yoshihira, H. Kura, T. Ogawa, T. Sato, and H. Maki, "Coulomb blockade phenomenon in ultra-thin gold nanowires," *J. Appl. Phys.*, vol. 111, no. 5, p. 54304, 2012.

[64] A. Bezryadin, C. Dekker, and G. Schmid, "Electrostatic trapping of single conducting nanoparticles between nanoelectrodes," *Appl. Phys. Lett.*, vol. 71, no. 9, pp. 1273–1275, 1997.

[65] H. Park, A. K. L. Lim, A. P. Alivisatos, J. Park, and P. L. McEuen, "Fabrication of metallic electrodes with nanometer separation by electromigration," *Appl. Phys. Lett.*, vol. 75, no. 2, pp. 301–303, 1999.

[66] M. Fuechsle *et al.*, "A single-atom transistor," *Nat. Nanotechnol.*, vol. 7, p. 242, Feb. 2012.

[67] T. A. Fulton and G. J. Dolan, "Observation of single-electron charging effects in small tunnel junctions," *Phys. Rev. Lett.*, vol. 59, no. 1, pp. 109–112, Jul. 1987.

[68] S. I. Khondaker and Z. Yao, "Fabrication of nanometer-spaced electrodes using gold nanoparticles," *Appl. Phys. Lett.*, vol. 81, no. 24, pp. 4613–4615, 2002.

[69] K. Tsukagoshi, E. Watanabe, I. Yagi, and Y. Aoyagi, "The formation of nanometer-scale gaps by electrical degradation and their application to C60 transport measurements," *Microelectron. Eng.*, vol. 73–74, pp. 686–688, Jun. 2004.

[70] K. I. Bolotin, F. Kuemmeth, A. N. Pasupathy, and D. C. Ralph, "Metal-nanoparticle single-electron transistors fabricated using electromigration," *Appl. Phys. Lett.*, vol. 84, no. 16, pp. 3154–3156, 2004.

[71] K. Luo, D.-H. Chae, and Z. Yao, "Room-temperature single-electron transistors using alkanedithiols," *Nanotechnology*, vol. 18, no. 46, p. 465203, 2007.

[72] E. M. Ford and H. Ahmed, "Control of Coulomb blockade characteristics with dot size and density in planar metallic multiple tunnel junctions," *Appl. Phys. Lett.*, vol. 75, no. 3, pp. 421–423, 1999.

[73] P. S. K. Karre, P. L. Bergstrom, G. Mallick, and S. P. Karna, "Room temperature operational single electron transistor fabricated by focused ion beam deposition," *J. Appl. Phys.*, vol. 102, no. 2, p. 24316, 2007.

[74] K. Nishiguchi, Y. Ono, and A. Fujiwara, "Operation of silicon single-electron devices at room temperature," *NTT Tech. Rev.*, vol. 5, Jun. 2007.

[75] R. Krahne *et al.*, “Nanoparticles and nanogaps: controlled positioning and fabrication,” *Phys. E Low-dimensional Syst. Nanostructures*, vol. 17, pp. 498–502, Apr. 2003.

[76] S. I. Khondaker, K. Luo, and Z. Yao, “The fabrication of single-electron transistors using dielectrophoretic trapping of individual gold nanoparticles,” *Nanotechnology*, vol. 21, no. 9, p. 95204, Feb. 2010.

[77] Z. Chen, X. Lan, and Q. Wang, “DNA Origami Directed Large-Scale Fabrication of Nanostructures Resembling Room Temperature Single-Electron Transistors,” *Small*, vol. 9, no. 21, pp. 3567–3571, 2013.

[78] C. Single, F. Zhou, H. Heidemeyer, F. E. Prins, D. P. Kern, and E. Plies, “Oxidation properties of silicon dots on silicon oxide investigated using energy filtering transmission electron microscopy,” *J. Vac. Sci. Technol. B Microelectron. Nanom. Struct. Process. Meas. Phenom.*, vol. 16, no. 6, pp. 3938–3942, 1998.

[79] H. I. Liu, D. K. Biegelsen, N. M. Johnson, F. A. Ponce, and R. F. W. Pease, “Self-limiting oxidation of Si nanowires,” *J. Vac. Sci. Technol. B Microelectron. Nanom. Struct. Process. Meas. Phenom.*, vol. 11, no. 6, pp. 2532–2537, 1993.

[80] Y. Takahashi *et al.*, “Fabrication technique for Si single-electron transistor operating at room temperature,” *Electron. Lett.*, vol. 31, no. 2, pp. 136–137, Jan. 1995.

[81] Y. Takahashi, H. Namatsu, K. Kurihara, K. Iwadate, M. Nagase, and K. Murase, “Size dependence of the characteristics of Si single-electron transistors on SIMOX substrates,” *IEEE Trans. Electron Devices*, vol. 43, no. 8, pp. 1213–1217, Aug. 1996.

[82] A. Fujiwara, Y. Takahashi, H. Namatsu, K. Kurihara, and K. Murase, “Suppression of Effects of Parasitic Metal-Oxide-Semiconductor Field-Effect Transistors on Si Single-Electron Transistors,” *Jpn. J. Appl. Phys.*, vol. 37, no. Part 1, No. 6A, pp. 3257–3263, Jun. 1998.

[83] M. Jo *et al.*, “Fabrication of double-dot single-electron transistor in silicon nanowire,” *Thin Solid Films*, vol. 518, no. 6, pp. S186–S189, Jan. 2010.

[84] K. S. Makarenko, Z. Liu, M. P. de Jong, F. A. Zwanenburg, J. Huskens, and W. G. van der Wiel, “Bottom-Up Single-Electron Transistors,” *Adv. Mater.*, vol. 29, no. 42, p. 1702920, 2017.

[85] T. Müller, “Low Energy Ion Beam Synthesis of Si Nanocrystals for Nonvolatile Memories – Kinetic Monte Carlo Studies on Phase Separation,” TU Dresden.

[86] HZDR, “IONS4SET; Ion-irradiation-induced Si nanodot self-assembly for hybrid SET-CMOS technology; Project funded by the European Commission under Grant Agreement No. 688072,” 2016.

[87] NEON, “Influence of ion implantation conditions on nanocrystal positioning within thin oxides, GRD1-2000-25619,” 2002.

[88] A. Gharbi *et al.*, “Pillars fabrication by DSA lithography: material and process options,” in *Proc.SPIE*, 2018, vol. 10586.

[89] X. Xu *et al.*, “Site-controlled formation of single Si nanocrystals in a buried SiO2 matrix using ion beam mixing,” *Beilstein J. Nanotechnol.*, vol. 9, pp. 2883–2892, 2018.

[90] M. Strobel, “Modeling and Computer Simulation of Ion Beam Synthesis of Nanos- tructures,” TU Dresden, 1999.

[91] M. Strobel, “Modeling and computer simulation of ion beam synthesis of nanostructures,” 1999.

[92] P. W. Voorhees and M. E. Glicksman, “Solution to the multi-particle diffusion problem with applications to ostwald ripening—II. Computer simulations,” *Acta Metall.*, vol. 32, no. 11, pp. 2013–2030, Nov. 1984.

[93] I. M. Lifshitz and V. V. Slyozov, “The kinetics of precipitation from supersaturated solid solutions,” *J. Phys. Chem. Solids*, vol. 19, no. 1–2, pp. 35–50, Apr. 1961.

[94] C. Wagner, “Theorie der Alterung von Niederschlägen durch Umlösen (Ostwald-Reifung),” *Zeitschrift für Elektrochemie, Berichte der Bunsengesellschaft für Phys. Chemie*, vol. 65, no. 7-8, pp. 581–591, 1961.

[95] R. C. Ball and R. L. H. Essery, “Spinodal decomposition and pattern formation near surfaces,” *J. Phys. Condens. Matter*, vol. 2, no. 51, pp. 10303–10320, 1990.

[96] K. Binder and P. Fratzl, “Spinodal decomposition,” *Phase Transform. Mater.*, pp. 409–480, 2001.

[97] J. F. Marko, “Influence of surface interactions on spinodal decomposition,” *Phys. Rev. E*, vol. 48, no. 4, pp. 2861–2879, Oct. 1993.

[98] V. A. Borodin, K.-H. Heinig, and S. Reiss, “Self-organization kinetics in finite precipitate ensembles during coarsening,” *Phys. Rev. B*, vol. 56, 1997.

[99] S. Reiss and K. H. Heinig, “Ostwald ripening during ion beam synthesis — a computer simulation for inhomogeneous systems,” *Nucl. Instruments Methods Phys. Res. Sect. B Beam Interact. with Mater. Atoms*, vol. 84, no. 2, pp. 229–233, Feb. 1994.

[100] A. M. Lacasta, F. Sagués, J. M. Sancho, and I. M. Sokolov, “Evaporation and coarsening dynamics with open boundaries,” *Phys. Rev. E*, vol. 59, no. 1, pp. 189–193, Jan. 1999.

[101] G. Brown, A. Chakrabarti, and J. F. Marko, “Surface-induced nucleation,” *Phys. Rev. E*, vol. 50, no. 2, pp. 1674–1677, Aug. 1994.

[102] K. H. Heinig, T. Müller, B. Schmidt, M. Strobel, and W. Möller, “Interfaces under ion irradiation: growth and taming of nanostructures,” *Appl. Phys. A*, vol. 77, no. 1, pp. 17–25, Jun. 2003.

[103] T. Müller *et al.*, “Multi-dot floating-gates for nonvolatile semiconductor memories: Their ion beam synthesis and morphology,” *Appl. Phys. Lett.*, vol. 85, no. 12, pp. 2373–2375, Sep. 2004.

[104] B. Schmidt and K. -H. Heinig, “Ion Beam Synthesis Of Silicon Nano-Crystals For Electronics And Photonics,” *AIP Conf. Proc.*, vol. 1336, no. 1, pp. 233–238, Jun. 2011.

[105] S. Reiss, K.-H. Heinig, R. Weber, and W. Skorupa, “Is Self-Organisation During Ostwald Ripening a Crucial Process in Ion Beam Synthesis ?,” *MRS Proc.*, vol. 316, p. 819, 1993.

[106] S. Roy and A. Maciołek, “Phase separation around a heated colloid in bulk and under confinement,” *Soft Matter*, vol. 14, no. 46, pp. 9326–9335, 2018.

[107] R. Kurita, “Control of pattern formation during phase separation initiated by a propagated trigger,” *Sci. Rep.*, vol. 7, no. 1, p. 6912, 2017.

[108] W. Köhler, A. Krekhov, and W. Zimmermann, “Thermal Diffusion in Polymer Blends: Criticality and Pattern Formation BT - Complex Macromolecular Systems I,” A. H. E. Müller and H.-W. Schmidt, Eds. Berlin, Heidelberg: Springer Berlin Heidelberg, 2010, pp. 145–198.

[109] A. D. Brailsford, “Diffusion to a random array of identical spherical sinks,” *J. Nucl. Mater.*, vol. 60, no. 3, pp. 257–278, 1976.

[110] E. Torino, R. Aruta, T. Sibillano, C. Giannini, and P. A. Netti, “Synthesis of semicrystalline nanocapsular structures obtained by Thermally Induced Phase Separation in nanoconfinement,” *Sci. Rep.*, vol. 6, p. 32727, Sep. 2016.

[111] T. Prüfer *et al.*, “Computer modeling of single-layer nanocluster formation in a thin SiO2 layer buried in Si by ion mixing and thermal phase decomposition,” *J. Appl. Phys.*, vol. 125, no. 22, p. 225708, 2019.

[112] M. Nastasi, N. Michael, J. Mayer, J. K. Hirvonen, and M. James, *Ion-solid interactions: fundamentals and applications*. Cambridge University Press, 1996.

[113] P. Sigmund, “Particle penetration and radiation effects, vol. 151 of Springer Series in Solid-State Sciences.” Springer, Berlin, 2006.

[114] C. Bonafos *et al.*, “Si nanocrystals by ultra-low-energy ion beam-synthesis for non-volatile memory applications,” *Solid. State. Electron.*, vol. 49, pp. 1734–1744, Nov. 2005.

[115] B. Schmidt, D. Grambole, and F. Herrmann, “Impact of ambient atmosphere on as-implanted amorphous insulating layers,” *Nucl. Inst. Methods Phys. Res. B*, vol. 191, no. 1–4, pp. 482–486, 2002.

[116] A. Fick, “Ueber Diffusion,” *Ann. Phys.*, vol. 170, no. 1, pp. 59–86, Jan. 1855.

[117] R. O. Jones and O. Gunnarsson, “The density functional formalism, its applications and prospects,” *Rev. Mod. Phys.*, vol. 61, no. 3, pp. 689–746, Jul. 1989.

[118] J. P. Perdew and Y. Wang, “Accurate and simple analytic representation of the electron-gas correlation energy,” *Phys. Rev. B*, vol. 45, no. 23, pp. 13244–13249, Jun. 1992.

[119] S. Kurth, J. P. Perdew, and P. Blaha, “Molecular and solid-state tests of density functional approximations: LSD, GGAs, and meta-GGAs,” *Int. J. Quantum Chem.*, vol. 75, no. 4-5, pp. 889–909, Jan. 1999.

[120] C. Fridlund, J. Laakso, K. Nordlund, and F. Djurabekova, “Atomistic simulation of ion irradiation of semiconductor heterostructures,” *Nucl. Instruments Methods Phys. Res. Sect. B Beam Interact. with Mater. Atoms*, vol. 409, pp. 14–18, 2017.

[121] E. Rutherford, “LXXIX. The scattering of α and β particles by matter and the structure of the atom,” *London, Edinburgh, Dublin Philos. Mag. J. Sci.*, vol. 21, no. 125, pp. 669–688, May 1911.

[122] H. Bethe, “The theory of the passage of rapid neutron radiation through matter,” *Ann. Phys.*, vol. 5, no. 3, pp. 325–400, 1930.

[123] M. Born, “Quantum mechanics in impact processes,” *Z. Phys*, vol. 38, pp. 803–827, 1926.

[124] N. Bohr, “II. On the theory of the decrease of velocity of moving electrified particles on passing through matter,” *London, Edinburgh, Dublin Philos. Mag. J. Sci.*, vol. 25, no. 145, pp. 10–31, 1913.

[125] J. J. Thomson, “XLII. Ionization by moving electrified particles,” *London, Edinburgh, Dublin Philos. Mag. J. Sci.*, vol. 23, no. 136, pp. 449–457, 1912.

[126] W. Eckstein, *Computer simulation of ion-solid interactions*, vol. 10. Springer Science & Business Media, 2013.

[127] J. B. Gibson, A. N. Goland, M. Milgram, and G. Vineyard, “Dynamics of radiation damage,” *Phys. Rev.*, vol. 120, no. 4, p. 1229, 1960.

[128] P. Sigmund, “Theory of sputtering. I. Sputtering yield of amorphous and polycrystalline targets,” *Phys. Rev.*, vol. 184, no. 2, p. 383, 1969.

[129] M. W. Thompson, “Defects and radiation damage in metals,” *Defects Radiat. Damage Met. by MW Thompson, Cambridge, UK Cambridge Univ. Press. 1974*, 1974.

[130] G. Carter and W. A. Grant, *Ion implantation of semiconductors*. Hodder Arnold, 1976.

[131] M. Meddelelser, “Ion Beam Science: Solved and Unsolved Problems,” 2006.

[132] P. Sigmund, *Stopping of heavy ions: a theoretical approach*, vol. 204. Springer Science & Business Media, 2004.

[133] P. Sigmund, “Collision theory of displacement damage, ion ranges, and sputtering,” Univ. of Copenhagen, 1972.

[134] W. Möller, W. Eckstein, and J. P. Biersack, “Tridyn-binary collision simulation of atomic collisions and dynamic composition changes in solids,” *Comput. Phys. Commun.*, vol. 51, no. 3, pp. 355–368, 1988.

[135] W. Möller and W. Eckstein, “Tridyn — A TRIM simulation code including dynamic composition changes,” *Nucl. Instruments Methods Phys. Res. Sect. B Beam Interact. with Mater. Atoms*, vol. 2, no. 1, pp. 814–818, 1984.

[136] M. T. Robinson and I. M. Torrens, “Computer simulation of atomic-displacement cascades in solids in the binary-collision approximation,” *Phys. Rev. B*, vol. 9, no. 12, pp. 5008–5024, Jun. 1974.

[137] J. P. Biersack and L. G. Haggmark, “A Monte Carlo computer program for the transport of energetic ions in amorphous targets,” *Nucl. Instruments Methods*, vol. 174, no. 1, pp. 257–269, 1980.

[138] J. F. Ziegler, J. P. Biersack, and U. Littmark, “Stopping power and ranges of ion in matter,” *Pergamon, New York*, vol. 1, 1985.

[139] W. D. Wilson, L. G. Haggmark, and J. P. Biersack, “Calculations of nuclear stopping, ranges, and straggling in the low-energy region,” *Phys. Rev. B*, vol. 15, no. 5, p. 2458, 1977.

[140] O. B. Firsov, “A qualitative interpretation of the mean electron excitation energy in atomic collisions,” *Zhur. Eksptl’. i Teoret. Fiz.*, vol. 36, 1959.

[141] E. Fermi and E. Teller, “The capture of negative mesotrons in matter,” *Phys. Rev.*, vol. 72, no. 5, p. 399, 1947.

[142] J. F. Ziegler, “SRIM-2003,” *Nucl. instruments methods Phys. Res. Sect. B Beam Interact. with Mater. atoms*, vol. 219, pp. 1027–1036, 2004.

[143] W. Möller, “A computer study of the collisional mixing of Pt in Si,” *Nucl. Instruments Methods Phys. Res. Sect. B Beam Interact. with Mater. Atoms*, vol. 15, no. 1–6, pp. 688–691, 1986.

[144] P. Sigmund and A. Gras-Marti, “Theoretical aspects of atomic mixing by ion beams,” *Nucl. Instruments Methods*, vol. 182, pp. 25–41, 1981.

[145] J. P. Biersack and W. Eckstein, “Sputtering studies with the Monte Carlo program TRIM. SP,” *Appl. Phys. A*, vol. 34, no. 2, pp. 73–94, 1984.

[146] W. Möller and W. Eckstein, “Ion mixing and recoil implantation simulations by means of TRIDYN,” *Nucl. Instruments Methods Phys. Res. Sect. B Beam Interact. with Mater. Atoms*, vol. 7, pp. 645–649, 1985.

[147] P. K. Haff and Z. E. Switkowski, “Ion-beam-induced atomic mixing,” *J. Appl. Phys.*, vol. 48, no. 8, pp. 3383–3386, 1977.

[148] A. Oliva, R. Kelly, and G. Falcone, “Sputtering of multicomponent materials: The diffusion limit,” *Surf. Sci.*, vol. 166, no. 2–3, pp. 403–418, 1986.

[149] B. Liedke, “Ion beam processing of surfaces and interfaces - Modeling and atomsitic simulations,” TU Dresden, 2011.

[150] K. Binder and D. Heermann, *Monte Carlo Simulation in Statistical Physics*. Springer Series in Solid State Sciences, 1992.

[151] N. Metropolis, A. W. Rosenbluth, M. N. Rosenbluth, A. H. Teller, and E. Teller, “Equation of State Calculations by Fast Computing Machines,” *J. Chem. Phys.*, vol. 21, no. 6, pp. 1087–1092, 1953.

[152] M. E. J. Newman and G. T. Barkema, *Monte Carlo Methods in Statistical Physics*. Clarendon Press, 1999.

[153] M. Strobel, K.-H. Heinig, and W. Möller, “Three-dimensional domain growth on the size scale of the capillary length: Effective growth exponent and comparative atomistic and mean-field simulations,” *Phys. Rev. B*, vol. 64, no. 24, p. 245422, 2001.

[154] P. W. Voorhees and M. E. Glicksman, “Solution to the multi-particle diffusion problem with applications to Ostwald ripening—I. Theory,” *Acta Metall.*, vol. 32, no. 11, pp. 2001–2011, Nov. 1984.

[155] J. W. Cahn, “On spinodal decomposition,” *Acta Metall.*, vol. 9, no. 9, pp. 795–801, Sep. 1961.

[156] J. W. Cahn and J. E. Hilliard, “Free Energy of a Nonuniform System. I. Interfacial Free Energy,” *J. Chem. Phys.*, vol. 28, no. 2, pp. 258–267, 1958.

[157] J. W. Cahn, “Free Energy of a Nonuniform System. II. Thermodynamic Basis,” *J. Chem. Phys.*, vol. 30, no. 5, pp. 1121–1124, 1959.

[158] J. W. Cahn and J. E. Hilliard, “Free Energy of a Nonuniform System. III. Nucleation in a Two-Component Incompressible Fluid,” *J. Chem. Phys.*, vol. 31, no. 3, pp. 688–699, 1959.

[159] A. F. Voter, “Classically exact overlayer dynamics: Diffusion of rhodium clusters on Rh(100),” *Phys. Rev. B*, vol. 34, no. 10, pp. 6819–6829, Nov. 1986.

[160] M. Rao, M. Kalos, and J. Marro, “Time evolution of a quenched binary alloy. III. Computer simulation of a two-dimensional model system,” *Phys. Rev. B*, vol. 13, 1976.

[161] J. Marro, A. Bortz, M. Kalos, and J. Lebowitz, “Time evolution of a quenched binary alloy. II. Computer simulation of a three-dimensional model system,” *Phys. Rev. B*, vol. 12, 1975.

[162] D. Friedrich *et al.*, “Sponge-like Si-SiO2 nanocomposite—Morphology studies of spinodally decomposed silicon-rich oxide,” *Appl. Phys. Lett.*, vol. 103, no. 13, p. 131911, Sep. 2013.

[163] M. Roussel, E. Talbot, C. Pareige, R. Pratibha Nalini, F. Gourbilleau, and P. Pareige, “Confined phase separation in SiOX nanometric thin layers,” *Appl. Phys. Lett.*, vol. 103, p. 203109, Nov. 2013.

[164] M. Strobel *et al.*, “Ion beam synthesis of gold nanoclusters in SiO2: Computer simulations versus experiments,” *Nucl. Instruments Methods Phys. Res. Sect. B Beam Interact. with Mater. Atoms*, vol. 147, no. 1–4, pp. 343–349, Jan. 1999.

[165] T. Michely, M. Kalff, G. Comsa, M. Strobel, and K.-H. Heinig, “Step Edge Diffusion and Step Atom Detachment in Surface Evolution: Ion Erosion of Pt(111),” *Phys. Rev. Lett.*, vol. 86, no. 12, pp. 2589–2592, 2001.

[166] T. Michely, M. Kalff, G. Comsa, M. Strobel, and K.-H. Heinig, “Coarsening mechanisms in surface morphological evolution,” *J. Phys. Condens. Matter*, vol. 14, no. 16, pp. 4177–4185, Apr. 2002.

[167] T. Müller, K.-H. Heinig, and B. Schmidt, “Template-directed self-assembly of buried nanowires and the pearling instability,” *Mater. Sci. Eng. C*, vol. 19, no. 1–2, pp. 209–213, Jan. 2002.

[168] S. Il Park, B.-J. Lee, and H. Mo Lee, “Estimation of order–disorder transition temperature in Pt–Co alloy by Monte Carlo simulation using modified embedded atom method,” *Scr. Mater.*, vol. 45, pp. 495–502, 2001.

[169] H. Bernas *et al.*, “Ordering Intermetallic Alloys by Ion Irradiation: A Way to Tailor Magnetic Media,” *Phys. Rev. Lett.*, vol. 91, no. 7, p. 77203, Aug. 2003.

[170] M. Müller and K. Albe, “Lattice Monte Carlo simulations of FePt nanoparticles: Influence of size, composition, and surface segregation on order-disorder phenomena,” *Phys. Rev. B*, vol.

72, no. 9, p. 94203, Sep. 2005.

[171] W. Schweika, *Disordered Alloys*. Springer Berlin Heidelberg, 1998.

[172] K. Binder, “Ordering of the Face-Centered-Cubic Lattice with Nearest-Neighbor Interaction,” *Phys. Rev. Lett. - PHYS REV LETT*, vol. 45, pp. 811–814, 1980.

[173] T. A. Abinandanan, F. Haider, and G. Martin, “Computer simulations of diffusional phase transformations: Monte Carlo algorithm and application to precipitation of ordered phases,” *Acta Mater.*, vol. 46, no. 12, pp. 4243–4255, Jul. 1998.

[174] S. Mitchell and D. Landau, “Phase Separation in a Compressible 2D Ising Model,” *Phys. Rev. Lett.*, vol. 97, p. 25701, 2006.

[175] T. Müller, K.-H. Heinig, and W. Möller, “Size and location control of Si nanocrystals at ion beam synthesis in thin SiO2 films,” *Appl. Phys. Lett.*, vol. 81, no. 16, pp. 3049–3051, 2002.

[176] A. A. Markov, “Rasprostranenie zakona bol’shih chisel na velichiny, zavisyaschie drug ot druga, Izvestiya Fiziko-Matematicheskogo Obschestva pri Kazanskom Universitete, 2-ya seriya 15, 135--156,” *Russ. English Transl. law large numbers to Depend. Quant.*, 1906.

[177] B. Liedke, K. Heinig, and W. Möller, “Surface morphology and interface chemistry under ion and thermal kinetics,” *Nucl. Inst. Methods Phys. Res. B*, vol. 316, pp. 56–61, 2013.

[178] T. Müller, K.-H. Heinig, and W. Möller, “Nanocrystal formation in Si implanted thin SiO2 layers under the influence of an absorbing interface,” *Mater. Sci. Eng. B*, vol. 101, no. 1, pp. 49–54, 2003.

[179] J. Song, L. R. Corrales, G. Kresse, and H. Jónsson, “Migration of O vacancies in \ensuremath{\alpha}-quartz: The effect of excitons and electron holes,” *Phys. Rev. B*, vol. 64, no. 13, p. 134102, Sep. 2001.

[180] N. Mousseau, G. T. Barkema, and S. W. de Leeuw, “Elementary mechanisms governing the dynamics of silica,” *J. Chem. Phys.*, vol. 112, no. 2, pp. 960–964, 2000.

[181] A. Bortz, M. Kalos, J. Lebowitz, and M. A. Zendejas, “Time evolution of a quenched binary alloy: computer simulation of a two-dimensional model system,” *Phys. Rev. B*, vol. 10, pp. 535–541, 1974.

[182] D. A. Huse, “Corrections to late-stage behavior in spinodal decomposition: Lifshitz-Slyozov scaling and Monte Carlo simulations,” *Phys. Rev. B*, vol. 34, no. 11, pp. 7845–7850, 1986.

[183] J. G. Amar, F. E. Sullivan, and R. D. Mountain, “Monte Carlo study of growth in the two-dimensional spin-exchange kinetic Ising model,” *Phys. Rev. B*, vol. 37, no. 1, pp. 196–208, Jan. 1988.

[184] J. Marro, J. Lebowitz, and M. Kalos, “Computer Simulation of the Time Evolution of a Quenched Model Alloy in the Nucleation Region,” *Phys. Rev. Lett. - PHYS REV LETT*, vol. 43, pp. 282–285, 1979.

[185] E. Ising, “Beitrag zur Theorie des Ferromagnetismus,” *Zeitschrift für Phys.*, vol. 31, no. 1, pp. 253–258, Feb. 1925.

[186] K. Kawasaki, “Diffusion Constants near the Critical Point for Time-Dependent Ising Models. I,” *Phys. Rev.*, vol. 145, no. 1, pp. 224–230, 1966.

[187] G. H. Vineyard, “Frequency factors and isotope effects in solid state rate processes,” *J. Phys. Chem. Solids*, vol. 3, no. 1–2, pp. 121–127, Jan. 1957.

[188] F. Cleri and V. Rosato, “Tight-binding potentials for transition metals and alloys,” *Phys. Rev. B*, vol. 48, no. 1, pp. 22–33, Jul. 1993.

[189] E. W. Montroll and G. H. Weiss, “Random Walks on Lattices. II,” *J. Math. Phys.*, vol. 6, no. 2,

pp. 167–181, 1965.

[190] D. Mathiot, M. Perego, M. Fanciulli, and G. Ben Assayag, “Evidence for a dose dependence for thermal redistribution of implanted silicon in SiO2,” *Nucl. Instruments Methods Phys. Res. Sect. B Beam Interact. with Mater. Atoms*, vol. 254, no. 1, pp. 139–142, Jan. 2007.

[191] D. Tsoukalas, C. Tsamis, and P. Normand, “Diffusivity measurements of silicon in silicon dioxide layers using isotopically pure material,” *J. Appl. Phys.*, vol. 89, no. 12, pp. 7809–7813, 2001.

[192] D. Mathiot *et al.*, “Silicon self-diffusivity measurement in thermal SiO2 by 30Si/28Si isotopic exchange,” *J. Appl. Phys.*, vol. 94, no. 3, pp. 2136–2138, 2003.

[193] T. Takahashi *et al.*, “Self-diffusion of Si in thermally grown SiO2 under equilibrium conditions,” *J. Appl. Phys.*, vol. 93, no. 6, pp. 3674–3676, 2003.

[194] D. A. Litton and S. H. Garofalini, “Vitreous silica bulk and surface self-diffusion analysis by molecular dynamics,” *J. Non. Cryst. Solids*, vol. 217, no. 2–3, pp. 250–263, Sep. 1997.

[195] W. Kob and K. Binder, “How can computer simulations contribute to the understanding of the dynamics of glasses and glass melts?,” 1998.

[196] G. Brebec, R. Seguin, C. Sella, J. Bevenot, and J. C. Martin, “Diffusion du silicium dans la silice amorphe,” *Acta Metall.*, vol. 28, no. 3, pp. 327–333, Mar. 1980.

[197] O. Jaoul, F. Béjina, F. Élie, and F. Abel, “Silicon Self-Diffusion in Quartz,” *Phys. Rev. Lett.*, vol. 74, no. 11, pp. 2038–2041, 1995.

[198] F. Béjina and O. Jaoul, “Silicon self-diffusion in quartz and diopside measured by nuclear micro-analysis methods,” *Phys. Earth Planet. Inter.*, vol. 97, no. 1–4, pp. 145–162, Oct. 1996.

[199] S. Fukatsu *et al.*, “Effect of the Si/SiO2 interface on self-diffusion of Si in semiconductor-grade SiO2,” *Appl. Phys. Lett.*, vol. 83, no. 19, pp. 3897–3899, Nov. 2003.

[200] F. Iacona, C. Bongiorno, C. Spinella, S. Boninelli, and F. Priolo, “Formation and evolution of luminescent Si nanoclusters produced by thermal annealing of SiOx films,” *J. Appl. Phys.*, vol. 95, no. 7, pp. 3723–3732, 2004.

[201] L. A. Nesbit, “Annealing characteristics of Si-rich SiO2 films,” *Appl. Phys. Lett.*, vol. 46, no. 1, pp. 38–40, 1985.

[202] B. J. HINDS, F. Wang, and D. M. WOLFE, “Investigation of postoxidation thermal treatments of Si/SiO2 interface in relationship to the kinetics of amorphous Si suboxide decomposition,” *J. Vac. Sci. Technol. B*, vol. 16, pp. 2171–2176, 1998.

[203] C. Haas, “The diffusion of oxygen in silicon and germanium,” *J. Phys. Chem. Solids*, vol. 15, no. 1, pp. 108–111, 1960.

[204] J. Gass, H. H. Müller, H. Stüssi, and S. Schweitzer, “Oxygen diffusion in silicon and the influence of different dopants,” *J. Appl. Phys.*, vol. 51, no. 4, pp. 2030–2037, 1980.

[205] J. W. Corbett, R. S. McDonald, and G. D. Watkins, “The configuration and diffusion of isolated oxygen in silicon and germanium,” *J. Phys. Chem. Solids*, vol. 25, no. 8, pp. 873–879, 1964.

[206] Y. Itoh and T. Nozaki, “Solubility and Diffusion Coefficient of Oxygen in Silicon,” *Jpn. J. Appl. Phys.*, vol. 24, no. Part 1, No. 3, pp. 279–284, 1985.

[207] J. C. Mikkelsen, “Diffusivity of oxygen in silicon during steam oxidation,” *Appl. Phys. Lett.*, vol. 40, no. 4, pp. 336–337, Feb. 1982.

[208] Z. Jiang and R. A. Brown, “Atomistic Calculation of Oxygen Diffusivity in Crystalline Silicon,” *Phys. Rev. Lett.*, vol. 74, no. 11, pp. 2046–2049, Mar. 1995.

[209] R. C. Newman, “Oxygen Diffusion and Aggregation in Silicon,” *Defect Diffus. Forum*, vol. 143–147, pp. 993–998, 1997.

[210] M. Stavola, J. R. Patel, L. C. Kimerling, and P. E. Freeland, “Diffusivity of oxygen in silicon at the donor formation temperature,” *Appl. Phys. Lett.*, vol. 42, no. 1, pp. 73–75, Jan. 1983.

[211] S.-T. Lee and D. Nichols, “Diffusivity and Diffusion Mechanism of Oxygen in Silicon,” *MRS Proc.*, vol. 59, p. 31, 1985.

[212] F. M. Livingston *et al.*, “An infrared and neutron scattering analysis of the precipitation of oxygen in dislocation-free silicon,” *J. Phys. C Solid State Phys.*, vol. 17, no. 34, pp. 6253–6276, 1984.

[213] H. J. Hrostowski and R. H. Kaiser, “The solubility of oxygen in silicon,” *J. Phys. Chem. Solids*, vol. 9, no. 3–4, pp. 214–216, Mar. 1959.

[214] A. R. Bean and R. C. Newman, “The solubility of carbon in pulled silicon crystals,” *J. Phys. Chem. Solids*, vol. 32, no. 6, pp. 1211–1219, Jan. 1971.

[215] J. J. C. Mikkelsen, “Self-Diffusivity of Network Oxygen in Vitreous SiO2,” *Appl. Phys. Lett.*, vol. 45, pp. 1187–1189, 1985.

[216] M. Roussel, E. Talbot, P. Pareige, and F. Gourbilleau, “Influence of the supersaturation on Si diffusion and growth of Si nanoparticles in silicon-rich silica,” *J. Appl. Phys.*, vol. 113, no. 6, p. 63519, 2013.

[217] S. M. Schnurre, J. Gröbner, and R. Schmid-Fetzer, “Thermodynamics and phase stability in the Si–O system,” *J. Non. Cryst. Solids*, vol. 336, no. 1, pp. 1–25, 2004.

[218] O. Aleksandrov and A. Dus’, “Model of Thermal Oxidation of Silicon with Diffusion Coefficient Relaxation,” *Semiconductors*, vol. 44, pp. 1637–1643, Dec. 2010.

[219] J. C. Mikkelsen, “The Diffusivity and Solubility of Oxygen in Silicon,” *MRS Proc.*, vol. 59, p. 19, 1985.

[220] J. D. Gunton, “Kinetics of First-Order Phase Transitions,” in *Magnetic Phase Transitions*, 1983, pp. 154–169.

[221] R. Wagner, R. Kampmann, and P. W. Voorhees, “Homogeneous Second-Phase Precipitation,” in *Phase Transformations in Materials*, John Wiley & Sons, Ltd, 2005, pp. 309–407.

[222] B. J. Alder and T. E. Wainwright, “Studies in Molecular Dynamics. I. General Method,” *J. Chem. Phys.*, vol. 31, no. 2, pp. 459–466, 1959.

[223] D. C Rapaport, *The art of molecular dynamics simulation*. 2004.

[224] G. Schmitz and P. Haasen, “Decomposition of an Al□Li alloy—The early stages observed by HREM,” *Acta Metall. Mater.*, vol. 40, no. 9, pp. 2209–2217, Sep. 1992.

[225] H. A. Calderon, P. W. Voorhees, J. L. Murray, and G. Kostorz, “Ostwald ripening in concentrated alloys,” *Acta Metall. Mater.*, vol. 42, no. 3, pp. 991–1000, Mar. 1994.

[226] M. Marder, “Correlations and Ostwald ripening,” *Phys. Rev. A*, vol. 36, no. 2, pp. 858–874, Jul. 1987.

[227] J. A. Marqusee and J. Ross, “Theory of Ostwald ripening: Competitive growth and its dependence on volume fraction,” *J. Chem. Phys.*, vol. 80, no. 1, pp. 536–543, 1984.

[228] K. Tsumuraya and Y. Miyata, “Coarsening models incorporating both diffusion geometry and volume fraction of particles,” *Acta Metall.*, vol. 31, no. 3, pp. 437–452, Mar. 1983.

[229] A. . Brailsford and P. Wynblatt, “The dependence of ostwald ripening kinetics on particle volume fraction,” *Acta Metall.*, vol. 27, no. 3, pp. 489–497, Mar. 1979.

[230] P. W. Voorhees, “The theory of Ostwald ripening,” *J. Stat. Phys.*, vol. 38, no. 1, pp. 231–252, Jan. 1985.

[231] J. H. Yao, K. R. Elder, H. Guo, and M. Grant, “Theory and simulation of Ostwald ripening,” *Phys. Rev. B*, vol. 47, no. 21, pp. 14110–14125, Jun. 1993.

[232] S. Reiss and K.-H. Heinig, “Self-structuring of buried SiO2 precipitate layers during IBS: A computer simulation,” *Nucl. Instruments Methods Phys. Res. Sect. B Beam Interact. with Mater. Atoms*, vol. 112, no. 1–4, pp. 223–227, May 1996.

[233] K. Binder and P. Fratzl, “Spinodal Decomposition,” in *Phase Transformations in Materials*, John Wiley & Sons, Ltd, 2005, pp. 409–480.

[234] M. Perego, S. Ferrari, S. Spiga, E. Bonera, M. Fanciulli, and V. Soncini, “Time of flight secondary ion mass spectrometry study of silicon nanoclusters embedded in thin silicon oxide layers,” *Appl. Phys. Lett.*, vol. 82, no. 1, pp. 121–123, 2003.

[235] G. Ben Assayag, C. Bonafos, M. Carrada, A. Claverie, P. Normand, and D. Tsoukalas, “Transmission electron microscopy measurements of the injection distances in nanocrystal-based memories,” *Appl. Phys. Lett.*, vol. 82, no. 2, pp. 200–202, 2003.

[236] M. Carrada *et al.*, “Effect of ion energy and dose on the positioning of 2D-arrays of Si nanocrystals ion beam synthesized in thin SiO2 layers,” *Phys. E Low-dimensional Syst. Nanostructures*, vol. 17, pp. 513–515, Apr. 2003.

[237] P. Normand *et al.*, “Formation of 2-D arrays of semiconductor nanocrystals or semiconductor-rich nanolayers by very low-energy Si or Ge ion implantation in silicon oxide films,” *Nucl. Instruments Methods Phys. Res. Sect. B Beam Interact. with Mater. Atoms*, vol. 178, no. 1–4, pp. 74–77, May 2001.

[238] C. Bonafos *et al.*, “Manipulation of two-dimensional arrays of Si nanocrystals embedded in thin SiO2 layers by low energy ion implantation,” *J. Appl. Phys.*, vol. 95, no. 10, pp. 5696–5702, 2004.

[239] I. Iosilevskiy, V. Gryaznov, and A. Solov’ev, “Properties of high-temperature phase diagram and critical point parameters in silica,” *High Temp. Press.*, vol. 43, 2013.

[240] R. Becker and W. Döring, “Kinetische Behandlung der Keimbildung in übersättigten Dämpfen,” *Ann. Phys.*, vol. 416, no. 8, pp. 719–752, 1935.

[241] M. Volmer and A. Weber, “Keimbildung in übersättigten Gebilden,” *Zeitschrift für Phys. Chemie*, vol. 119, no. 1, pp. 277–301, 1926.

[242] Y. B. Zeldovich, “On the theory of new phase formation: cavitation,” *Acta Physicochem. USSR*, vol. 18, p. 1, 1943.

[243] W. Kurz and F. Fischer, “J.(1986) Fundamentals of Solidification,” *Trans Tech Publ. Switz.*, vol. 54.

[244] D. A. Porter, K. E. Easterling, and M. Sherif, *Phase Transformations in Metals and Alloys, (Revised Reprint)*. CRC press, 2009.

[245] J. E. McDonald, “Homogeneous nucleation of vapor condensation. I. Thermodynamic aspects,” *Am. J. Phys.*, vol. 30, no. 12, pp. 870–877, 1962.

[246] T. Sugimoto, *Monodispersed particles*. Elsevier, 2001.

[247] M. E. Glicksman, “Diffusion in solids: field theory, solid-state principles, and applications,” *New York*, pp. 54–56, 2000.

[248] A. Scheludko, B. V Toshev, and D. Platikanov, “Goodrich FC, Rusanov AI (eds) The Modern Theory of Capillarity.” Akademie-Verlag, Berlin, 1981.

[249] J. D. Livingston, “Critical particle size for precipitation hardening,” *Trans. Am. Inst. Min. Metall. Eng.*, vol. 215, no. 4, pp. 566–571, 1959.

[250] A. J. Ardell and R. B. Nicholson, “The coarsening of γ’in Ni-Al alloys,” *J. Phys. Chem. Solids*, vol. 27, no. 11–12, pp. 1793–1794, 1966.

[251] C. K. L. Davies, P. Nash, and R. N. Stevens, “Precipitation in ni-co-al alloys,” *J. Mater. Sci.*, vol. 15, no. 6, pp. 1521–1532, 1980.

[252] M. Tokuyama and K. Kawazaki, “Statistical-mechanical theory of coarsening of spherical droplets,” *Phys. A Stat. Mech. its Appl.*, vol. 123, no. 2–3, pp. 386–411, 1984.

[253] R. J. White, “The particle size distributions in systems evolving from interface-controlled to diffusion-controlled coarsening kinetics,” *Mater. Sci. Eng.*, vol. 40, no. 1, pp. 15–20, 1979.

[254] D. Lee, J.-Y. Huh, D. Jeong, J. Shin, A. Yun, and J. Kim, “Physical, mathematical, and numerical derivations of the Cahn–Hilliard equation,” *Comput. Mater. Sci.*, vol. 81, pp. 216–225, Jan. 2014.

[255] A. Johannes, H. Holland-Moritz, and C. Ronning, “Ion beam irradiation of nanostructures: sputtering, dopant incorporation, and dynamic annealing,” *Semicond. Sci. Technol.*, vol. 30, no. 3, p. 33001, 2015.

[256] V. Beyer, B. Schmidt, K.-H. Heinig, and K.-H. Stegemann, “Light emitting field effect transistor with two self-aligned Si nanocrystal layers,” *Appl. Phys. Lett.*, vol. 95, p. 193501, Dec. 2009.

[257] P. Sigmund, “Mechanism of Ion Beam Induced Mixing of Layered Solids,” vol. 46, pp. 43–46, 1983.

[258] M. Carlo, P. Bellon, Y. Grandjean, and M. Przybylowicz, “Phase evolution under irradiation :,” vol. 102, pp. 72–76, 1995.

[259] Blender Online Community, “Blender - a 3D modelling and rendering package.” Blender Institute, Amsterdam, 2016.

[260] H. J. Fitting *et al.*, “Electron microscopic imaging of an ion beam mixed SiO2/Si interface correlated with photo- and cathodoluminescence,” vol. 1108, no. 6, pp. 1101–1108, 2012.

[261] H. J. Fitting, L. Fitting Kourkoutis, R. Salh, M. V. Zamoryanskaya, and B. Schmidt, “Silicon nanocluster aggregation in SiO2 Si layers,” vol. 123, no. 1, pp. 117–123, 2010.

[262] W. Möller and M. Posselt, “TRIDYN_FZR user manual Wissenschaftlich-Technische Berichte Forschungszentrum Rossendorf.” FZR-317, 2001.

[263] Y. Tu, Z. Mao, R. D. Noebe, and D. Seidman, *Morphological, nanostructural, and compositional evolution during phase separation of a model Ni-Al-Mo superalloy: Atom-probe tomographic experiments and lattice-kinetic Monte Carlo simulations*. 2018.

[264] J. Zhou *et al.*, “Effect of solution treatment on spinodal decomposition during aging of an Fe-46.5 at.% Cr alloy,” *J. Mater. Sci.*, vol. 52, no. 1, pp. 326–335, 2017.

[265] H. H. Andersen, “The depth resolution of sputter profiling,” *Appl. Phys.*, vol. 18, no. 2, pp. 131–140, 1979.

[266] D. Marton, “Wiley Series in ion Chemistry and Physics.” Wiley, Chichester, 1994.

[267] S. J. Zinkle and C. Kinoshita, “Defect production in ceramics,” *J. Nucl. Mater.*, vol. 251, pp. 200–217, 1997.

[268] B. Wang, Y. Yu, I. Pignatelli, G. Sant, and M. Bauchy, “Nature of radiation-induced defects in quartz,” *J. Chem. Phys.*, vol. 143, no. 2, p. 24505, 2015.

[269] J. S. Zhen *et al.*, “Molecular dynamics study of structural damage in amorphous silica induced

by swift heavy-ion radiation," *Radiat. Eff. Defects Solids*, vol. 171, pp. 1–10, Jun. 2016.

[270] P. Sigmund, "ON THE NUMBER OF ATOMS DISPLACED BY IMPLANTED IONS OR ENERGETIC RECOIL ATOMS," *Appl. Phys. Lett.*, vol. 14, pp. 114–117, Mar. 1969.

[271] G. H. Kinchin and R. S. Pease, "The Displacement of Atoms in Solids by Radiation," *Reports Prog. Phys.*, vol. 18, no. 1, pp. 1–51, 1955.

[272] D. Peak and R. S. Averback, "INFLUENCES OF THERMAL SPIKES IN ION BEAM mNG," vol. 8, pp. 561–565, 1985.

[273] A. Miotello and R. Kelly, "Ion-beam mixing with chemical guidance I. The bilayer problem," vol. 268, pp. 340–350, 1992.

[274] R. Collins and R. Collins, "Factors determining radiation-induced mixing at interfaces," vol. 7579, 1986.

[275] K. Nordlund, M. Ghaly, and R. S. Averback, "Mechanisms of ion beam mixing in metals and semiconductors," *J. Appl. Phys.*, vol. 83, no. 3, pp. 1238–1246, Feb. 1998.

[276] B. Park and H. Lee, "Ion-beam mixing in energetic collision cascades : Thermal-spike model and experiments," pp. 281–285, 1999.

[277] V. Cheng, M. Van Rossum, M. Nicolet, and W. L. Johnson, "Influence of chemical driving forces in ion mixing of metallic bilayers Influence of chemical driving forces in ion mixing of metallic bilayers," vol. 185, no. 1984, pp. 2–5, 1984.

[278] W. L. Johnson, Y. T. Cheng, M. Van Rossum, and M.-A. Nicolet, "When is thermodynamics relevant to ion-induced atomic rearrangements in metals?," *Nucl. Instruments Methods Phys. Res. Sect. B Beam Interact. with Mater. Atoms*, vol. 7–8, pp. 657–665, 1985.

[279] M. Van Rossum, Y. Cheng, M. Nicolet, and W. L. Johnson, "Correlation between cohesive energy and mixing rate in ion mixing of metallic bilayers," *Appl. Phys. Lett.*, vol. 46, no. 6, pp. 610–612, Mar. 1985.

[280] Z. Wang, Y. Li, and J. Zhang, "A DESCRIPTION OF THE ATOMIC PROCESSES FOR ION BEAM MIXING," vol. 13, pp. 453–456, 1986.

[281] B. V King and R. P. Webb, "Calculation of ion mixing and energy deposition using a modified version of TRIM," vol. 64, 1992.

[282] E. IBE, "PICOSECOND DIFFUSION IN A THERMAL SPIKE DURING ION MIXING," pp. 148–152, 1989.

[283] R. A. Enrique and P. Bellon, "Compositional patterning in immiscible alloys driven by irradiation," *Phys. Rev. B*, vol. 63, Apr. 2001.

[284] J. W. Mayer, B. Y. Tsaur, S. S. Lau, and L. S. Hung, "Ion-Beam-Induced Reactions in Metal-Semiconductor and Metal-Metal Thin Film Structures.," *Nucl. instruments methods*, vol. 182 /183, no. pt 1, pp. 1–13, 1980.

[285] R. S. Averback, L. J. Thompson, J. Moyle, and M. Schalit, "Ion beam mixing at nickel-silicon interfaces," vol. 1342, no. 1982, 1982.

[286] R. S. Averback, D. Peak, and L. J. Thompson, "Ion-beam mixing in pure and in immiscible copper bilayer systems," *Appl. Phys. A*, vol. 39, no. 1, pp. 59–64, 1986.

[287] J. Fine and D. Marton, "ION BOMBARDMENT INDUCED DIFFUSION: A CASE STUDY ON A SPUTTERED Ag/Ni LAYERED SYSTEM," *Period. Polytech. Chem. Eng.*, vol. 34, no. 1–3 SE–Articles, Aug. 2019.

[288] L. Q. Chen and J. Shen, "Applications of semi-implicit Fourier-spectral method to phase field equations," *Comput. Phys. Commun.*, vol. 108, no. 2, pp. 147–158, 1998.

[289] D. J. Eyre, “Unconditionally Gradient Stable Time Marching the Cahn-Hilliard Equation,” *MRS Proc.*, vol. 529, p. 39, 1998.

[290] N. Ahmed, T. Natarajan, and K. R. Rao, “Discrete Cosine Transform,” *IEEE Trans. Comput.*, vol. C-23, no. 1, pp. 90–93, 1974.

[291] A. K. Jain, “Image data compression: A review,” *Proc. IEEE*, vol. 69, no. 3, pp. 349–389, 1981.

[292] Www.scilab.org, “Free and Open Source software for numerical computation (Windows, Version 5.52) [Software].” 2016.

[293] A. E. Stuchbery and E. Bezak, “Thermal-Spike Lifetime from Picosecond-Duration Preequilibrium Effects in Hyperfine Magnetic Fields Following Ion Implantation,” *Phys. Rev. Lett. - PHYS REV LETT*, vol. 82, pp. 3637–3640, May 1999.

[294] R. E. Stoller, “1.11 - Primary Radiation Damage Formation,” R. J. M. B. T.-C. N. M. Konings, Ed. Oxford: Elsevier, 2012, pp. 293–332.

[295] R. E. Stoller, “Primary damage formation in irradiated materials,” *JOM*, vol. 48, no. 12, pp. 23–27, 1996.

[296] T. D. de la Rubia, R. S. Averback, R. Benedek, and W. E. King, “Role of thermal spikes in energetic displacement cascades,” *Phys. Rev. Lett.*, vol. 59, no. 17, pp. 1930–1933, Oct. 1987.

[297] D. E. Tsatis, “Transient diffusion in ion beam mixing,” vol. 115, no. 95, pp. 569–571, 1996.

[298] K. Nordlund and R. S. Averback, “Atomic displacement processes in irradiated amorphous and crystalline silicon,” *Appl. Phys. Lett.*, vol. 70, pp. 3103–3105, Jun. 1997.

[299] P. Sigmund, “Energy density and time constant of heavy-ion-induced elastic-collision spikes in solids,” *Appl. Phys. Lett.*, vol. 25, no. 3, pp. 169–171, Aug. 1974.

[300] K. Nordlund, L. Wei, Y. Zhong, and R. S. Averback, “Role of electron-phonon coupling on collision cascade development in Ni, Pd and Pt,” *Phys. Rev. B (Rapid Comm.)*, vol. 57, pp. 13965–13968, Jun. 1998.

[301] E. Zarkadoula, G. Samolyuk, and W. J. Weber, “Effects of the electron-phonon coupling activation in collision cascades,” *J. Nucl. Mater.*, vol. 490, pp. 317–322, 2017.

[302] S. Gupta *et al.*, “PbTe nanocrystal formation by interface mixing of Te Pb bilayer using low energy ions.pdf,” *Mater. Sci. Engeneering*, 2014.

[303] T. J. Colla, H. M. Urbassek, K. Nordlund, and R. S. Averback, “Ion-induced mixing and demixing in the immiscible Ni-Ag system,” *Phys. Rev. B*, vol. 63, no. 10, p. 104206, Feb. 2001.

[304] R. A. Enrique and P. Bellon, “Compositional Patterning in Systems Driven by Competing Dynamics Of Different Length Scale,” *Phys. Rev. Lett.*, vol. 84, pp. 2885–2888, Apr. 2000.

[305] J. Buescu, “Attractors in Dynamical Systems BT - Exotic Attractors: From Liapunov Stability to Riddled Basins,” J. Buescu, Ed. Basel: Birkhäuser Basel, 1997, pp. 1–33.

[306] F. F. Abraham and A. C. Zettlemoyer, “Homogeneous Nucleation Theory,” *Phys. Today*, vol. 27, p. 52, 1974.

[307] J. W. Gibbs, “On the equilibrium of heterogeneous substances,” *Am. J. Sci.*, no. 96, pp. 441–458, 1878.

[308] P. C. Hohenberg and B. I. Halperin, “Theory of dynamic critical phenomena,” *Rev. Mod. Phys.*, vol. 49, no. 3, pp. 435–479, Jul. 1977.

[309] F. Podmaniczky, G. I. Tóth, T. Pusztai, and L. Gránásy, “Investigating nucleation using the phase-field method,” 2016.

[310] J. P. Simmons, Y. Wen, C. Shen, and Y. Z. Wang, “Microstructural development involving

nucleation and growth phenomena simulated with the phase field method," *Mater. Sci. Eng. A*, vol. 365, no. 1–2, pp. 136–143, 2004.

[311] J. P. Simmons, C. Shen, and Y. Wang, "Phase field modeling of simultaneous nucleation and growth by explicitly incorporating nucleation events," *Scr. Mater.*, vol. 43, no. 10, pp. 935–942, 2000.

[312] D. Blömker, E. Sander, and T. Wanner, "Degenerate Nucleation in the Cahn--Hilliard--Cook Model," *SIAM J. Appl. Dyn. Syst.*, vol. 15, no. 1, pp. 459–494, 2016.

[313] M. Born and V. Fock, "Beweis des adiabatensatzes," *Zeitschrift für Phys.*, vol. 51, no. 3–4, pp. 165–180, 1928.

[314] T. W. Heo, L. Zhang, Q. Du, and L.-Q. Chen, "Incorporating diffuse-interface nuclei in phase-field simulations," *Scr. Mater.*, vol. 63, no. 1, pp. 8–11, 2010.

[315] A. N. Shiryayev, "On The Statistical Theory of Metal Crystallization BT - Selected Works of A. N. Kolmogorov: Volume II Probability Theory and Mathematical Statistics," A. N. Shiryayev, Ed. Dordrecht: Springer Netherlands, 1992, pp. 188–192.

[316] W. H. . Press, S. A. . Teukolsky, W. T. . Vetterling, and B. P. Flannery, *Numerical Recipes 3rd Edition: The Art of Scientific Computing*. 2007.

[317] D. Jacqmin, "Calculation of Two-Phase Navier–Stokes Flows Using Phase-Field Modeling," *J. Comput. Phys.*, vol. 155, no. 1, pp. 96–127, 1999.

[318] U. Khalilov, G. Pourtois, A. C. T. van Duin, and E. C. Neyts, "On the c-Si|a-SiO2 Interface in Hyperthermal Si Oxidation at Room Temperature," *J. Phys. Chem. C*, vol. 116, no. 41, pp. 21856–21863, Oct. 2012.

[319] F. Giustino, "Infrared properties of the Si-SiO2 interface from first principles," Jan. 2005.

[320] P. A. V Johnson, A. C. Wright, and R. N. Sinclair, "Neutron scattering from vitreous silica II. Twin-axis diffraction experiments," *J. Non. Cryst. Solids*, vol. 58, no. 1, pp. 109–130, 1983.

[321] L. Röntzsch, "Shape Evolution of Nanostructures by Thermal and Ion Beam Processing," 2007.

[322] L. A. Maksimov, A. I. Ryazanov, K.-H. Heinig, and S. Reiss, "Self-organization of precipitates during Ostwald ripening," *Phys. Lett. A*, vol. 213, no. 1, pp. 73–76, 1996.

Acknowledgements

An dieser Stellemöchte ich mich bei all denjenigen bedanken, die mich während meiner Zeit am HZDR untersützt haben, meine Belastungen mittragen mussten und als Quelle der Motivation zur Seite standen.

Zuerst gebührt mein Dank Herrn Heinig, dessen außerordentliche Art mein Arbeitsleben mit ausreichend Humor genährt hat. Seine didaktischen Fähigkeiten haben sich vor allem in der Qualität meiner Vorträge manifestiert. Die Geduld, die konstruktive Kritik meiner Arbeit, nette Gespräche und hilfreiche Anregungen waren unbezahlbar und verdienen einen besonderen Dank.

Ich möchte auch Herrn Möller für seine Beteiligungen danken. Die fachliche Unterstützung und Hilfe beim Schreiben meiner Manuskripte war wesentlich für den Erfolg der Arbeit.

Die wichtigsten Personen, deren Schultern eine bemerkenswerte Last tragen mussten um mich zu unterstützen, war jedoch die Familie zu Hause. Energie schöpfen und Ausgleich finden hätte nicht besser funktionieren können als beim Puzzlen mit Jasmine oder beim Beobachten von Lilianes hochfrequenter Atemübungen vor dem Schlafengehen. Auch meine Frau Nadine hat sich einen besonderen Dank verdient. Ihr Verständnis und Unterstützung in allen Bereichen hat den Erfolg erst ermöglicht.

Meinen Eltern verdienen ebenfalls den gleichen Dank wie der Rest der Familie. Die Betreuung der Kinder zu jeder Zeit und unter jeglichen Umständen senkte Sorge und erhöhte Freude in einem unermesslichen Ausmaß. Die unzähligen Familientage im Garten, begleitet von aufregenden Gespräche und gutem Essen gaben ebenfalls einen exzellenten Ausgleich.

Ich bin unglaublich dankbar, dass Gott mich mit dieser Familie gesegnet hat.

This work has been funded by the European Union's Horizon 2020 research and innovation program under grant agreement No 688072.

Publications and Awards

Awards

- **Graduate Student Award** (2018) "*Atomistic Simulations to Design a Room-Tempearture Single Electron Transistor*" E-MRS Fall Meeting, Warsaw, Poland

Articles

- **T. Prüfer**, W. Möller, K. H. Heinig, D. Wolf, H. J. Engelmann, X. Xu, J. v. Borany (2019) "*Computer modeling of single-layer nanocluster formation in a thin SiO2 layer buried in Si by ion mixing and thermal phase decomposition*" J. Appl. Phys., vol. 125, no. 22, p. 225708
- X. Xu, **T. Prüfer**, D. Wolf, H. J. Engelmann, L. Bischoff, R. Hübner, K. H. Heinig, W. Möller, S. Facsko, J. v. Borany, G. Hlawacek (2018) "*Site-controlled formation of single Si nanocrystals in a buried SiO2 matrix using ion beam mixing*" Beilstein J. Nanotechnol., vol. 9, pp. 2883–2892

Conference Talks

- **T. Prüfer**, K.H.Heinig, W. Möller, J. v. Borany (2018) EMRS Fall Meeting, Warsaw, Poland, "*Atomistic Simulations to Design a Room-Temperature Single Electron Transistor*"
- **T. Prüfer**, D. Wolf, H.-J. Engelmann, R. Hübner, L. Bischoff, G. Hlawacek, K.-H. Heinig, S. Facsko, X. Xu, J. von Borany (2018) EMRS Fall Meeting, Warsaw, Poland, "*Si Quantum Dots for Single Electron Transistor: Synthesis, Characterization and Theoretical Comparison*"
- **T. Prüfer**, K.H.Heinig, W. Möller, J. v. Borany (2017) MRS Fall Meeting, Boston, USA, "*Atomistic Simulation of Interface-Driven Self-Alignment of Si-SiO2 Nanostructures*"
- **T. Prüfer**, K.H. Heinig, W. Möller, X. Xu, G. Hlawacek, S. Facsko, R. Hübner, D. Wolf, L. Bischoff, J. von Borany (2017) EIPBN Conference, Orlando, USA, "*Process Simulation of Si Dot Fabrication for SETs by Ion Beam Mixing and Phase Separation in Nanopillars*"
- **T. Prüfer**, K.H. Heinig, W. Möller, G. Hlawacek, X. Xu, C. Friedlund, F. Djurabekova , J. von Borany (2017) DPG Frühjahrstagung, Dresden, Germany, "*Process Simulation of Single Si Quantum Dot Formation for Single Electron Transistors*"
- **T. Prüfer**, K.H. Heinig, W. Möller, G. Hlawacek, X. Xu, J. von Borany, S. Facsko, R. Hübner, D. Wolf, L. Bischoff (2017) Ionentreffen, Göttingen, Deutschland, "*Process Simulation of Single Si Quantum Dot Formation for Single Electron Transistors*"
- **T. Prüfer**, K.-H. Heinig, W. Möller (2016) EMRS Fall Meeting, Warsaw, Poland, "*Atomic scale simulations of Si quantum dot self-assembly for single electron transistors*"
- K.-H. Heinig, G. Hlawacek, H.-J. Engelmann, **T. Prüfer**, X. Xu, W. Möller, L. Bischoff, A. Gharbi, R. Tiron, M. Rommel, J. von Borany (2019) EMRS Fall Meeting, Warsaw, Poland, "*CMOS-compatible Single Si Quantum Dot fabrication in a SiO_2 layer sandwiched in a Si nanopillar for a Room Temperature Single Electron Transistor*"

- K.-H. Heinig, H.-J. Engelmann, A. Gharbi, R. Tiron, **T. Prüfer**, J. von Borany (2019) *"Dramatic SiO_2 Thickness Reduction by Reactive Ion Etching of Nanopillars from Si/SiO_2/Si layer stacks",* EMRS Fall Meeting, Warsaw, Poland
- K.-H. Heinig, J. von Borany, **T. Prüfer**, X. Xu, W. Möller, G. Ahmed, R. Tiron, H. Gregor, L. Bischoff, H.-J. Engelmann, S. Facsko (2018) *"Organized Single Si Quantum Dots in tiny SiO2 volumes: Self-alignment for Single Electron Transistors",* EMRS Fall Meeting, Warsaw, Poland
- K.-H. Heinig, J. von Borany, **T. Prüfer**, X. Xu, W. Möller, A. Gharbi, R. Tiron, G. Hlawacek, L. Bischoff, H.-J. Engelmann, S. Facsko (2018) *"Manufacturability of Single Si Quantum Dots for Single Electron Transistors operating at Room Temperature",* EMRS Fall Meeting, Warsaw, Poland
- X. Xu, G. Hlawacek, H.-J. Engelmann, K.-H. Heinig, W. Möller, A. Gharbi, R. Tiron, L. Bischoff, **T. Prüfer**, R. Hübner, S. Facsko, J. von Borany (2019) *"Avoiding Amorphization Related Shape Changes of Nanostructures during Medium Fluence Ion Beam Irradiation of Semiconductor Materials",* AVS 65th International Symposium & Exhibition, Long Beach, USA
- X. Xu, K.-H. Heinig, W. Möller, A. Gharbi, R. Tiron, H.-J. Engelmann, L. Bischoff, **T. Prüfer**, R. Hübner, S. Facsko, G. Hlawacek, J. von Borany (2018) *"Towards a Vertical Nanopillar-Based Single Electron Transistor – A High-Temperature Ion Beam Irradiation Approach",* MRS Fall Meeting & Exhibit, Boston, USA
- X. Xu, G. Hlawacek, D. Wolf, H.-J. Engelmann, **T. Prüfer**, R. Hübner, L. Bischoff, J. von Borany, S. Facsko, K.-H. Heinig (2018) *"Localized ion beam mixing using a focused Neon beam for future SET applicatons",* picoFIB, 31.01.2018, Dresden, Germany
- K.-H. Heinig, J. von Borany, G. Hlawacek, R. Hübner, D. Wolf, H.-J. Engelmann, L. Bischoff, X. Xu, **T. Prüfer**, W. Möller, S. Facsko (2017) *"Vertical Nanowire Based Single Electron Transistor Self-Assembled by Ion Beam Mixing and Phase Separation",* Fall Meeting of the Materials Research Society, 26.11.-01.12.2017, Boston, USA
- K.-H. Heinig, **T. Prüfer**, W. Möller, G. Hlawacek, X. Xu, L. Bischoff, R. Hübner, D. Wolf, S. Facsko, J. von Borany (2017) *"Ion-Beam-Induced Self-Organisation of Nanostructures at Interfaces",* FOR3NANO: Formation of 3D Nanostructures by Ion Beams, 28.-30.06.2017, Helsinki, Finland
- G. Hlawacek, X. Xu, **T. Prüfer**, D. Wolf, R. Hübner, L. Bischoff, W. Möller, S. Facsko, J. von Borany, K.-H. Heinig (2017) *"Spatially controlled fabrication of individual silicon nano clusters using ion beam mixing and thermal treatment",* EIPBN, 30.05.-02.06.2017, Orlando, USA
- X. Xu, **T. Prüfer**, D. Wolf, R. Hübner, L. Bischoff, H.-J. Engelmann, A. Gharbi, K.-H. Heinig, G. Hlawacek, J. von Borany (2018) *"Site-controlled Si Nanodot Formation for a RT-SET via Ion Beam Mixing and Phase Separation",* HeFIB2018 Helium and emerging Focused Ion Beams, Dresden, Germany
- X. Xu, D. Wolf, G. Hlawacek, M. Engler, R. Hübner, L. Bischoff, **T. Prüfer**, K.-H. Heinig, J. von Borany (2017) "*Site-controlled Si quantum dots in buried SiO2 layer formed by ion-beam implantation and phase separation",* Ionenstrahltreffen 2017, 13.02.2017, Göttingen, Germany
- X. Xu, D. Wolf, G. Hlawacek, R. Hübner, A. Gharbi, **T. Prüfer**, L. Bischoff, K.-H. Heinig, S. Facsko, J. von Borany (2017) „*Site-controlled formation of Si nanodots in a buried SiO2 layer via ion-beam implantation and phase separation",* 81. DPG-Jahrestagung und DPG-Frühjahrstagung der Sektion Kondensierte Materie, 22.03.2017, Dresden, Germany

- X. Xu, D. Wolf, **T. Prüfer**, G. Hlawacek, R. Hübner, L. Bischoff, M. Perego, A. Gharbi, K.-H. Heinig, J. von Borany (2017) *"Site-controlled Si Nanodot Formation for a RT-SET via Ion Beam Mixing and Phase Separation",* FOR3NANO: Formation of 3D Nanostructures by Ion Beams, 29.06.2017, Helsinki, Finnland
- X. Xu, G. Hlawacek, D. Wolf, **T. Prüfer**, R. Hübner, L. Bischoff, Perego, M.; A. Gharbi, H.-J. Engelmann, S. Facsko, K.-H. Heinig, J. von Borany (2017) *"Site-controlled Si Nanodot Formation for a RT-SET via Ion Beam Mixing and Phase Separation",* AVS 64th International Symposium & Exhibition, 01.11.2017, Tampa, FL, USA
- M. Belli, M. Alia, X. Xu, C. Laviron, A. Gharbi, M. Rommel, F. Stumpf, **T. Prüfer**, D. Wolf, L. Bischoff, R. Hübner, G. Hlawacek, S. Facsko, K.-H. Heinig, J. von Borany, M. Fanciulli (2017) *"Electrical characterization of Si nanocrystal devices suitable for RT-SET operation",* EUROMAT 2017, 17.-22.09.2017, Thessaloniki, Greece
- S. Facsko, K.-H. Heinig, K. H. Stegemann, **T. Prüfer**, X. Xu, G. Hlawacek, R. Hübner; D. Wolf, L. Bischoff, W. Möller, J. von Borany (2017) *"Ion Beam-Enabled CMOS-Compatible Manufacturing of SETs Operating at Room Temperature",* Ion-Surface Interactions 2017, 21.-25.08.2017, Moskow, Russia
- D. Wolf, X. Xu, **T. Prüfer**, G. Hlawacek, L. Bischoff, W. Möller, H.-J. Engelmann, S. Facsko, J. von Borany, K.-H. Heinig, R. Hübner, (2017) *"Energy-filtered TEM studies on silicon nanoparticles acting as quantum dots in single electron transistors",* Microscopy Conference 2017, MC 2017, 21.-25.08.2017, Lausanne, Switzerland
- K.-H. Heinig, K. H. Stegemann, J. von Borany, S. Facsko, G. Hlawacek, R. Hübner, L. Bischoff, W. Möller, **T. Prüfer**, X. Xu, (2016) *"Self-assembly of single Si quantum dots in SiO2",* E-MRS 2016 Fall Meeting, 19.-22.09.2016, Warszawa, Poland
- K.-H. Heinig, S. Facsko, K. H. Stegemann, **T. Prüfer**, X. Xu, G. Hlawacek, R. Hübner, D. Wolf, L. Bischoff, W. Möller, J. von Borany (2016) *"Ion Irradiation Assisted Fabrication of Si Quantum Dots for Ultra-Low Power Electronics",* 20th International Conference on Ion Beam Modification of Materials (IBMM 2016), 30.10.-4.11.2016, Wellington, New Zealand

Erklärung

Hiermit versichere ich, dass ich die vorliegende Arbeit ohne zulässige Hilfe Dritter und ohne Benutzung anderer als der angegebenen Hilfsmittel angefertigt habe. Die aus fremden Quellen direkt oder indirekt übernommenen Gedanken sind als solche kenntlich gemacht. Die Arbeit wurde bisher weder im Inland noch im Ausland in gleicher oder ähnlicher Form einer anderen Prüfungsbehörde vorgelegt.

Die Dissertation wurde unter der Betreuung von Dr. Karl-Heinz Heinig und Prof. Dr. Jürgen Faßbender am Helmholtz-Zentrum-Dresden-Rossendorf angefertigt.

Dresden, den